A multidisciplinary investigation of magmatic overpressure and its implications for volcanic eruption triggering





Anna Brookfield

Pembroke College

University of Oxford

Supervised by Dr. Michael Cassidy and Professor Lars Hansen.

An integrated thesis submitted for the degree of Doctor of Philosophy

June 2023

Declaration

I declare that the content of this thesis is entirely my own, unless stated otherwise.

Abstract

Magmatic overpressure – pressure in excess of lithostatic – can be generated by processes such as thermal expansion, crystallisation or magma injection. We cannot observe these processes directly, yet the magnitude and timescale of overpressure build-up are both critical for understanding failure limits and forecasting volcanic eruptions. This thesis explores variations in the magnitude and rate of overpressure build-up with varying magmatic and crustal properties. It also assesses the use of electron backscatter diffraction as a new tool for probing reservoir overpressurisation and storage conditions.

Chapter 2 demonstrates that there are variations in the intrinsic overpressure-generating capacity of magmas according to their initial fluid content. Overpressure due to second boiling increases in magnitude with increasing X_{H2O}, and is at a peak in magmas with initial H_2O contents which are at the solubility limit. The implications of this variability in overpressure are discussed in the context of eruption style, and results are coupled with a thermal model to determine the associated timescales of overpressurisation. Chapter 3 continues with this novel coupling of thermodynamic and thermal models by quantifying the effect of changes in magma reservoir volume, geometry and crustal properties on timescales of overpressurisation. These timescales are discussed in the context of other overpressurisation mechanisms, including magma buoyancy and bubble rise. The importance of overpressurisation rate, as well as the absolute value, is highlighted in the context of eruption triggering. Chapter 4 explores overpressurisation from a different angle, by analysing deformation in natural and experimentally deformed volcanic samples to investigate physical signals of overpressurisation. Crystal plastic deformation is quantified using electron backscatter diffraction, and demonstrates potential for determining long-term magma storage conditions. Further experimentation to assess the effect of crystallinity, and analysis of samples from a range of explosive eruptions are the most useful next steps to achieve this goal.

Acknowledgements

I would like to thank my primary supervisor Dr. Mike Cassidy for his kindness, support, insights and enthusiasm. I am extremely lucky to have benefitted from his knowledge, experience and mentorship. Thank you to Prof. Lars Hansen for sharing his expertise in collecting, processing and interpreting EBSD data, and for his helpful feedback on my work. Thank you to the National Environmental Research Council for funding this project.

Thank you to all of my collaborators, in particular Dr. Gregor Weber, for being so generous with their time, and for the interesting discussions we had which improved my work. Huge thanks to Dr. Katie Kumamoto and Dr. Rellie Goddard for their assistance, encouragement and patience in using the scanning electron microscope in Earth Sciences. Thanks to Dr. Phani Karamched from the Materials Science department at Oxford for his expertise and incredible organization skills. Thank you to Dr. Richard Walshaw at the University of Leeds for collecting high quality EBSD data for me during lockdown. Thanks also to Dr. Mark Thomas, Prof. Jurgen Neuberg, Dr. Catherine Annen, Dr. Diana Roman and Dr. Amy Ryan for taking the time to comment on my work.

It has been a pleasure to be part of the Volcanology group at Oxford. Special thanks to David, Tamsin, Victoria, Mike, Amber, Grace, Alice, Annika and Bei-Bei for some fascinating discussions, tasty pub lunches and film screenings. Thanks also to the fabulous inhabitants of office 20.16 for their encouragement, biscuits and plants.

I am extremely fortunate to be part of the greatest DTP cohort ever, where I have made lifelong friends. In particular thank you to David Colby and Kirsty Harrington for being wonderful people, and to all those in Parker St and Addison Crescent who have made my life so much richer (although definitely not in a financial sense). Thank you to David Pyle and Victoria Forth for making all of that possible.

Thank you to my best friends Sarah, Colette, Ailsa and Amy for cheering me on and taking the mick out of me in equal measure. I am also very grateful to my Uncle Martin for his support

and encouragement. A huge thank you to my parents Bill and Caron Brookfield for their love, kindness and sense of humour, and for helping me to always see the bigger picture. Finally and most importantly thank you so much to my partner Mike Simpson for his love, support and encouragement.

This is dedicated to my grandparents, Peter and Patricia Barrie and Mary and Arthur Brookfield, and to Sheila Bell.

Contents

Declaration……i
Abstract……ii
Acknowledgements……iii
Contents……v

List of figures……ix

Chapter 1 - Introduction 1

1.1 Definition of overpressure 1

1.2 Importance of overpressure 2

1.3 Methods for estimating overpressure 3

1.3.1 Methods applicable to any pressurisation mechanism 3

1.3.2 Methods relevant to a specific pressurisation mechanism 5

1.4 Critical overpressure 7

1.5 Aims of this study 8

1.6 Thesis overview 10

Chapter 2 - Magmatic volatile content and the overpressure 'sweet spot': implications for volcanic eruption triggering and style 11

Abstract 11

2.1. Introduction 12

2.2. Methods 15

2.2.1 Rhyolite-MELTS thermodynamic modelling 15

2.2.2 Thermal modelling 17

2.3. Modelling results 19

2.3.1 Thermodynamic modelling 19

2.3.2 Thermal modelling 22

2.4. Discussion 26

2.4.1 Critical overpressures and timescales of pressurization 26

2.4.2 Implications for eruption triggering 29

2.4.3 Implications for eruption style 31

2.5 Model limitations 33

2.5.1 Pressure dissolution feedbacks 33

2.5.2 Closed system assumption 35

2.6. Conclusions 37

Chapter 3 - Constraining the magnitude and rate of overpressure build-up with varying magmatic parameters 38

Abstract 38

3.1. Introduction 39

3.2. Methods 41

3.2.1 Rhyolite- MELTS thermodynamic modelling 41

3.2.2 Thermal modelling 42

3.2.3 Critical overpressure and crustal relaxation timescales 45

3.3. Modelling results 47

3.3.1 Varying reservoir shape 47

3.3.2 Varying X_{H2O} 49

3.3.3 Varying reservoir size 50

3.3.4 Varying reservoir depth 52

3.3.5 Varying geothermal gradient 53

3.3.6 Varying thermal conductivity 55

3.3.7 Temporal evolution of other magma properties 56

3.4. Discussion 58

3.4.1 Variations in time taken to reach critical overpressure 58

3.4.2 Effect of overpressure-induced strain rate 64

3.4.3 Effect of crustal behaviour on internal magma properties 65

3.4.4 Overpressure due to magma buoyancy 66

3.4.5 Overpressure due to bubble rise 66

3.4.6 Pressure distribution within a magma reservoir 70

3.4.7 Modelling magma properties in the run up to eruption 71

3.4.8 Implications for eruption triggering 71

3.5. Conclusions 74

Chapter 4 - Exploring crystal-plastic deformation in natural and experimentally-overpressurised magmas 75

Abstract 75

4.1. Introduction 76

4.2. Methods 80

4.2.1 Experimental petrology 80

4.2.2 EBSD data collection 82

4.2.3 EBSD data analysis 83

4.3. Results 85

4.3.1 Kernel average misorientation maps 85

4.3.2 Kernel average misorientation histograms 92
4.3.3 Grain reference orientation deviation and grain orientation spread maps 94
4.3.4 Grain reference orientation deviation histograms 101
4.3.5 Misorientation line profiles 102
4.4. Discussion 108
4.4.1 Extent and location of crystal deformation 108
4.4.2 Magnitude of crystal deformation 108
4.4.3 Duration of experimental overpressurisation 110
4.4.4 Effect of experimental quenching 111
4.4.5 Effect of sample preparation 112
4.4.6 Assigning deformation to magmatic processes 113
4.5. Future work 116
4.5.1 Work on natural volcanic samples 116
4.5.2 Work on experimentally deformed/ synthetic samples 117

Chapter 5 - Conclusions and future work 120
5.1 Conclusions 120
5.2 Future work 122
5.2.1 Coupling magma thermodynamics and crustal thermomechanics 122
5.2.2 Linking reservoir and conduit models 122
5.2.3 Investigating magma storage with EBSD 123

References 124

Appendices 137

Appendix 1: Rhyolite-MELTS P-T-composition table 137

Appendix 2: Rhyolite-MELTS composition plots 138

Appendix 3: Melt fraction- temperature curves..... 142

Appendix 4: Overpressure evolution at 0.05 wt% H_2O increments..... 143

Appendix 5: Overpressure evolution for basalt and rhyolite end-members 144

Appendix 6: Overpressure with reservoir compressibility term..... 145

Appendix 7: Overpressure evolution for varying reservoir size 146

Appendix 8: Volume change and compressibility evolution..... 147

Appendix 9: EBSD map step sizes 148

Appendix 10: Phase maps..... 149

Appendix 11: KAM maps with no threshold 164

Appendix 12: KAM histograms raw data. 179

Data appendices 181

Data appendix 1 181

Data appendix 2 181

Data appendix 3 181

List of tables and figures

Chapter 1

Table 1.1. A selection of overpressure terms used in key references 2

Figure 1.1. Trade-off between magma source radius and overpressure 4

Figure 1.2. Magmatic overpressure calculated from dyke aspect ratios 6

Chapter 2

Figure 2.1. Overpressure evolution for varying initial H2O content 20

Figure 2.2. Overpressure evolution for varying initial XH2O 21

Figure 2.3. Temporal evolution of average intrusion overpressure for varying initial H2O content 24

Figure 2.4. Temporal evolution of average intrusion overpressure for varying initial XH2O 26

Figure 2.5. Summary of the time taken to reach critical overpressures of 10 MPa and 20 MPa 28

Figure 2.6. Magmatic H2O content, eruption style and peak overpressure 33

Figure 2.7. Pressure (lithostatic) plus overpressure curves for Kelud 34

Figure 2.8. Comparing the effect of open- versus closed-system behaviour on overpressurisation 36

Chapter 3

Figure 3.1. Magma reservoir geometries used in thermal modelling 45

Figure 3.2. Temporal evolution of overpressure for varying H2O contents and reservoir shapes 48

Figure 3.3. Temporal evolution of overpressure for varying initial H2O content and XH2O 50

Figure 3.4. Temporal evolution of overpressure for varying reservoir shape, size and H2O content 51

Figure 3.5. Temporal evolution of overpressure for varying Rhyolite-MELTS storage pressures 53

Figure 3.6. Temporal evolution of overpressure for varying geothermal gradients 54

Figure 3.7. Temporal evolution of overpressure for varying thermal conductivity values 56

Figure 3.8. Temporal evolution of average compressibility and overpressure 57

Figure 3.9. Summary of the time taken to reach 20 MPa critical overpressure 59

Figure 3.10. Overpressure for varying lithostatic (storage) pressures of 50 - 300 MPa 62

Figure 3.11. Schematic diagram of overpressurisation mechanisms 68

Figure 3.12. Summary of the maximum average reservoir overpressure for different scenarios 73

Chapter 4

Figure 4.1. Summary diagram and table showing experimental conditions 81

Figure 4.2. Area of each map collected in this study and sample EBSD map 84

Figure 4.3. Phase map and KAM map of sample SHV_00 87

Figure 4.4. Phase map and KAM map of sample SHV_00 88

Figure 4.5. Phase map and KAM map of sample SHV_01 89

Figure 4.6. Phase map and KAM map of sample SHV_02 90

Figure 4.7. Phase map and KAM map of sample SHV_04 91

Figure 4.8. Kernel average misorientation histogram envelopes 93

Figure 4.9. GROD and GOS maps for sample SHV_00 96

Figure 4.10. GROD and GOS maps for sample SHV_00 97

Figure 4.11. GROD and GOS maps for sample SHV_01 98

Figure 4.12. GROD and GOS maps for sample SHV_02 99

Figure 4.13. GROD and GOS maps for sample SHV_04 100

Figure 4.14. Grain reference orientation deviation histogram envelopes 101

Figure 4.15. Misorientation profile across grain 1798, sample SHV_00 104

Figure 4.16. Misorientation profiles across grains 813 and 1254, sample SHV_01 105

Figure 4.17. Misorientation profiles across grains 511 and 524, sample SHV_02 106

Figure 4.18. Misorientation profile across grain 526, sample SHV_04 107

Figure 4.19. Strain rate from dislocation creep in wet plagioclase for varying temperatures 111

Figure 4.20. Kernel average misorientation and band contrast maps 113

Figure 4.21. Comparison of crystal proximity and crystal deformation 115

Chapter 1 - Introduction

1.1 Definition of overpressure

Overpressure build-up within a magma reservoir can lead to fracturing of the surrounding crust, propagation of dykes to the surface, and volcanic eruption. Within the geosciences, the term overpressure is used in the fields of volcanology, structural geology and hydrocarbon exploration (Peacock *et al.*, 2017). In this work we focus on overpressure in the context of a magma storage area prior to eruption. We define overpressure as a pressure in excess of the expected lithostatic pressure for a given depth, and we represent it using the symbol ΔP with units of MPa. This definition is equivalent to the ΔP term of Trasatti *et al.* (2005) and the Pe ('excess pressure') term of Gudmundsson (2012). Overpressure can be generated by a variety of mechanisms, including magma injection, volatile exsolution (second boiling), buoyancy and thermal expansion (Cañón-Tapia, 2014). Overpressure is sometimes defined in the context of magma reservoir pressurisation prior to eruption, and sometimes in the context of the pressure needed to propagate a dyke from a magma storage zone. Some studies are concerned with a specific mechanism of overpressurisation, whilst some are concerned only with overpressure values and not the driving mechanism. As a result, there are various terms used in the literature to describe overpressure, and a selection of these are compiled in **table 1.1**. The variety of terms used to describe overpressure, and the occasional lack of a definition altogether (Peacock *et al.*, 2017) is surprising given the importance of this term. The disparity in usage of overpressure is very different to the treatment of elastic moduli which are often used in overpressure calculations, and are generally well-defined with a consistency of usage. In chapters 2 and 3 we focus on the magnitude and timescales of overpressure generated by second boiling. In chapter 4 we use experiments to mimic pressurisation caused by magma injection.

Term	Definition	Author	Year
P	Total pressure due to second boiling	Tait	1989
Po	Excess pressure	Rubin	1995a
ΔPmax	Maximum overpressure	Jellinek and DePaolo	2003
ΔP	Overpressure	Trasatti et al.	2005
k	Additional uniform pressure	Grosfils	2007
Po	Overpressure within a dyke	Gudmundsson	2012
Pe	Excess pressure in a magma chamber	Gudmundsson	2012
ΔPinject	Overpressure generated by magma injection	Caricchi et al.	2014
ΔPbuoy	Overpressure generated by magma buoyancy	Caricchi et al.	2014

Table 1.1. A selection of overpressure terms from key references.

1.2 Importance of overpressure

Volcanic eruptions can be grouped into two categories, 1) those which are internally triggered via processes such as magma injection and mixing (Morgavi *et al.*, 2019), CO_2 flushing (Caricchi *et al.*, 2018), and second boiling (Arzilli *et al.*, 2019), and 2) those which are externally triggered, e.g. via volcanic flank collapse or earthquakes (Seropian *et al.*, 2021). Considering the first category only, an eruption can occur if the rate and magnitude of overpressure build-up is great enough to overcome the strength of the surrounding rock. Understanding magmatic overpressurisation, and in particular any variations in its magnitude and rate, is therefore important for forecasting volcanic eruptions. Geodetic modelling provides a link between ground deformation and the evolving conditions within a magma reservoir, including overpressure (Segall, 2019). Monitoring ground deformation therefore makes it possible to obtain overpressure estimates during phases of unrest (e.g. Bato *et al.*, 2017), which can aid in eruption forecasting. Advances in the characterisation of crustal properties (e.g. Heap *et al.*, 2020) and in geophysical imaging to determine reservoir shape and size (Paulatto *et al.*, 2022) will help improve the accuracy of real-time overpressure estimates.

Magmatic overpressure can also affect volcanic eruption style via its effect on magma ascent rate. Woods and Koyaguchi (1994) demonstrate that eruption style is dependent on magma

flow rate and reservoir overpressure, and identify a regime in which high overpressures can only generate explosive eruptions. In their conduit modelling study, Thomas and Neuberg (2014) find that increasing magmatic overpressure correlates with greater magma ascent velocities. Rapid ascent rates leave relatively little time for magma to degas, and so are often associated with explosive eruptions (e.g. Gonnermann and Manga, 2012).

1.3 Methods for estimating overpressure

Overpressure can be estimated or modelled in a variety of ways. We group these broadly into methods which are applicable to any pressurisation mechanism, and those which are concerned with specific mechanisms, such as second boiling or magma injection.

1.3.1 Methods applicable to any pressurisation mechanism

Some of the earliest work involving magmatic overpressure is that of Mogi (1958), which fits patterns of ground deformation to a spherical, pressurising magma source via the properties of the surrounding rock, which are assumed to be elastic. The Mogi model can be used to solve for magma source parameters such as depth, radius and pressure change, if elastic moduli and ground displacement are known. It has since been adapted to allow for a greater source radius/ depth ratio (McTigue, 1987). This type of model cannot provide unique values for overpressure, but it returns a combined overpressure – source volume term. The wealth of satellite data which has become available over the past few decades, coupled with advances in modelling capabilities (e.g finite element modelling) has fuelled many studies which use geodetic inversion to estimate magma source properties, including overpressure (e.g., Masterlark *et al.*, 2010; Bato *et al.*, 2017; Albino *et al.*, 2019; Morales Rivera *et al.*, 2019; Cabaniss *et al.*, 2020). Trasatti *et al.* (2005) use a finite element model and Mogi-type equation to estimate magma source properties at Campi Flegrei, Italy.

$$u_z\,(r, z = 0) = \frac{1-v}{\mu}\,\Delta P a^3\,\frac{d}{(r^2 + d^2)^{3/2}} \qquad \text{eq 1.1}$$

Where U_z is vertical ground displacement at the free surface (z=0), v is Poisson's ratio, μ is crustal rigidity, ΔP is overpressure, a is magma source radius, d is source depth and r is horizontal distance from the uplift symmetry axis. To illustrate the non-unique trade-off between magma source radius and overpressure in this type of model, we rearrange equation 1.1 to find the ΔPa^3 term, and then vary overpressure to find the corresponding source radius. Results are shown in **figure 1.1** for a variety of crustal rigidity values and a vertical displacement of 1 metre.

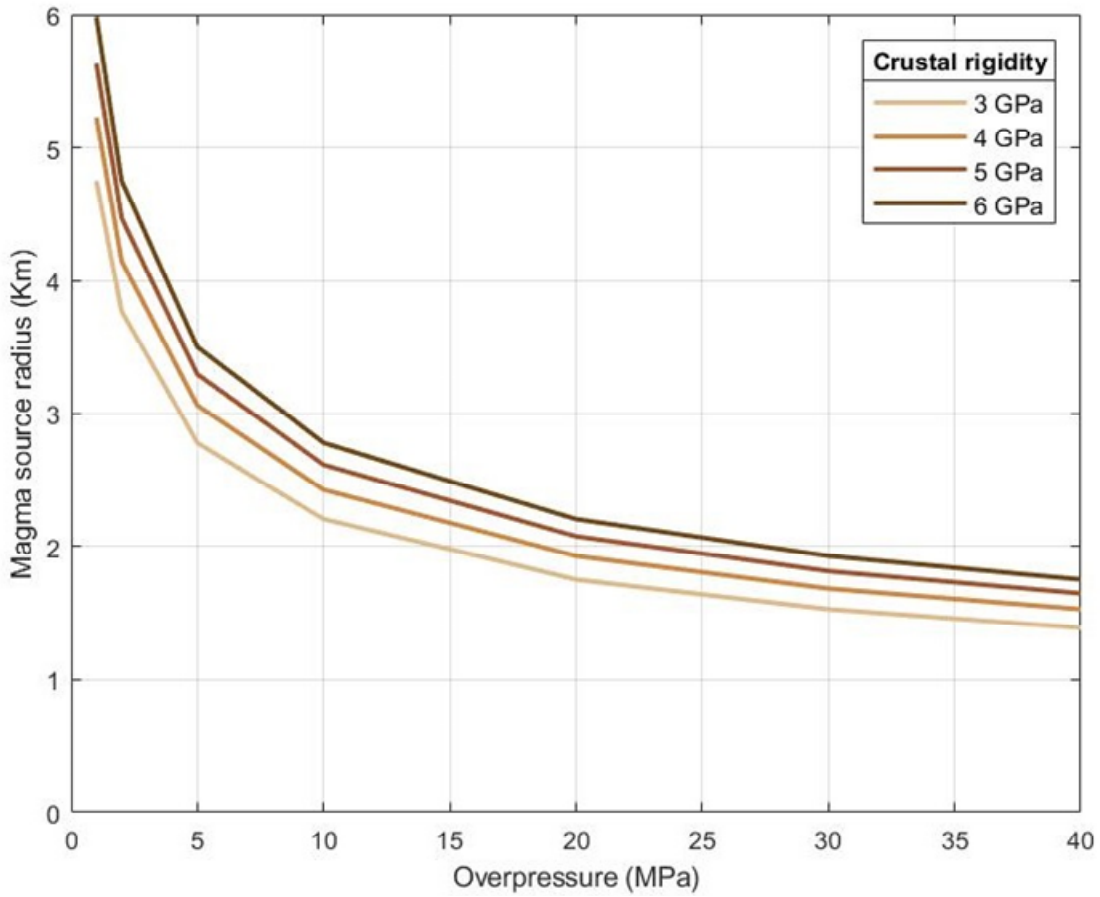


Figure 1.1. Trade-off between magma source radius and overpressure, calculated from equation 1 of Trasatti et al. (2005). Rearranging this equation we find ΔPa^3, and then vary overpressure to find the source radius for various values of crustal rigidity. This assumes a Poisson's ratio of 0.3, a crustal rigidity range of 3- 6 GPa (Trasatti et al. use 4 GPa), a source depth of 5000 m, a vertical ground displacement of 1 m, and a horizontal distance from the uplift of 0 m.

For a given reservoir radius, higher crustal rigidity values require higher overpressures to generate the same amount of vertical displacement. Smaller magma bodies also require higher overpressures to generate the same amount of uplift.

Other early, influential work relating to reservoir overpressurisation is that of Pollard (1987), which uses dyke aspect ratios and elastic moduli to approximate a driving pressure.

$$\frac{t}{l} \sim \frac{(P-S)}{\mu/(1-v)} \qquad \text{(eq 1.2)}$$

Where t is dyke thickness, l is dyke length, P is total magma pressure, S is remote compressive stress, μ is host rock shear modulus and v is Poisson's ratio. P-S can be considered equivalent to our definition of overpressure, and is adapted to mean 'excess source pressure at the dyke entrance' (Po) by Rubin (1995a). Pollard (1987) uses t/l values on the order of 0.001 - 0.0001, a μ range of 1-6 GPa and a v of 0.25 to constrain driving pressure (overpressure) values to ~0.1 – 8 MPa. There is some uncertainty over the values of elastic moduli relevant for volcanic areas. Gudmundsson (2011) quotes typical Young's modulus values of 50-90 GPa for basalt - which translate into μ values of 19.2 GPa and 34.6 GPa respectively, using v = 0.30. However, Heap *et al.* (2020) recommend that the shear modulus for a typical volcanic rock is much lower than this, at 2.1 GPa. We demonstrate how this range in potential shear modulus values affects overpressure estimates in **figure 1.2**, using dyke aspect ratios measured by Gudmundsson (1983, 2011) and Geshi *et al.* (2020), v = 0.30 and a range of shear modulus values. This plot demonstrates that uncertainties in the elastic properties of the surrounding rock can result in an order of magnitude difference in overpressure values using this method.

1.3.2 Methods relevant to a specific pressurisation mechanism

Magmatic recharge (involving magma of any composition relative to the initial magma) is the most commonly cited eruption trigger according to Kent *et al.* (2021). Degruyter and Huber (2014) present a numerical model which tracks the thermodynamic state of a spherical magma body as new magma is added to it. Their model is later adapted to consider the effect of

episodic recharge on magma reservoir growth (Degruyter *et al.*, 2016), and the effect of pre-existing volatiles on magma recharge dynamics (Degruyter *et al.*, 2017).

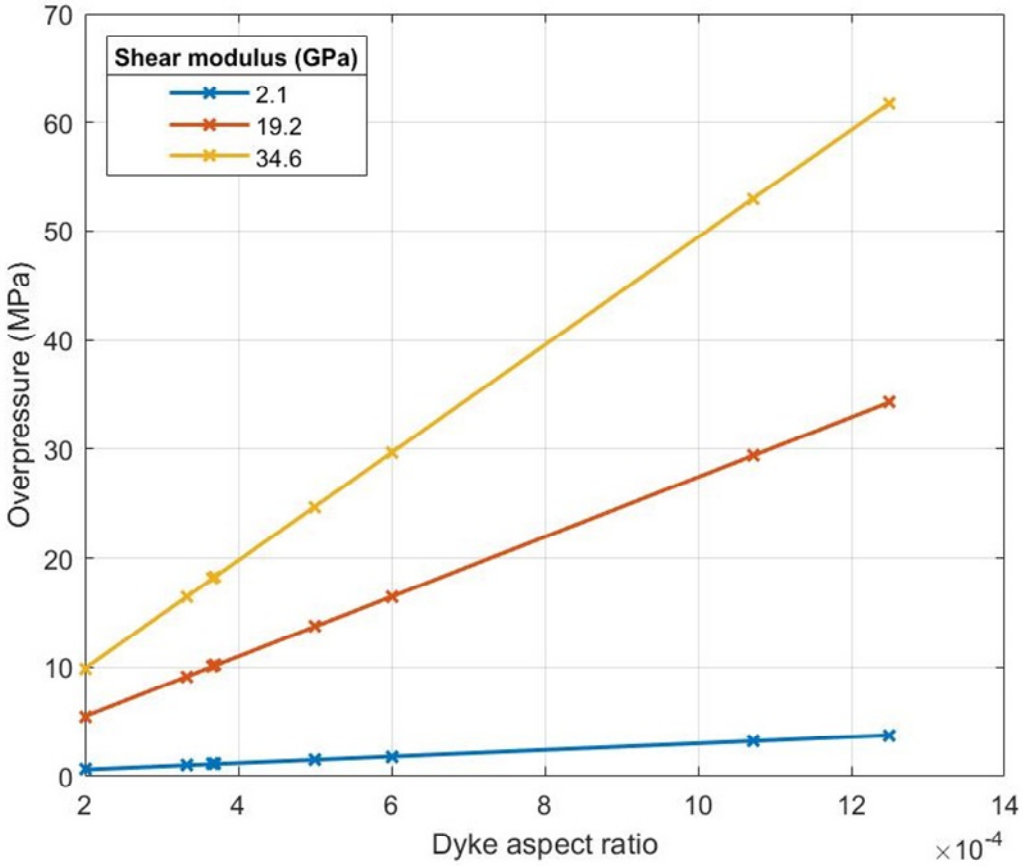


Figure 1.2. Overpressure for varying dyke aspect ratios (half-thickness/ half-length) and crustal shear modulus, calculated from Pollard (1987), using a Poisson's ratio of 0.30. A shear modulus of 2.10 GPa is recommended by Heap et al. (2020). Shear moduli of 19.23 and 34.62 GPa are calculated from Young's modulus values for basalt of 50 and 90 GPa respectively, representing the 'typical' range quoted in Gudmundsson (2011).

Caricchi *et al.* (2014) estimate the overpressure generated by magma injection ΔP_{inject}

$$\Delta P_{inject} = \frac{2n_{crust}\ Q_{inst}}{3V_{res}} \qquad \text{(eq 1.3)}$$

Where n_{crust} is crustal viscosity, Q_{inst} is magma influx and V_{res} is reservoir volume. Magma recharge is now a relatively widely-accepted eruption triggering mechanism, as the evidence

for this process can be observed in eruptive products (e.g. Barclay *et al.*, 2010; Morgavi *et al.*, 2019)

Second boiling occurs when increasing crystallisation results in volatile oversaturation in the melt, leading to volatile exsolution and volume expansion. Early work on this process includes Tait *et al.* (1989), who suggested that second boiling is a viable eruption trigger on its own, without needing an influx of fresh magma. Tramontano *et al.* (2017) also focus on second boiling, using Rhyolite-Melts cooling simulations to calculate overpressure using the equation

$$\Delta P = \frac{\Delta V}{V * \beta} \quad \text{(eq 1.4)}$$

Where ΔV is volume change, V is system volume and β is system compressibility. We use this same methodology in chapters 2 and 3 as it is easily adapted for a variety of magmas, and accounts for evolving magma compressibility, crystallisation contraction and thermal properties of the magma during cooling. One key limitation of this method is that it does not account for the properties of the surrounding crust, effectively assuming that the crust is rigid, or that timescales of volatile-exsolution are faster than those of crustal relaxation. These limitations are discussed and explored further in chapters 2 and 3. The importance of second boiling as an eruption trigger is debated. For example, Cañón-Tapia (2014) states that it has a first order control on eruption triggering, whilst Annen *et al.* (2023) state that second boiling will always be subordinate to magma recharge.

Finally, Caricchi *et al.* (2014) state that overpressure generated by magma buoyancy (ΔP_{buoy}) is a key trigger for super-eruptions, and is capable of generating overpressures on the order of 10s of MPa. However, this is debated by Gregg *et al.* (2015) who suggest that magma buoyancy is not capable of triggering eruptions. This is discussed further in section 3.4.4.

1.4 Critical overpressure

Critical overpressure, $(\Delta P)_{critical}$, refers to the overpressure required to fracture the material surrounding a magma reservoir and potentially generate an eruption. A process can therefore

be considered a viable eruption trigger if it can generate overpressure equal to $(\Delta P)_{critical.}$ Early work on dyke aspect ratios (Pollard, 1987) and dyke propagation (Rubin, 1995a) put limits on the critical overpressure which could drive magma ascent of ~ 0 -10 MPa. Jellinek and DePaolo (2003) then adapted this concept, finding critical overpressures in the range of 10 – 40 MPa for rhyolitic dykes. As a general rule it is thought that critical overpressure is equal to twice the tensile strength of the surrounding rock (e.g. Tait *et al.*, 1989; Parfitt *et al.*, 1993), so around 10 – 20 MPa, based on tensile strength estimates of 5 – 10 MPa for volcanic rocks (Gudmundsson, 2011). However, this is debated with some researchers suggesting that $(\Delta P)_{critical}$ may instead be ~ 100 MPa (Grosfils, 2007). In addition, as mentioned previously there are a range of possible values for elastic moduli, which will in turn will affect critical overpressure.

The behaviour of the crust surrounding a magma reservoir can modify overpressure build-up, resulting in deviations from models which assume a rigid surrounding crust. For example, Jellinek and DePaolo (2003), Del Negro *et al.* (2009), and Head *et al.* (2022) all demonstrate that a viscous crustal response results in an increase in $(\Delta P)_{critical}$, so more pressurisation is needed to initiate failure in these systems. Although these models consider the effect of crustal rheology on overpressure, there are no models which fully couple the behaviour of the crust with feedbacks on magma thermodynamics. We highlight this as a major gap in the research in section 4.3. The timescale of overpressurisation versus that of crustal deformation is also important when considering eruption triggering. Work by Degruyter and Huber (2014) and Townsend *et al.* (2019) has defined various eruptive regimes which are governed by the timescales of crustal response, magma injection and magma cooling. The work we present in chapters 2 and 3 is relevant for relatively small, shallow reservoirs, placing them in a cooling-dominated regime where the crust behaves in a non-viscous manner.

1.5 Aims of this study

The previous discussion shows that the effectiveness of second boiling as an eruption trigger is debated. It also demonstrates that geodetic estimates of overpressure give non-unique

values. Therefore, one main aim of this work is to determine the magnitude and timescales of pressurisation from second boiling. We explore overpressurisation for varying intrinsic magma properties, and for variations in the thermal properties of the surrounding crust. This aim is framed in the context of second boiling as an eruption trigger. Another main aim is to assess whether there is a fingerprint of overpressurisation in eruptive products via analysis of crystal-plastic deformation. This aim is framed in the context of providing a new tool to probe magma storage conditions. These aims are broken down further as follows.

1) Quantify the magnitude of overpressurisation from second boiling for a variety of realistic volcanic systems. (Chapter 2.)

2) Explore the effect of variations in overpressurisation on eruption style. (Chapter 2.)

3) Quantify the timescales of overpressurisation from second boiling for a variety of realistic volcanic systems. (Chapters 2 and 3.)

4) Determine the extent to which intrinsic magma conditions, such as fluid content, affect the magnitude and timescales of overpressurisation. (Chapters 2 and 3.)

5) Determine the extent to which reservoir size and shape, and the thermal properties of the surrounding crust affect the magnitude and timescales of overpressurisation. (Chapter 3.)

6) Based on typical crustal relaxation timescales, assess the conditions in which second boiling is or is not a viable eruption trigger. (Chapter 3.)

7) Quantify the magnitude, location and extent of crystal-plastic deformation in natural and experimentally overpressured volcanic samples. (Chapter 4.)

8) Assess the potential of electron backscatter diffraction to provide information on *in situ* reservoir overpressurisation. (Chapter 4.)

1.6 Thesis overview

This thesis explores magmatic overpressure using Rhyolite-MELTS thermodynamic modelling, thermal modelling, and analysis of crystal-deformation in experimentally deformed samples. In chapter 2 we use thermodynamic modelling to explore volatile-exsolution driven overpressure within a variety of volcanic systems. We build on previous work by analyzing the effect of initial H_2O oversaturation, and also the effect of adding CO_2 to the magma. We also consider the effect of gas loss and volatile dissolution on our overpressure calculations. Outputs from our MELTS modelling are then linked with a thermal model in order to determine the timescales of overpressurisation. Comparisons between 'real world' systems and their volatile contents and relationship with eruptive style are also presented.

In chapter 3 we extend the methodology from chapter 2 and vary parameters in the thermal model to determine the effect this has on the timescales of overpressurisation. We do this for varying magma reservoir shape, size and depth, and for varying crustal parameters such as geothermal gradient and thermal conductivity. We compare our rates of overpressurisation to those derived from other mechanisms, and also consider the modifying effect of the surrounding crust.

In chapter 4 we explore overpressurisation from an experimental perspective. We deform pumice samples to determine if there is a physical imprint of overpressurisation which can be detected using electron backscatter analysis. We describe the magnitude and extent of crystal-plastic deformation in natural and experimentally deformed samples, and suggest next steps for this novel area of research.

Chapter 2 - Magmatic volatile content and the overpressure 'sweet spot': implications for volcanic eruption triggering and style

Anna Brookfield[1], Mike Cassidy[2], Gregor Weber[3], Răzvan-Gabriel Popa[4], Olivier Bachmann[4], Michael J Stock[5]

[1]Department of Earth Sciences, University of Oxford, Oxford, UK

[2]School of Geography, Earth and Environmental Science, University of Birmingham, Birmingham, UK

[3]School of Earth Sciences, University of Bristol, Bristol, UK

[4]Institute of Geochemistry and Petrology, ETH Zürich, Zürich, Switzerland

[5]Discipline of Geology, School of Natural Sciences, Trinity College Dublin, Dublin, Ireland

Abstract

Crystallisation-induced volatile exsolution - or second boiling - is one mechanism of generating magmatic overpressure and triggering volcanic eruptions. Despite its role as an eruption trigger, exsolution-driven overpressurisation is relatively poorly understood. Part of the problem is that thermodynamic models do not consider how the behaviour of small quantities of magma scales up to reservoir level – where variations in temperature and crystallinity become important. In contrast, many thermomechanical models focus only on magma injection, and do not consider how overpressure evolves spatially or temporally, when related to crystallisation and volatile exsolution. Here, we use Rhyolite-MELTS to track exsolution-driven overpressure during cooling for a variety of natural magma compositions, storage pressures, initial volatile contents and magmatic X_{H2O} (molar H_2O/ (CO_2+H_2O)). We then

couple these outputs to a thermal model to determine the timescales of overpressurisation with varying volatile content.

We find that the highest overpressures occur in magmas which are initially at their H_2O solubility limit, with the addition or removal of H_2O resulting in a decrease in peak overpressure. We also find that maximum overpressure decreases with the addition of CO_2 (decreasing X_{H2O}) at typical magma storage pressures of 100-230 MPa. The higher overpressures generated at the volatile 'sweet spot' have a greater potential to trigger eruptions – or to favour their initiation by making the system more susceptible to other triggers, such as magma injection. The reduction in overpressure with increasing or decreasing initial H_2O suggests that triggering by volatile exsolution is less likely for these magmas. Peak overpressure at the volatile sweet spot also coincides with an increased incidence of explosive eruptions at water contents ~4 - 5.5 wt%. This suggests that higher magmatic overpressures may produce more explosive eruptions, by driving faster initial ascent rates and decreasing outgassing efficiency in the conduit. Our thermal modelling demonstrates that, for small magmatic systems, exsolution-driven overpressurisation can operate on timescales which are much shorter than the crustal relaxation timescale. In these cases, overpressure cannot be dissipated by a visco-elastic crustal response, and therefore has the potential to trigger a volcanic eruption.

2.1. Introduction

Physical and chemical processes operating within a magma reservoir can lead to pressure fluctuations and the build-up of significant overpressures. We define magmatic overpressure (ΔP) as a pressure in excess of the expected lithostatic pressure for a given depth – equivalent to the excess pressure (P_e) term of Gudmundsson (2012). In some cases, negative overpressure, or underpressurisation, may also occur as a system cools and contracts. Overpressurisation may occur via melting, thermal expansion, buoyancy, volatile exsolution,

CO_2-flushing, magma recharge, or a combination of these mechanisms (Cañón-Tapia, 2014; Caricchi *et al.*, 2018). Here, we focus on the overpressure generated by volatile exsolution, termed 'second boiling' when driven by crystallisation of anhydrous mineral phases. Second boiling has long been considered a viable eruption triggering mechanism (Blake, 1984; Tait *et al.*, 1989), and has been identified as a potential trigger at Campi Flegrei, Italy (Stock *et al.*, 2016), Kelud, Indonesia (Cassidy *et al.*, 2016, 2019), Mount St Helens, USA (Kent *et al.*, 2007) and Calbuco, Chile (Arzilli *et al.*, 2019). However, some researchers do not consider second boiling to be a realistic eruption trigger (e.g. Annen *et al.*, 2023), especially in the context of other mechanisms, such as magma injection.

Regardless of the underlying mechanism, if overpressure exceeds a threshold value (often termed the 'critical overpressure'), then magma may ascend towards the Earth's surface, triggering a volcanic eruption. The critical overpressure $(\Delta P)_{critical}$ applicable to a given system is dependent primarily on host rock strength (Pollard, 1987; Rubin, 1995) and is commonly considered to be on the order of tens of MPa (Gudmundsson, 2012). However, it is debated that $(\Delta P)_{critical}$ may be higher than this, on the order of ~100 MPa (Grosfils, 2007), and is particularly sensitive to pore fluid pressure (Albino *et al.*, 2018). The timescale of overpressure build-up is also important for determining whether a volcanic eruption will occur. For exsolution-driven overpressurisation, two important timescales have been identified: 1) the crustal relaxation timescale (τ_{relax}), and 2) the cooling timescale (τ_{cool}) (Degruyter and Huber, 2014). If $\tau_{relax} < \tau_{cool}$ then overpressure can be dissipated by the surrounding crust, and an eruption is unlikely. However, if $\tau_{cool} < \tau_{relax}$, overpressure cannot be dissipated by viscous crustal behavior, and could potentially trigger an eruption by brittle failure of the reservoir wall.

In addition to its role in triggering volcanic eruptions, magmatic overpressure is thought to be linked to eruption style (Jaupart and Allègre, 1991; Woods and Koyaguchi, 1994), most likely via its control on magma ascent rate and outgassing efficiency (Cassidy et al., 2018). One factor influencing both overpressure and ascent rate is magmatic volatile content. Water-rich

magmas are often associated with explosive eruptions (Papale *et al.*, 1998; Cashman, 2004; Gonnermann and Manga, 2012) due to the volumetric expansion and increased buoyancy associated with volatile-exsolution in the conduit, and also the effect of volatiles on increasing magma ascent rate, allowing less time for degassing prior to eruption. However, there is also evidence for effusive, water-saturated eruptions at Volcan Quizapu (Ruprecht and Bachmann, 2010) and Nisyros and Yali volcanoes (Popa *et al.*, 2019; 2021a). This demonstrates that magmas stored in the presence of exsolved volatiles can be associated with both explosive and effusive activity.

Our ability to conceptualise exsolution-driven overpressurisation would be greatly improved by the integration of different types of models which are commonly used when investigating the evolution of magmatic properties. For example, thermodynamic models can describe the chemical state of a magmatic system as it cools, but they do not incorporate important physical factors such as reservoir size, shape or the physical and thermal properties of the surrounding crust. In contrast, thermomechanical models do incorporate the physical properties of the surrounding crust, but they often assume an instantaneous and homogenous pressurisation source, and tend to focus on magma injection as the pressurising mechanism. Additionally, the temperature within a cooling reservoir will vary with proximity to the surrounding crust, resulting in variations in crystallinity and the amount of volatile exsolution throughout the reservoir. By coupling thermodynamic and thermal models we provide a first-order method for determining changes in pressurization induced by cooling and crystallisation. This represents a step forward in that we model temporal and spatial changes in overpressure connected to evolving physical parameters, rather than assuming an instantaneous overpressure throughout the whole reservoir.

In this study we aim to answer the following key questions: How does the magnitude of overpressurisation vary for a variety of realistic volcanic systems? How do variations in fluid content affect overpressurisation? How does overpressure vary spatially as different parts of the reservoir reach high crystallinities? Can this type of overpressure (volatile exsolution-

driven) accumulate on timescales rapid enough to trigger an eruption? And finally, do these internal pressurisation processes have any effect on eruption style?

2.2. Methods

2.2.1 Rhyolite-MELTS thermodynamic modelling

To investigate the overpressure evolution of magma during cooling we use Rhyolite-MELTS thermodynamic modelling software, version 1.2 (Gualda *et al.*, 2012; Ghiorso and Gualda, 2015; Gualda and Ghiorso, 2015). We model the following volcanic systems: Nisyros-Yali dacite (Greece), Calbuco basaltic andesite (Chile), Kelud basaltic andesite (Indonesia) and Mount St Helens dacite (USA) – all of which have shown a variety of eruption styles. Magma composition, pressure, temperature and fluid inputs for these simulations are shown in **Appendix 1**, and melt composition plots are shown in **Appendix 2**. Although these systems all have relatively well-constrained storage conditions, these parameters are often debated as research progresses. Therefore, we seek to present general trends in overpressurisation with varying fluid content, rather than replicate exactly the conditions for each system.

We run isobaric cooling simulations for each of the four volcanic systems at 2°C temperature increments, starting at the liquidus, for two sets of simulations:

1) A set of simulations with varying initial H_2O contents which are CO_2-free.

2) A set of simulations with varying proportions of H_2O and CO_2 (X_{H2O} = $(H_2O+CO_2)/H_2O$).

For set 1, H_2O solubility is determined in Rhyolite-MELTS by incrementally increasing H_2O content at the liquidus temperature, for a fixed pressure and composition (**Appendix 1**) until a fluid phase exsolves. We then add or subtract H_2O at the same pressure, adjusting the temperature to the new liquidus value. In this way, we can compare the effect of initial H_2O-undersaturation and oversaturation with simulations where H_2O content is at the solubility limit,

where all simulations begin at the liquidus temperature. For set 2, the simulation at water saturation (from set 1) is used as the X_{H2O} = 1 case, and X_{H2O} is then decreased at a fixed total fluid content through the addition of CO_2. We note that starting our simulations at the same temperature (rather than adjusting to the liquidus) still results in the same trends in overpressure described in the results section. Outputs from the Rhyolite-MELTS cooling simulations are used to calculate magmatic overpressure at each temperature increment, using the equation of Tramontano *et al.* (2017) and (Caricchi *et al.*, 2021):

$$\Delta P = \frac{\Delta V}{V * \beta} \quad \text{(eq 2.1)}$$

Where ΔP is magmatic overpressure (MPa), ΔV is potential volume change relative to initial volume at the liquidus (m^3), V is system volume (m^3) and β is system compressibility (1/MPa). Compressibility is a measure of volume change (ΔV) in response to a change in pressure (ΔP), and is defined as

$$\beta = -\frac{1}{V}\frac{\Delta V}{\Delta P} \quad \text{(eq 2.2)}$$

The compressibility output is calculated in MELTS as the sum of the liquid, crystal and fluid compressibilities, multiplied by the respective volume fraction of each phase. For the systems investigated here, Rhyolite-MELTS generates β values on the order of 10^{-9} to 10^{-11} Pa^{-1}. These values are consistent with multiple independent estimates of magma compressibility from numerical modelling (Huppert and Woods, 2002 [10^{-8} to 10^{-10} Pa^{-1}]), ground deformation studies (Gottsmann and Odbert, 2014 [1 x 10^{-9} - 4 x 10^{-11} Pa^{-1}]), and multidisciplinary constraints (Wasser *et al.*, 2021 [~3.8 x 10^{-10} Pa^{-1}]). For access to the Rhyolite-MELTS system outputs and overpressure calculations, see Data Appendix 1.

For the majority of our calculations (**figs 2.1 – 2.6**) we assume closed-system conditions where exsolved volatiles are not lost via degassing, and so these overpressures are likely to represent maximum values. However, in section 2.5.2 we also quantify the effect of open-system degassing on overpressure generation. Implicit in the isobaric cooling calculations is

the assumption that the crust surrounding the magma reservoir is rigid, and so does not dissipate any of the pressure caused by volume increase. This is the same as assuming that the timescale for cooling, crystallisation and volatile exsolution is shorter than the timescale of crustal relaxation. Based on the overpressure timescales for a generic, shallow reservoir reported here, and typical crustal relaxation timescales discussed below, this assumption is valid for small reservoirs at relatively shallow depths. However, the assumption may not hold for larger, deeper reservoirs, which have longer cooling timescales. This method does not account for the effect of changes in pressure on volatile solubility. As stated in Tramontano *et al.* (2017), this is a valid assumption for overpressures $\lesssim$ 25 MPa, but may have effects for overpressures larger than this. Model limitations and their implications for our findings are discussed further in section 2.5. Despite its limitations, this method provides a useful way of comparing relative magnitudes of overpressure with varying fluid content, and timescales to reach critical overpressure.

2.2.2 Thermal modelling

To determine the timescales of pressurization from cooling and volatile exsolution, we input melt fraction and overpressure outputs from Rhyolite-MELTS into a thermal model (Weber *et al.*, 2020). We use a 2.5-dimensional, axisymmetric cylindrical model to simulate magma reservoir cooling via conductive heat transfer. We use an initial geothermal gradient of 25°C/km, a thermal conductivity of 2.3 W/m/K, a density of 2700 kg/m^3, a latent heat of 320,000 J/kg and a specific heat of 1050 J/Kg/K. These values are within the range of those used in other studies (e.g, Whittington *et al.*, 2009; Degruyter and Huber, 2014; Trasatti *et al.*, 2019) and are broadly applicable to magma stored at shallow to mid-crustal levels. We model a cylindrical magma body with a top surface at 4 km depth, representing shallow crustal storage towards the upper boundary of common storage depths for intermediate arc magmas (Rasmussen *et al.*, 2022). To present a generically applicable case, reservoir height and radius are both fixed at 1 km, representing a total volume of 3.14 km^3. This represents a relatively small reservoir, and is in line with volumes considered in other studies (Odbert et al.,

2014; Albino et al., 2018; Forni et al., 2018). Melt fraction and temperature data from Rhyolite-MELTS outputs are used to implement latent heat of crystallisation by fitting a fourth-order polynomial curve to these data (**Appendix 3**). We use outputs for the Kelud volcanic system (basaltic andesite) here, but our method could be applied to any other system of interest. The thermal model uses a finite difference method to solve the axisymmetric formulation of the heat conduction equation. To extract variations in overpressure as the reservoir cools, we track the temperature in numerical cells and link this to overpressure via the overpressure-temperature relationship derived from the Rhyolite-MELTS calculations. We present average overpressure values for the whole reservoir over time, assuming an average lithostatic reservoir pressure of 100 MPa (**Appendix 1**). To distinguish between the average overpressures from our thermal modeling and those derived from Rhyolite-MELTS, we refer to the thermal model-derived overpressures as 'average reservoir overpressure'. For access to the Matlab code used to generate our overpressure evolution plots, see Data Appendix 2.

Using average reservoir overpressure values assumes that the magma can transfer stress evenly throughout its volume, an assumption which may not be valid for mushy, heterogeneous reservoirs (e.g. Mullet and Segall, 2022). However Parmigiani *et al.* (2017) show that the random distribution of bubbles associated with volatile-exsolution hinders the development of pore-scale degassing channels in a reservoir, so average pressurization may be the best way to model this complex process. Our model does not account for the movement of volatiles through the magma reservoir (Annen and Burgisser, 2021), or the effect of buoyancy in generating overpressure (Caricchi *et al.*, 2014), which we discuss further in section 3.4.4. We also note that our thermal model only accounts for heat transfer via conduction, it does not incorporate convection or advection. It has been shown that convective heat transfer via a hydrothermal system can increase cooling rates by orders of magnitude (Kelly *et al.*, 2021). Therefore, the timescales presented here are upper estimates, and cooling rates are likely to be shorter in natural systems, assuming no magmatic recharge.

2.3. Modelling results

2.3.1 Thermodynamic modelling

2.3.1.1 Effect of varying initial H_2O content (no CO_2)

The evolution of magmatic overpressure during cooling for the four different systems investigated here is shown in **figure 2.1**. Initial H_2O content is varied, and there is no CO_2 present in these simulations. We use a crystallinity cut-off of 60 vol% (dashed lines on plots denote >60% crystallinity) to separate eruptible from non-eruptible magmas (Cooper and Kent, 2014) although, in some cases, it may be possible to exceed this limit and erupt (Klein *et al.*, 2017). In agreement with Tramontano *et al.* (2017), we find that maximum overpressures are attained when initial H_2O concentrations are set at their solubility limit (thicker lines in figures). However, we also find that increasing the initial H_2O concentration above the solubility limit results in a decrease in peak overpressure for all our modelled systems. For example, at Nisyros-Yali (**fig 2.1a**) the simulation initiated at the H_2O solubility limit (5.4 wt% in this case) generates a peak overpressure of 56 MPa. However, reducing the initial H_2O concentration to 4.9 wt% (initial water undersaturation) and increasing it to 5.9 wt% (initial water oversaturation) both lower the peak overpressure to 33 MPa and 34 MPa, respectively. Similar trends in overpressure are seen consistently across all the systems that we model (**figs 2.1b-d**), suggesting that the reduction in overpressure with increasing or decreasing initial H_2O content occurs regardless of storage depth, temperature or magma composition. This trend in overpressure with varying initial H_2O content is also apparent at smaller H_2O increments of 0.05 wt% (**Appendix 4**), and for basaltic and rhyolitic compositional end-members (**Appendix 5**). Simulations with initial H_2O concentrations at the solubility limit have the maximum potential for volume change (ΔV), without the dampening effect (increased compressibility (β)) of excess exsolved volatiles. The addition or removal of H_2O shifts this balance and reduces overpressure. Hence, initial H_2O contents at the water solubility limit result in a 'sweet spot' where magmas generate maximum peak overpressure. The eventual decline in overpressure

seen across all systems - and all initial water contents - is due to the effect of crystallisation and liquid contraction during cooling which both decrease system volume.

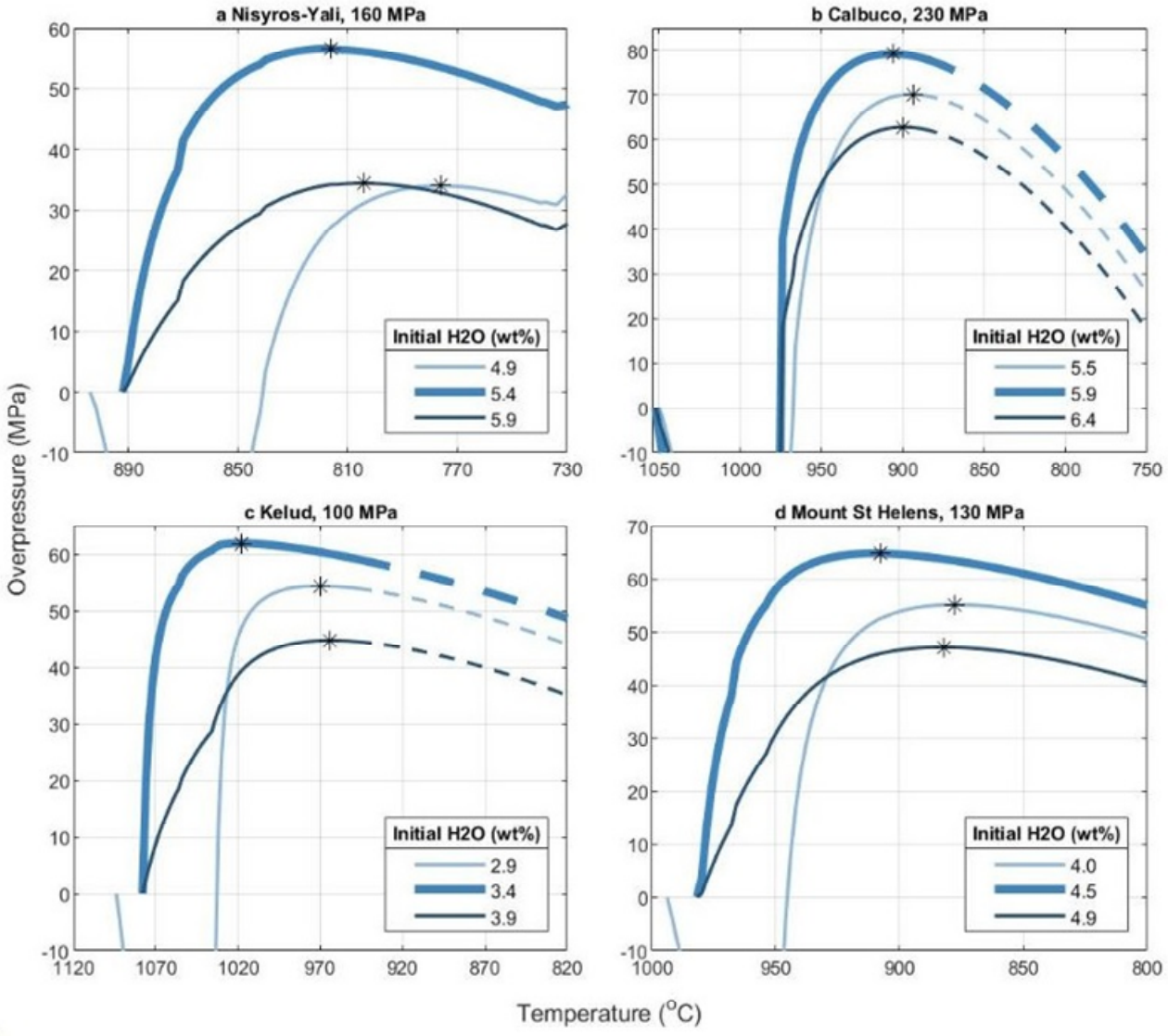


Figure 2.1. Overpressure evolution for varying volcanic systems calculated from Rhyolite-MELTS for varying initial H_2O content, no CO_2. All simulations begin at the liquidus, and overpressure is calculated relative to the liquidus. Stars indicate peak overpressure.

2.3.1.2 Effect of varying X_{H2O} (adding CO_2)

To investigate the effect of mixed volatile exsolution on the generation of overpressure we modelled each volcanic system with varying X_{H2O} from 0.9 –1 by adding a CO_2 phase (**fig 2.2**). The simulations initially at the water solubility limit (thicker lines in **fig 2.1**) are used as the X_{H2O} = 1 case, and total fluids are fixed at this value. Our results indicate that the highest

overpressures occur in pure-H_2O systems (X_{H2O} = 1), with overpressure decreasing as X_{H2O} decreases. For example, a maximum overpressure of 62 MPa is attained at Kelud in the X_{H2O} = 1 simulation (**fig 2.2c**). As X_{H2O} decreases, peak overpressure also decreases to 42 MPa for X_{H2O} = 0.98, and 23 MPa for X_{H2O} = 0.80. The same trend is seen across all the volcanic systems modelled here, although the magnitude of the overpressure reduction varies with magma composition and storage conditions. **Figure 2.2** demonstrates that reducing initial X_{H2O} past a certain point – which varies for each system - means that no positive overpressure is generated via volatile exsolution.

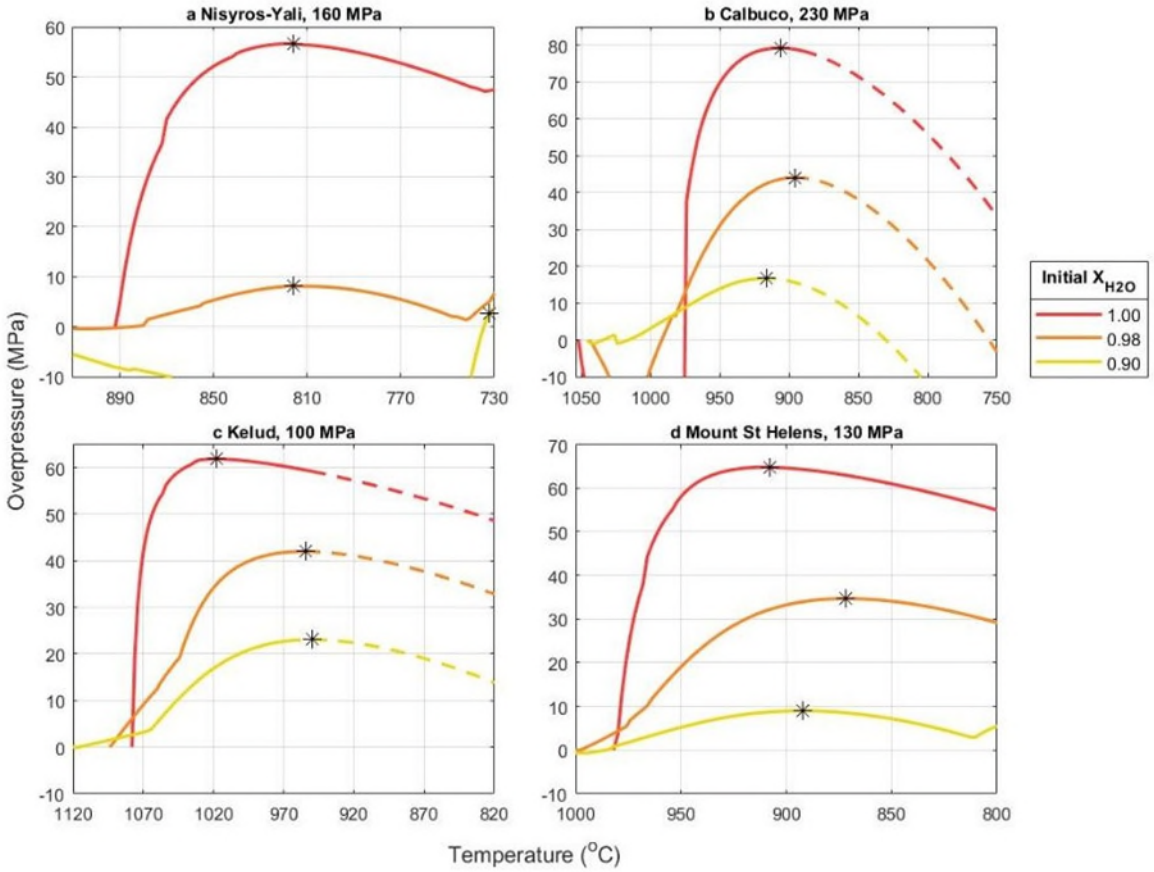


Figure 2.2. Overpressure evolution for varying volcanic systems calculated from Rhyolite-MELTS for varying initial X_{H2O}. All simulations begin at the liquidus, and overpressure is calculated relative to the liquidus. Stars indicate peak overpressure. Dashed lines indicate crystallinity > 60 vol%.

2.3.1.3 Effect of reservoir compressibility

The compressibility of the rock surrounding a magma reservoir is termed the reservoir compressibility (β_r), and is dependent on reservoir dimensions and the physical properties of the host rock (Wasser *et al.*, 2021). We do not include reservoir compressibility in our overpressure calculations, as we assume that the crust surrounding our shallow (4 km depth) magma reservoir is rigid. This is a reasonable assumption, as a crustal viscosity of 10^{20} Pa s - which is likely to be appropriate for systems shallower than ~ 7.5 km (Townsend *et al.*, 2019) - gives a relaxation timescale of 158 ka. Hence, the host rock crust is effectively rigid over the volatile exsolution timescales reported here. However, taking β_r into account, overpressure can be recalculated using equation 2.3

$$\Delta P = \Delta V / (V^*(\beta + \beta_r)) \qquad \text{(eq 2.3)}$$

Using a β_r value of 2.0×10^{-10} Pa^{-1} (Wasser *et al.*, 2021) results in an increase in total compressibility (magma plus reservoir), and a decrease in ΔP of 0.5 – 20 MPa. This comparison is plotted in **Appendix 6**, which demonstrates that trends in overpressure remain the same, despite a decrease in absolute values.

2.3.2 Thermal modelling

The results presented above do not give any indication of the timescales of overpressurisation with varying initial parameters. In this section we present the temporal evolution of overpressure for a small, shallow magma body, using ΔP values from our Kelud MELTS simulations, which have been averaged over the whole eruptible volume (<60% crystals) of the reservoir. The rate of cooling is dependent on the thermal conductivity, specific heat and density of the crust, and the latent heat of crystallisation and geothermal gradient.

2.3.2.1 Timescales of overpressurisation: varying initial H_2O content

Figure 2.3a shows the effect of varying initial H_2O content (no CO_2) on the temporal evolution of average reservoir overpressure for a cylindrical reservoir situated at 4 km depth, with a

radius and height of 1,000 m. We only consider magma with crystallinity <60 vol% in our plots. The highest average reservoir overpressure is attained in the simulation which is initially H_2O saturated (3.4 wt%), reaching a peak of 61 MPa after ~3 Ka. The initially fluid undersaturated simulations (2.5 and 2.9 wt% H_2O) show a phase of net underpressurisation, due to prolonged periods of crystallisation in the absence of a fluid phase. After several ka, average reservoir overpressure in the initially undersaturated simulations begins to increase due to fluid exsolution, and eventually positive overpressures are attained. This contrasts with the initially fluid oversaturated simulations (3.9 and 4.3 wt% H_2O), which do not generate any net underpressure, and show a relatively steady average reservoir overpressure increase. There is a clear contrast in the rate of average reservoir overpressure increase between the initially undersaturated and oversaturated simulations. Although the lower H_2O scenarios take longer to reach a given overpressure (e.g. 10 MPa), they show more rapid rates of overpressurisation (e.g. up to 50 MPa in ~0.5 ka for the 2.9 wt% example). In contrast, the higher H_2O cases reach 10 MPa more rapidly, but show a much slower rate of overpressurisation (e.g. requiring ~3 ka to build up 40 MPa of overpressure for the 3.9 wt% H_2O case).

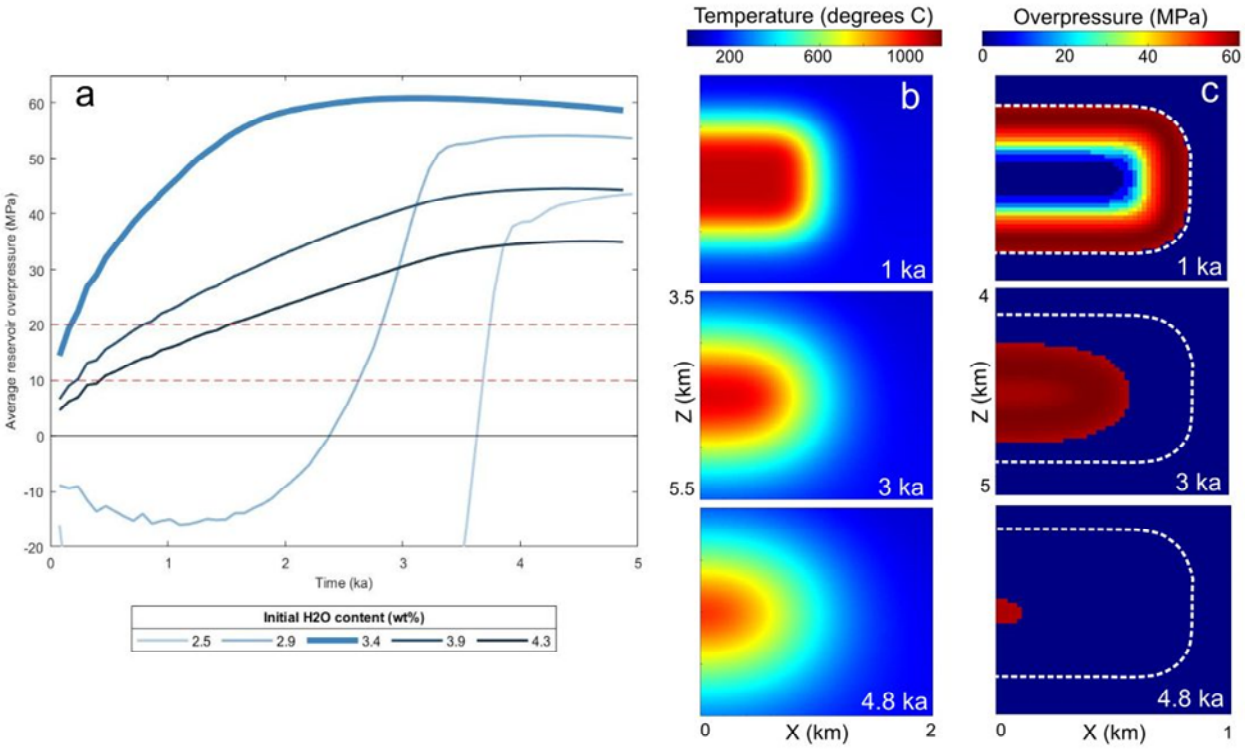


Figure 2.3. Temporal evolution of average reservoir overpressure for varying initial H_2O content. a) Overpressure evolution for Kelud at 4km reservoir depth. Thermal model uses a 1 x 1 km reservoir (3.14 km^3 volume) and the simulations are truncated at 60% crystallinity. Red dashed lines highlight 10 and 20 MPa overpressure thresholds (see discussion). b) Thermal model outputs showing temperature variations for the 3.4 wt% H_2O case after 1 ka, 3ka and 4.8 ka. c) Thermal model outputs showing overpressure variations for the same case. White dashed line shows extent of magma reservoir at 1 ka. Blue space within this outline at 3 ka and 4.8 ka represents uneruptible magma.

Figures 2.3b and c show the spatial evolution of temperature and overpressure within the cooling reservoir for the 3.4 wt% H_2O case. As we apply a crystallinity cut-off of 60 vol%, the volume of the eruptible magma decreases with time, as no recharge events are considered. The spatial distribution of overpressure is governed by the overpressure-temperature relationship shown in **figure 2.1c**, whereby overpressure increases during cooling, until it reaches a peak at 1020°C, then begins to decrease again as expansion due to fluid exsolution is outweighed by crystallisation contraction. After 1 ka, the interior of the reservoir is still relatively hot, resulting in lower overpressures than those at the outer edge of the reservoir, which has cooled sufficiently to generate peak overpressures. By 3 ka, the peak overpressure

'front' has shifted toward the centre of the reservoir, whilst the outer edge has cooled past peak overpressure, and the centre is still increasing in temperature. After 4.8 ka of cooling, the volume of eruptible magma has decreased, and the highest overpressure occurs in the centre of the reservoir.

2.3.2.2 Timescales of overpressurisation: varying initial X_{H2O}

Figure 2.4a shows the effect of varying initial X_{H2O} content on the temporal evolution of average reservoir overpressure. Parameters are the same as in section 2.3.2.1, and the X_{H2O} = 1 case is the same as the 3.4 wt% H_2O case presented in **figure 2.3a**. Magma with X_{H2O} = 1 generates the greatest average reservoir overpressure, and overpressure decreases as X_{H2O} decreases. Maximum average reservoir overpressure is 61 MPa for X_{H2O} = 1, and decreases to 42 MPa for X_{H2O} = 0.98 and 23 MPa for X_{H2O} =0.90. The X_{H2O} = 0.70 and 0.50 cases do not generate any positive average reservoir overpressure due the effect of CO_2 which is described in section 2.4.2. The rate of average reservoir overpressure build-up also decreases with decreasing X_{H2O}. For example, the X_{H2O} = 1 case reaches 20 MPa in ~0.2 ka, whilst the X_{H2O} = 0.90 simulation reaches 20 MPa in ~3.8 ka. **Figures 2.4b and c** show the spatial evolution of temperature and overpressure within the cooling reservoir for the 0.90 X_{H2O} case. This is governed by the overpressure-temperature profile shown in **figure 2.2c**, which demonstrates that the highest overpressures for this scenario occur above 60 vol% crystallinity. For this reason, the highest overpressure always occurs at the cooling edge of the reservoir, at high crystallinities and moves inwards as the eruptible volume decreases.

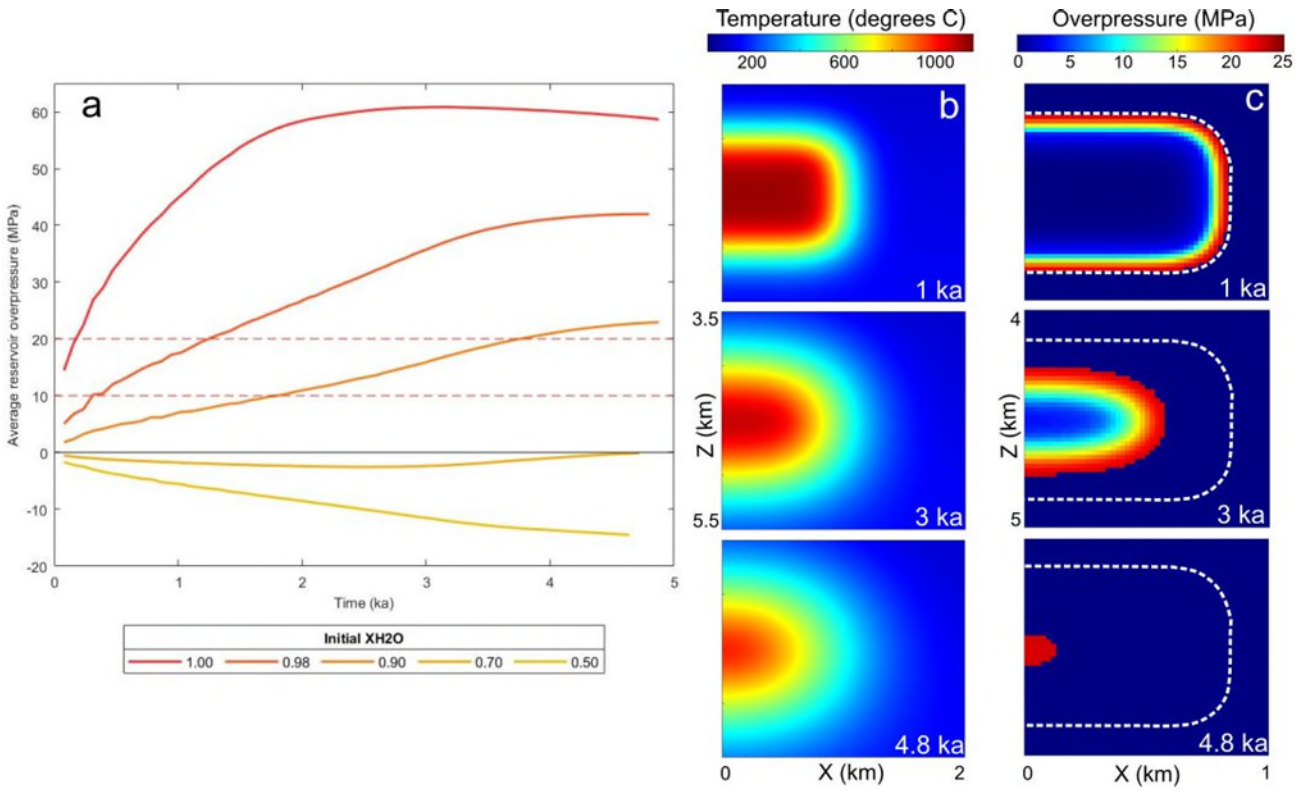


Figure 2.4. Temporal evolution of average reservoir overpressure for varying initial X_{H2O}. a) Overpressure evolution for Kelud at 4km reservoir depth. Thermal model uses a 1 x 1 km reservoir (3.14 km^3 volume) and the simulations are truncated at 60% crystallinity. Red dashed lines highlight 10 and 20 MPa overpressure thresholds (see discussion). b) Thermal model outputs showing temperature variations for the 0.90 X_{H2O} case after 1 ka, 3ka and 4.8 ka. c) Thermal model outputs showing overpressure variations for the same case White dashed line shows extent of magma reservoir at 1 ka. Blue space within this outline at 3 ka and 4.8 ka represents uneruptible magma.

2.4. Discussion

2.4.1 Critical overpressures and timescales of pressurization

To assess whether volatile exsolution is a viable eruption trigger for the different cases we have investigated, we frame our results in the context of a critical overpressure $(\Delta P)_{critical}$. Most researchers define failure as possible when overpressure exceeds twice the tensile strength (T_S) of the host rock (Tait et al., 1989; Parfitt et al., 1993). A reasonable estimate of T_S for volcanic rocks is 5–10 MPa (Gudmundsson, 2011; Albino et al., 2018), giving a critical

overpressure range of 10–20 MPa, which we adopt here. We note that, in natural systems, the presence of fractures in the host rock will result in a reduction in T_S, and therefore also in (ΔP)c (Zhan and Gregg, 2019).

For volatile-exsolution to trigger an eruption, overpressure build-up must occur on a timescale shorter than that of crustal relaxation. The average reservoir overpressure timescales shown in **figures 2.3** and **2.4** can be compared to timescales of viscous crustal relaxation (τ_{relax}) to determine whether they are fast enough to potentially trigger an eruption. τ_{relax} can be calculated from the equation of Degruyter and Huber (2014):

$$T_{relax} = \frac{n_r}{(\Delta P)_C} \qquad \text{(eq. 2.4)}$$

Where ηr is host rock viscosity and $(\Delta P)_c$ is critical overpressure. Using ηr = 10^{19} Pa s (Townsend *et al.*, 2019) and $(\Delta P)_c$ = 20 MPa gives a crustal relaxation timescale of 15.8 ka. Using a host rock viscosity of 10^{18} Pa s, representing warmer crust, gives τ_{relax} = 1.6 ka, whilst increasing ηr to 10^{20} Pa s, representing cooler crust, gives τ_{relax} = 158 ka. For the reservoir at 4 km depth modelled here, higher viscosities and therefore longer relaxation timescales may be more appropriate. However, for long-lived, larger and deeper systems, considering the effect of periodic magma recharge on the heat budget of the upper crustal reservoir (e.g, Annen *et al.*, 2015), τ_{relax} may be equal to or shorter than the cooling and overpressurisation timescale. **Figure 2.3** shows that all the modelled scenarios reach a critical overpressure of 10 MPa well within a relaxation timescale of 15.8 ka. If a more conservative τ_{relax} of 1.6 ka is used, the 3.4–4.3 wt% H_2O simulations still have the potential to trigger an eruption, whilst the initially H_2O- undersaturated simulations do not, as they pressurise to critical levels more slowly than τ_{relax}. These initially H_2O-undersaturated scenarios display periods of average underpressurisation over several ka, but once fluids begin to exsolve overpressure increases rapidly over the course of ~0.5 ka. For the mixed H_2O-CO_2 scenarios shown in **Figure 2.4**, magmas with initial X_{H2O} ≥0.90 reach 10 MPa within a τ_{relax} of 15.8 ka, and those with X_{H2O} ≥0.98 reach 10 MPa using a more conservative τ_{relax} of 1.6 ka. A summary of the timescales

taken to reach critical overpressures of 10 and 20 MPa, for a reservoir volume of 3.14 km^3, is shown in **figure 2.5.** This highlights that eruption triggering via volatile-exsolution becomes less likely with greater degrees of initial H_2O undersaturation, and as initial magmatic X_{H2O} decreases. It also demonstrates that magmas with higher X_{H2O} values can attain critical overpressures on timescales < τ_{relax}, even when using conservative τ_{relax} estimates which are likely to be more characteristic of deeper, hotter (lower viscosity) systems. The effect of varying reservoir volume on timescales to reach critical overpressure is shown in **Appendix 7**. This demonstrates the sensitivity of overpressure build-up not only to reservoir volume, but also to initial H_2O content and fluid composition, discussed further in chapter 3.

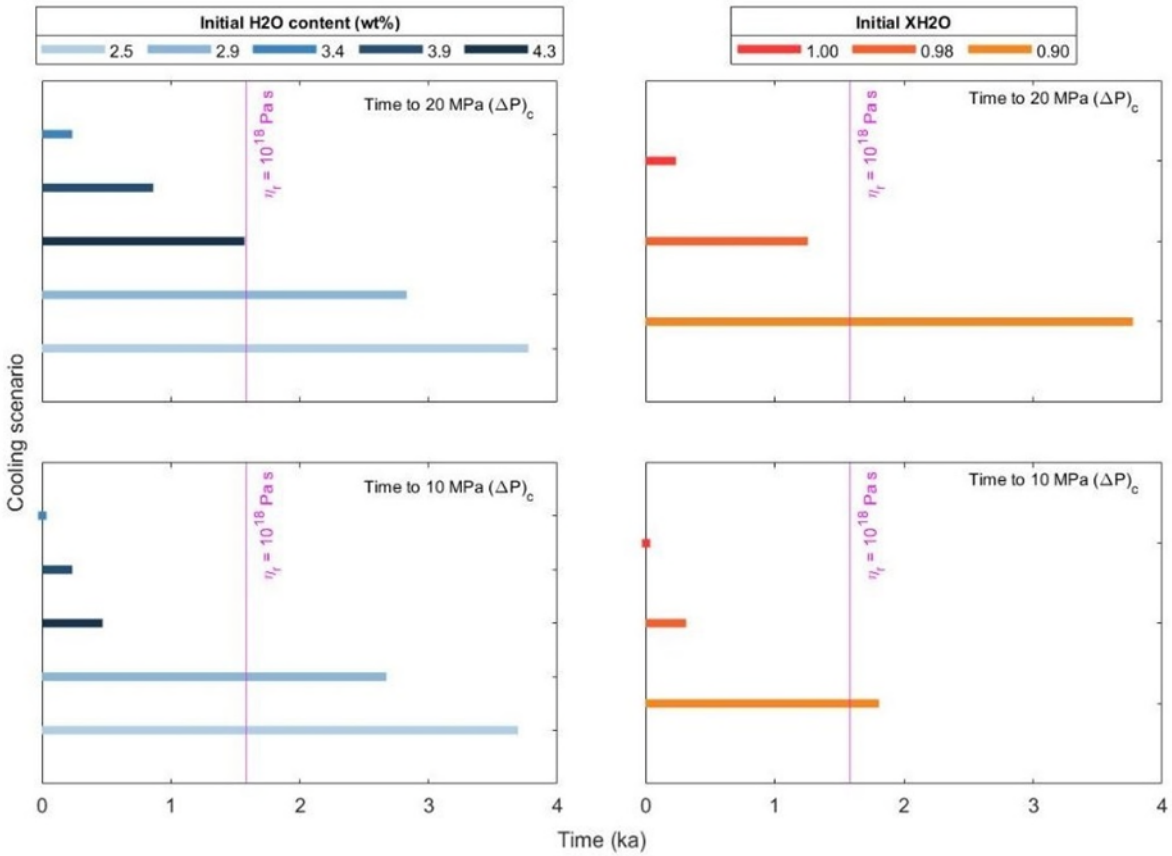


Figure 2.5. Summary of the time taken to reach critical overpressures of 20 MPa (top row) and 10 MPa (bottom row) for the scenarios shown in figures 2.3 and 2.4. Left side shows varying initial H_2O content, right side shows varying initial X_{H2O}. Note that the 0.5 and 0.7 X_{H2O} scenarios shown in figure 2.4 do not generate any positive overpressure, so are not shown here. A relaxation timescale of 1.58 ka is shown by the pink line, which assumes a crustal viscosity of

10^{18} Pa s^{-1} (Townsend *et al*., 2019). Using a crustal viscosity of 10^{19} Pa s^{-1}, which is more realistic for the small, shallow system modelled here, gives a relaxation timescale of 15.8 ka.

For cases where peak overpressure is attained after reaching 60% crystallinity, the highest overpressures are confined to the cooling edge of the reservoir, and decrease inwards (**fig 2.4c**). However, if peak overpressure is attained prior to reaching 60% crystallinity, high overpressures are not only restricted to the edge of the cooling magma body, they can also develop within the reservoir (**fig 2.3c**). Our results demonstrate that volatile-exsolution driven overpressure can attain critical magnitudes on timescales shorter than that of crustal relaxation, when considering small reservoirs situated at shallow depths. The lack of convective heat transfer in our thermal model means that the timescales presented here are likely to be maximum estimates, as the presence of a hydrothermal system can increase the rate of heat loss by an order of magnitude (Kelly *et al.*, 2021), though this is also dependent on reservoir size.

2.4.2 Implications for eruption triggering

When we vary the CO_2 content of our mixed fluid simulations, we find that overpressure increases as X_{H2O} increases (**figs 2.2** and **2.4**). The reduction in overpressure with decreasing X_{H2O} occurs because CO_2 is less soluble than H_2O at shallow magma storage depths. As X_{H2O} decreases, the volume of exsolved fluids at the liquidus increases – and this results in a smaller volumetric expansion relative to simulations with higher X_{H2O} (see **Appendix 8**). In addition, simulations with a greater proportion of CO_2 (lower X_{H2O}) initially have higher compressibilities due to their greater volumes of exsolved fluids (H_2O and CO_2), and tendency to exsolve fluids earlier. This results in lower overpressures relative to simulations with higher X_{H2O}. This is consistent with Tait *et al.* (1989), who identified that more soluble volatile species (*i.e.* H_2O) play a greater role in overpressure generation. Once initial X_{H2O} is reduced below a certain point, the system does not generate any positive overpressure during cooling, limiting the potential for eruption triggering via volatile exsolution. At Kelud, Cassidy *et al.* (2019) identified variations in X_{H2O} and their potential link to eruption triggering mechanism. The 2007 effusive eruption of Kelud was associated with low X_{H2O} values (~0.55), and was preceded by

influx of a CO_2-rich magma, which triggered the eruption. In contrast, the explosive eruption in 2014 was characterized by higher X_{H2O} values (~1.00) and is thought to have been triggered by second boiling. Our thermal modelling results show that average reservoir overpressures of 10s of MPa can be generated with magmatic X_{H2O} of 0.90–1.00 (**fig 2.4a**). In contrast, our simulations with X_{H2O} values ≤0.70 do not generate any positive overpressure during cooling. This supports the idea that volatile exsolution was a possible trigger for the explosive 2014 eruption, whilst it is an unlikely trigger for the 2007 eruption – instead requiring an alternative triggering mechanism, such as magma injection. If this is the case, then $(\Delta P)_{critical}$ for the 2014 eruption must have been attained within seven years (the time interval between the two eruptions). As shown in **figure 2.4a**, average reservoir overpressure for our X_{H2O} = 1 case can build to critical levels of 10 MPa very rapidly, due to the high overpressure-generating potential of magma which is initially H_2O saturated. Rates of overpressurisation are discussed further in chapter 3. As previously mentioned, these timescales will be modified due to volcano-specific factors, such as the presence of a hydrothermal system, local fracturing and crustal properties.

Our modelling shows the decrease in eruptible reservoir volume with time as magma cools below the 60 vol% crystallinity cut-off (**figs 2.3c and 2.4c**). Eruptions generated by magmas which take longer to attain critical overpressure may have smaller volumes, as there is less eruptible magma in the reservoir (assuming no recharge). In contrast, eruptions which attain critical overpressure earlier in their cooling history may be more voluminous, as there is a greater volume of potentially eruptible magma in the reservoir. For example, the 3.4 wt% H_2O scenario (initially at the H_2O solubility limit) shown in **figure 2.3** has an eruptible volume of 2.3 km^3 by the time it attains 20 MPa of average reservoir overpressure after ~0.16 ka. In contrast, the 4.3 wt% H_2O magma (initially H_2O-oversaturated) has an eruptible volume of 1.2 km^3 when it reaches 20 MPa at ~ 1.6 ka. For the 2.5 wt% H_2O magma (initially H_2O-undersaturated) the eruptible volume is reduced to 0.30 km^3 once it reaches the same critical overpressure after ~3.7 ka.

Our study focuses solely on the role of initial fluid content, with no external addition of magma or fluids. However, flushing of a reservoir by CO_2-rich fluids can also result in reservoir pressurisation, provided that flushing occurs prior to rheological lock-up (Caricchi *et al.*, 2018). CO_2 flushing may increase magma compressibility, but if the process is rapid and voluminous enough, it may still meet the overpressure threshold for triggering an eruption. For flushing to trigger an eruption for the cases considered here, the supply of CO_2-rich fluids would have to occur on a timescale shorter than τ_{relax}, and also shorter than the exsolution-driven overpressurisation timescale. This process of CO_2 flushing is distinct from the role of CO_2 exsolution described here, where the lower solubility of this phase has less intrinsic overpressure generating potential when compared to H_2O.

2.4.3 Implications for eruption style

Our modelling shows that magmas generate the greatest exsolution-driven overpressures when their initial H_2O contents are at the solubility limit (**figs 2.1 & 2.3**). Reducing the H_2O content so that the magma is initially undersaturated reduces potential volume change, resulting in a reduction in overpressure. Increasing the initial H_2O content, so that the magma is initially water-oversaturated, results in an increase in compressibility and a reduction in overpressure due to the ability of exsolved fluids to accommodate pressure increase (Woods and Pyle, 1997; Popa *et al.*, 2021b). This variation in overpressure-generating capacity with varying initial fluid content may have implications for magma ascent rate and eruption style. Whilst it is well-established that magma ascent rate is a major control on eruption style (Cassidy *et al.*, 2018), the factors controlling initial ascent rate are not well-constrained. One of the proposed controls on ascent rate is magma reservoir overpressure (Jaupart and Allègre, 1991; Woods and Koyaguchi, 1994). Indeed, conduit flow models show that increasing magmatic overpressure results in faster initial magma ascent speeds (Thomas and Neuberg, 2014). Popa *et al.* (2021b) compiled global magmatic H_2O contents and found that magmas close to or at their water solubility limit tend to be associated with explosive eruptions, whilst effusive eruptions are more commonly linked to either very high or low H_2O contents (albeit

with crystallinity also as a factor). This compilation of magmatic H_2O content, separated by eruption style, is shown alongside peak overpressure from our Rhyolite-MELTS simulations in **figure 2.6**, where we propose a potential link between overpressure and eruption style. The higher overpressures generated by magmas with H_2O contents at the solubility limit broadly correlates with the distribution of pre-eruptive H_2O contents of explosive eruptions. We propose that the high overpressures at the volatile 'sweet spot' may be contributing to faster initial ascent rates and therefore to more explosive eruptions. In contrast, the reduction in overpressure with increasing or decreasing initial H_2O content could potentially lower ascent rates, increasing degassing efficiency in the conduit and favouring effusive eruptions. This may provide another, concurrent mechanism for the abundance of water-rich effusive events, in addition to the effect of exsolved volatiles on melt viscosity and early conduit ascent, as described in Popa *et al.* (2021b).

However, our proposed link between overpressure and eruption style does not account for the occurrence of explosive volatile-over saturated eruptions. Our results show that high magmatic H_2O contents increase magma compressibility, resulting in lower reservoir overpressures. Whilst this makes eruption triggering generally less likely, if these magmas do erupt their increased buoyancy and low viscosity may increase ascent rate, promoting an explosive eruption (La Spina *et al.*, 2022). This suggests that processes operating during magma ascent can modify and 'override' the effects of overpressurisation in the reservoir. Alternatively, high levels of exsolved volatiles in magmas may increase permeability during ascent, favouring gas loss and promoting an effusive eruption (Popa *et al.*, 2021b). Studies which couple models of reservoir overpressurisation with ascent rate and fragmentation - especially focusing on volatile content, crystallinity, viscosity and buoyancy - would help to advance our understanding of the many factors which contribute to volcanic eruption style.

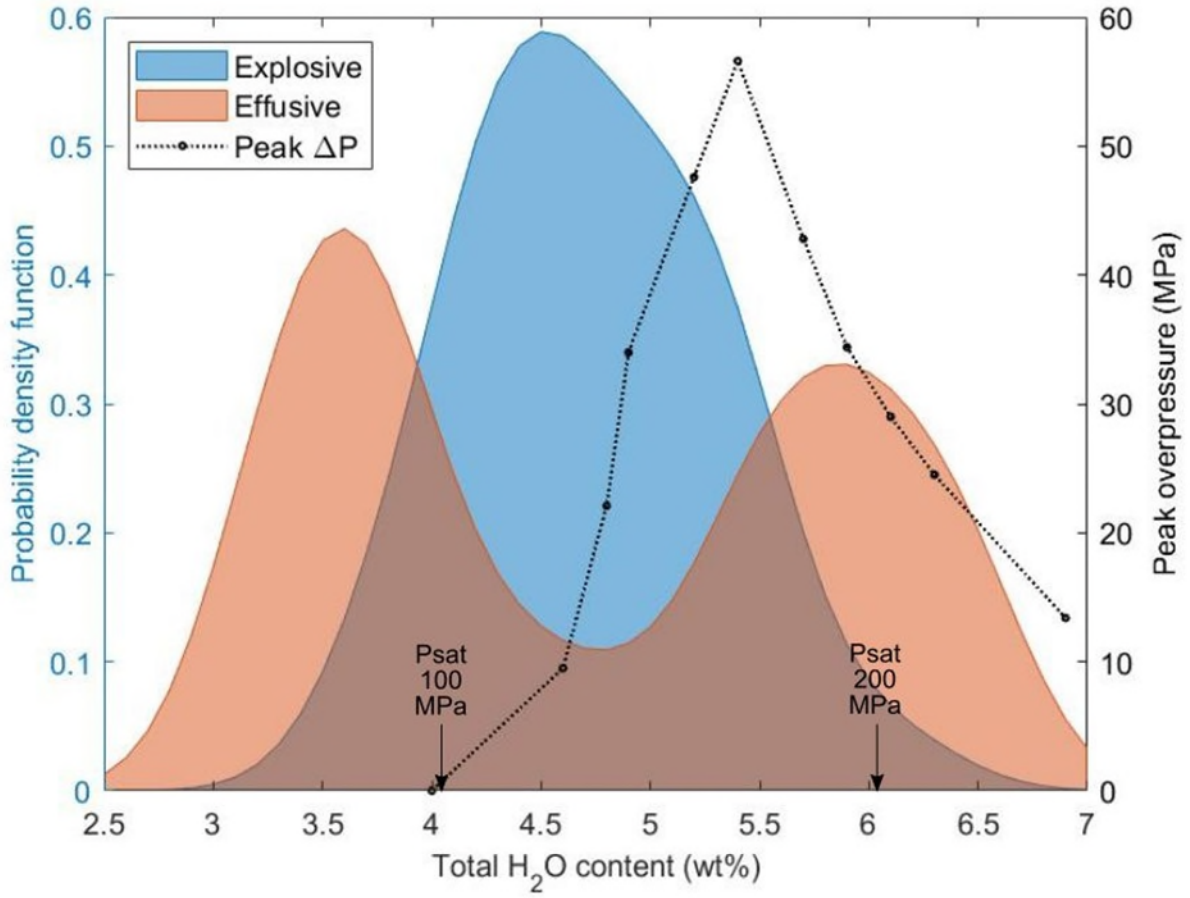


Figure 2.6. Magmatic H_2O content, eruption style and peak overpressure. Shaded areas show kernel density estimation for H_2O content/ eruption style data from Popa *et al*. (2021b), which comprises global data from 245 eruptions from 75 volcanoes. The black dotted line shows peak overpressure from our Rhyolite-MELTS modelling for Nisyros-Yali. Arrows show H_2O contents corresponding to saturation pressures (Psat) of 100 and 200 MPa, a common magma reservoir pressure range. Psat is determined using Volatilecalc (Newman and Lowenstern, 2002), for rhyolitic melt at 800°C.

2.5 Model limitations

2.5.1 Pressure dissolution feedbacks

The assumption of a rigid crust surrounding the magma reservoir means that any overpressure generated by cooling and crystallisation cannot be dissipated by expansion of the host rock. This build-up of ΔP will increase the total pressure in the reservoir and affect the solubility of volatiles in the system, potentially resulting in volatile redissolution and system volume

decrease. To investigate the effect of overpressurisation on total reservoir pressure and volatile solubility, we run a series of Rhyolite-MELTS simulations in which the overpressure generated in the previous step is added to the lithostatic pressure. We do this for temperature intervals of 0.5°C, and do not allow reservoir pressure to drop below 100 MPa (the initial lithostatic pressure used in the isobaric simulations).

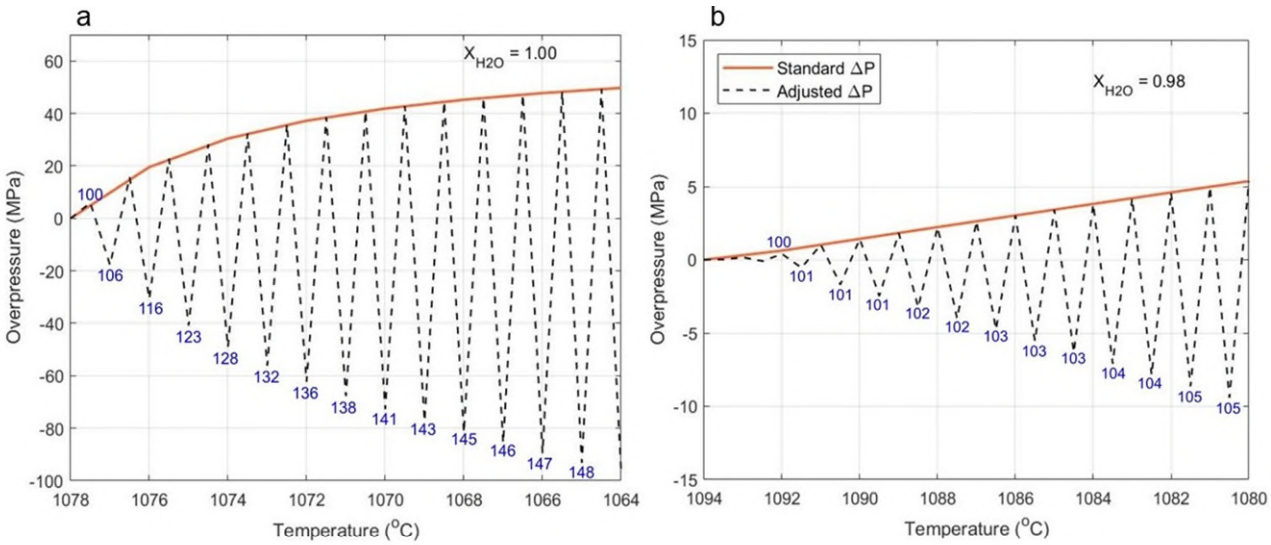


Figure 2.7. Pressure (lithostatic) plus overpressure curves for Kelud, 100 MPa initial reservoir pressure. Red line shows our standard isobaric simulations, run with 100 MPa constant pressure (as shown in figure 2.2C). The black dashed line shows the effect of adding volatile overpressure on to lithostatic reservoir pressure at 0.5°C intervals. The new total reservoir pressure at the start of each simulation is labelled in blue. We do not allow reservoir pressure to fall below 100 MPa.

Figure 2.7 shows that incorporating overpressure into the total pressure of the simulations results in multiple cycles of under- and overpressurisation. For example, adding on 6 MPa of exsolution-driven overpressure (**fig 2.7a**) results in a reservoir pressure of 106 MPa. Running a simulation at this increased reservoir pressure (106 MPa) leads to a melt density increase, and redissolution of exsolved volatiles as solubility is increased at higher pressure. Both of these factors lead to a volume decrease relative to the initial volume at 100 MPa, resulting in underpressurisation of -17 MPa. This then reduces the reservoir pressure for the next set of

simulations, which are run at 100 MPa, leading to fluid exsolution, volume increase and overpressurisation to 16 MPa. This results in another cycle of fluid dissolution, this time at a higher reservoir pressure of 116 MPa. The system continues to swing between these two states of increased and decreased pressure. Although the overpressure profiles are altered, the relative magnitudes for the varying X_{H2O} simulations are similar to their isobaric counterparts. **Figure 2.7** suggests that timescales to reach critical overpressures may be altered when fluctuations due to overpressurisation are accounted for. However, it is difficult to quantify this as the fluctuations in crystallinity as pressure changes mean this cannot be input into the thermal model. Our model is therefore limited for simulating the effect of system change due to incremental, non-isobaric overpressure increase, and is unlikely to reflect the full complexity of a natural system. A fully coupled thermodynamic-thermomechanical model which can model these feedback processes would help to improve our understanding of overpressurisation generated in cooling magma systems.

2.5.2 Closed system assumption

When calculating overpressure we assume a closed system, where all exsolved fluids are retained within the magma reservoir. This is a common assumption when modelling magmatic systems (e.g.,Gleeson *et al.*, 2017; Tramontano *et al.*, 2017; Caricchi *et al.*, 2018), but it is at odds with observations of volcanic degassing. However, numerical modelling of bubble migration in melts has shown that the majority of degassing (~ 50% of the available fluid phase) occurs at medium to high crystallinities of 40 - 70% (Parmigiani *et al.*, 2017). At crystallinities < 40%, bubble migration is inefficient, and only a very small volume of fluids (~ 1% of the available fluid phase) are lost this way. For the cases presented here, all of the scenarios shown in **figure 2.3a** reach 20 MPa critical overpressure prior to attaining 40% crystallinity. This can effectively be considered as a closed system, as fluid loss during this time will be negligible. However, whilst the X_{H2O} = 1 and 0.98 cases shown in **figure 2.4a** also attain $(\Delta P)_{critical}$ prior to 40% crystallinity, the lower X_{H2O} cases (≤ 0.90 X_{H2O}) do not. For example, the 0.90 X_{H2O} scenario attains $(\Delta P)_{critical}$ at a crystallinity of ~50%. This suggests that

the closed system assumption may not be valid for the lower X_{H2O} scenarios presented here, as degassing via merging fluid pathways begins to play a more significant role prior to attaining $(\Delta P)_{critical}$.

To quantify the effect of gas loss from the reservoir, we remove 10% of the available exsolved fluid volume at 50% crystallinity, and recalculate the system volume, compressibility, and overpressure accordingly. We use the 50% crystallinity interval as this is within the high outgassing range specified in Parmigiani *et al.* (2017), as outlined above, and we use 10% fluid loss as an arbitrary volume, to illustrate the effect of open-system degassing. **Figure 2.8** shows that, for the open system model, overpressures (at 50% crystallinity) are reduced by ~ 4-10 MPa when 10% of the available fluids are lost from the system. Although overpressure is reduced across all the simulations, the trend in overpressure with varying fluid content is the same as in the closed system simulations.

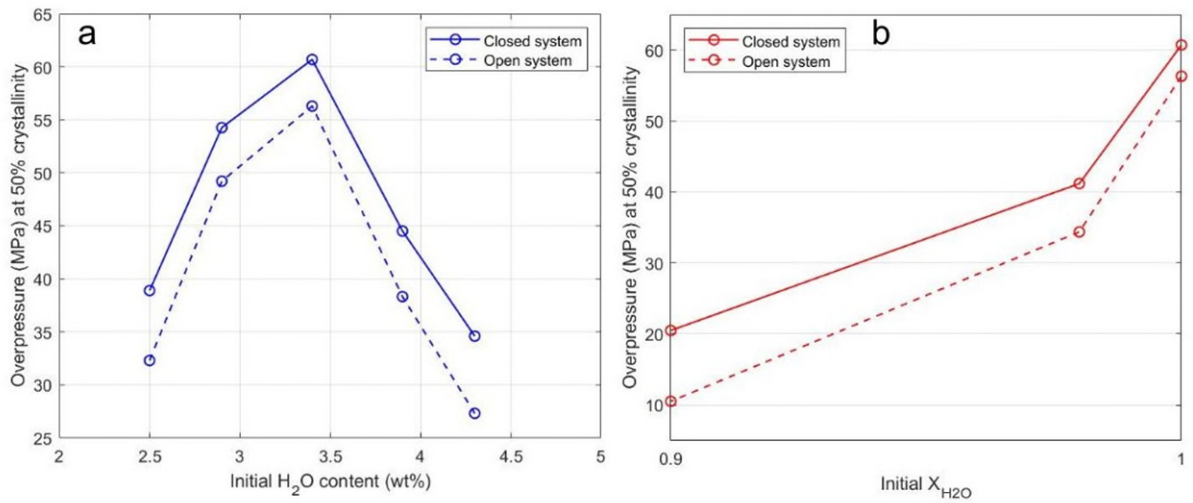


Figure 2.8. Comparing the effect of open- versus closed-system behaviour on overpressure magnitude for a) varying initial H_2O content, and b) varying initial X_{H2O}. Both examples using Kelud (100 MPa). The closed-system results are the same as those shown in figures 2.1c and 2.2c, where all fluids are retained within the system. The open-system results were calculated by subtracting 10% of the exsolved fluid volume at 50% crystallinity. The system volume and compressibility are then adjusted accordingly, and overpressure is recalculated based on the new values.

This reduction in overpressure due to gas loss means that open systems may take longer to reach critical overpressures than those with no gas loss. Although, as outlined above, this will only be relevant for systems where $(\Delta P)_{critical.}$ is attained after reaching ~40% crystallinity.

2.6. Conclusions

Our thermodynamic modelling demonstrates that magmas with initial H_2O contents at their solubility limit, and those with low CO_2 contents, generate the highest exsolution-driven overpressures and have the greatest potential for internal eruption triggering (**figs 2.1** and **2.2**). When coupled to a thermal model, our results show that overpressurisation to critical values can be achieved well within typical relaxation timescales, for small and shallow magma reservoirs (**figs 2.3**, **2.4** and **2.5**). For CO_2-free scenarios, the greatest rates of overpressure increase are seen in magmas which are initially H_2O-undersaturated. As initial H_2O content increases, the rate of overpressure build-up is reduced (**fig 2.3a**). For the mixed H_2O-CO_2 scenarios, rate of overpressurisation decreases as X_{H2O} decreases. The reduction in overpressure with decreasing magmatic X_{H2O} suggests that, below a certain point, volatile-exsolution is not a viable eruption triggering mechanism (**fig 2.4a**). We propose that the variation in overpressure with initial H_2O content may be one factor affecting magma ascent rate and explosivity (**fig 2.6**). Peak overpressures at the volatile 'sweet spot' may drive faster ascent rates, which, combined with other factors, allows less time for volatile outgassing and ultimately favours magma fragmentation and explosive eruptions. At low H_2O initial contents, magmas have a reduced potential for volumetric expansion, whilst high initial H_2O contents have increased system compressibilities – both of these factors reduce overpressure and make eruption triggering via volatile-exsolution less likely. Our methodology could be used to link reservoir processes with conduit models, where overpressure, volatile content, crystallinity and viscosity are important factors which govern magma ascent rate and eruption style.

Chapter 3 - Constraining the magnitude and rate of overpressure build-up with varying magmatic parameters

Anna Brookfield[1], Mike Cassidy[2] and Gregor Weber[3]

[1]Department of Earth Sciences, University of Oxford, Oxford, UK

[2]School of Geography, Earth and Environmental Science, University of Birmingham, Birmingham, UK

[3]School of Earth Sciences, University of Bristol, Bristol, UK

Abstract

The magnitude and timescales of magmatic overpressurization are fundamental to our understanding of volcanic eruption triggering. However, there is some debate as to whether the process of second boiling can generate enough overpressure in slowly cooling intrusions to be a viable eruption trigger. Magma reservoir failure is typically modelled using a uniform value of overpressure which is applied instantaneously. However, given that volatile exsolution is coupled to the thermal evolution of the reservoir, pressurisation can be expected to evolve over time, and may vary for different systems. We address this gap in the research by determining the temporal evolution of reservoir overpressure for a variety of realistic magma storage scenarios, focusing on overpressure generated by second boiling.

We use Rhyolite-MELTS to calculate overpressure during cooling for a basaltic andesite magma composition from Kelud, Indonesia. These outputs are coupled to a thermal model, where we vary reservoir shape, size, depth, and crustal thermal conductivity and geothermal gradient for cooling reservoirs with volumes of 1.4 km^3 and 11.2 km^3. By doing this, we can

assess the effect of varying both magmatic and crustal properties on pressurization timescales, evaluating them in the context of crustal relaxation timescales and eruption triggering potential.

We find that the time taken to reach critical overpressure is highly dependent on reservoir shape, size and depth. For example, varying the reservoir shape from flat to blocky increases the time taken to reach a critical overpressure of 10 MPa by ~ 1.7 ka, whilst increasing the reservoir size by an order of magnitude can result in a time difference of ~ 3.2 ka to reach 10 MPa of average reservoir overpressure. Pressurization to critical levels sufficient to trigger an eruption can happen on timescales shorter than that of crustal relaxation, even when using a conservative relaxation timescale of 1.6 ka. We also highlight the importance of strain rates due to rapid overpressurisation, and their potential for eruption triggering. More accurate methods of quantifying magma reservoir volume, shape, depth, and crustal properties will improve our estimates of magma cooling and overpressurisation rates, which have implications for the eruption triggering potential of a given system.

3.1. Introduction

Magmatic overpressurisation is implied in all internally-triggered volcanic eruptions (Cañón-Tapia, 2014), and can occur due to magma recharge, second boiling, magma buoyancy, or a combination of these. We define overpressure (ΔP) as a pressure in excess of the expected lithostatic pressure, which is generated by magmatic processes. Early work on dyke aspect ratios and crustal strength (Pollard, 1987) suggested typical critical overpressures $(\Delta P)_{critical}$ up to ~ 8 MPa, where $(\Delta P)_{critical}$ is the overpressure needed to initiate failure of the reservoir wall. These estimates were modified by numerical modelling work (Rubin, 1995a; Jellinek and DePaolo, 2003), leading to a commonly accepted $(\Delta P)_{critical}$ range of ~ 10 – 40 MPa. Equally important in terms of eruption triggering are the characteristic timescales of overpressure build-up and crustal relaxation. The identification of different volcanic regimes, governed by

timescales of magma cooling, magma injection and crustal relaxation (Degruyter and Huber, 2014) have been fundamental in framing our understanding of eruption triggering.

Overpressurisation of a magma reservoir is investigated in two fundamentally different ways. The first method considers the properties of the surrounding crust and any observable surface deformation, which then places limitations on the overpressure which can accumulate. These modelling studies indicate pre-eruptive magmatic overpressures on the order of tens of MPa, for example 40-50 MPa at Campi Flegrei, Italy (Trasatti *et al.*, 2005), 22-25 MPa at Colima, Mexico (Salzer *et al.*, 2014), and 17.6 MPa at Taal, Philippines (Morales Rivera *et al.*, 2019). Albright *et al.* (2019) use finite element modelling to hindcast the reservoir conditions at Okmok volcano, finding pressure changes of ~ 60 MPa - which interestingly exceeds the commonly accepted critical overpressure values quoted here. One limitation of these approaches is that overpressures derived from geodetic inversion are non-unique (Lisowski, 2007), as they are dependent on the values chosen for source depth, volume and elastic moduli, as demonstrated in Heap *et al.* (2020). In addition, ground displacement can also be generated by pressurisation within the volcanic conduit (Melnik and Sparks, 1999), or by hydrothermal systems (Troise *et al.*, 2019), meaning that assignment of a pressurisation source is not always straightforward. The second method of estimating overpressure is to consider the thermodynamic and/ or thermal properties of a magma, often using numerical modelling to determine overpressure due to variations in magma injection rate. For example, Caricchi *et al.* (2014) use a thermomechanical model to assess the effect of magma buoyancy and injection, whilst Degruyter and Huber (2014) develop a thermodynamic model of magma injection. In terms of overpressurisation rates, Albright *et al.* (2019) quote a pressure increase of 60 MPa yr^{-1} at Okmok, Alaska, Mittal and Richards (2019) show overpressure rates of ~ 0.02 MPa yr^{-1} derived from thermomechanical modelling, and Annen *et al.* (2023) present maximum overpressure rates of ~ 0.006 MPa yr^{-1} due to magma buoyancy.

Aside from the early work of Tait *et al.* (1989), the majority of modelling studies involving magmatic overpressure focus on magma recharge processes. They also often use a fixed

value of $(\Delta P)_{critical}$, and do not consider how overpressure evolves temporally and spatially for different systems. The ability of second boiling to generate enough overpressure to trigger volcanic eruptions is debated. Some authors think that second boiling alone can be an eruption trigger (Cañón-Tapia, 2014; Tramontano *et al.*, 2017; Arzilli *et al.*, 2019), whilst others think it has a subordinate role when compared to other mechanisms such as magma buoyancy or magma injection (Annen *et al.*, 2023).

In this study we seek to address the fact that overpressure generated by second boiling is not currently well-resolved, either spatially or temporally. We use a thermodynamic model to determine the magnitude of internally-generated overpressure for varying fluid contents. We then link these outputs to a thermal model, allowing us to 1) determine timescales of overpressurisation, and 2) determine the sensitivity of overpressurisation timescale to variations in reservoir size, shape and crustal properties. This provides a novel way to investigate the magnitude and timescale of overpressure build-up for a variety of key parameters, and allows us to assess variations in overpressurisation in the context of eruption triggering potential.

3.2. Methods

3.2.1 Rhyolite- MELTS thermodynamic modelling

We use Rhyolite-MELTS version 1.2 (Gualda *et al.*, 2012; Ghiorso and Gualda, 2015; Gualda and Ghiorso, 2015) to track the overpressure evolution of cooling magma. Using Kelud volcano, Indonesia, as an example, we use a basaltic andesite magma starting composition, based on bulk rock pumice data from the 1990 eruption reported in Jeffery *et al.* (2013) (sample KLT-901). Magma storage pressure is fixed at 100 MPa (~4 km), based on experimental petrology data from Cassidy *et al.* (2019).

Our first set of simulations contains H_2O only (no CO_2), whilst the second set contains a mixed H_2O-CO_2 volatile phase. For the first set, H_2O solubility is determined in Rhyolite-MELTS and

we define one initially-H_2O undersaturated magma (2.9 wt% H_2O), one which is initially at the solubility limit (3.4 wt% H_2O), and one which is initially H_2O-oversaturated (3.9 wt% H_2O). This set of simulations is coloured blue in subsequent figures. For the second set of mixed volatile simulations we vary the molar X_{H2O} ((H_2O+CO_2)/H_2O) between 1.0 and 0.9. We take the CO_2-free simulation from set 1 and use this as the X_{H2O} = 1 case. X_{H2O} is then decreased at a fixed total fluid content through the addition of CO_2 and removal of H_2O. This set of simulations is coloured red to orange in subsequent figures.

We run isobaric cooling simulations (at 100 MPa) starting at the liquidus and running in 2°C temperature increments until crystallinities > 60% have been reached. Using the Rhyolite-MELTS system outputs we calculate overpressure (ΔP, MPa) due to cooling and fluid exsolution following the method of Tramontano *et al.* (2017):

$$\Delta P = \frac{\Delta V}{V * \beta} \qquad \text{(eq 3.1)}$$

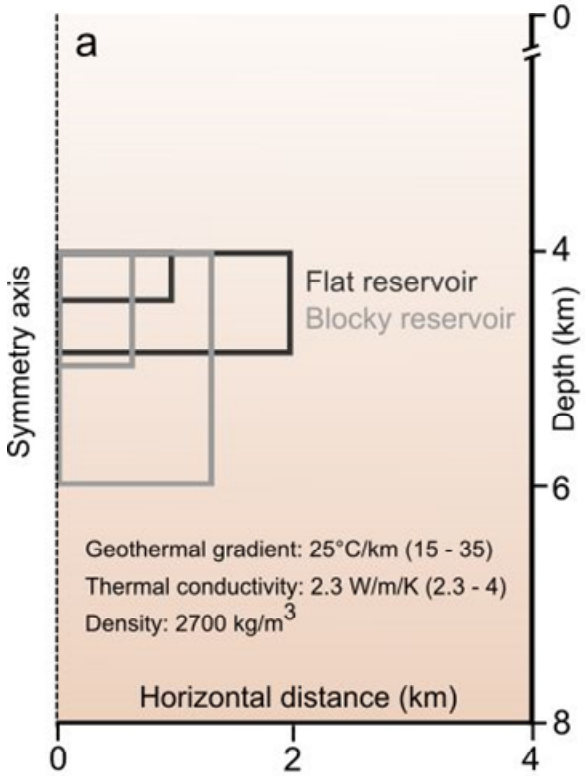
Where ΔV is volume change, relative to the initial volume at the liquidus (m^3), V is system volume (m^3) and β is system compressibility (1/MPa). The ΔV should be considered as a potential volume change, as this method assumes a rigid surrounding crust, with any volume changes due to cooling resulting in pressurization, instead of reservoir expansion. See section 2.2.1 for more detail on this method.

3.2.2 Thermal modelling

Timescales of internally-generated overpressure build-up are directly related to the cooling timescales of the magma. In order to track overpressure evolution both temporally and spatially, we input ΔP values calculated using Rhyolite-MELTS into the thermal model of Weber *et al.* (2020), as described also in section 2.2.2. This numerical model uses a finite difference method to solve the heat conduction equation for a cylindrical magma body, embedded about a vertical symmetry axis. We use this model to explore cooling timescales for reservoirs of varying size and shape, giving us an insight into variations in overpressurisation which would not be possible from thermodynamic modelling alone.

For the cooling scenarios described in sections 3.3.1 – 3.3.4 we use a geothermal gradient of 25°C/km, a thermal conductivity of 2.3 $W/m^{-1}/K^{-1}$, and a density of 2700 kg/m^3. In section 3.3.5 we explore the effect of varying the geothermal gradient between 15°C/km and 35°C/km, and in section 3.3.6 we explore the effect of increasing thermal conductivity up to 4 $W/m^{-1}/K^{-1}$. The melt fraction and temperature data from our Rhyolite-MELTS output was fitted using a fourth-order polynomial, and implemented in the thermal model. Latent heat release was then computed using this melt fraction-temperature relationship using a non-linear iteration loop (Weber *et al.*, 2020). Reservoir top depth is fixed at 4 km, and we vary reservoir volume and geometry as shown in **figure 3.1**. Considering an eruptive volume range of 0.14 – 0.28 km^3 for the 2014 eruption of Kelud (Maeno *et al.*, 2019) and a general intrusive: extrusive ratio of 5:1 (White *et al.*, 2006) results in magma reservoir volumes ranging from 0.70 – 1.40 km^3. Based on this upper estimate of reservoir volume, we define two, small end member reservoir geometries, 'flat' and 'blocky'. The flat reservoir is defined by a radius of 1000 m and a height of 446 m, and the blocky reservoir is defined by a radius of 668 m and a height of 1000 m - both have a volume of 1.4 km^3. We also vary reservoir size, modelling overpressure for a large, flat reservoir (defined by a radius of 2000 m and a height of 892 m), and a large, blocky reservoir (defined by a radius of 1336 m and height of 2000 m). These both have a volume of 11.2 km^3, and the same aspect ratio as their smaller counterparts (**fig 3.1**). We only consider overpressure generated by volatile exsolution in our model, and we do not explore the effect of successive pulses of magma injection, assuming that cooling continues uninterrupted after the magma is emplaced.

We model variations in overpressure within the cooling magma reservoir by linking the overpressure-temperature relationship derived from Rhyolite-MELTS to the temperature in each numerical cell of the thermal model. In each cell we assign the corresponding overpressure value based on its temperature, and so track the temporal evolution of average overpressure for all cells in the model. For access to the Matlab code used to generate our overpressure evolution plots, see Data Appendix 2.



b		Radius (m)	Height (m)	Volume (km3)	Aspect ratio
Small	Flat	1000	446	1.4	2.2
	Blocky	668	1000	1.4	0.7
Large	Flat	2000	892	11.2	2.2
	Blocky	1336	2000	11.2	0.7

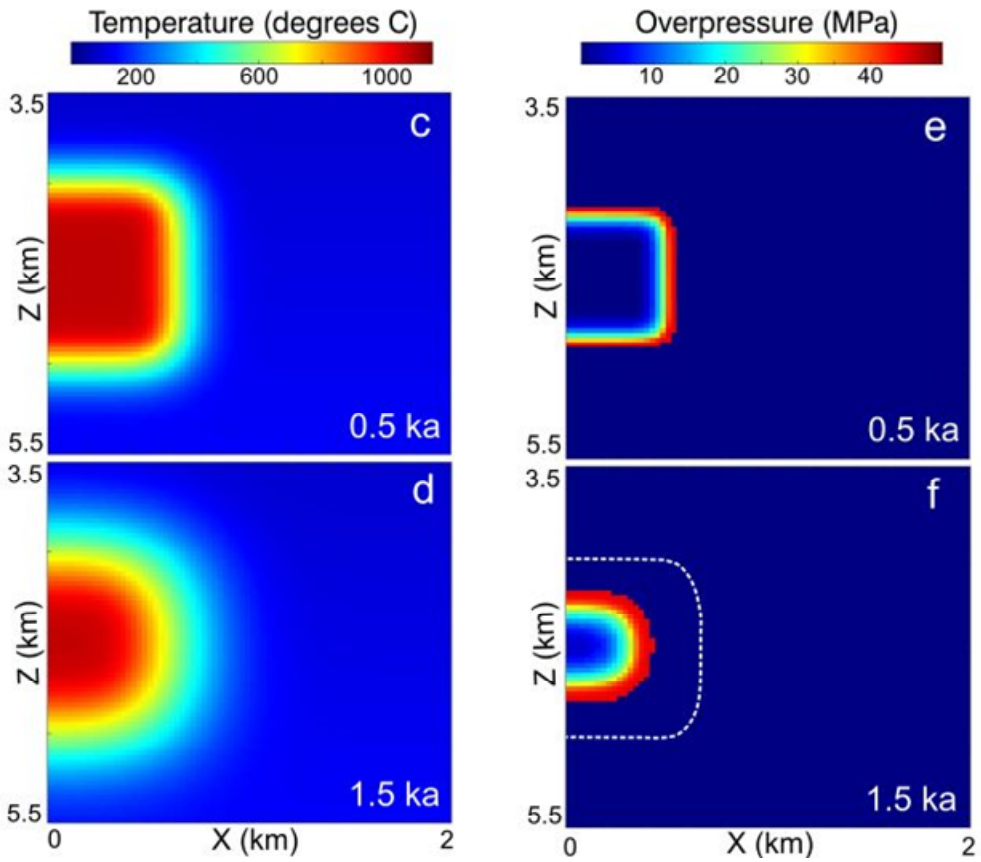


Figure 3.1 (above). Magma reservoir geometries used in thermal modelling. a) All reservoirs are embedded about a vertical symmetry axis at 4km depth and are cylindrical in shape. Key model parameters are also shown, with the range of values tested here given in brackets. b) Magma reservoir dimensions and aspect ratios discussed in the text. c) and d) Thermal model temperature outputs for 0.5 and 1.5 ka, for a small, blocky reservoir. e) and f) Corresponding thermal model overpressure outputs for 0.5 and 1.5 ka. White dashed line shows extent of magma reservoir at the beginning of the simulations. Magma which exceeds 60% crystallinity (by volume) is excluded from the average overpressure calculations, as it is assumed to be uneruptible.

This provides a unique way of incorporating thermodynamic properties specific to each magma type into the cooling and pressurisation history. Example thermal model outputs for temperature and overpressure evolution are shown in **figure 3.1(c-f)**. In section 3.3 we present average reservoir overpressure values. Using average values assumes that the magma can transfer stress evenly throughout its volume, an assumption which may not be valid for mushy, heterogeneous reservoirs. We also track the crystallinity (vol %) of the magma, and once a cell cools below 60% crystallinity we remove it from our calculations as it is assumed to be uneruptible by this point. Developing a fully coupled thermo-mechanical model to incorporate the response of the surrounding crust is beyond the scope of this study. Instead we compare our timescales of overpressurisation to crustal relaxation timescales, as described below.

3.2.3 Critical overpressure and crustal relaxation timescales

3.2.3.1 Critical overpressure

Critical overpressure $(\Delta P)_{critical}$ is the overpressure needed to initiate failure of the surrounding rock, and is dependent on host rock strength. The tensile strength of the crust will vary due to fracturing (Zhan and Gregg, 2019) and hydrothermal alteration (Heap *et al.*, 2022). It is also very sensitive to pore fluid pressure – which can affect whether $(\Delta P)_{critical}$ is on the order of tensile strength values (~10 MPa) or the order of confining pressure (100s of MPa) (Albino *et al.* 2018). In the absence of information on pore fluid pressure at Kelud, we adopt a $(\Delta P)_{critical}$ range of 10 - 20 MPa, based on tensile strength (T_S) estimates of 5 - 10 MPa for volcanic rocks (Gudmundsson, 2011; Albino *et al.*, 2018), and shear strength estimates ~2x that of tensile

strength (Gudmundsson, 2011). We also note that the rheology of the crust will modify critical overpressure values. Head *et al.* (2022) show that $(\Delta P)_{critical}$ can be increased by up to 60% if the crustal response is thermo-viscoelastic (i.e. temperature-dependent viscoelasticity). This effect is dependent on reservoir temperature, geothermal gradient, rate of overpressurisation, and reservoir geometry. For the factors considered in our study, this translates into a maximum modifying effect of +20% to $(\Delta P)_{critical}$, considering a reservoir temperature of ~1000° C, geothermal gradient of 25°C/ km, overpressure loading rate of 1 MPa/yr, and an oblate reservoir geometry. We therefore include a threshold of 24 MPa $(\Delta P)_{critical}$ to our figures, to incorporate an upper bound relevant to thermo-viscoelastic crustal response.

We model the evolution of overpressure within the magma reservoir but we do not consider the specific failure mechanism or location - i.e, whether eruption occurs due to tensile (extensional) or Mohr-Coulomb (shear) failure. Stresses acting on the surrounding crust are generated, in our case, by volatile exsolution and subsequent reservoir pressurization. However, Albright *et al.* (2019) demonstrate that variations in tensile stress are the most likely trigger for the 2008 eruption of Okmok, Alaska – suggesting that high overpressure alone was not sufficient to cause reservoir failure. Gregg *et al.* (2012) demonstrate that Mohr-Coulomb failure is sensitive to reservoir size and geometry, with larger, ($>10^3$ km^3) more oblate reservoirs able to generate failure at lower overpressures than smaller, more prolate ones.

3.2.3.2 Crustal relaxation timescales

In order to trigger an eruption, overpressure has to build-up more quickly than it can be dissipated by relaxation of the surrounding crust. A crustal relaxation timescale (τ_{relax}) can be calculated from Degruyter and Huber (2014):

$$\tau_{relax} = \eta r / (\Delta P)_{critical} \quad \text{(eq. 3.2)}$$

Where ηr is host rock viscosity. We use $\eta r = 10^{18}$ Pa s, and a critical overpressure of 20 MPa, giving a characteristic crustal relaxation timescale of 1.6 ka. For comparison, Jellinek and DePaolo (2003) use a crustal viscosity range of 10^{17} - 10^{20} Pa s, Townsend *et al.* (2019) use

a ηr of 10^{19} Pa s for a reservoir at 7.5 km depth, Caricchi *et al.* (2014) use a range of 10^{17} - 10^{19} Pa s, and Mittal and Richards (2021) use a viscosity of 5 x 10^{18} Pa s for the viscous shell surrounding their magma reservoir. Our calculated relaxation timescale is highly dependent on the value of ηr. Head *et al.* (2022) demonstrate that increasing the temperature of the crust from 400°C to 500°C results in a viscosity reduction from 1.22 x 10^{19} Pa s to 6.07 x 10^{17} Pa s respectively. This decreases the relaxation timescale from 19.3 ka to 0.96 ka, based on eq 2 and a $(\Delta P)_{critical}$ of 20 MPa. As crustal viscosity will vary with distance away from the reservoir, we adopt the approach of Townsend *et al.* (2019) and use a single, effective value for ηr.

3.3. Modelling results

3.3.1 Varying reservoir shape

Figure 3.2 shows the effect that varying reservoir shape has on the temporal evolution of average reservoir overpressure, for magmas of varying initial H_2O content. As discussed in chapter 2, overpressure-generating capacity is greatest for magmas with initial H_2O contents at the water solubility limit, and decreases with the addition or removal of H_2O. Across all of the varying initial H_2O content scenarios, the blocky reservoir takes longer to attain critical overpressures than its flat counterpart of the same volume. This difference in overpressurisation timescale with varying reservoir shape is most pronounced for the scenario which is initially H_2O-undersaturated. In this case (**fig 3.2a**), the flat reservoir takes 0.60 ka to reach 10 MPa, whilst the blocky reservoir takes 1.90 ka - a time difference of 1.30 ka. If $(\Delta P)_{critical}$ is raised to 20 MPa, then the flat reservoir takes 0.63 ka to reach critical levels, whilst the blocky reservoir takes 2.08 ka - a time difference of 1.45 ka. For the case modelled here, the blocky reservoir reaches $(\Delta P)_{critical}$ on a timescale greater than that of crustal relaxation, meaning eruption triggering via second boiling is not possible for this set of conditions. For the initially H_2O-oversaturated scenario (**fig 3.2c**), the blocky reservoir takes ~ 0.35 ka longer to reach 20 MPa than the flat reservoir, but eruption triggering is possible in both cases. The scenario which begins cooling at the H_2O-solubility limit (**fig 3.2b**) shows rapid

overpressurisation to critical levels, and this is due to the greater intrinsic overpressure-generating capacity of this magma.

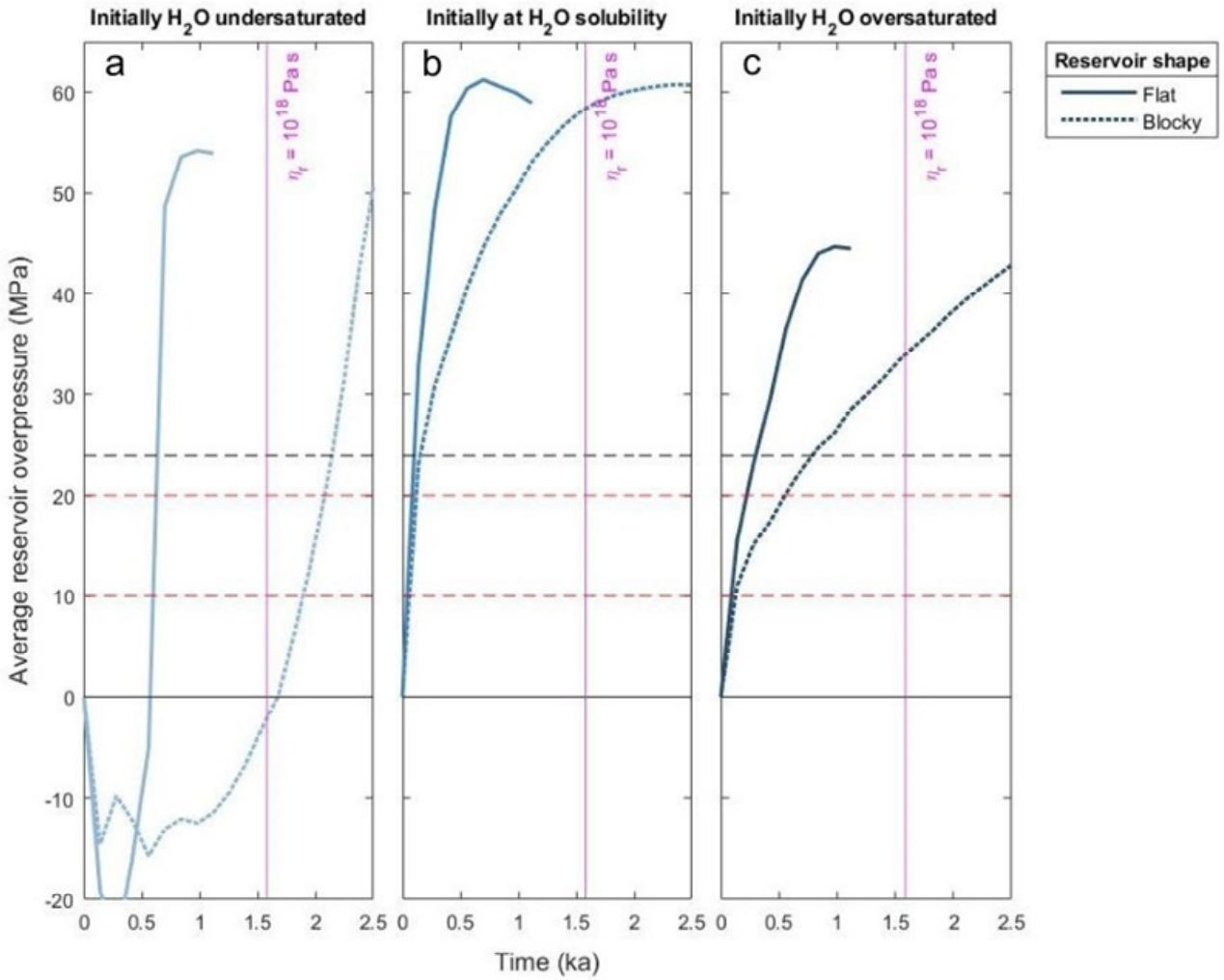
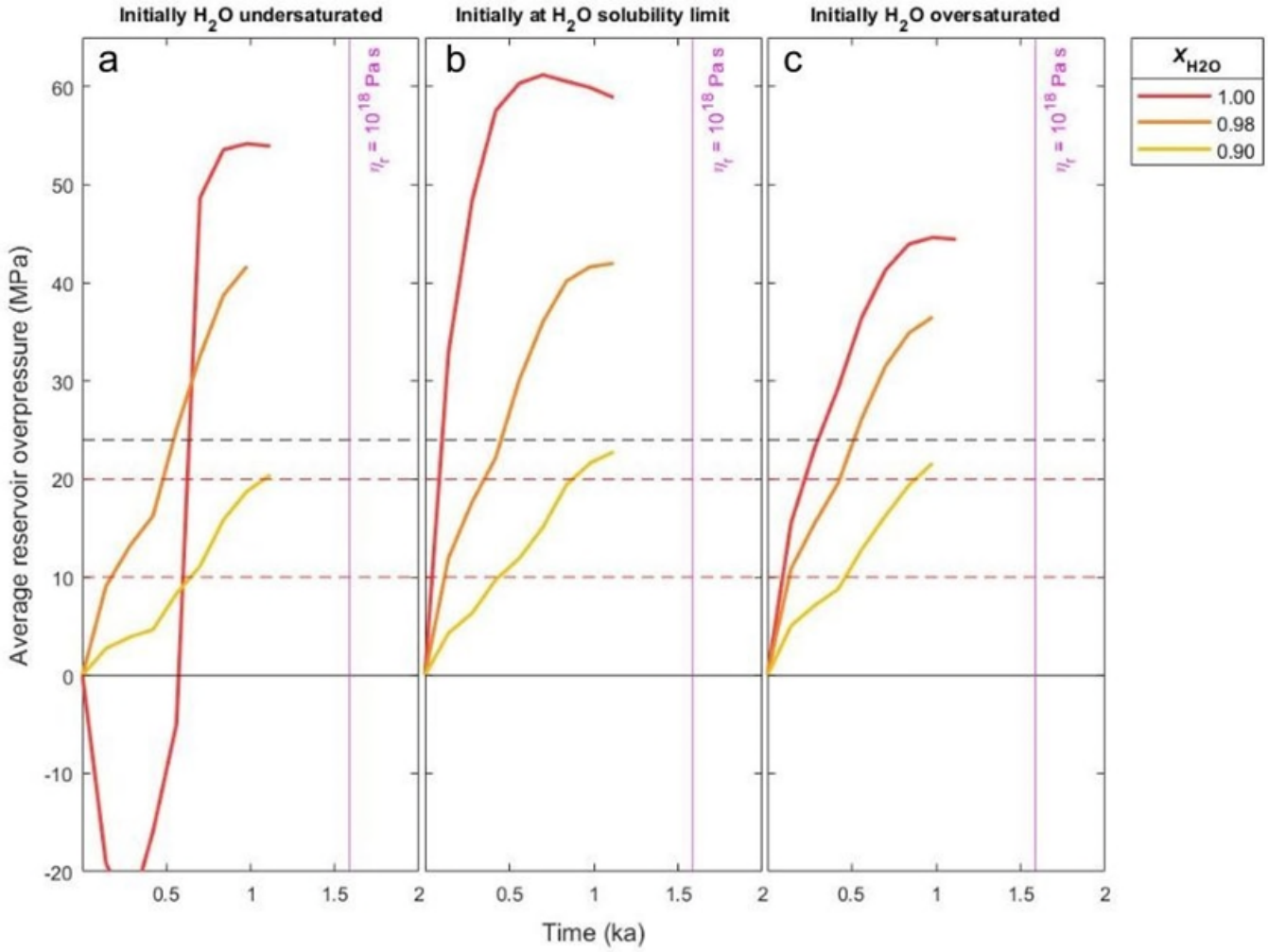


Figure 3.2. Temporal evolution of average reservoir overpressure for varying initial H_2O contents and reservoir shapes. a) Magma is initially H_2O undersaturated. b) Magma is initially at the H_2O solubility limit. c) Magma is initially H_2O oversaturated. Red, horizontal dashed lines highlight 10 and 20 MPa critical overpressure thresholds. Black dashed line highlights 24 MPa overpressure, as adjusted for a thermo-viscoelastic crustal response. Vertical pink line highlights a crustal relaxation timescale of 1.6 ka.

3.3.2 Varying X_{H2O}

Figure 3.3 shows the effect on average reservoir overpressurisation timescales when magmatic X_{H2O} is varied from 1.00 to 0.90, all for a flat reservoir geometry. The initial H_2O content of each of the X_{H2O} = 1 simulations is the same as that shown for the flat scenarios in **figure 3.2**, and X_{H2O} is decreased by substituting H_2O for CO_2. As discussed in section 2.3.2.2, the rate of overpressurisation, and also the peak overpressure, both increase with increasing X_{H2O}, as demonstrated in **figure 3.3**. However, the relative times taken to reach $(\Delta P)_{critical}$ vary



with initial H_2O content. For the initially H_2O undersaturated case shown in **figure 3.3a**, the X_{H2O} = 1 scenario shows a period of average reservoir underpressurisation lasting ~ 0.5 ka, followed by a rapid increase in overpressure. For these scenarios, the X_{H2O} = 0.98 case reaches 20 MPa most rapidly (0.49 ka), followed by X_{H2O} = 1 (0.62 ka), then X_{H2O} = 0.90 (1.10 ka).

Figure 3.3. Temporal evolution of average reservoir overpressure for varying initial H_2O content and X_{H2O}. All scenarios are for a small, flat reservoir, located at 4 km depth. a) X_{H2O} = 1 case is initially H_2O undersaturated. b) X_{H2O} = 1 case is initially at the H_2O solubility limit. c) X_{H2O} = 1 case is initially H_2O oversaturated. Red, horizontal dashed lines highlight 10 and 20 MPa critical overpressure thresholds. Black dashed line highlights 24 MPa overpressure, as adjusted for a thermo-viscoelastic crustal response. Vertical pink line highlights a crustal relaxation timescale of 1.6 ka.

The magmas which are initially at the H_2O solubility limit (**fig 3.3b**), and initially H_2O oversaturated (**fig 3.3c**) do not display a period of average underpressurisation, and a different trend is observed. In these scenarios, the X_{H2O} = 1 case reaches $(\Delta P)_{critical}$ most rapidly, followed by X_{H2O} = 0.98, then X_{H2O} = 0.90. All of the simulations shown here attain critical overpressures within the crustal relaxation timescale.

3.3.3 Varying reservoir size

We increase the size of the flat and blocky reservoir scenarios from 1.4 km^3 to 11.2 km^3 (**fig 3.1**), and plot the resulting average reservoir overpressures for a variety of initial H_2O contents (no CO_2) in **figure 3.4**. Across each different initial H_2O content, the larger reservoirs take longer to attain critical overpressure than their smaller counterparts. The small (1.4 km^3), flat reservoir scenario attains $(\Delta P)_{critical}$ most rapidly, followed by the small, blocky scenario, then the large (11.2 km^3), flat scenario. The large, blocky scenario takes the longest to reach $(\Delta P)_{critical}$, regardless of initial H_2O content. For the magma which is initially H_2O-undersaturated when it begins crystallizing (**fig 3.4a**), only the small, flat scenario attains critical overpressure more quickly than the surrounding crust can relax. The other three scenarios attain $(\Delta P)_{critical}$ more slowly than 1.6 ka, with the large, blocky scenario failing to attain average positive overpressure within 3 ka. The scenarios involving magma which is initially at the H_2O solubility limit as it begins crystallizing (**fig 3.4b**) all show rapid overpressure increases, and all attain $(\Delta P)_{critical}$ more rapidly than the crust can relax. The magma which is initially H_2O-oversaturated (**fig 3.4c**) attains 10 MPa $(\Delta P)_{critical}$ for each of the modelled scenarios. However, if a critical overpressure of 20 MPa is required to fracture the crust, then

the large, blocky scenario would not generate overpressure quickly enough to trigger an eruption.

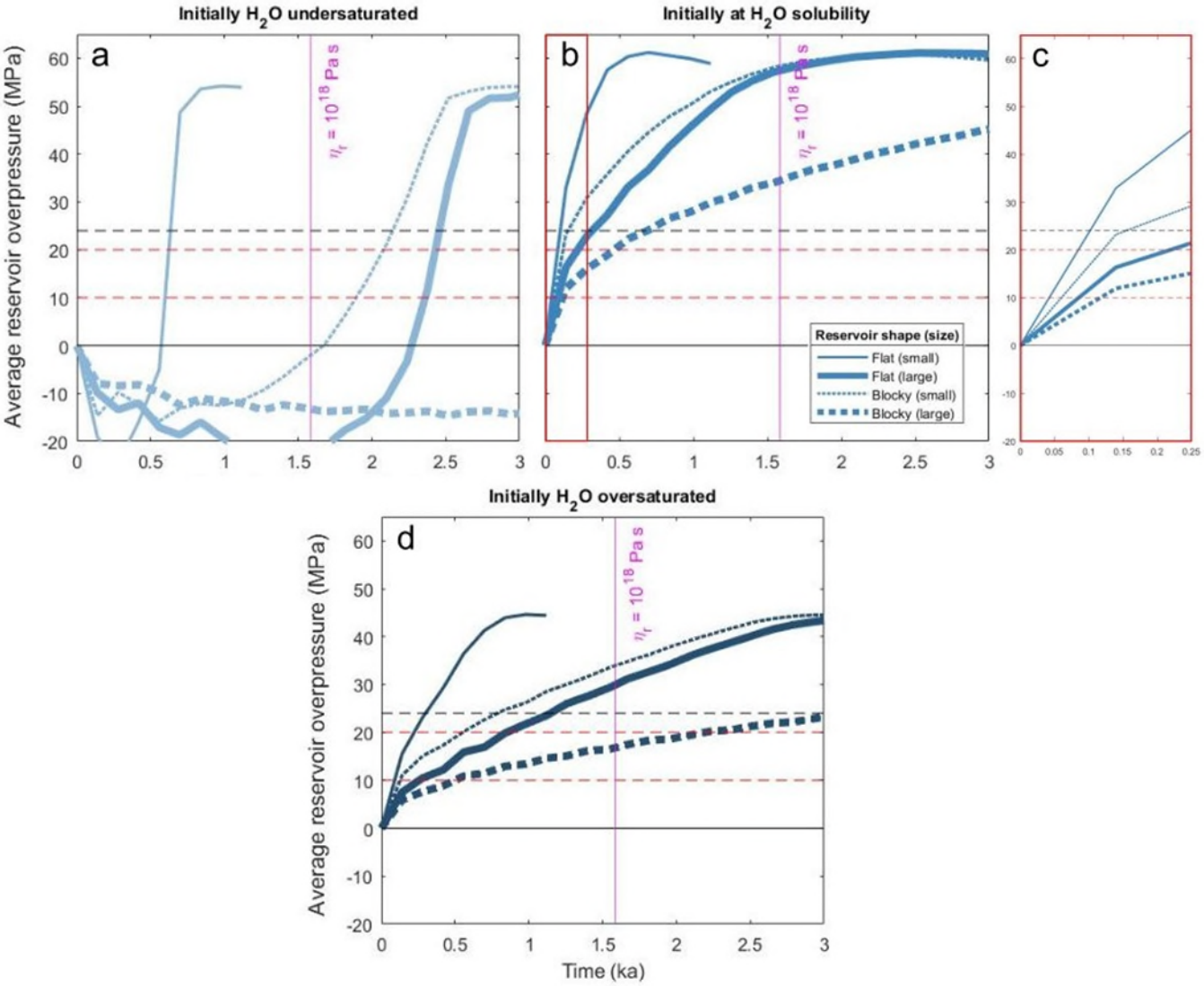


Figure 3.4. Temporal evolution of average reservoir overpressure with varying magma reservoir shape, size and initial H_2O content. a) Magma is initially H_2O undersaturated at the liquidus. b) Magma is initially at the H_2O solubility limit). Red rectangle highlights the area shown in c. d) Magma is initially H_2O oversaturated. Red, horizontal dashed lines highlight 10 and 20 MPa critical overpressure thresholds. Black dashed line highlights 24 MPa overpressure, as adjusted for a thermo-viscoelastic crustal response. Vertical pink line highlights a crustal relaxation timescale of 1.6 ka.

3.3.4 Varying reservoir depth

To investigate the effect of magma reservoir depth on overpressurisation timescales, we run additional Rhyolite-MELTS simulations using the same starting composition, at lithostatic pressures of 50 MPa (~ 2 km depth), 150 MPa (~ 6 km depth) and 300 MPa (~ 12 km depth). For each of these depths, we determine water solubility at the liquidus in Rhyolite-MELTS, and then perform one simulation which is initially H_2O undersaturated, one which is at the H_2O solubility limit, and one which is initially H_2O oversaturated. The MELTS temperature-overpressure profiles are then input into the thermal model as described in section 3.2.2, and reservoir top depth is varied accordingly. All scenarios are run for a small, blocky reservoir geometry. **Figures 3.5b** and **3.5c** show that maximum average reservoir overpressure increases from 2 km to 6 km, and then begins to decrease again as reservoir depth is increased to 12 km. The 12 km depth scenarios all display a period of average reservoir underpressurisation - even when the magma is initially H_2O-oversaturated (**fig 3.5c**). The effect of reservoir depth on pressurization timescale varies with initial H_2O saturation state. For the initially H_2O undersaturated scenarios (**fig 3.5a**), the magma at 4 km depth reaches critical levels most rapidly, followed by the 6 km scenario, the 2 km one and finally the 12 km depth one. The initial period of average underpressurisation which occurs in these magmas means that none of them reach $(\Delta P)_{critical}$ more quickly than the relaxation timescale of 1.6 ka. For magmas with H_2O contents which are initially at the solubility limit (**fig 3.5b**), the 6 km depth scenario generates overpressure most rapidly, followed by the 4 km, 2 km and 12 km scenarios. All of these scenarios reach 10 MPa prior to τ_{relax}, and all but the 12 km depth scenario reach 20 MPa prior to $\tau_{relax.}$ For the initially H_2O oversaturated magmas (**Fig 3.5c**), the time taken to reach 10 MPa $(\Delta P)_{critical}$ follows the same order as in **figure 3.5b**. However, if the critical overpressure is raised to 20 MPa, then the 12 km scenario reaches critical levels more rapidly than the 2 km one. The 12 km depth, initially H_2O oversaturated scenario reaches $(\Delta P)_{critical}$ more slowly than τ_{relax}, so is not a viable eruption trigger for the case modelled here.

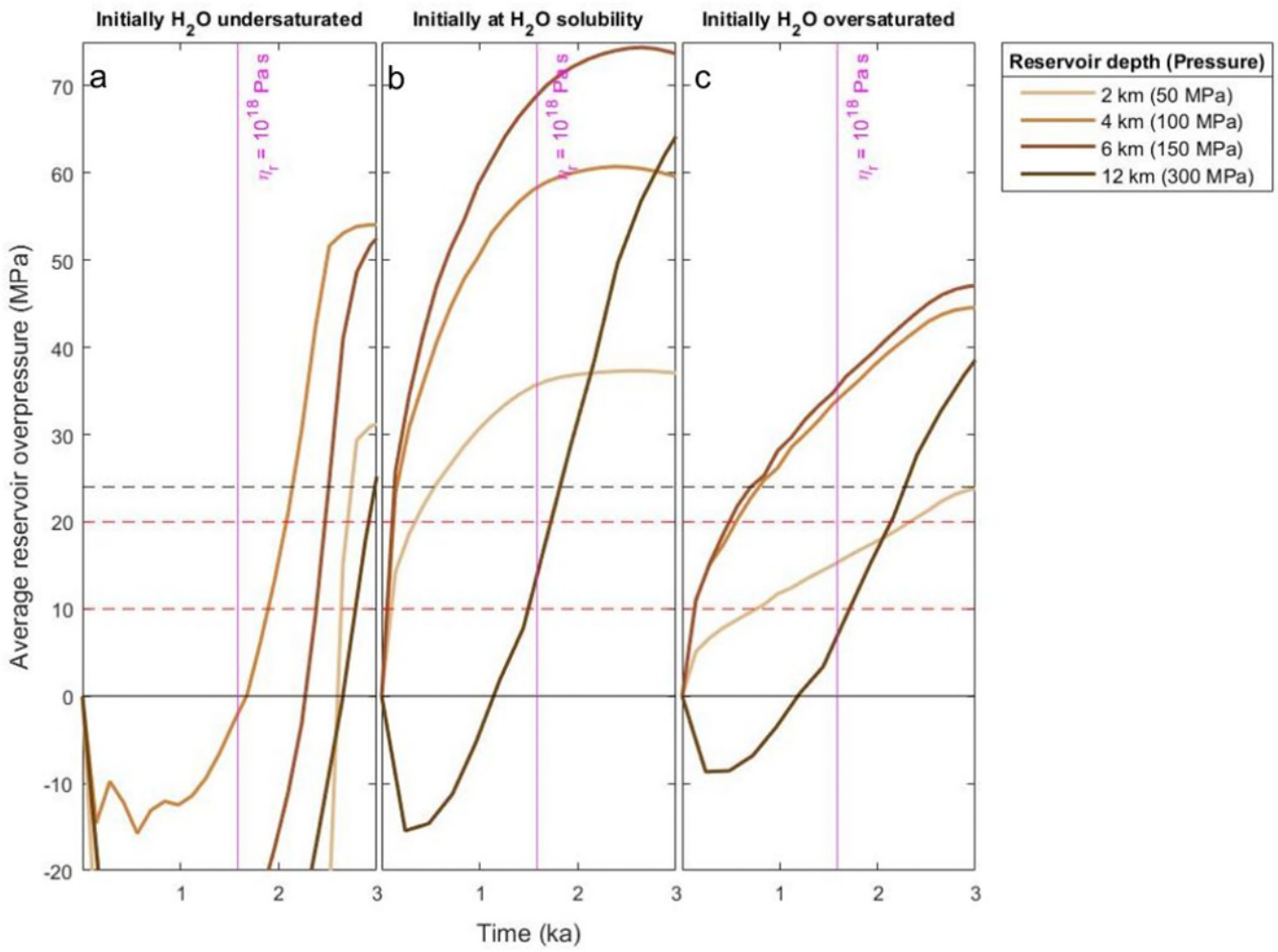


Figure 3.5. Temporal evolution of average reservoir overpressure with varying Rhyolite-MELTS storage pressures of 50 - 300 MPa (depth range of ~ 2 - 12 km), for a small, blocky reservoir. Top depth in the thermal model is also varied accordingly. a) Magma is initially H_2O undersaturated. b) Magma is initially at the H_2O solubility limit. c) Magma is initially H_2O oversaturated. Red, horizontal dashed lines highlight 10 and 20 MPa critical overpressure thresholds. Black dashed line highlights 24 MPa overpressure, as adjusted for a thermo-viscoelastic crustal response. Vertical pink line highlights a crustal relaxation timescale of 1.6 ka.

3.3.5 Varying geothermal gradient

We perform additional simulations with varying geothermal gradient in order to assess its effect on reservoir pressurization timescales. Heat flow maps of Indonesia (Hall, 2002) show heat flow values between ~45 - 75 mW/m^2 for eastern Java, resulting in geothermal gradients of ~ 20 - 33°C/km, assuming a thermal conductivity of 2.3 W/m^{-1}/K^{-1} (which we use as standard in our thermal modelling). We use a geothermal gradient range of 15 - 35°C/km, to represent

cooler and warmer end-members and explore uncertainty in these estimates. **Figure 3.6** shows the effect of varying the geothermal gradient for reservoirs of different shape and size, all with the same initial H_2O content of 3.9 wt% and a reservoir top depth of 4 km. This demonstrates that varying the geothermal gradient does not have a significant effect on timescales of overpressure build-up for the scenarios modelled here. There is a negligible difference in the overpressurisation timescales across each reservoir geometry and size.

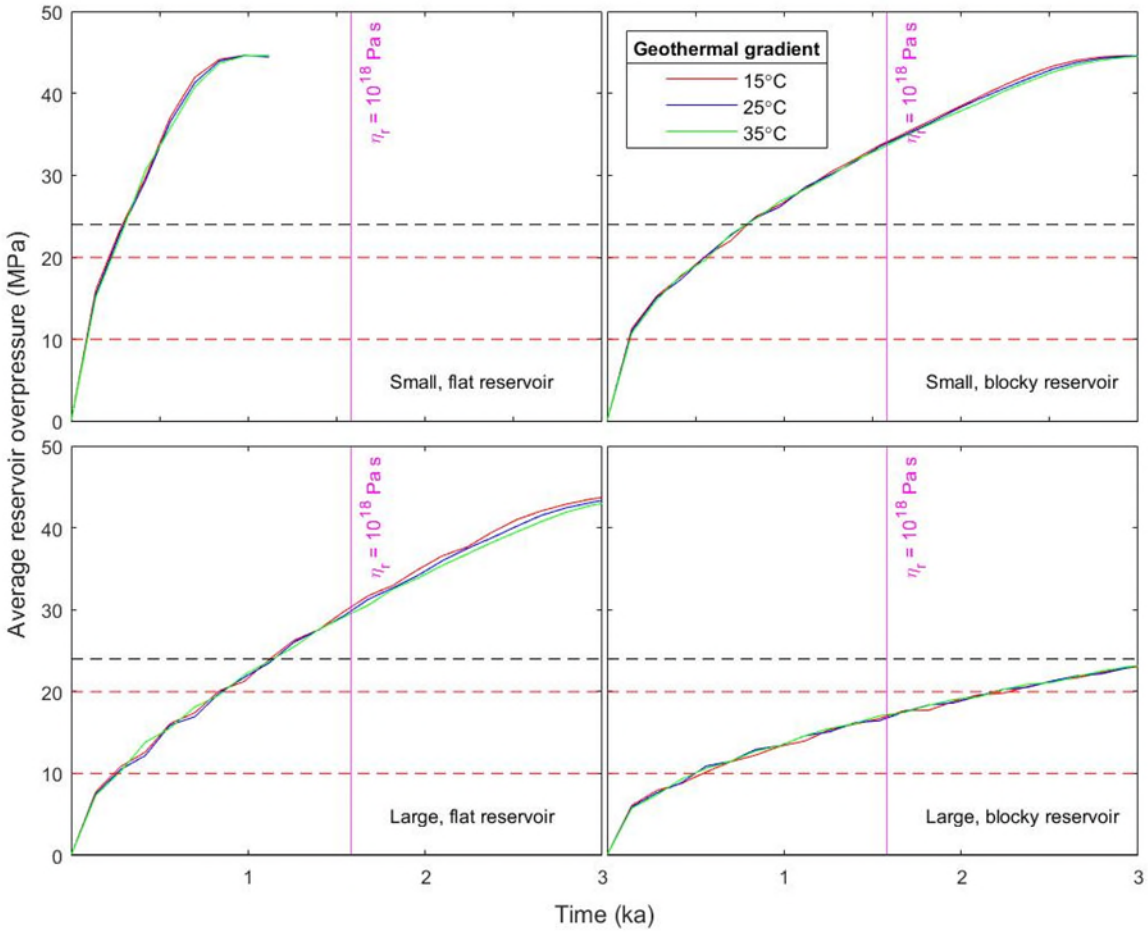


Figure 3.6. Temporal evolution of average reservoir overpressure with varying geothermal gradients of 15°C, 25°C and 35°C. All scenarios are initially H_2O oversaturated (3.9 wt% H_2O). a) Small, flat reservoir. b) Small, blocky reservoir. c) Large, flat reservoir. d) Large, blocky reservoir. Red, horizontal dashed lines highlight 10 and 20 MPa critical overpressure thresholds. Black dashed line highlights 24 MPa overpressure, as adjusted for a thermo-viscoelastic crustal response. Vertical pink line highlights a crustal relaxation timescale of 1.6 ka.

This effect is the same for magma reservoirs which are initially H_2O undersaturated when they begin crystallising (**fig 3.9**). However, we note that the effect of varying the geothermal gradient is likely to become more significant as reservoir depth and size increases.

3.3.6 Varying thermal conductivity

For the overpressurisation timescales presented so far we have used a crustal thermal conductivity (k) value of 2.3 $W/m^{-1}/K^{-1}$ in our thermal modelling, which is within the range of average and upper crustal values reported in Whittington *et al.* (2009). However the range of thermal conductivity values used in different studies varies, e.g, 3.25 $W/m^{-1}/K^{-1}$ in Degruyter and Huber (2014) and 4 $W/m^{-1}/K^{-1}$ in Del Negro *et al.* (2009), and it is known that k decreases with increasing temperature. We therefore perform additional cooling simulations with k values of 3.0 and 4.0 $W/m^{-1}/K^{-1}$, in order to analyse the effect on cooling and overpressurisation timescales. Fracturing of the upper crust will increase heat transfer and cooling rates, so increasing the thermal conductivity could simulate cooling timescales in areas with fractured upper crust. **Figure 3.7** shows that increasing the thermal conductivity of the crust results in an increased rate of average overpressurisation. For the small, flat reservoir (**fig 3.7a**), the 2.3 W/m/K scenario reaches 20 MPa ~ 0.15 ka later than the 4.0 Wm/K scenario. For the small, blocky scenario this difference increases to ~ 0.25 ka, and for the large, flat reservoir it increases to ~ 0.75 ka. For the large, blocky reservoir (**fig 3.7d**), the 2.3 W/m/K scenario reaches 20 MPa ~ 1 ka later than the 4.0 Wm/K scenario. This difference in overpressurisation rate with varying thermal conductivity could be significant for eruption triggering potential – as increasing thermal conductivity from 2.3 W/m/K (the standard value used in our modelling) to 4 W/m/K results in pressurisation to $(\Delta P)_{critical}$, occurring prior to the 1.6 ka crustal relaxation timescale. The effect of increasing thermal conductivity on overpressurisation timescales is the same for magma reservoirs which are initially H_2O undersaturated when they begin crystallising, as illustrated in **figure 3.9**.

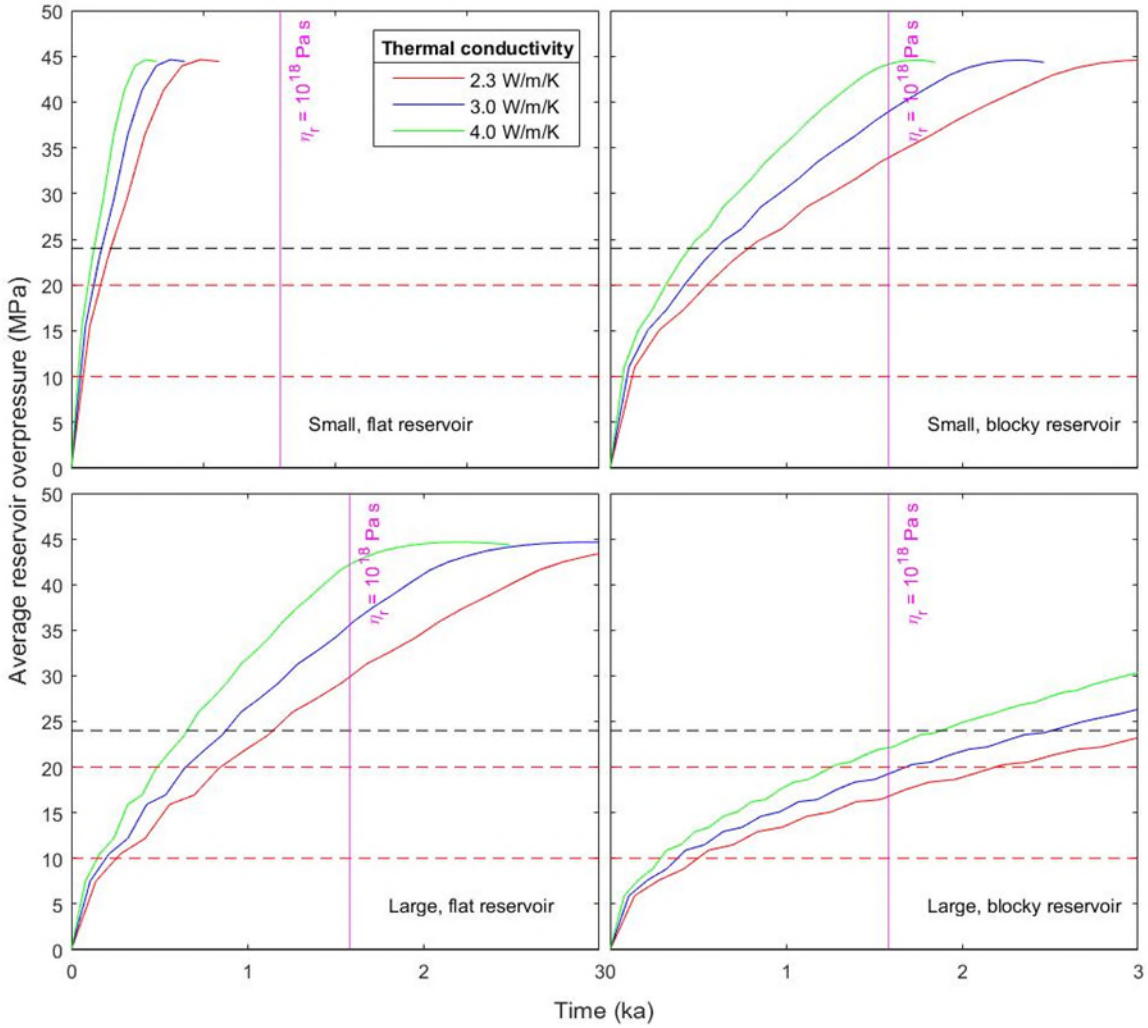


Figure 3.7. Temporal evolution of average reservoir overpressure with varying thermal conductivity values of 2.3, 3.0 and 4.0 W/m/K. All scenarios are initially H_2O oversaturated (3.9 wt% H_2O). a) Small, flat reservoir. b) Small, blocky reservoir. c) Large, flat reservoir. d) Large, blocky reservoir. Red, horizontal dashed lines highlight 10 and 20 MPa critical overpressure thresholds. Black dashed line highlights 24 MPa overpressure, as adjusted for a thermo-viscoelastic crustal response. Vertical pink line highlights crustal relaxation timescale of 1.6 ka.

3.3.7 Temporal evolution of other magma properties

Our method of linking thermodynamic and thermal models provides a unique insight into overpressurisation timescales. This same method can be applied to gain insights into the evolution of other relevant magma properties prior to eruption. Here we extract system compressibility (β) values from Rhyolite-MELTS, and track the temporal evolution of average magma compressibility during cooling. We chose β for this example because of its importance

in muting ground displacement prior to eruption (Rivalta and Segall, 2008; Kilbride *et al.*, 2016), making it an interesting parameter to monitor in terms of pre-eruptive processes (Hautmann *et al.*, 2010).

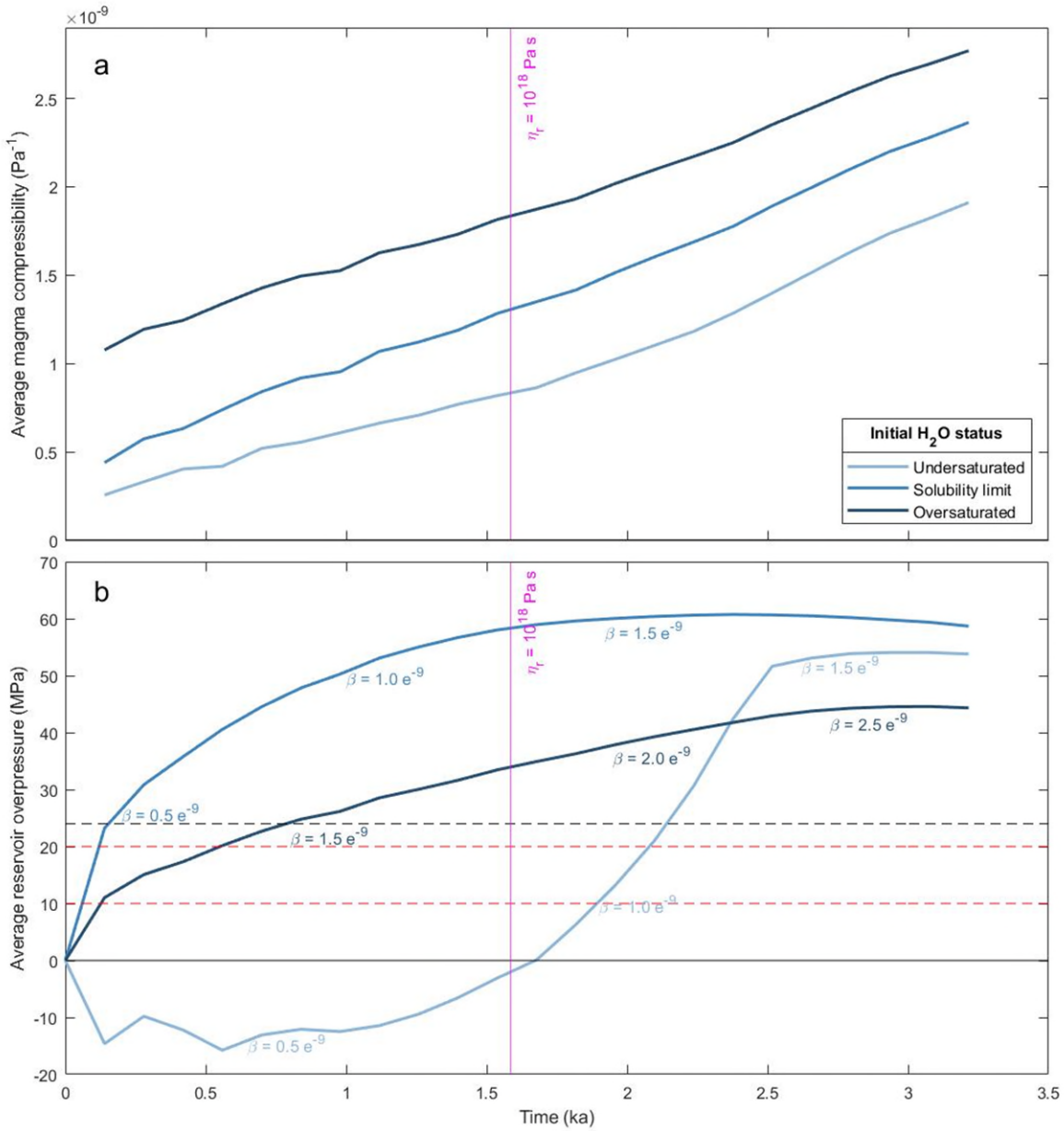


Figure 3.8. Temporal evolution of magma compressibility and overpressure for a small, blocky magma reservoir at 4 km depth, with varying initial H_2O contents. a) Average magma compressibility from Rhyolite-MELTS outputs. b) Average reservoir overpressure. Coloured annotations indicate evolving magma compressibility values (Pa^{-1}) for each different initial H_2O content. Red, horizontal dashed lines highlight 10 and 20 MPa critical overpressure thresholds. Black dashed line highlights 24 MPa overpressure, as adjusted for a thermo-viscoelastic crustal response. Vertical pink line highlights a crustal relaxation timescale of 1.6 ka.

However, this same approach could be applied to investigate any other parameter of interest which can be extracted from or calculated using MELTS outputs, for example crystallinity, exsolved volume fraction or viscosity. **Figure 3.8** shows magma compressibility and overpressure evolution for magmas with different initial H_2O contents. Throughout the cooling period, average magma compressibility is highest for the magma which is initially H_2O-oversaturated, and lowest for the magma which is initially H_2O-undersaturated (**fig 3.8a**), with a maximum difference in β of ~ 1 x 10^{-9} Pa^{-1} between the two scenarios. Average magma compressibility values are projected onto the overpressure evolution curves in **figure 3.8b**. This demonstrates that average compressibility values for magmas with different initial fluid contents can be estimated during the approach to eruption triggering.

3.4. Discussion

3.4.1 Variations in time taken to reach critical overpressure

The effect of varying magmatic and crustal properties is summarized in **Figure 3.9**, which shows the time taken to reach 20 MPa $(\Delta P)_{critical}$ for various magma storage scenarios. We use this metric to compare the different scenarios because the rate of overpressurisation is not constant for each case, so using time to 20 MPa provides a clearer comparison of the ability of each scenario to potentially trigger an eruption. However, we also discuss the effect of overpressurisation rate in section 3.4.2. Timescales are plotted relative to the 'reference' scenario. This is defined as a magma with no CO_2 (X_{H2O} = 1) stored within a small, flat reservoir with a top depth of 4 km, a geothermal gradient of 25° C/km, and a thermal conductivity of 2.3 W/m/K. We plot these timescales for magma which is initially H_2O undersaturated (**fig 3.9a**) and initially H_2O oversaturated (**fig 3.9b**). Our results show that varying the magma storage depth or the molar X_{H2O} have different effects (increased or decreased timescales relative to the reference scenario) depending on initial H_2O content. However, varying the reservoir shape, size, geothermal gradient or thermal conductivity has the same effect with respect to the reference scenario, regardless of initial H_2O content.

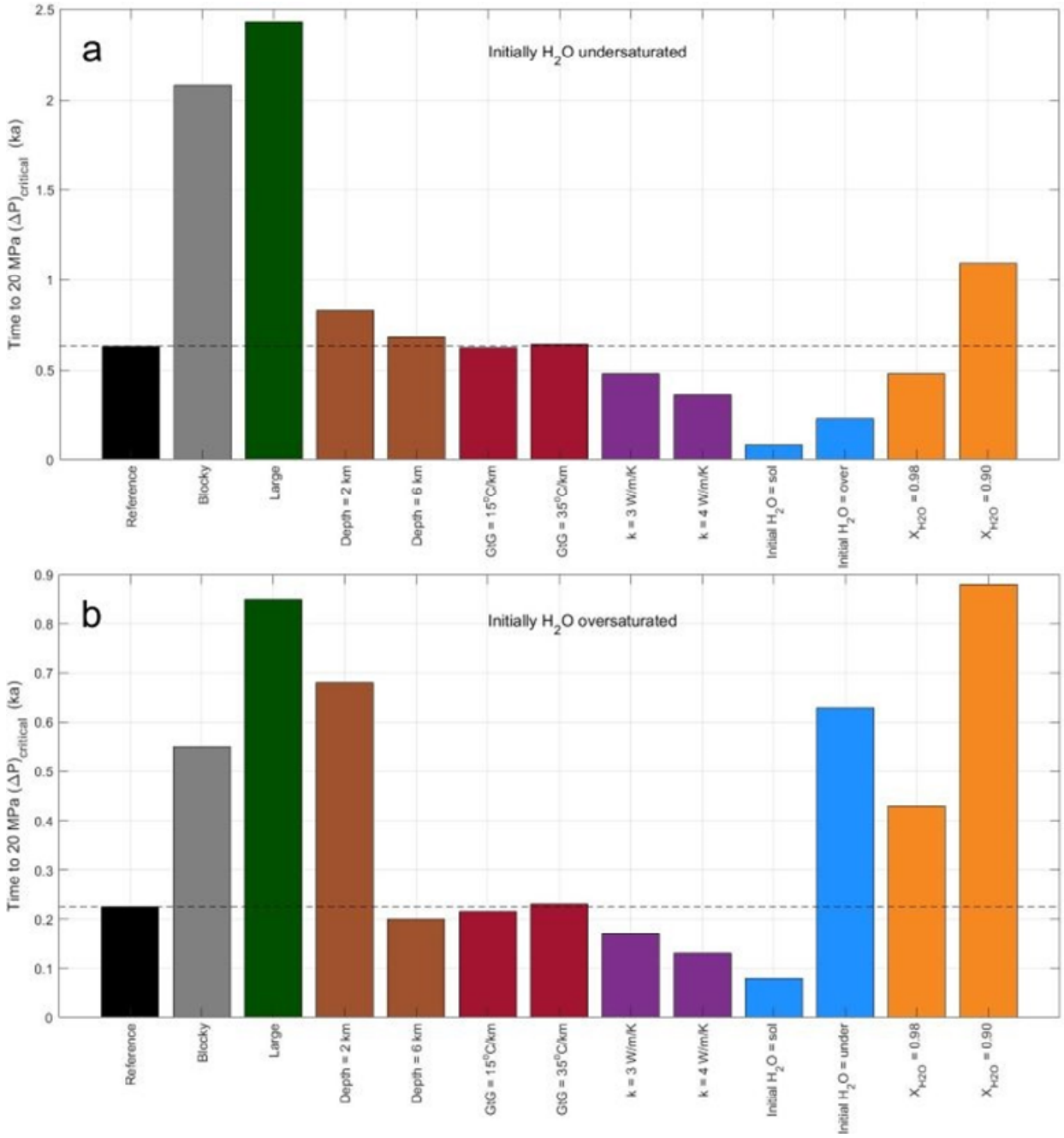


Figure 3.9. Summary of the time taken to reach 20 MPa critical overpressure for different scenarios. a) For magma that is initially H_2O undersaturated at the liquidus, and b) for magma that is initially H_2O oversaturated. In both cases, the reference scenario is a flat, small reservoir situated at 4km depth, with a geothermal gradient of 25°C/km, a thermal conductivity of 2.3 W/m/K, and an X_{H2O} of 1. The horizontal black line indicates the reference scenario timescale for comparison. In each case, the only variable changed from the reference scenario is the one indicated on the x-axis. 'GtG' is the geothermal gradient and 'k' is thermal conductivity. For the initial H_2O content variables (blue), 'sol' refers to magma with an initial H_2O content at the solubility limit, 'over' is H_2O oversaturated, and 'under' is H_2O undersaturated, all with respect to the liquidus.

Increasing the reservoir size by one order of magnitude can increase the time taken to reach 20 MPa by 1.8 ka (**fig 3.9a**). Decreasing initial magmatic X_{H2O} to 0.90 means that an additional 0.7 ka of cooling is required to reach 20 MPa, relative to the initially H_2O oversaturated reference scenario (**fig 3.9b**). In contrast, a magma which begins crystallising with a H_2O content equal to the solubility limit can attain 20 MPa overpressure 0.5 ka quicker than if the magma is initially H_2O undersaturated (**fig 3.9a**)

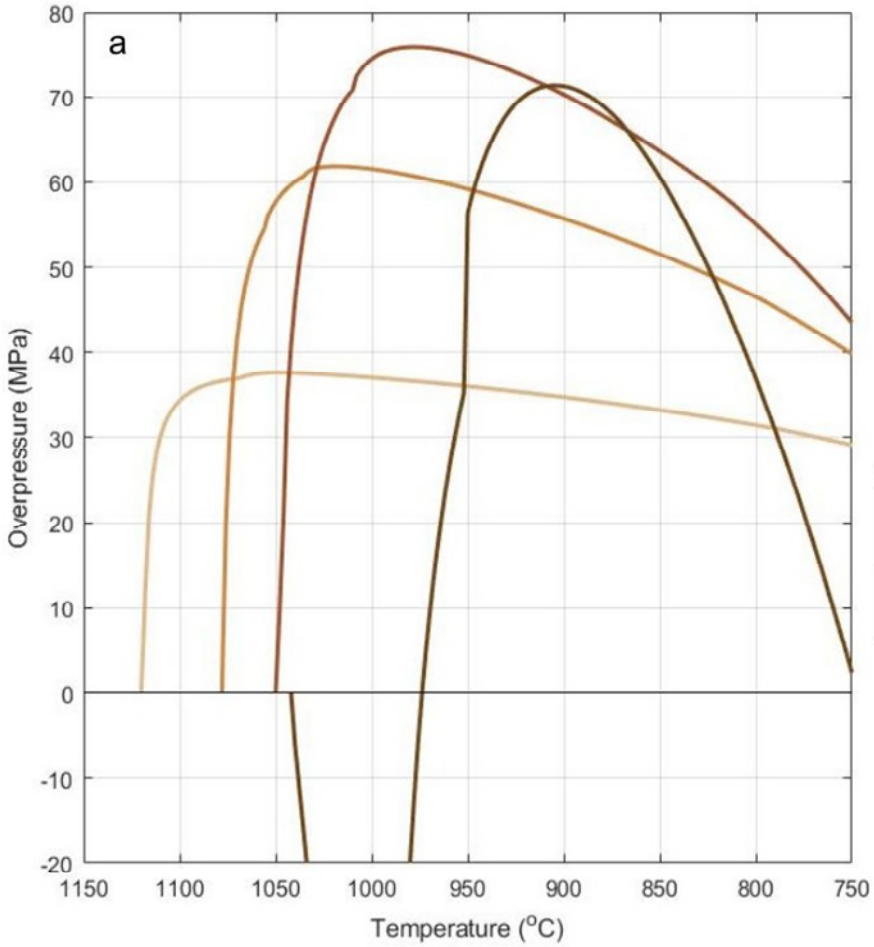
Our thermal model simulations demonstrate that blocky reservoirs consistently take longer to reach $(\Delta P)_{critical}$ than flat reservoirs. This is due to the lower surface area to volume ratio of blocky reservoirs compared to flat ones, which results in longer cooling timescales for reservoirs of the same volume. For the initially H_2O undersaturated magma (**fig 3.2a**), the difference in cooling timescale with varying reservoir geometry is significant enough that the flat reservoir could potentially trigger an eruption, but the blocky scenario could not, based on the relaxation timescale used here. In addition to their more rapid overpressurisation rates, flatter reservoirs can also fail at lower overpressures when compared to more prolate ones (Gregg *et al.*, 2012) - although reservoir volume is also a factor. Therefore the timescales to $(\Delta P)_{critical}$ for flat reservoirs presented here may be underestimates.

Figure 3.3 shows that increasing the initial magmatic X_{H2O} increases both the rate of overpressurisation, and the maximum average reservoir overpressure. For the initially H_2O undersaturated scenario (**fig 3.3a**), maximum overpressure values are highest (55 MPa) for the X_{H2O} = 1 case. However, this scenario displays a period of average reservoir underpressurisation, lasting for ~ 0.5 ka, which is due to initial crystallisation in the absence of a fluid phase – resulting in volume contraction and underpressurisation. Magma reservoir underpressurisation has been noted by various authors, and can occur due to crystallisation contraction, volatile loss or magma outflow (Blake, 1984; Folch and Martí, 1998; Girona *et al.*, 2015; Tramontano *et al.*, 2017; Sigmundsson *et al.*, 2020). When we decrease X_{H2O} to 0.98, the decreased solubility of CO_2 (relative to H_2O) results in a magma which begins crystallizing in the presence of a fluid phase. This means there is no underpressurisation of the system –

so although maximum overpressure values are lower than in the X_{H2O} = 1 case, $(\Delta P)_{critical}$ is attained sooner for the 0.98 case. If X_{H2O} is decreased further to 0.90, there is again no period of average underpressurisation. However, the relatively low overpressures generated by this simulation mean that average reservoir overpressure builds to critical levels more slowly than the X_{H2O} = 1 case, even when accounting for underpressurisation. The reduction in maximum overpressure with decreasing X_{H2O} occurs because the early presence of an exsolved fluid phase (mixed CO_2 and H_2O) increases the system compressibility, resulting in a dampening of the overpressure caused by volume change. The greater solubility of H_2O relative to CO_2 also results in a greater volume change as X_{H2O} increases. As a result, the addition of CO_2 results in an increase in the time taken to reach $(\Delta P)_{critical}$ for the scenarios which do not show underpressurisation (**figs 3.3b** and **3.3c**).

Increasing the reservoir volume results in an increase in the time taken to reach $(\Delta P)_{critical}$, due to the longer cooling timescales for larger bodies of magma. The effect of increasing reservoir size is most pronounced for the magma which is initially H_2O-undersaturated (**fig 3.4a**), where there is a time difference of ~ 1.6 ka between the small, flat and the large, flat scenarios attaining 10 MPa $(\Delta P)_{critical}$. For the magma with an initial water content at the H_2O solubility limit, each of the reservoir geometries attains 20 MPa $(\Delta P)_{critical}$ in < 0.5 ka (**fig 3.4b**). For this set of simulations, the small, flat scenario demonstrates the most rapid rate of overpressurisation at 0.24 MPa yr^{-1}, whilst the large, blocky scenario has a maximum overpressurisation rate of 0.09 MPa yr^{-1}. These relatively rapid overpressurisation rates highlight the important control that fluid content has on magma overpressurisation. With advances in geophysical imaging of magma systems (Paulatto *et al.*, 2022) it will hopefully become easier to constrain magma volumes and dimensions, particularly for small reservoirs which may be poorly resolved with current geophysical techniques. These more accurate volume estimates could be incorporated into models like ours, giving us a better understanding of overpressurisation timescales, which are governed by cooling rates.

Varying the reservoir depth affects pressurisation timescales as shown in **figure 3.5**. The thermal model outputs show that the reservoir at 6 km depth generates the highest peak overpressures. This is because a reservoir storage depth of 6 km generates the highest overpressure in the thermodynamic model, when comparing across a storage depth range of 2 – 12 km. This is illustrated in the Rhyolite-MELTS outputs shown in **figure 3.10** which show that peak overpressure increases as reservoir depth increases from 2 km to 6 km, and then begins to decrease again as reservoir depth is increased to 12 km.



b

	2 km	4 km	6 km	12 km
β (Pa^{-1})	3.6 e^{-9}	1.3 e^{-9}	9.2 e^{-10}	3.8 e^{-10}
ΔV (m^3)	6.5 e^{-6}	3.7 e^{-6}	3.3 e^{-6}	1.3 e^{-6}

Figure 3.10. a) Magmatic overpressures calculated from Rhyolite-MELTS for varying lithostatic (storage) pressures of 50 - 300 MPa. The starting magma composition is the same (Jeffery *et al*., 2013) and in each case, initial water content is set to the H_2O solubility limit for that depth and liquidus temperature. b) Compressibility (Pa^{-1}) and volume change (m3) values at peak overpressure for each of the plots shown in a).

This variation in overpressure-generating capacity occurs because, as lithostatic pressure increases, the system compressibility (β) and volume change (ΔV) both decrease (**fig 3.10b**). The simulation with a reservoir depth of 6 km represents a balance between these two factors which is optimized for overpressure generation for these scenarios. For the initially H_2O-undersaturated scenarios shown in **figure 3.5a**, the situation is complicated by the underpressures which are generated by magmas crystallizing in the absence of an exsolved fluid phase. These underpressures are greatest (most negative) as depth increases, and so in this case the 4 km scenario reaches $(\Delta P)_{critical}$ most rapidly. Underpressurisation is also seen across all of the 12 km depth scenarios, even those which are initially H_2O oversaturated (**figs 3.5c & 3.10**). In this case, underpressurisation is not due to crystallisation in the absence of exsolved fluids. Instead underpressure occurs because the initial exsolved fluid volumes are not enough to counteract the effect of increasing depth (lithostatic pressure) on decreasing system volume change. It is only when feldspar begins to crystallize that fluid volume increase becomes large enough to counteract this effect, eventually resulting in system volume increase and overpressurisation. Girona *et al.* (2015) propose that magma reservoir depressurization caused by degassing can draw magma upwards from a connected, deeper reservoir - a mechanism requiring underpressures of only a few MPa. We speculate that the underpressures described here may provide an additional mechanism for moving magma upwards from deeper levels.

Increasing the thermal conductivity (k) of the surrounding crust results in an increase in cooling and average overpressurisation rates (**figs 3.7 and 3.9**). For the large, blocky scenario (**fig 3.7d**), the difference in the time taken to reach $(\Delta P)_{critical}$ for the 2.3 W/m/K and 4.0 W/m/K scenarios may be significant for eruption triggering potential. Crustal k values can range from ~ 1.4 – 4 W/m/K (Whittington *et al.*, 2009), so improved constraints on this parameter would help to improve our estimates of magma pressurization timescales and eruption triggering potential. Our thermal model only considers heat transfer via conduction – we do not account for convective cooling (e.g. via hydrothermal systems). Kelly *et al.* (2021) compare heat loss

timescales for conductive and convective regimes in the Taupo volcanic zone, New Zealand and find that cooling timescales for pure conduction are on the order of thousands of years. However, if convective heat transfer via hydrothermal fluid circulation is incorporated, then cooling timescales are reduced to decades to centuries. Our overpressurisation estimates can therefore be considered as maximum timescales in this respect.

3.4.2 Effect of overpressure-induced strain rate

We assess whether different scenarios reach $(\Delta P)_{critical}$ prior to $\tau_{relax,}$ but we do not specifically consider the effect of incremental strain rate in our model. In the context of a magma reservoir, high strain rates can produce a brittle crustal response, with the likelihood of reservoir failure increasing with increasing strain rate (Caricchi *et al.*, 2021). Experimental work on acoustic emissions (Smith *et al.*, 2009) has also shown that brittle fracturing can occur even in rocks heated to 900°C, if the strain rate is high enough. Whilst some of the scenarios presented here, in particular the initially H_2O-undersaturated ones, attain $(\Delta P)_{critical}$ more slowly than τ_{relax}, they display relatively rapid rates of overpressurisation. For example, the initially H_2O undersaturated magma stored in the small flat reservoir (**fig 3.2a**) has a maximum overpressurisation rate of 0.4 MPa yr^{-1}. This could lead to correspondingly high strain rates, potentially resulting in brittle failure and eruption. This poses the question of whether rapid rates of overpressurisation may be sufficient to trigger an eruption, even if overpressure is lower than the critical overpressure threshold. As a counterpoint to this idea, Head *et al.* (2022) suggest that high overpressure loading rates can actually increase $(\Delta P)_{critical}$ if thermo-viscoelasticity is accounted for. This effect is further complicated as increasing the strain rate (due to high rates of overpressurisation) will decrease crustal viscosity (Jellinek and DePaolo, 2003), resulting in a reduction in the crustal relaxation timescale. There may therefore be an optimum strain rate, generated by overpressurisation, which promotes magma reservoir failure. If the strain rate is too low, then overpressurisation to critical levels may occur on longer timescales than that of crustal relaxation, so no eruption is triggered. However, if the strain rate is too high, then the resulting reduction in crustal viscosity and relaxation timescale may

mean that overpressure cannot build-up more rapidly than τ_{relax}, so again an eruption will not occur.

3.4.3 Effect of crustal behaviour on internal magma properties

Reservoir pressurisation models which account for non-elastic variations in crustal rheology have demonstrated that both overpressure and ground deformation can be modified by crustal behaviour (e.g. Jellinek and DePaolo, 2003). Similarly, Mullet and Segall (2022) demonstrate that treating the magmatic system as a melt lens, surrounded by poroelastic mush embedded within elastic crust also affects surface deformation when compared to a standard elastic crustal model. Modelling the pressurisation of viscoelastic (e.g. Head *et al.*, 2019) and thermo-viscoelastic (e.g., Head *et al.*, 2022) material has greatly improved our understanding of the potential range in overpressure magnitudes and timescales. However, very few studies can fully account for the effect of crustal relaxation on internal magma properties – in particular the behaviour of the volatile phase. Gregg *et al.* (2013) use a thermomechanical model with an adaptive reservoir boundary to quantify the effect of reservoir expansion on overpressure. They find that overpressure can decrease by up to 70% when viscoelasticity is accounted for, and that deviations from a rigid crustal model increase as reservoir size increases. However, the internal evolution of magma properties in response to reservoir expansion is neglected in their model. As the crust expands to accommodate overpressure, the total pressure in the reservoir will decrease, potentially resulting in volatile exsolution and a subsequent increase in pressure (and volume). In order to fully address the feedbacks between overpressure evolution and crustal response, thermomechanical models of reservoir pressurisation (e.g., Gregg *et al.* (2013), Head *et al.* (2022)), should be combined with thermodynamic models that can describe evolving magma properties and their response to volume changes in the crust. The knowledge and modelling for each separate part exists, but collaboration between the 'internal' and 'external' modelling camps is needed to advance our understanding of these processes.

3.4.4 Overpressure due to magma buoyancy

Our methodology represents a step forward in conceptualizing overpressure related to volatile exsolution. However, we do not consider the effect of overpressure generated by magma buoyancy. Caricchi *et al.* (2014) present an equation for calculating buoyancy overpressure for a cylindrical reservoir;

$$\Delta P_{buoy} = \Delta\rho \; g \; V_{er} / (d/2)^2\pi \qquad \text{(eq.3.3)}$$

Where $\Delta\rho$ is the density contrast between eruptible magma and host rock, g is gravity, V_{er} is volume of eruptible magma, and d is sill diameter. We calculate initial ΔP_{buoy} for the small, flat and small, blocky reservoirs (see **fig 3.1b** for dimensions), using a fixed $\Delta\rho$ of 370 kg/m^3, which is consistent with average Rhyolite-MELTS densities of ~ 2300 kg/cm^3 and an andesite density of 2670 kg/m^3 (Heap *et al.*, 2020). Initial buoyancy overpressure is 35.7 MPa for the blocky reservoir, and 15.9 MPa for the flat reservoir – although this calculation does not give any information on timescales of pressurisation. This highlights an interesting competition between more rapid rates of overpressurisation in flatter reservoirs (due to faster cooling), versus higher buoyancy-driven overpressures in blocky reservoirs (due to a smaller roof area). We note that there is some debate over the applicability of eq.3.3 for determining overpressurisation at the top of a magma reservoir. Gregg *et al.* (2015) suggest that buoyancy overpressures are actually much smaller (< 1 MPa) and buoyant forces could promote reservoir stability rather than rupture. However, we include the buoyancy calculations here in order to compare effects between different reservoir shapes, even though the actual ΔP_{buoy} values may be overestimates.

3.4.5 Overpressure due to bubble rise

The coalescence and rise of exsolved volatiles can also generate overpressure at the roof of a magma reservoir (**fig 3.11**), and is not a process we consider in our model. We use the equation of Pyle and Pyle (1995) to calculate pressure change due to bubble rise (P_f - P_i), for the small, flat and small, blocky reservoirs.

$$(P_f - P_i) = f \rho g h_f / RT K \rho y h_f P_O^{y-1} + f \quad \text{(eq. 3.4)}$$

Where *f* is bubble depth per unit area of the reservoir base, ρ is melt density, g is gravity, h_f is height at the reservoir top, R is the ideal gas constant, T is temperature, K and y are solubility law constants, and P_O is initial pressure. Using *f* = 0.1, ρ = 2300 kg/m3 (consistent with Rhyolite-MELTS outputs), T = 1300 K, P_O = 100 MPa, K and y values for H_2O in basalt of 3.8 x 10^{-6} and 0.7 respectively (from Pyle and Pyle, 1995), and modifying h_f for the thickness of the flat and blocky reservoirs, we calculate an additional overpressure due to bubble rise of 1.7 MPa for the flat reservoir, and 8.6 MPa for the blocky one. However, this pressure is likely to accumulate on relatively long timescales. Pyle and Pyle (1995) note that the timescales for overpressurisation from bubble rise are on the order of 300 – 300,000 years for basaltic magma, and increase to 3,000,000 – 300,000,000 years for an andesitic magma. For the basaltic andesite magma considered here, timescales for bubble rise pressurisation are likely to be intermediate between these two ranges. When compared to the rates of overpressurisation determined from our thermal model – for example, pressurisation to 20 MPa within 85 years for the small, flat scenario shown in **figure 3.2b** - the effect of overpressurisation due to bubble rise is likely to be subordinate to the effect of second boiling. However, overpressurisation from bubble rise will become more important as reservoir size increases.

In terms of the transport mechanism of exsolved magmatic volatiles, it has been established that they can merge together in elongated channels within a magma mush system (Parmigiani *et al.*, 2016) (**fig 3.11**). This process of channel formation is most efficient over a crystallinity range of 40 – 70%, and is less efficient for second boiling mechanisms (relative to magma injection), due to the randomly distributed nature of the bubbles generated by volatile exsolution (Parmigiani *et al.*, 2017). The same authors also note that small reservoirs, and/ or those hosted in colder crust, are less likely to form bubble channels due to adverse pressure gradients. In these cases, degassing is more likely to occur via capillary fracturing– a process

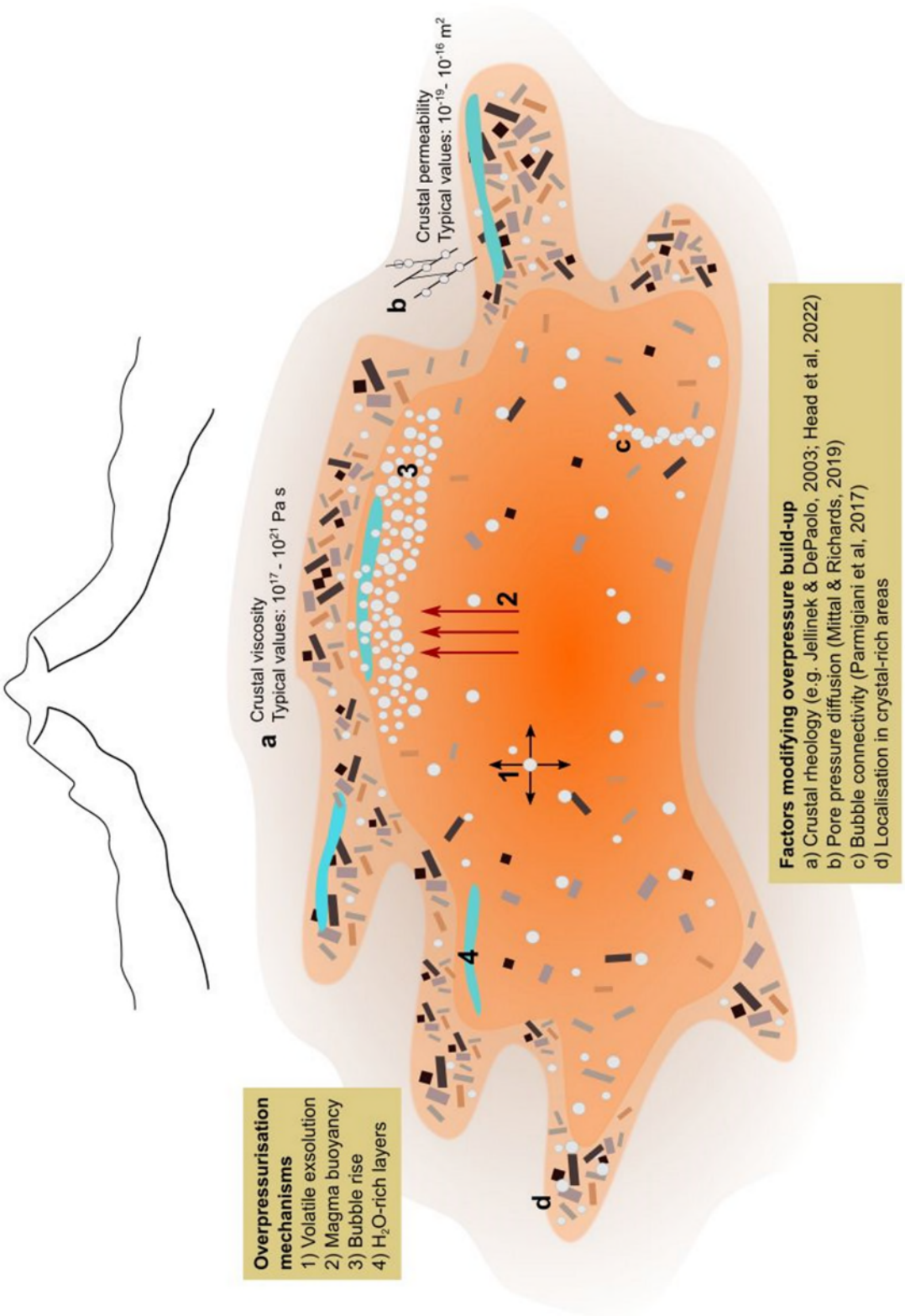


Figure 3.11. Schematic diagram showing the overpressurisation mechanisms discussed in section 3.4, and the factors that may modify them.

which occurs at crystallinities greater than 70% (Parmigiani *et al.*, 2017). For the small, shallow magma reservoir at Kelud, it is likely that bubble migration through the reservoir is inefficient at lower crystallinities, meaning an assumption of minimal gas loss via volatile coalescence is reasonable.

The effect of pressurisation from the volatile phase is also discussed in Annen *et al.* (2023), who consider the role of buoyant H_2O-rich layers which rise to the top of the reservoir (**fig 3.11**). For a magma growth rate of 1 m/ yr, it takes ~1 ka to generate 6 MPa of overpressure (for a reservoir volume of 25 km^3 at a depth of 5.5 km). We run our model for the same reservoir volume and depth, using a magma which is initially H_2O-oversaturated, and find that it takes ~ 0.1 ka to reach 6 MPa average reservoir overpressure – although this is not a like for like comparison as our initial magma composition differs from Annen *et al.* (2023). The difference in these timescales is likely to be due to the different pressurisation mechanisms - the H_2O-rich layers have to exsolve, coalesce (which begins only at crystallinities > 40% (Parmigiani *et al.*, 2017)), and then rise through the magma. In contrast, pressurisation due to second boiling happens 'in situ', without the requirement that volatiles must be transported upwards through the magma. This is supported by the fact that we find overpressurisation rates as high as 0.4 MPa yr^{-1}, compared to maximum rates of ~0.005 MPa yr^{-1} generated by buoyancy overpressure (Annen *et al.*, 2023). As we do not model the effect of H_2O-rich layers here, there may be additional overpressurisation from this process which would decrease our timescales to $(\Delta P)_{critical}$. We note that Annen *et al.* (2023) do not consider second boiling a viable eruption trigger, because volatile exsolution rate will always be significantly lower than magma recharge rate. We agree that in systems with high rates of magma recharge, the volume increase due to second boiling is likely to be secondary to the volume increase caused by new magma input. However, in scenarios where recharge is low, cooling is rapid, and the crustal response is elastic (Townsend *et al.*, 2019), we find that second boiling can be a viable eruption trigger under certain circumstances.

3.4.6 Pressure distribution within a magma reservoir

Up until now our analysis has assumed that the stress generated by overpressure is distributed uniformly across the magma reservoir. However, this assumption may not be valid within high viscosity and high crystallinity magmas. The spatial and temporal evolution of temperature and overpressure in the thermal model is shown in **figure 3.1**. This relationship is governed by the temperature-overpressure curves from Rhyolite-MELTS (see **fig 3.10** for an example). The heterogeneous temperature distribution within the reservoir translates into spatial variations in the degree of overpressurisation. In some parts of the reservoir the magma has just begun cooling and expanding, in others it has cooled to its peak overpressure generating capacity, and in other parts closer to the edge of the reservoir, the magma has crystallized to the extent that it is uneruptible (**fig 3.11**). In order to compare between scenarios with varying model parameters, we average the overpressure out across the whole reservoir volume. Implicit in this is the assumption that pressurization can be translated quickly and homogenously throughout the reservoir. This may be the case at low crystallinities, but as cooling continues, higher crystallinity regions of a mushy reservoir may alter the manner in which pressure is transferred. If pockets of volatiles become trapped in crystal-rich areas (Okumura *et al.*, 2019), perhaps near the walls of a magma reservoir, this could lead to high localized overpressures, which may be enough to initiate fracturing. This localization could be sufficient to initiate fracturing in larger reservoirs, which would otherwise attain $(\Delta P)_{critical}$ on timescales longer than τ_{relax}.

The permeability of the surrounding crust can also affect overpressure buildup within a reservoir. Mittal and Richards (2019) identify a pore pressure diffusion timescale, which accounts for the flow of volatiles from reservoir to crust. This can reduce overpressure by several MPa, with a greater reduction in ΔP as crustal permeability increases (typical values are ~ 10^{-19} – 10^{-16} m^2 (Mittal and Richards, 2019)). We do not include this effect in our model, so in this respect our average intrusion overpressure values represent maximum estimates. However, in section 2.5.2 we quantify the effect of open-system behaviour for a variety of initial

H_2O contents, and find that overpressures can still exceed 10s of MPa, even when volatile loss is accounted for.

3.4.7 Modelling magma properties in the run up to eruption

Our coupled thermodynamic-thermal modelling approach could be used to determine the evolution of bulk, pre-eruptive magma properties, which could then be used as inputs to magma ascent rate models. Accurate models of magma ascent are important for estimating the timing of an eruption once ascent has begun, and also for determining eruption style. Common parameters needed for ascent rate estimates are magmatic overpressure, H_2O content, and magma viscosity (e.g, Thomas and Neuberg (2014), Petrelli *et al.* (2023)). All of these variables can be input into or calculated from Rhyolite-MELTS, so our method shows potential for improving ascent rate estimates by providing a linked set of pre-eruptive magma dynamics data. For example, Thomas and Neuberg (2014) demonstrate that initial H_2O content is the most important factor governing magma ascent rate, and that magmatic overpressure is also important. However, these variables are treated independently in their model. Our work shows that both the magnitude and rate of overpressure build-up are affected by H_2O content and so using linked pre-eruptive magma properties could provide more realistic insights into the state of magma before it enters the conduit. One current limitation of this method is that the values extracted from the thermal model are averages. This means we do not capture the complexity of processes such as pre-eruptive magma mixing, or crystal settling, which could mean that the actual values (e.g, compressibility) are significantly different from the average values presented here.

3.4.8 Implications for eruption triggering

We demonstrate that overpressurisation to critical levels occurs most rapidly for magmas with initial H_2O contents at the solubility limit, which are stored in small, flat reservoirs in crust with a high cooling rate. Although magmas which are initially H_2O undersaturated take longer to reach critical overpressures, the relatively high rate of overpressurisation seen in these scenarios (up to 0.4 MPa yr^{-1}) may induce high strain rates capable of eruption triggering. In

chapter 2 we demonstrate that the highest overpressures are conditioned by initial fluid content, and we suggest that these high overpressures may drive faster magma ascent rates, contributing to an explosive eruption style. Our thermal modelling shows that the same factors, initial H_2O content and X_{H2O}, plus reservoir depth, have the biggest influence on maximum average reservoir overpressure (derived from the thermal model). This is summarised in **figure 3.12**.

If the overpressure generated at the margins of a cooling magma reservoir is not immediately transferred across the whole reservoir, then this influences how we model overpressure and understand eruption triggering. Non-uniform overpressure distribution may imply that the whole reservoir does not need to reach a critical threshold of overpressure. Instead, localised pockets of high overpressure may trigger rupture, before stress has time to be distributed uniformly throughout the reservoir. This localisation could be manifested in cooler parts of the eruptible reservoir, or within the un-eruptible mush regions, where it would be more contained (**fig 3.11**). The way that overpressure is distributed within a reservoir also has implications for underpressure. Prolonged periods of average reservoir underpressurisation are seen in our initially H_2O undersaturated magmas (**fig 3.2a**), and those stored at 12 km depth (**fig 3.5**). These periods of underpressurisation may act to draw in more melt from deeper, linked storage areas, as proposed by Girona *et al.* (2015), and therefore could be an important process by which reservoirs grow. This may be particularly true for deeper reservoirs, where underpressures are greater (most negative).

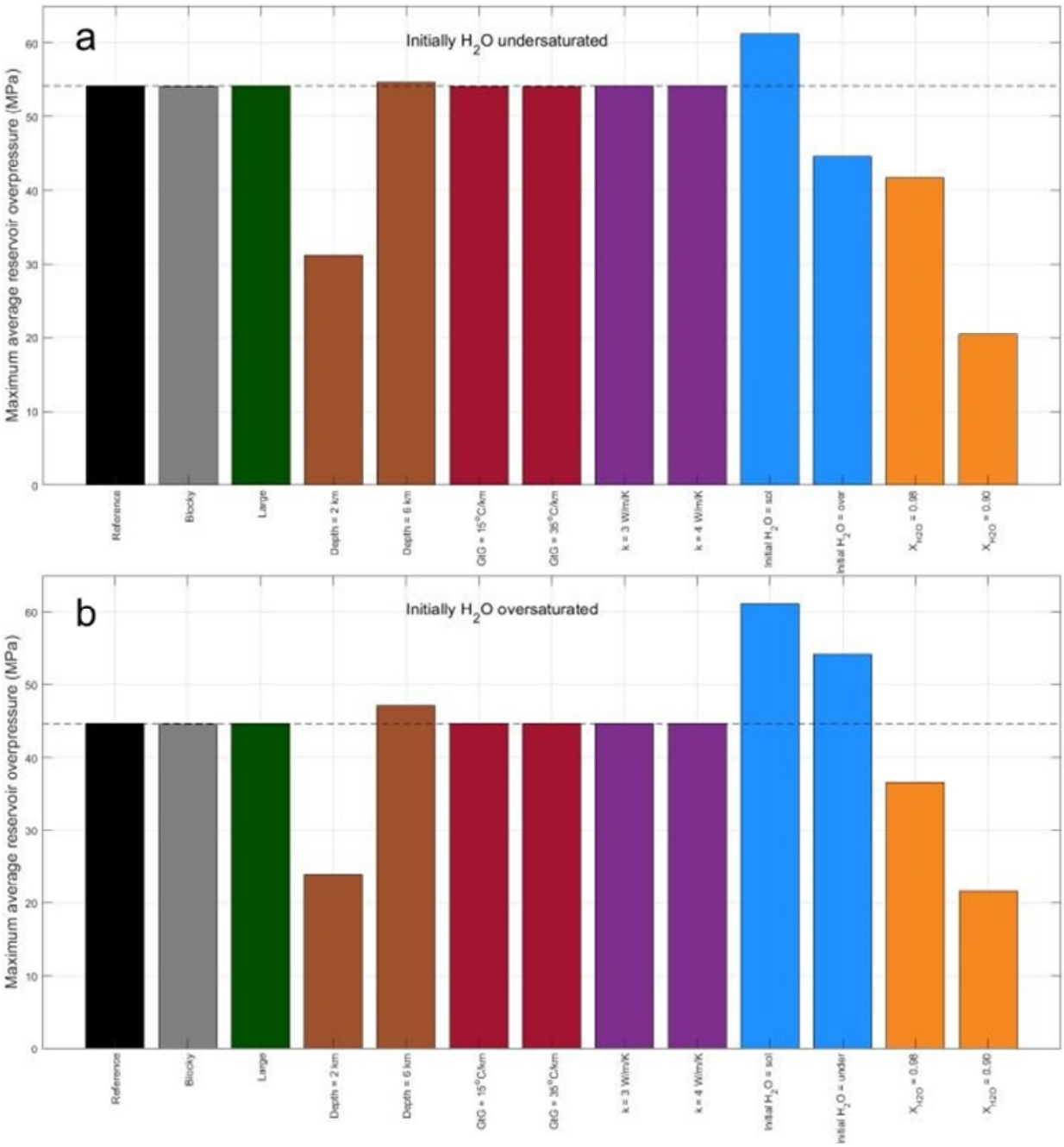


Figure 3.12. Summary of the maximum average reservoir overpressure for different scenarios. a) For magma that is initially H2O undersaturated, and b) for magma that is initially H2O oversaturated. In both cases, the reference scenario is a flat, small reservoir situated at 4km depth, with a geothermal gradient of 25°C/km, a thermal conductivity of 2.3 W/m/K, and an XH2O of 1. The horizontal black line indicates the reference scenario maximum average overpressure for comparison. In each case, the only variable changed from the reference scenario is the one indicated on the x-axis. 'Depth' refers to depth in MELTS and in the thermal model, 'GtG' is the geothermal gradient, and 'k' is thermal conductivity. For the initial H2O content variables (blue), 'sol' refers to magma with an initial H2O content at the solubility limit, 'over' is H2O oversaturated, and 'under' is H2O undersaturated, all with respect to the liquidus.

3.5. Conclusions

We show that second boiling is a viable eruption triggering mechanism for the relatively small and shallow reservoirs considered here, even when using a conservative crustal relaxation timescale. Our results demonstrate that variations in reservoir size and shape exert the strongest control on the time taken to reach critical overpressure – with larger, blockier reservoirs taking longer to reach $(\Delta P)_{critical}$ than their smaller, flatter counterparts (**fig 3.9**). Initial magmatic H_2O content, and also X_{H2O} are the next most important factors controlling overpressurisation timescales. We demonstrate that magmas which begin crystallising at the H_2O solubility limit generate greater maximum overpressures and reach $(\Delta P)_{critical}$ more rapidly than their initially H_2O under- or oversaturated counterparts. Varying the thermal conductivity of the surrounding crust has a lesser effect on pressurization timescales, potentially becoming more important as reservoirs increase in size.

Our method provides a novel way of tracking the evolution of bulk magma properties, which could form useful inputs into magma ascent models where parameters such as fluid content and overpressure are vital, but are often treated separately. The rapid overpressurisation rates which occur in the initially H_2O undersaturated magmas poses the question of whether strain rate may be as important as overpressure magnitude when considering eruption triggering. If this is the case, then more reservoir failure models should consider the rate of overpressurisation, instead of just one critical overpressure value. The instances of average reservoir underpressurisation discussed here require further research, as this process may provide another mechanism, in addition to degassing, for drawing magma upwards from deeper reservoirs.

Chapter 4 - Exploring crystal-plastic deformation in natural and experimentally-overpressurised magmas

Anna Brookfield[1], Mike Cassidy[2] and Lars Hansen[3]

[1]Department of Earth Sciences, University of Oxford, Oxford, UK

[2]School of Geography, Earth and Environmental Science, University of Birmingham, Birmingham, UK

[3]Department of Earth and Environmental Sciences, University of Minnesota, Minneapolis, MN, USA.

Abstract

Magmatic overpressurisation is implied in all internally-triggered eruptions and is linked to magma ascent rate and eruption style. However, overpressure is difficult to constrain, relying either on inversion of geodetic data, with non-unique solutions, or modelling studies where many parameters are unknown. Crystal-plastic deformation occurs in magmatic settings as diverse as silicic lava domes and basaltic cumulates, and has been used as a strain marker in shallow parts of the volcanic system. However, the nature and extent of crystal-plastic deformation within deeper parts of the magmatic system has not yet been assessed.

In this exploratory study, we use electron backscatter diffraction (EBSD) to map out the magnitude, extent and location of crystal-plastic deformation within explosive eruption products. We also assess the potential of EBSD to provide information on *in situ* reservoir overpressurisation, by experimentally deforming pumice from the 2010 eruption of Soufriere

Hills, Montserrat. We perform ‘static’ cold seal pressure vessel experiments, at pressures of 120 MPa and 155 MPa, and an ‘overpressured’ experiment, where pressure is increased from 120 to 155 MPa on the last day to mimic the effect of magma recharge. Shear stresses within the magma reservoir prior to eruption - or within the experimental capsule prior to quenching - can generate dislocations that cause permanent curvature of the lattice, which we measure as a misorientation angle (°) using EBSD. This is the first time that electron backscatter diffraction has been used to characterise deformation in explosively erupted volcanic rocks.

We find that misorientations are located along crystal edges and at curvilinear subgrain boundaries across all of the phases within the natural and experimental samples. Misorientation frequency peaks from the overpressured and low-pressure static samples occur at lower misorientation values than those from the natural sample, suggesting that some annealing of dislocations has occurred during the experimental process. However, we also find that the misorientation profile of the high-pressure static sample provides a good match to the natural one, suggesting that EBSD analysis of crystal-plastic deformation may have potential for estimating long-term magma storage conditions.

4.1. Introduction

Crystal-plastic deformation occurs due to the propagation of dislocations within a crystal lattice in response to shear stress. Dislocations are microstructural defects that produce permanent curvature of the crystal lattice (Wright *et al.*, 2011). This curvature is characterized by spatial changes in the lattice orientation, which can be measured as a misorientation angle relative to the rest of the lattice structure. The change in angle over a given distance is proportional to dislocation density. Crystal-plastic deformation can be quantified using electron backscatter diffraction (EBSD), which measures angular variations in crystal orientation. This technique can be applied to any crystalline material that has been appropriately prepared.

Electron backscatter diffraction has been used extensively in materials science to characterise microstructures and textures (Wright *et al.*, 2011; Wilkinson and Britton, 2012). In recent years, EBSD has been used by the volcanology community to reveal information about processes such as localised flow in magma bodies (Žák *et al.*, 2008), fracture sealing in geothermal systems (McNamara *et al.*, 2016), cumulate compaction (Bertolett *et al.*, 2019) and the formation of layering in oceanic core complexes (Boulanger *et al.*, 2021). It has also been used to investigate deformation within magmatic systems. Kendrick *et al.* (2017) and Wallace *et al.* (2019) examined crystal deformation within natural and experimentally-deformed lava dome samples from Colima, Mexico, and natural conduit samples from Unzen, Japan, respectively. They found a systematic increase in crystal-plastic deformation as stress and strain increased – highlighting the utility of crystal-deformation as a stress- strain marker. Wieser *et al.*, (2020) used EBSD to analyse plastic deformation within olivine crystals from Kilauea, Hawai'i and concluded that lattice distortions were generated at the base of mush piles a few hundred metres thick. However, EBSD has not yet been used to inform our understanding of pre-eruptive reservoir conditions within magma mush. Wallace *et al.* (2019) suggest that the melt is likely to relax stress, resulting typically in a lack of crystal-plastic deformation in explosive eruption products. However, Žák *et al.* (2008) demonstrate that the orientation of biotite in mafic schlieren partly reflects deformation transmitted across the crystal-rich mush in the late stages of crystallisation. In addition, Befus *et al*. (2019) measured residual stresses in quartz crystals and suggest that they originate from pre-eruptive processes. These stresses likely represent an *in situ* measure of the brittle fragmentation threshold within the volcanic conduit, but a pre-ascent storage origin cannot be ruled out. Ultimately the extent to which crystals stored in mushy magma can deform is likely to depend on the crystal fraction. In low-crystallinity regions the melt may be voluminous and extensive enough to relax stress. However in highly crystalline areas, especially where there are crystal-crystal interactions within the mush, crystal-plastic deformation may play a role in accommodating stress.

We define overpressure as a pressure in excess of lithostatic, which is generated by magmatic processes. These processes can include magma injection, second boiling, thermal expansion and buoyancy. Chapters 2 and 3 demonstrate that the overpressure-generating capacity of a magma is affected by initial fluid content, and that the rate of overpressurisation is affected by fluid content, reservoir geometry and crustal properties. For internally-triggered volcanic eruptions - those generated by magmatic processes, as opposed to those triggered by earthquakes, flank collapse etc (Cañón-Tapia, 2014) - it is helpful to define a critical overpressure term, $(\Delta P)_{critical}$, which is the overpressure required to initiate fracturing of the surrounding rock. Critical overpressure values are commonly quoted as ~10-20 MPa (Rubin, 1995a; Jellinek and DePaolo, 2003; Townsend *et al.*, 2019), based on host rock tensile strength estimates of ~ 5-10 MPa (Gudmundsson, 2011). However, critical overpressure can be modified by the rheology of the surrounding crust (Jellinek and DePaolo, 2003; Head *et al.*, 2022), reservoir size and shape (Gregg *et al.*, 2012), and strain rate (Head *et al.*, 2022), as discussed in chapter 3. Overpressure can be estimated via geodetic modelling if magma source volume and host rock elastic moduli are known. However, the resulting overpressure estimates are non-unique (Lisowski, 2007), resulting in a large range of potential overpressure/ source volume pairs (e.g., Trasatti *et al.* (2005); Odbert *et al.* (2014)), as illustrated in **figure 1.1**. In addition, there are no studies investigating the feedback between crustal response and magma thermodynamic properties and their effect on overpressure (see section 3.4.3). Due to these uncertainties, alternative methods of determining magmatic overpressure would be a welcome advance. In this study, we assess the potential of EBSD to reveal information about *in situ* pre-eruptive strains – which could then be linked to overpressure conditions.

We use pumice from the 2010 eruption of the Soufrière Hills volcano, Montserrat, to analyse crystal deformation in both natural and experimentally deformed samples. The relatively high crystallinity (45-55%) of Soufrière Hills eruptive products (Murphy *et al.*, 2000) increases the chances of crystal-crystal interaction which can result in plastic deformation, making it a good

candidate for analysis of crystal deformation. In addition, its relatively well-defined magma system means that experimental conditions can be well-constrained. Hautmann *et al.* (2014) infer that the magmatic system beneath Soufrière Hills consists of two, "vertically stacked" magma reservoirs, located directly beneath the volcano summit at around 12.5 km and 5.5 km depth - it is the upper magma reservoir for which we seek to replicate storage conditions. Cyclic activity at Soufrière Hills operates on sub-daily to multi-decadal timescales (Odbert *et al.*, 2014). Short-term unrest is thought to be caused by pressurisation within the upper conduit (e.g., Hautmann *et al.* (2009), Burgisser *et al.* (2019)), whilst longer-term unrest is controlled by magma reservoir processes (e.g., Melnik and Sparks (2002), Wadge *et al.* (2006)). Melnik and Sparks (2002) suggest that lava extrusion at Soufrière Hills is controlled by changes in reservoir pressure due to influx of new magma, with a minimum reservoir overpressure estimate of 7.3 MPa. Using a finite element model, Hautmann *et al.* (2010) favour a magma volume of 32 km^3 and an overpressure of 20 MPa for Soufrière Hills, but they note that overpressure could range from 25 - 205 MPa, depending on reservoir volume.

This is the first project to use EBSD to analyse crystal-plastic deformation within explosively erupted volcanic material. It represents the first steps towards developing this technique as a tool for determining pre-eruptive reservoir conditions, particularly overpressure. Using both natural and experimentally deformed samples, we determine the location, extent and magnitude of crystal-plastic deformation by plotting misorientation maps, crystal transects and misorientation histograms. We test the hypothesis that crystal mushes exposed to higher magmatic overpressures will record greater stresses at their crystal contacts, resulting in higher misorientation values. We also compare misorientation values between static low- and high-pressure experiments, to assess the extent to which annealing of deformation occurs across this pressure range. Comparing deformation across our suite of samples also provides insights into the effect of the experimental quenching process, which is an important consideration as EBSD becomes more widely used by the geoscience community. We discuss

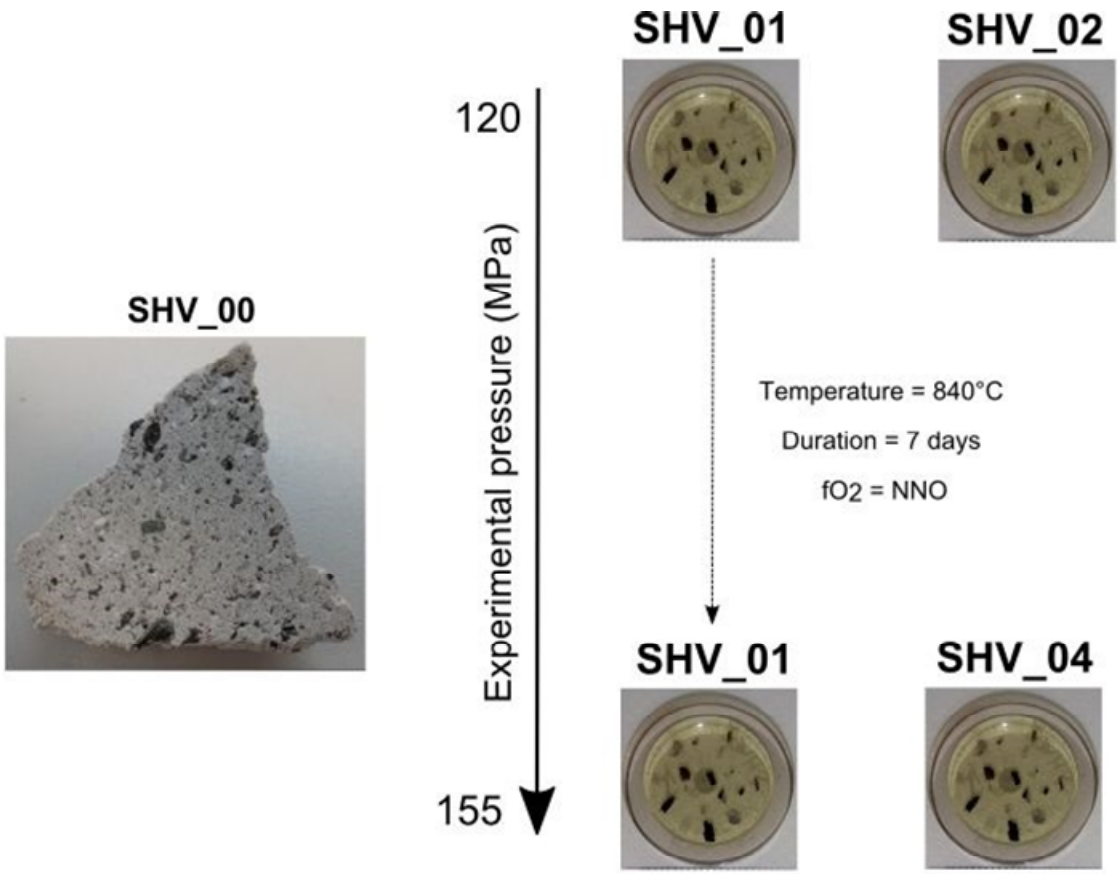
our results in the context of processes operating within a magma mush system, and propose next steps for the use of EBSD in determining pre-eruptive conditions.

4.2. Methods

4.2.1 Experimental petrology

Burgisser *et al.* (2019) report that pumice from the 2010 eruption of Soufrière Hills is composed of plagioclase, clinopyroxene, orthopyroxene, amphibole and titanomagnetite. Thin section microscope analysis and energy dispersive x-ray spectroscopy (EDS) corroborate that these are the major phases in the pumice analysed here. Pumice samples were deformed in water-pressurised cold-seal pressure vessels at the University of Oxford in order to replicate magma storage conditions at Soufrière Hills volcano. The samples were first coarsely crushed to preserve the phenocryst cores, and 0.9 g of crushed sample was loaded into silver-palladium capsules 3.3 mm in diameter. We added 10 wt% distilled water to ensure H_2O-saturated conditions within the capsule (Barclay *et al.*, 1998). The capsules were then crimped and welded closed, loaded into autoclaves connected to the pressure system and then loaded in to a furnace. A nickel rod was added to the autoclaves to buffer the oxygen fugacity of the experiments to ~ nickel-nickel oxide. We conducted three experiments, each of which was heated to 840°C and held in the autoclave for seven days to ensure thermal and crystal equilibrium. Sample SHV_02 (low-pressure static) was held at a constant pressure of 120 MPa for the duration of the experiment. SHV_01 (overpressured) was held at 120 MPa for six days, with a pressure increase of 35 MPa on the last day of the experiment, in order to simulate an increase in overpressure within the magma reservoir. SHV_04 (high-pressure static) was held at a constant pressure of 155 MPa for the duration of the experiment. Experimental conditions for each sample are summarised in **figure 4.1**. These pressure-temperature conditions are consistent with upper magma reservoir storage conditions at Soufrière Hills. For example, Barclay *et al.* (1998) use experimental phase equilibria to constrain magma storage conditions at Soufrière Hills to 115-130 MPa (~ 5-6 km depth) and 820-840°. Murphy

et al. (2000) obtain magma temperatures of ~ 858 ± 20 °C at 150 MPa, whilst Rutherford and Devine (2003) obtain temperatures of 830 ± 10 °C and pressures of 130 MPa for Soufrière Hills storage conditions.



Sample #	Description	Start pressure (MPa)	End presssure (MPa)	Temperature (°C)
SHV_00	Natural pumice	-	-	-
SHV_01	Overpressured	120	155	840
SHV_02	Static, low pressure	120	120	840
SHV_04	Static, high pressure	155	155	840

Figure 4.1. Summary diagram and table showing experimental conditions. SHV_00 is the Soufriere Hills natural pumice starting material. All other samples were experimentally deformed. SHV_01 was held at 120 MPa for six days, with a pressure increase of 35 MPa on day seven. SHV_02 was held at a constant pressure of 120 MPa and SHV_04 was held at a constant pressure of 155 MPa. After quenching, the capsule material was mounted in resin and polished for EBSD analysis

Our experiments are not heated above the liquidus temperature, but instead represent a mixture of melt and crystals known as partial-equilibrium experiments. After seven days, the experiments were terminated by quenching via compressed air followed by cold water immersion. The capsules were opened and the resulting samples were picked and mounted in resin within 2.5 cm diameter circular stubs (shown in **figure 4.1**). The sample surfaces were polished down to a grade of 0.05 μm with colloidal silica, and then lightly carbon-coated for EBSD analysis. Natural, undeformed pumice (SHV_00) was also mounted, polished and coated in exactly the same way to enable comparison of crystal deformation between the natural and experimental samples. We note that the cold seal pressure vessels generate a hydrostatic pressure on the sample, which may not be a good approximation of the anisotropic pressures generated by magma injection. However, as the sample is a mixture of different crystals and melt, all with different elastic properties, this may result in locally non-hydrostatic stresses, which are capable of generating plastic deformation.

4.2.2 EBSD data collection

We quantify deformation within our samples using electron backscatter diffraction, in which plastic distortion of the crystal lattice is measured as a misorientation angle (°). Misorientation is the difference in lattice orientation between two points on the same crystal, with the angle representing the degrees of rotation needed for the two points to be brought to a coincident orientation. The angular resolution of the standard EBSD technique is ~ 0.5° (Britton and Hickey, 2018). During electron backscatter diffraction analysis, a beam of electrons interacts with the sample surface, and some electrons are diffracted from crystal lattice planes within the sample. These diffracted electrons are detected by a phosphor screen, generating patterns known as electron backscatter patterns. The shape of these patterns is directly linked to the crystallographic structure of the phase being analysed.

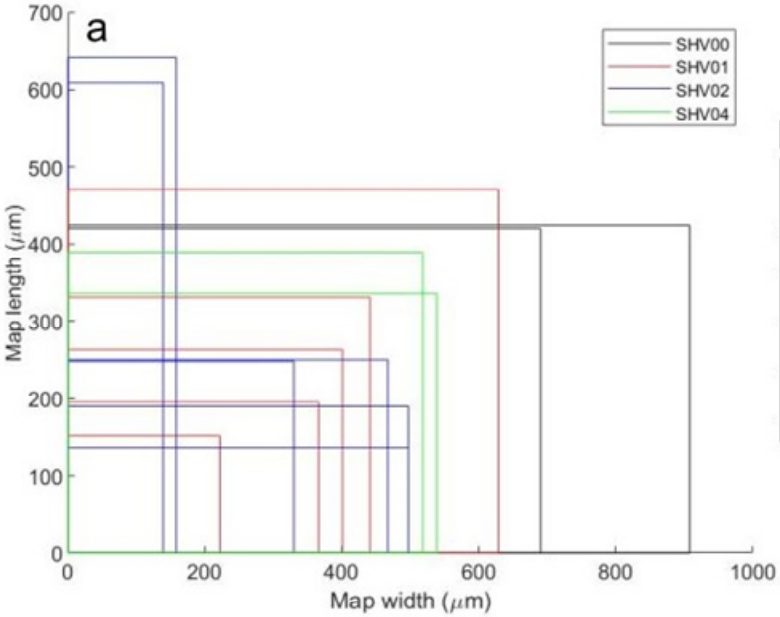
EBSD analysis was performed in the Department of Earth Sciences at the University of Oxford, using an FEI Quanta 650 scanning electron microscope (SEM), in the Materials Department at the University of Oxford using a Zeiss EVO SEM, and at the University of Leeds using an

FEI Quanta 650 FEG SEM. All samples were tilted at an angle of 70° to the incident beam in order to obtain optimum electron backscatter patterns. We used an accelerating voltage of 20–30 kV and step sizes varying from 0.5–3 μm (see **appendix 9** for individual map step sizes). Map widths range from 140–900 μm, and heights range from 140–640 μm, as shown in **figure 4.2a**. For access to the raw EBSD data used to generate the maps, plots and grain profiles presented in this chapter, see Data Appendix 3.

4.2.3 EBSD data analysis

All raw EBSD data were processed in HKLChannel5 software by first removing all isolated pixels which are significantly misoriented to neighbouring pixels (wild spikes), and then by replacing any pixels without a solution using the mean orientation of the six nearest neighbour pixels.

The cleaned data sets were then analysed using MTEX software (version 5.8.1) in Matlab. The MTEX method for grain reconstruction from EBSD data is based on Bachmann *et al.* (2011). When the orientation between two measurement points exceeds a certain value, a grain boundary is assumed. Here we use a value of 10° to define high-angle grain boundaries across all of the EBSD maps. Our data set comprises a total of 1,509,377 indexed pixels. The anorthite phase makes up 69 % of all the indexed pixels, and there are a minimum of 107,000 indexed pixels per sample type. An example EBSD phase map is shown in **figure 4.2**, and phase maps for each of the sampled areas are shown in **appendix 10**.



b

Sample number	Total number of indexed pixels	Total number of anorthite pixels
SHV_00	151454	126715
SHV_01	791124	499602
SHV_02	459776	314349
SHV_04	107023	94434
Total	**1509377**	**1035100**

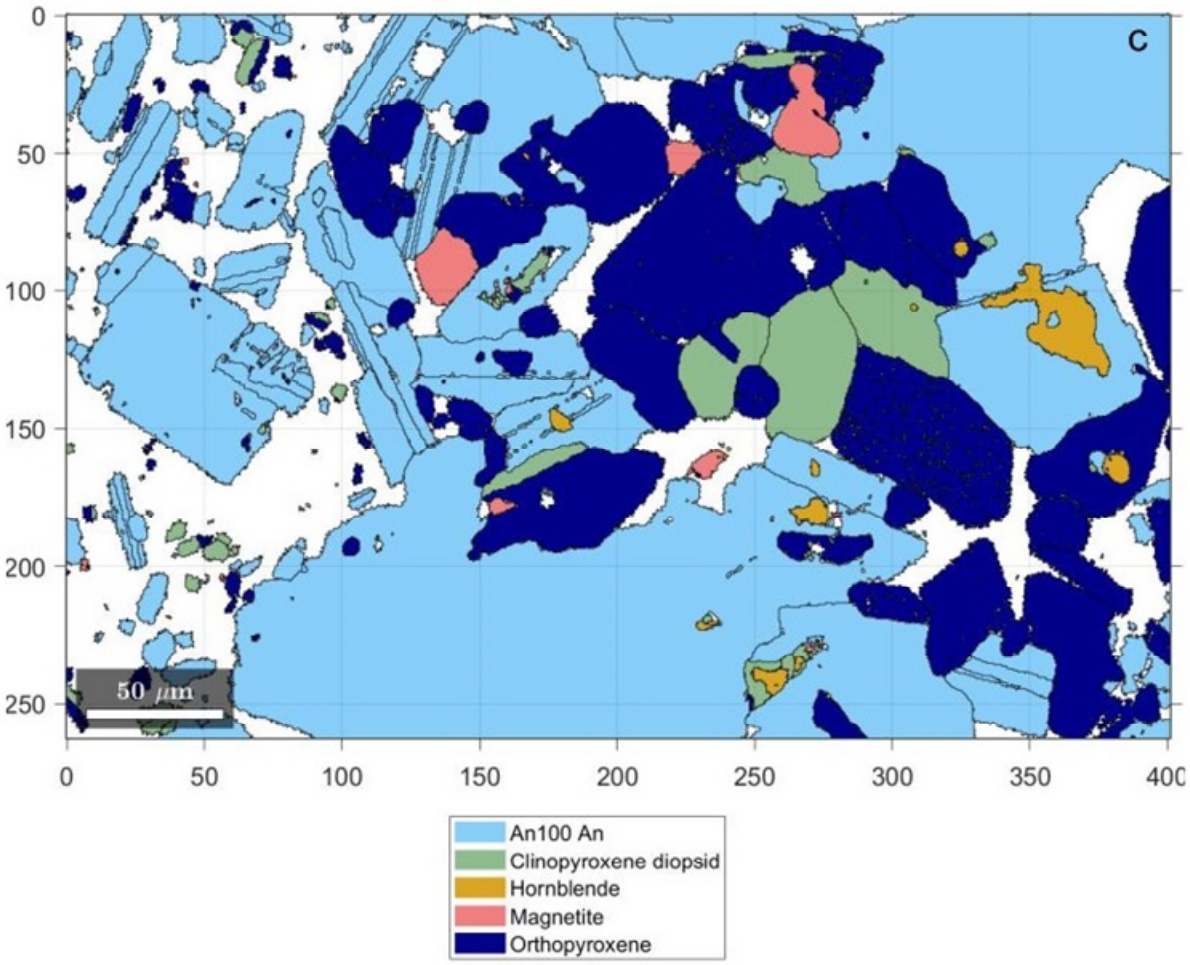


Figure 4.2. a) Plot showing the area of each EBSD map collected in this study. Colours indicate sample number. b) Table showing the total number of indexed and anorthite pixels per sample

analysed in this study. c) Example EBSD phase map for sample SHV_01. 'An100 An' refers to anorthite.

4.3. Results

There are a variety of ways to present misorientation data, as summarised in Wright *et al.* (2011). These methods are generally either grain-based, where a single misorientation value is calculated for the whole grain, or pixel-based, where a misorientation value is calculated for every measurement point within the grain. Here we analyse deformation using one grain-based method, grain orientation spread (GOS), and two pixel-based methods, grain reference orientation deviation (GROD) and kernel average misorientation (KAM). GROD and GOS both reference the whole grain orientation in their calculation, and so they provide information on misorientation relative to the grain as a whole. In contrast, KAM is referenced to a kernel (in this case the eight nearest neighbour pixels) within the grain, so it gives a localised view of strain. Using these different methods allows us to assess which are most suited to analysing crystal-plastic deformation within volcanic material.

4.3.1 Kernel average misorientation maps

Kernel average misorientation (KAM) is the average misorientation between one pixel and all neighbouring pixels. It provides a view of deformation at the local grain scale and can be used to visualise relative amounts of deformation between different samples. We consider neighbouring grains to one order (i.e., directly neighbouring grains only) and apply a threshold misorientation angle (δ) of 3°, meaning that any misorientation angles > 3 are excluded from the KAM maps. This value of δ was chosen as the majority of misorientations recorded across the samples are < 3°, so this allows us to see more variation than if a higher δ was used. This threshold value sets an upper bound for the KAM map scales, and does not alter the original data in any way. KAM maps created without a misorientation threshold are shown for all samples in **appendix 11**.

Figures 4.3 – 4.7 show selected KAM maps for each of the four different samples. These maps demonstrate that misorientations occur across all phases within the samples. In general, misorientation values are relatively low, with values < 1° being the most frequent.

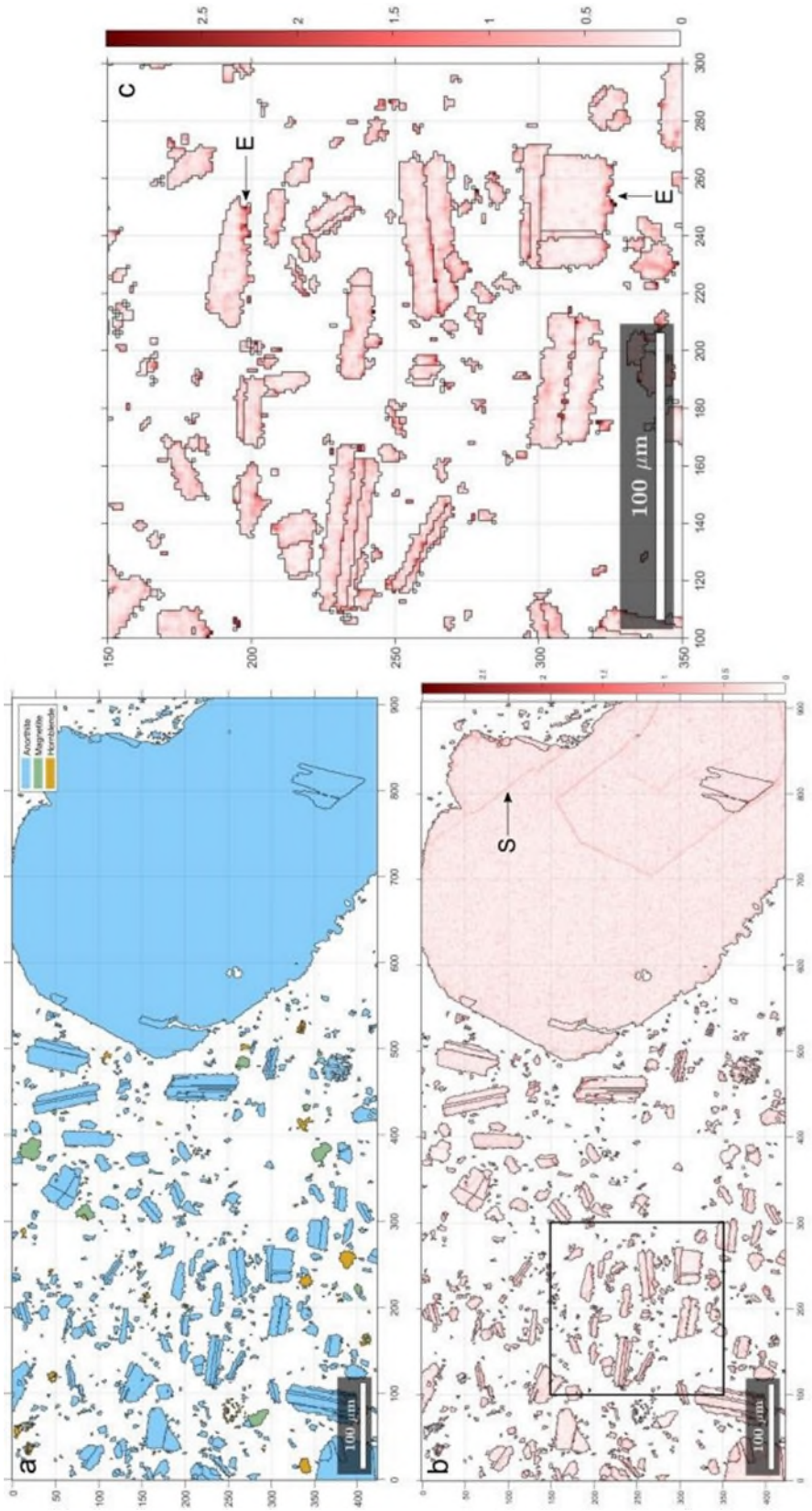


Figure 4.3. a) Phase map of sample SHV00. b) Kernel average misorientation (KAM) map (°). Black square highlights the area shown in c). c) 'E' denotes misorientations along the edges of grains, 'S' denotes subgrain boundary misorientations.

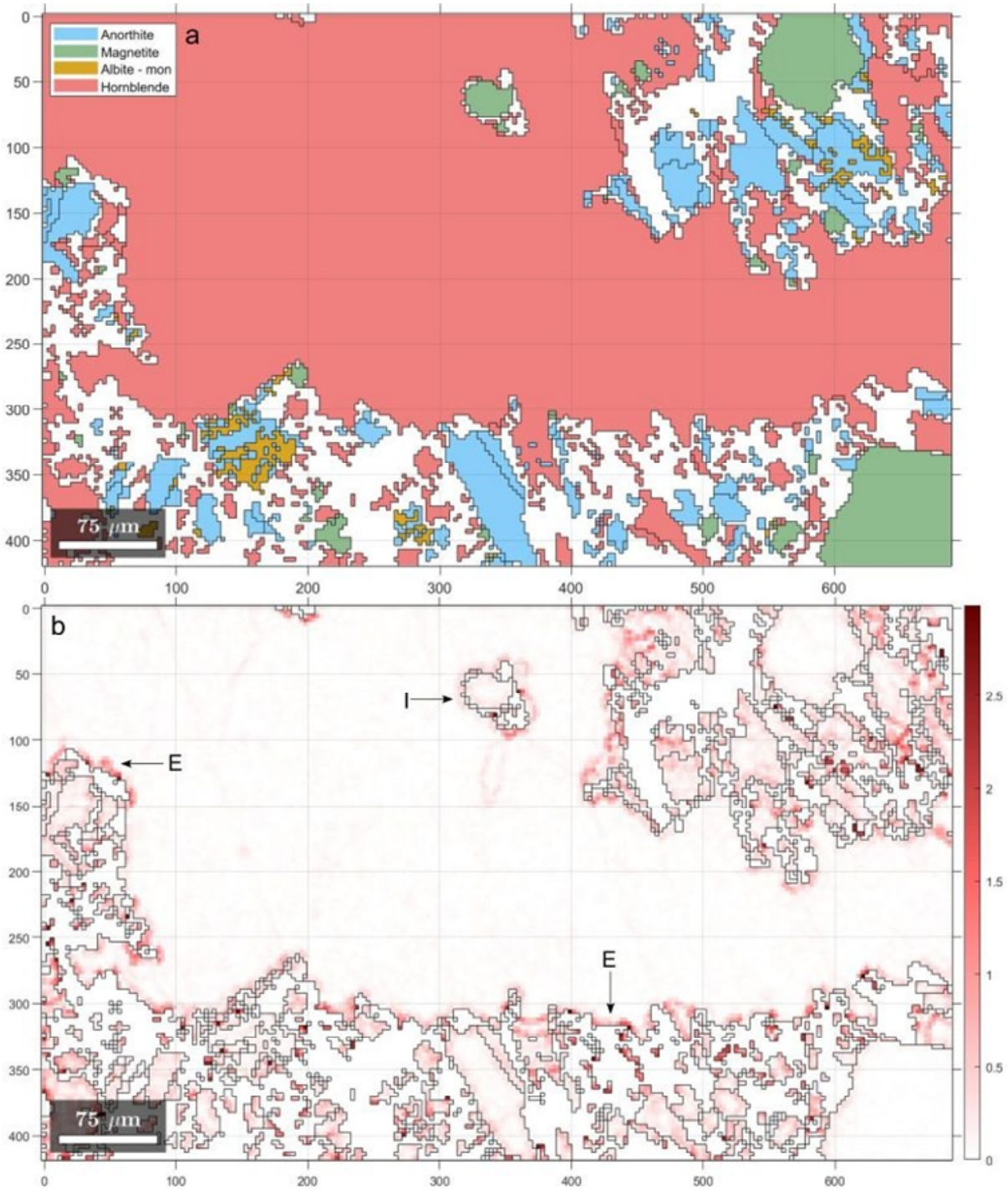


Figure 4.4. a) Phase map of sample SHV00. b) Kernel average misorientation (KAM) map (°). 'E' denotes misorientations along the edges of grains, 'I' denotes misorientations surrounding inclusions.

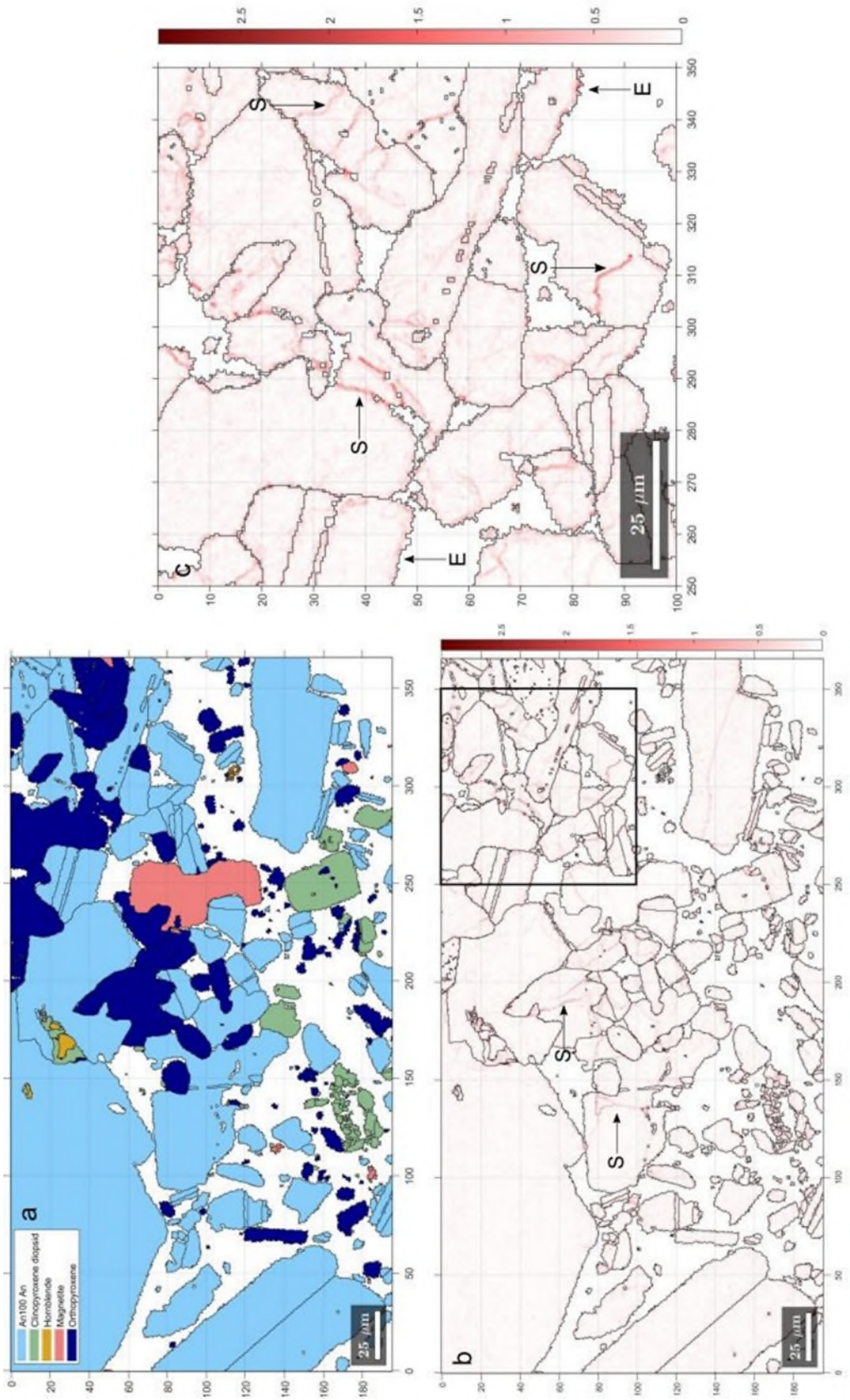


Figure 4.5. a) Phase map of sample SHV01. b) Kernel average misorientation (KAM) map (°). Black square highlights the area shown in c). c) 'E' denotes misorientations along the edges of grains, 'S' denotes subgrain boundary misorientations.

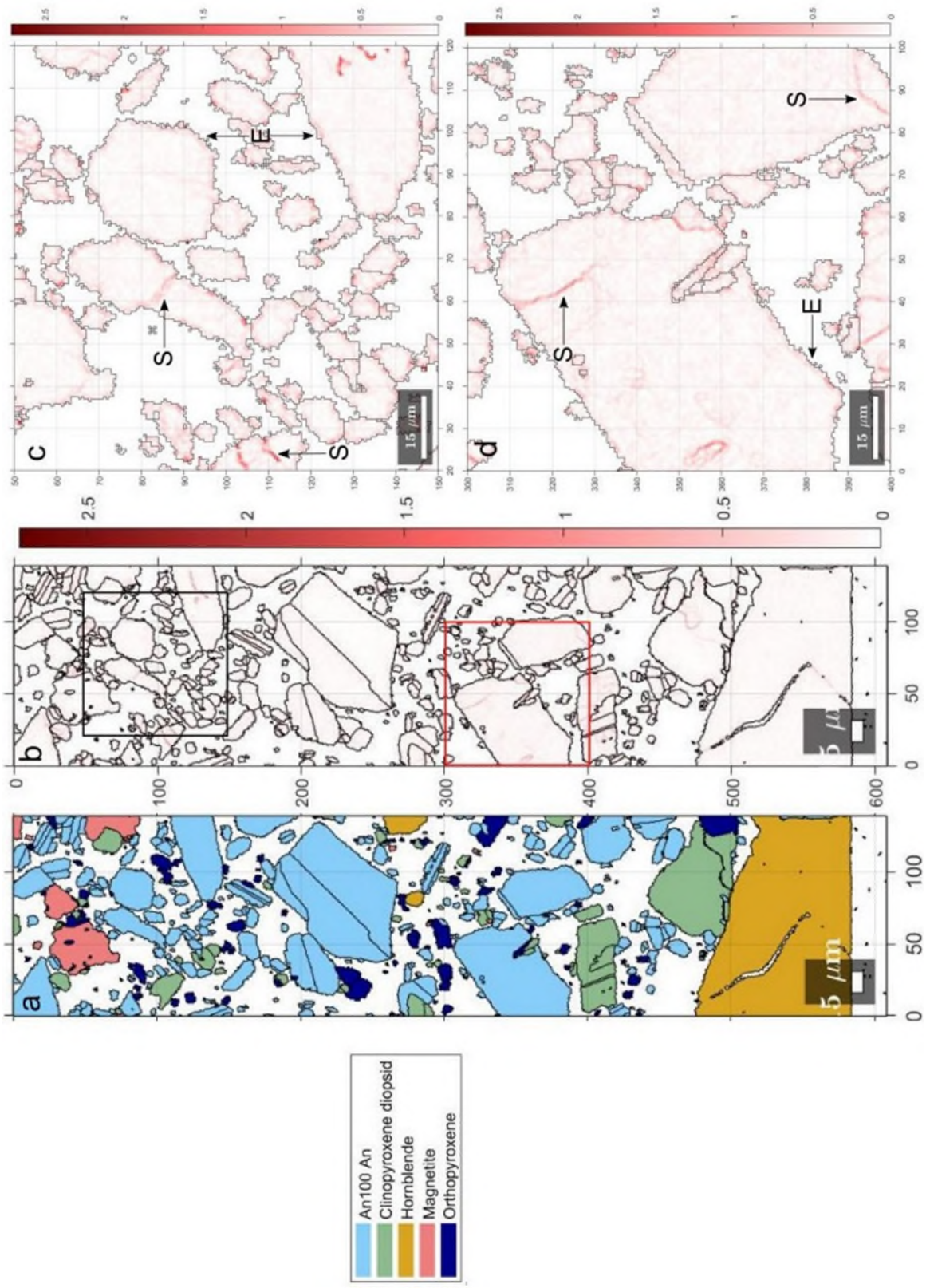


Figure 4.6. a) Phase map of sample SHV02. b) Kernel average misorientation (KAM) map (°). Black square highlights the area shown in c), red square highlights the area shown in d). c) and d) 'E' denotes misorientations along the edges of grains, 'S' denotes subgrain boundary misorientations.

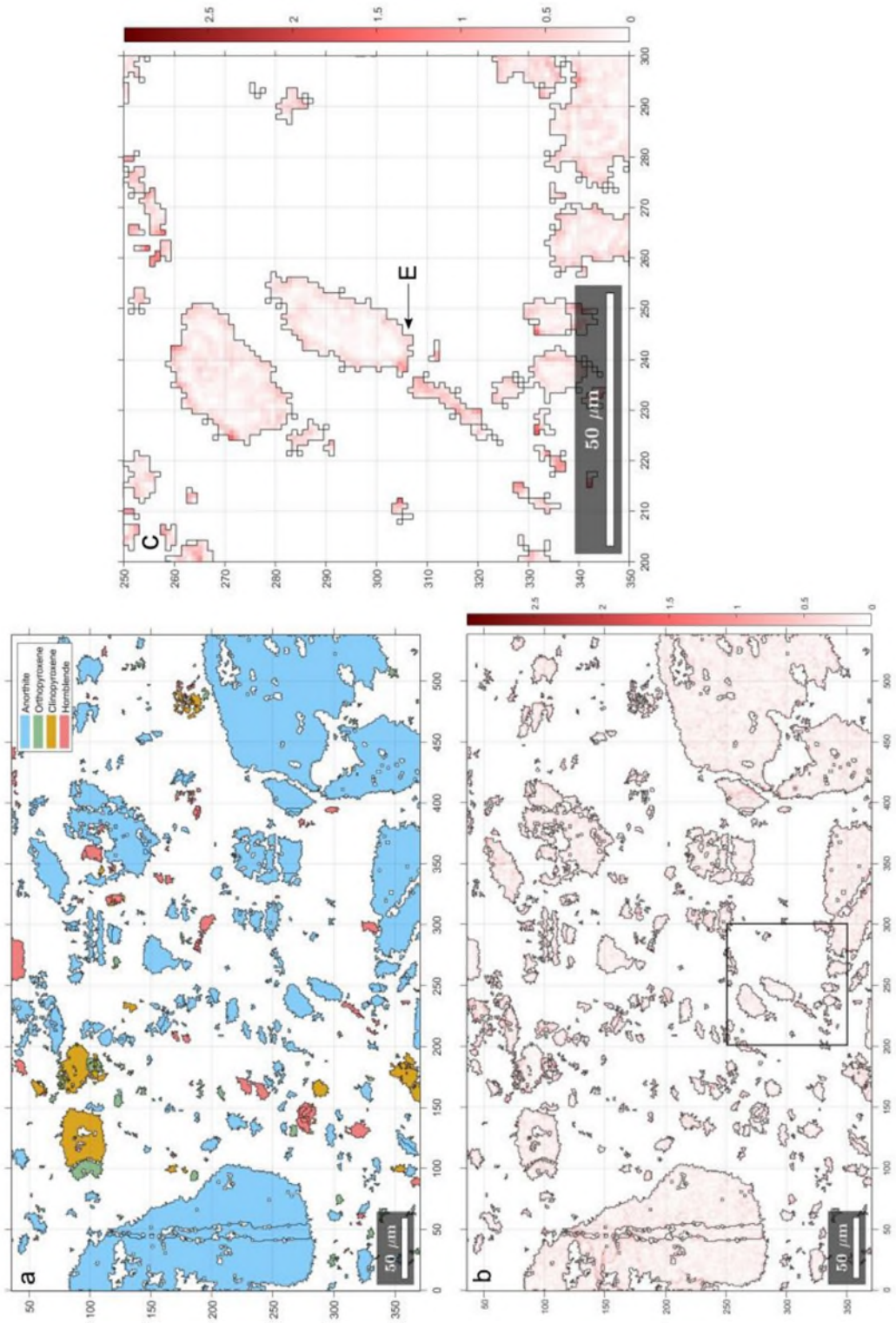


Figure 4.7. a) Phase map of sample SHV04. b) Kernel average misorientation (KAM) map (°). Black square highlights the area shown in c). c) 'E' denotes misorientations along the edges of grains.

Misorientations are most commonly located along the edges of grains and at subgrain boundaries. We pick out some of these features visually, marked ‘E’ for edge and ‘S’ for subgrain, in **figures 4.3 – 4.7**. Edge misorientations within the natural sample (SHV00) are shown in **figure 4.3**, whilst **figure 4.4** highlights an area of relatively high misorientations (>1°) surrounding a magnetite inclusion in hornblende. **Figures 4.5, 4.6 and 4.7** show the formation of subgrain and edge misorientations across each different phase within the experimentally-deformed samples. The area shown in **figure 4.5c** displays a high density of crystal-crystal contacts and subgrain boundaries within anorthite, orthopyroxene and magnetite crystals.

4.3.2 Kernel average misorientation histograms

In order compare deformation across the different samples, we plot misorientation histograms as demonstrated in Kendrick *et al.* (2017) and Wallace *et al.* (2019). KAM data is extracted for all four sample sets described in section 4.2.1. We initially focus our analysis on anorthite as this is the most abundant phase, allowing us to gather a more statistically robust data set. However, we also plot KAM values for magnetite in order to compare deformation between different phases. Our magnetite data set is relatively small, with a total of 29480 pixels and a maximum of 20 crystals per map. There are no magnetite data from sample SHV04, so this has not been included in the histograms. For one of our SHV01 maps there is a grain which has wrongly been indexed as a combination of magnetite and clinopyroxene (see appendix A10c) – we do not include these misorientation values in our KAM analysis. In order to extract the whole range of measured KAM values we do not use a threshold angle for extracting the KAM data (no δ), and our histograms are normalised, so counts are expressed in relation to the total number of pixels in each sample. For ease of viewing trends in these data, envelopes to the histograms are shown for two different misorientation ranges in **figure 4.8**, whilst the raw data are included in **appendix 12.**

Figure 4.8a shows KAM values focused on an interval of 0-1°. This shows that the natural sample (SHV_00), has the normalised frequency peak with highest KAM value, at ~ 0.22°.

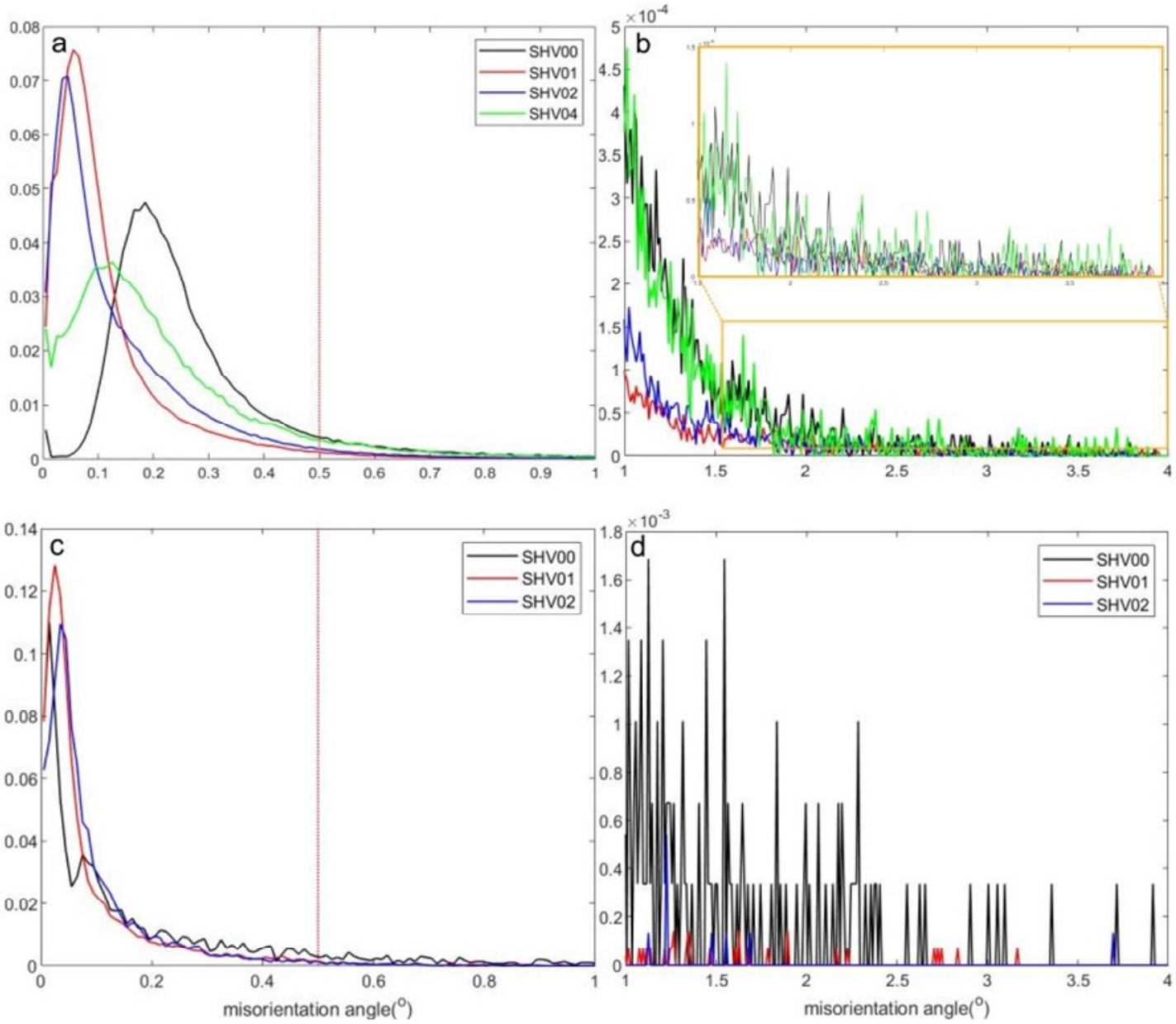


Figure 4.8. Kernel average misorientation (KAM) histogram envelopes. a) and b) Normalised frequency histogram envelopes for the anorthite phase only, focused on 0-1° and 1-4° misorientation ranges. The orange box in b) shows a close-up version of misorientations in the 1.5-4° range. c) and d) Normalised frequency histogram envelopes for the magnetite phase only, focused on 0-1° and 1-4° misorientation ranges. Vertical red dashed line in a) and c) highlights the resolution of the standard EBSD technique. Values are normalised to the total number of data points in each sample, and bin size is set to 0.01. Envelopes to each histogram were plotted using the 'histcount' function in Matlab. SHV00 = natural sample, SHV01 = overpressured sample, SHV02 = low-pressure static sample, SHV04 = high-pressure static sample.

The high-pressure static sample (SHV_04) peaks at ~ 0.12°, and the overpressured (SHV_01) and low-pressure static (SHV_02) samples have similar frequency peaks at ~ 0.05°. As indicated in **figure 4.8a**, the majority of these KAM values are below the ~0.5° resolution of the standard EBSD technique, and so these data cannot provide reliable information on deformation across the four samples. **Figure 4.8b** focuses on misorientations within the 1-4° range, representing the descending limb of the normalised frequency distributions. The natural and high-pressure static samples have similar profiles, both displaying a higher frequency of KAM values > 1, relative to the overpressured and low-pressure static samples. This difference is particularly pronounced within the 1-2° misorientation angle range. The magnetite histogram envelopes for the 0-1° range (**fig 4.8c**) also show that the majority of misorientations have values lower than the resolution of the technique – similar to the anorthite data. Focusing on the 1-4° misorientation range, the natural sample again has a higher frequency of KAM values > 1, relative to the overpressured and low-pressure static samples.

4.3.3 Grain reference orientation deviation and grain orientation spread maps

The KAM maps described in section 4.3.1 give a localized view of deformation at the kernel scale, but are sensitive to kernel size and local noise within the sample. In order to visualize deformation across each grain as a whole, we also plot maps of grain reference orientation deviation (GROD) and grain orientation spread (GOS). GROD is a measure of the misorientation between each measurement point (pixel) and the average grain orientation, resulting in one value for each pixel. Grain orientation spread (GOS) is the average GROD value of each grain, resulting in one value per grain. These techniques are well-suited to revealing information about grain-scale deformation gradients.

The GROD and GOS maps shown in **figures 4.9 – 4.13** highlight some areas of deformation which are not picked up in the KAM maps, and these areas have been annotated with an asterisk. The GROD maps also pick out orientation changes which occur due to the presence of subgrain boundaries. High GROD values occur across all of the indexed phases. **Figure 4.9** shows relatively high GROD values in the small magnetite crystal in the lower part of the

map. **Figure 4.10** highlights deformation within a promontory at the edge of a hornblende crystal. **Figure 4.11** shows relatively high GROD values within orthopyroxene crystals in an area of tight crystal-packing. **Figure 4.12** highlights orientation gradients within anorthite and clinopyroxene crystals, and **figure 4.13** shows orientation gradients within the anorthite crystal in the left-hand side of the image. The corresponding GOS maps highlight grains with high deformation throughout their whole area. GOS has the benefit of simplifying deformation data within a sample by providing one value per grain. However, it is not a good method for detecting subgrain boundaries within large grains – for example in the largest anorthite crystal in **figure 4.9** - as the subgrain deformation is averaged across the whole grain area.

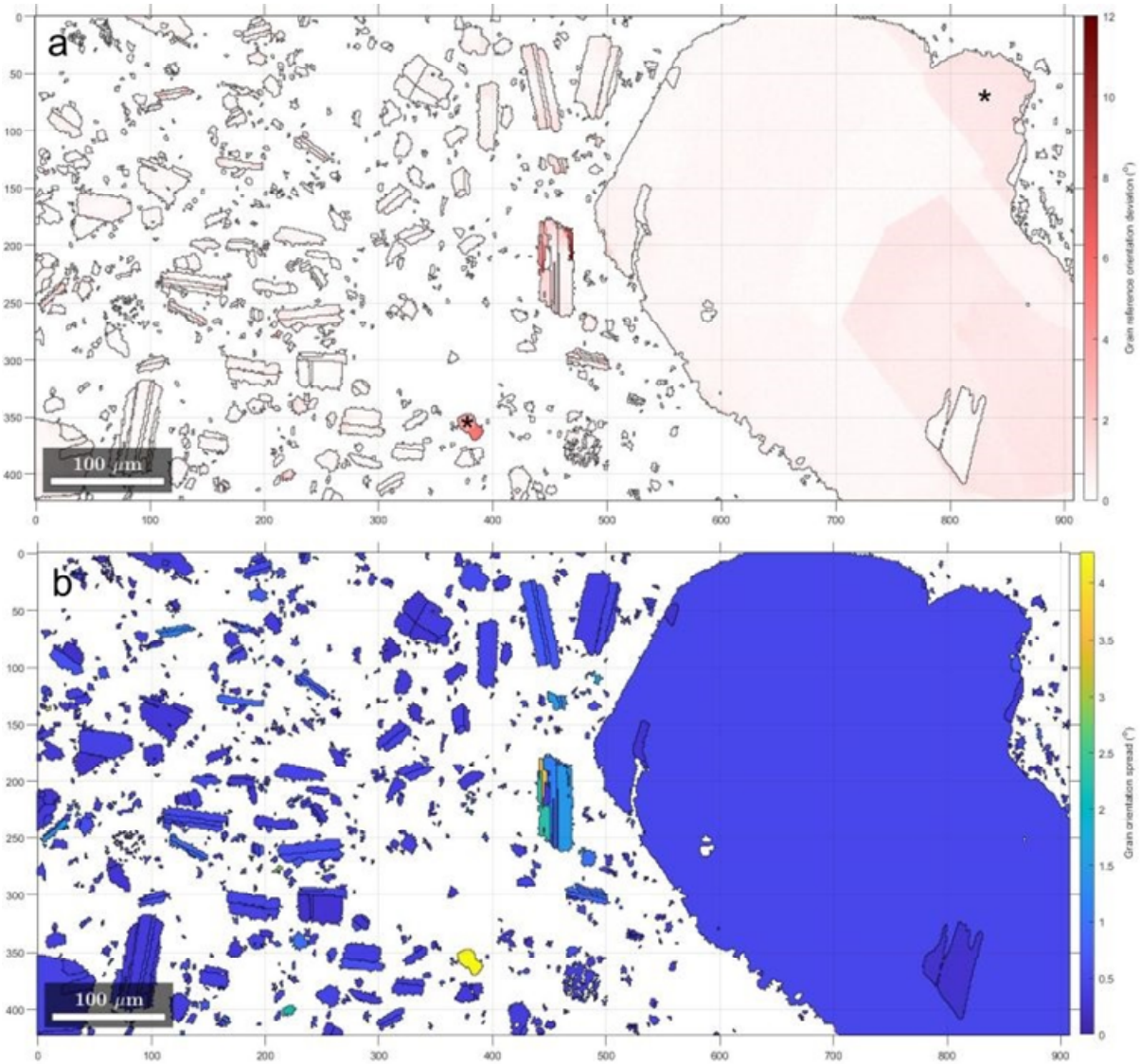


Figure 4.9. GROD and GOS maps for sample SHV_00. a) Grain reference orientation deviation (GROD) map. Asterisks highlight deformation gradients which are not apparent in the KAM maps. b) Grain orientation spread (GOS) map.

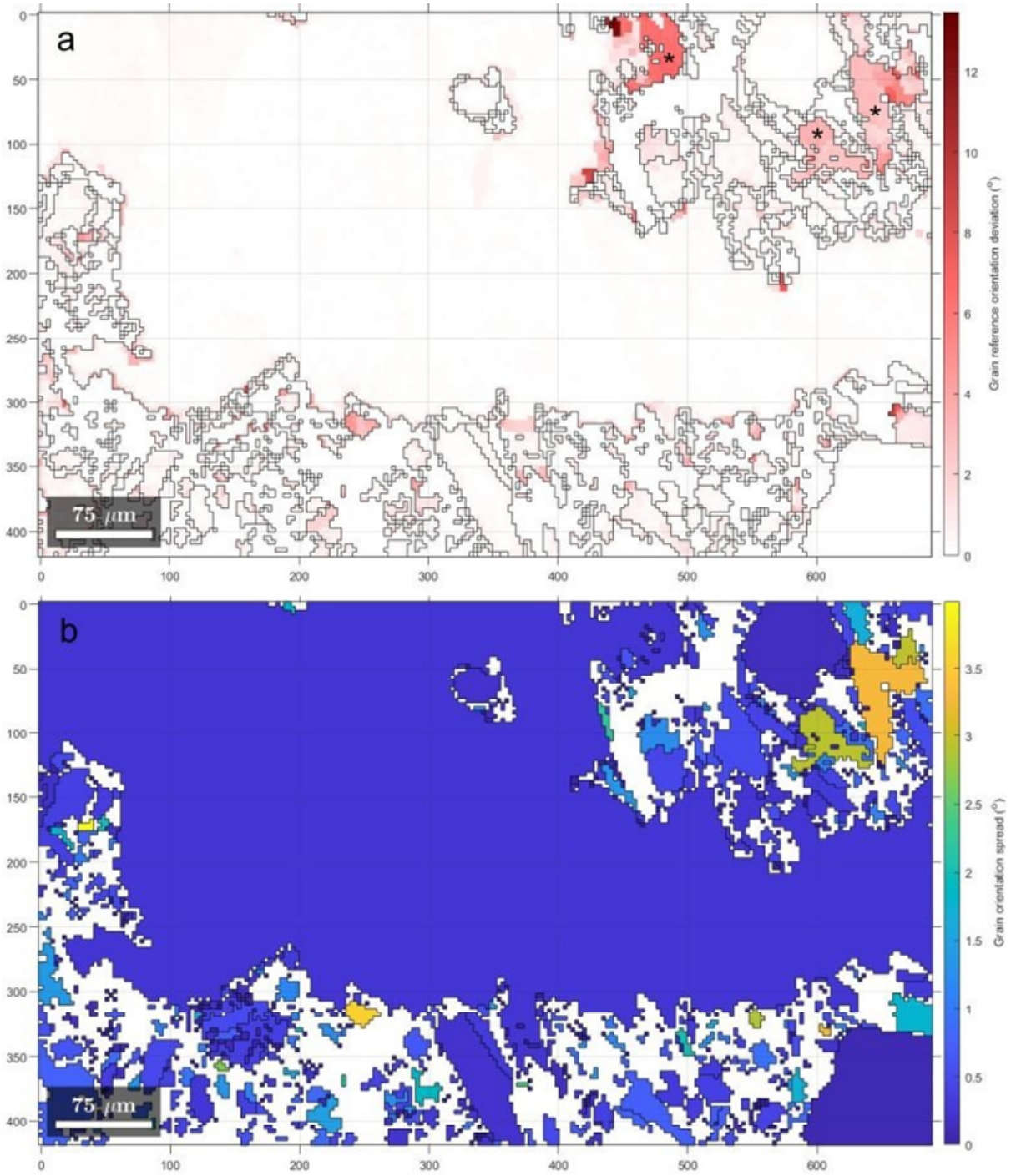


Figure 4.10. GROD and GOS maps for sample SHV_00. a) Grain reference orientation deviation (GROD) map. Asterisks highlight deformation gradients which are not apparent in the KAM maps. b) Grain orientation spread (GOS) map.

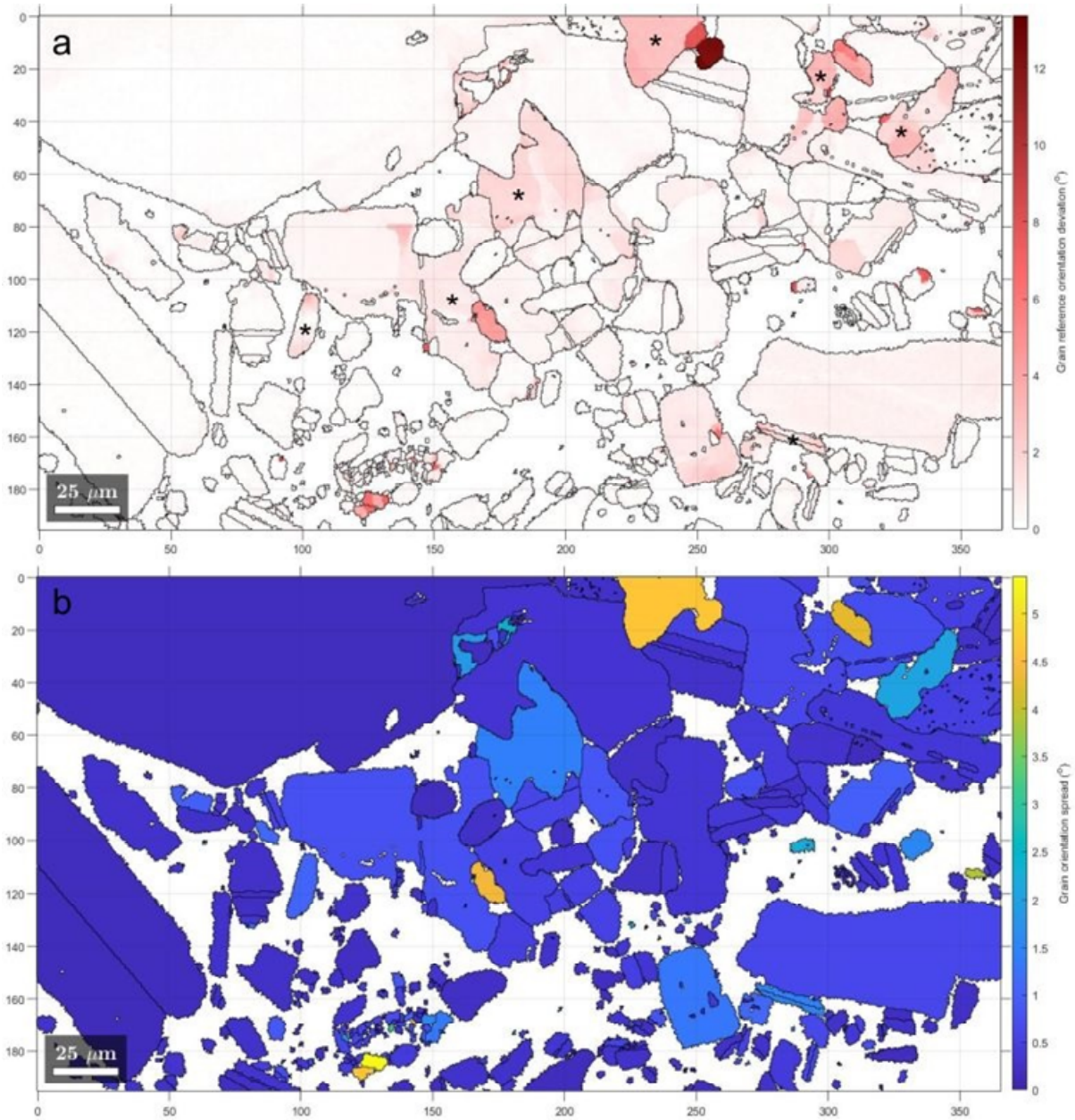


Figure 4.11. GROD and GOS maps for sample SHV_01. a) Grain reference orientation deviation (GROD) map. Asterisks highlight deformation gradients which are not apparent in the KAM maps. b) Grain orientation spread (GOS) map.

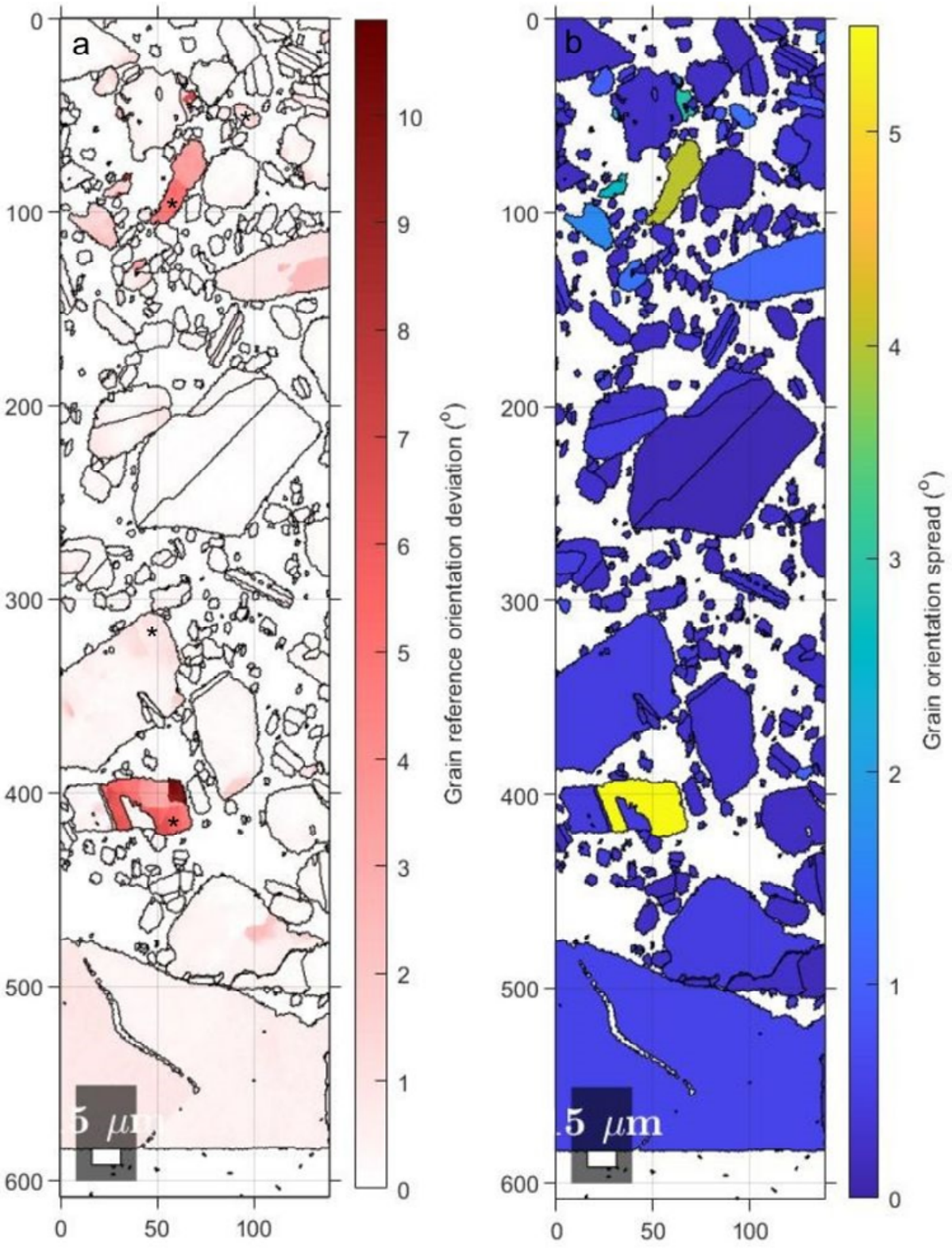


Figure 4.12. GROD and GOS maps for sample SHV_02. a) Grain reference orientation deviation (GROD) map. Asterisks highlight deformation gradients which are not apparent in the KAM maps. b) Grain orientation spread (GOS) map.

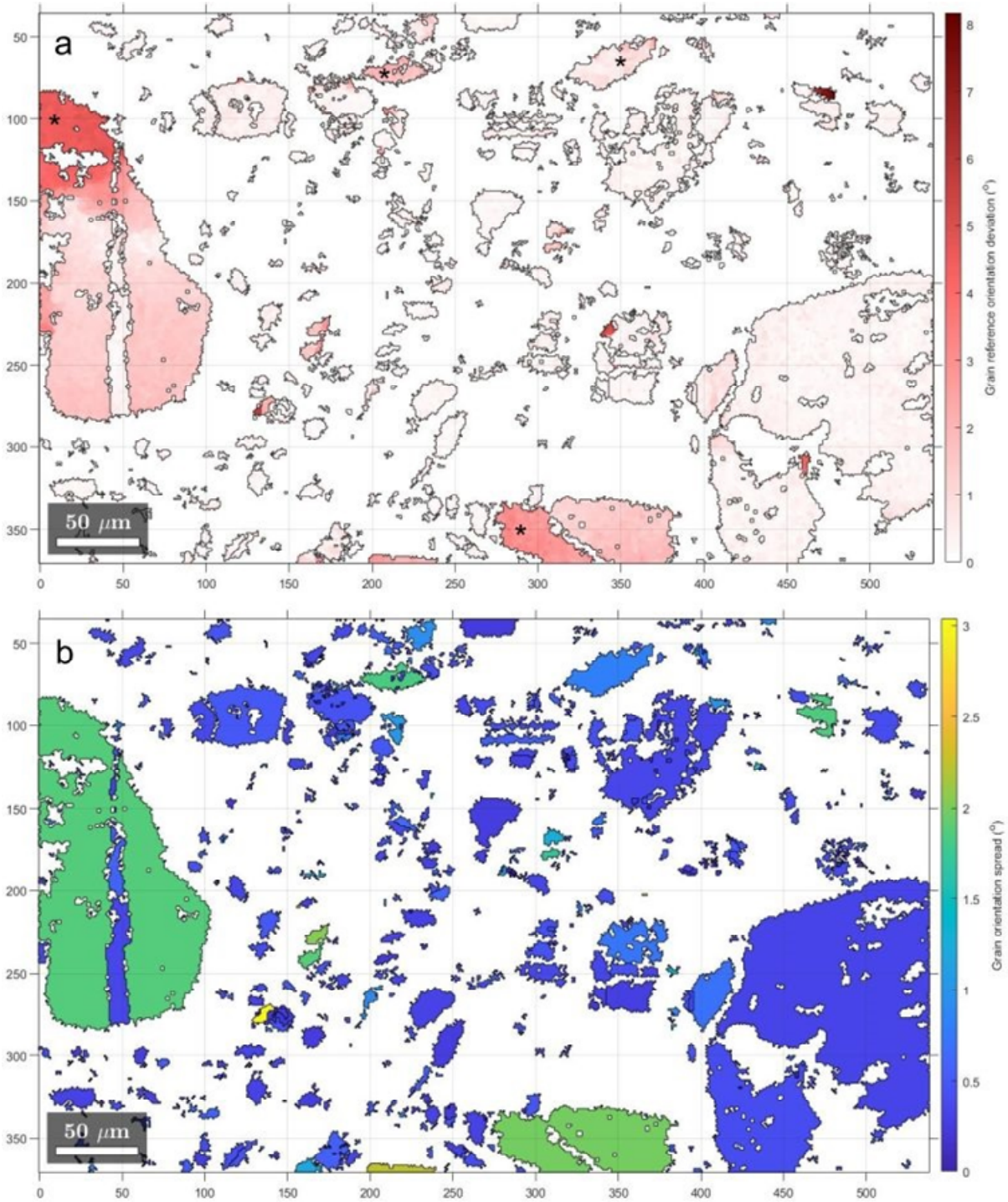


Figure 4.13. GROD and GOS maps for sample SHV_04. a) Grain reference orientation deviation (GROD) map. Asterisks highlight deformation gradients which are not apparent in the KAM maps. b) Grain orientation spread (GOS) map.

4.3.4 Grain reference orientation deviation histograms

In order to quantitatively compare the KAM and GROD techniques, we extract GROD values for the anorthite phase and plot them in histograms with envelopes in **figure 4.14**. When considering a misorientation range of 0-1°, the natural and high-pressure static samples (SHV00 and SHV04) have normalised frequency peaks at similar values (~0.3°), both of which are higher than the frequency peaks seen in the overpressured and low-pressure static samples (SHV01 and SHV02). These results are similar to the misorientation frequencies shown in the KAM anorthite histogram envelopes (**fig 4.8**). Focusing on misorientations with values from 1-4°, the high-pressure static sample (SHV04) displays a higher frequency of misorientations within this range than the other three samples (**fig 4.14b**). This is in contrast to the KAM envelopes, which show that the natural and high-pressure static samples have similar profiles (**fig 4.8b**). The overpressured and low-pressure static samples have a higher frequency of misorientations within the 1.5-3° range than the natural sample, which was not apparent from the KAM histograms.

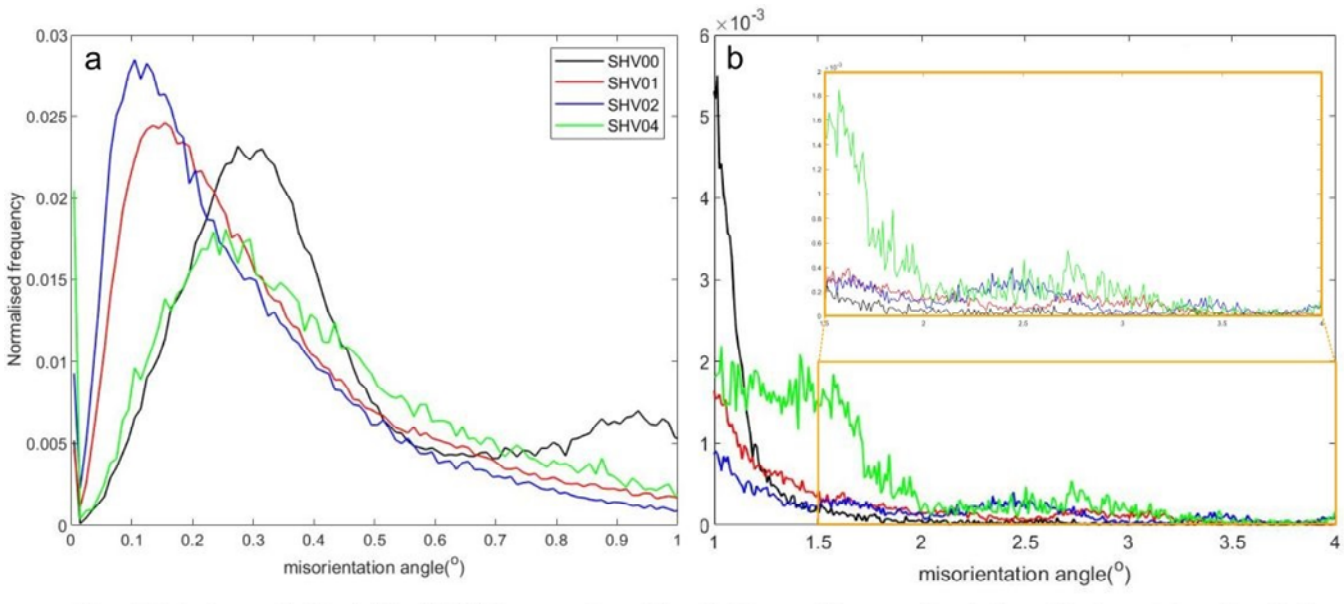


Figure 4.14. Grain reference orientation deviation (GROD) histogram envelopes for anorthite. a) Focused on a 0-1° misorientation range. b) Focused on a 1-4° misorientation range. The orange box in b) shows a close-up version of misorientations in the 1.5-4° range. Values are normalised to the total number of data points in each sample and bin size is set to 0.01. Envelopes to each histogram were plotted using the 'histcount' function in Matlab.

4.3.5 Misorientation line profiles

To further characterise spatial changes in crystal deformation, we plot misorientation profiles across individual grains (**figures 4.15 – 4.18**). We select grains with relatively high GOS or GROD values from each sample, and restrict misorientation data to a linear transect across the grain. At each point along this transect, misorientation is plotted relative to the first point on the line (point 'A', or the reference orientation), and also to the orientation gradient of the whole grain. The orientation gradient profiles (in orange) highlight the background "noise" in misorientation values across the grain, whilst the reference orientation profiles (in blue) highlight deformation gradients. We plot crystal misorientation profiles for each of the four samples, along with GROD maps and the line location on each grain. In general these profiles show that the noise within the grains ranges from ~ 0.1-0.3°. We note that high-angular resolution EBSD (Wilkinson, 1996; Wilkinson *et al.*, 2006) can increase the precision of misorientation measurements, resulting in a reduction in background noise level and an improvement in the resolution of orientation gradients, as demonstrated by Wallis *et al.* (2019). This is particularly valuable for samples with generally low misorientation values, where orientation gradients due to deformation may be obscured by noise levels which are poorly resolved by conventional EBSD.

Figure 4.15 shows misorientation profiles across an anorthite crystal from the natural sample (SHV00), illustrating background noise levels of ~ 0.3°. When the profile crosses the subgrain boundary (picked out by the localised misorientations shown in the KAM map in **figure 4.3b**) the misorientation relative to the reference orientation (point A) increases, reflecting the broad change in crystal orientation across this boundary. Deformation gradients within orthopyroxene and magnetite crystals from the experimentally overpressured sample (SHV01) are shown in **Figure 4.16**, which highlights an area of densely-packed crystals. Misorientations relative to the orientation gradient (orange line) show background noise levels of ~ 0.25° for the orthopyroxene and ~ 0.15° for the magnetite. These values increase to up to 2° when the profile crosses a subgrain boundary (picked out by the KAM map in **fig 4.5b**). The increase in

reference orientation profile values away from the background noise indicates that these are orientation gradients due to bending of the crystal lattice. **Figure 4.17** shows two misorientation transects within a twinned anorthite crystal from the low-pressure static sample (SHV02). This crystal is bent slightly about its centre, which may be due to the contacts from the surrounding crystals which could have applied opposing stresses to either side of the anorthite grain (**fig 4.17a**). The orientation gradient profiles show background noise levels of ~ 0.2-0.3°, with sharp increases up to 10° when crossing the most deformed part of the grain. The profiles plotted relative to point A show gradual orientation changes until the point of maximum deformation, where values increase rapidly. This deformation is not obvious from the KAM map, highlighting the benefit of using different methods to assess deformation. **Figure 4.18** shows a misorientation transect across an anorthite crystal from the high-pressure static sample (SHV04), which shows background noise levels around 0.3-0.4°. The misorientation relative to point A profile highlights a subtle orientation gradient across the grain, which again is not immediately obvious form the KAM maps.

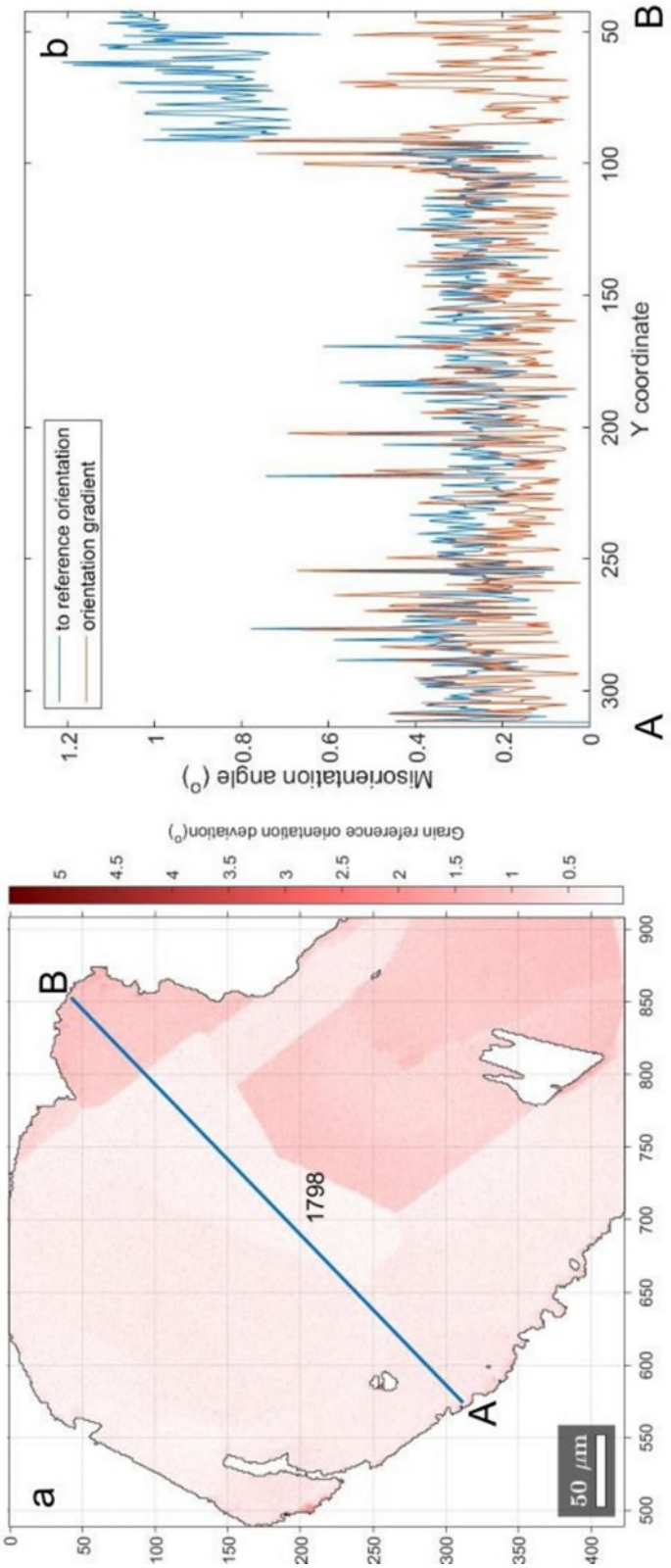


Figure 4.15. a) Grain reference orientation deviation (GROD) map of anorthite grain 1798 in sample SHV_00. Blue line shows the location of the profile in b. b) Misorientation profile across grain 1798. The blue line shows misorientation angle relative to point 'A'. The orange line shows misorientation angle relative to the grain orientation gradient.

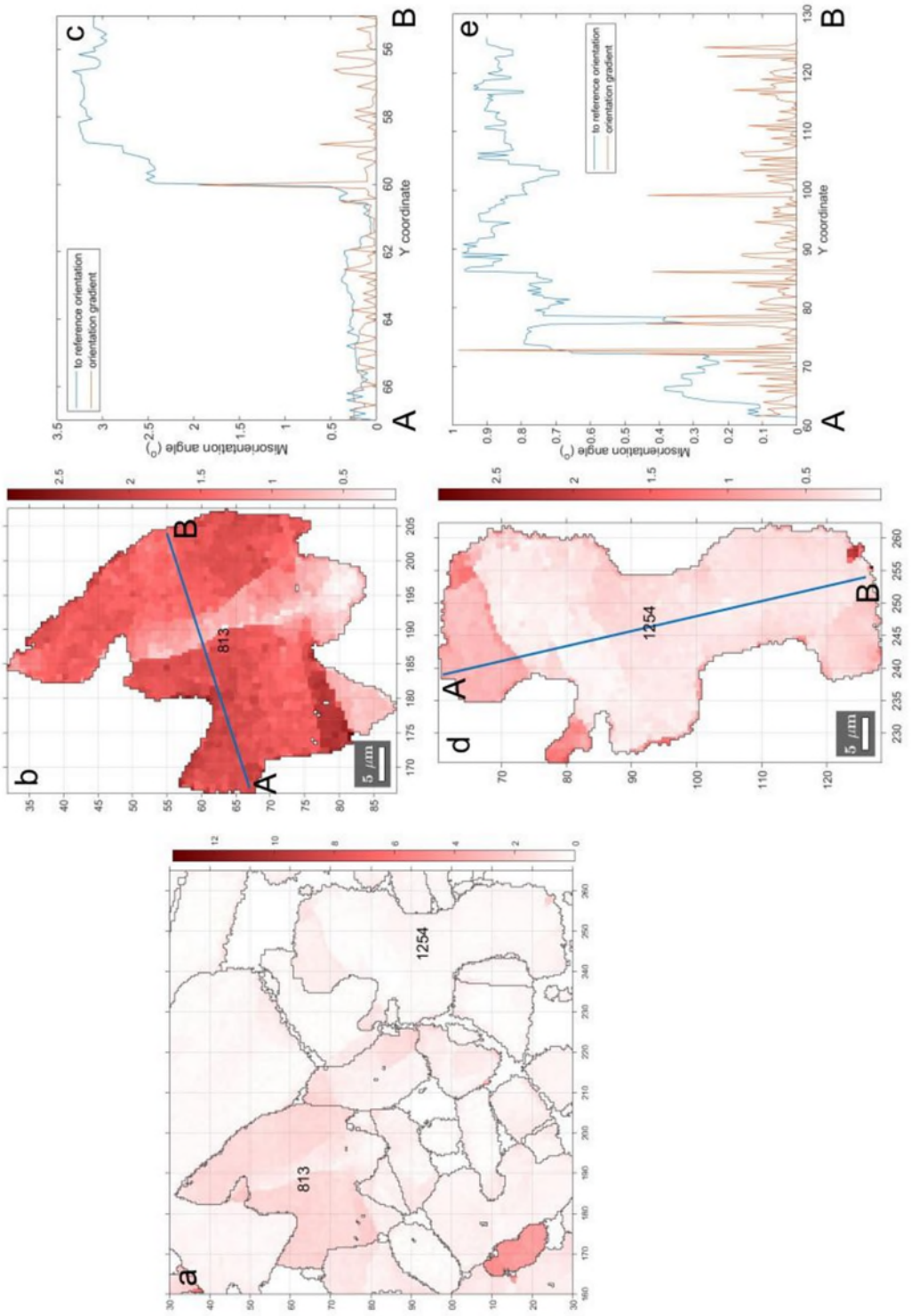


Figure 4.16. a) Grain reference orientation deviation (GROD) map showing the location of grains 813 and 1254 within sample SHV01. b) GROD map of orthopyroxene grain 813. Blue line shows the location of the profile in c. c) Misorientation profile across grain 813. d) GROD map of magnetite grain 1254. Blue line shows the location of the profile in e. e) Misorientation profile across grain 1254. For c) and e), the blue line shows misorientation angle relative to point 'A'. The orange line shows misorientation angle relative to the grain orientation gradient.

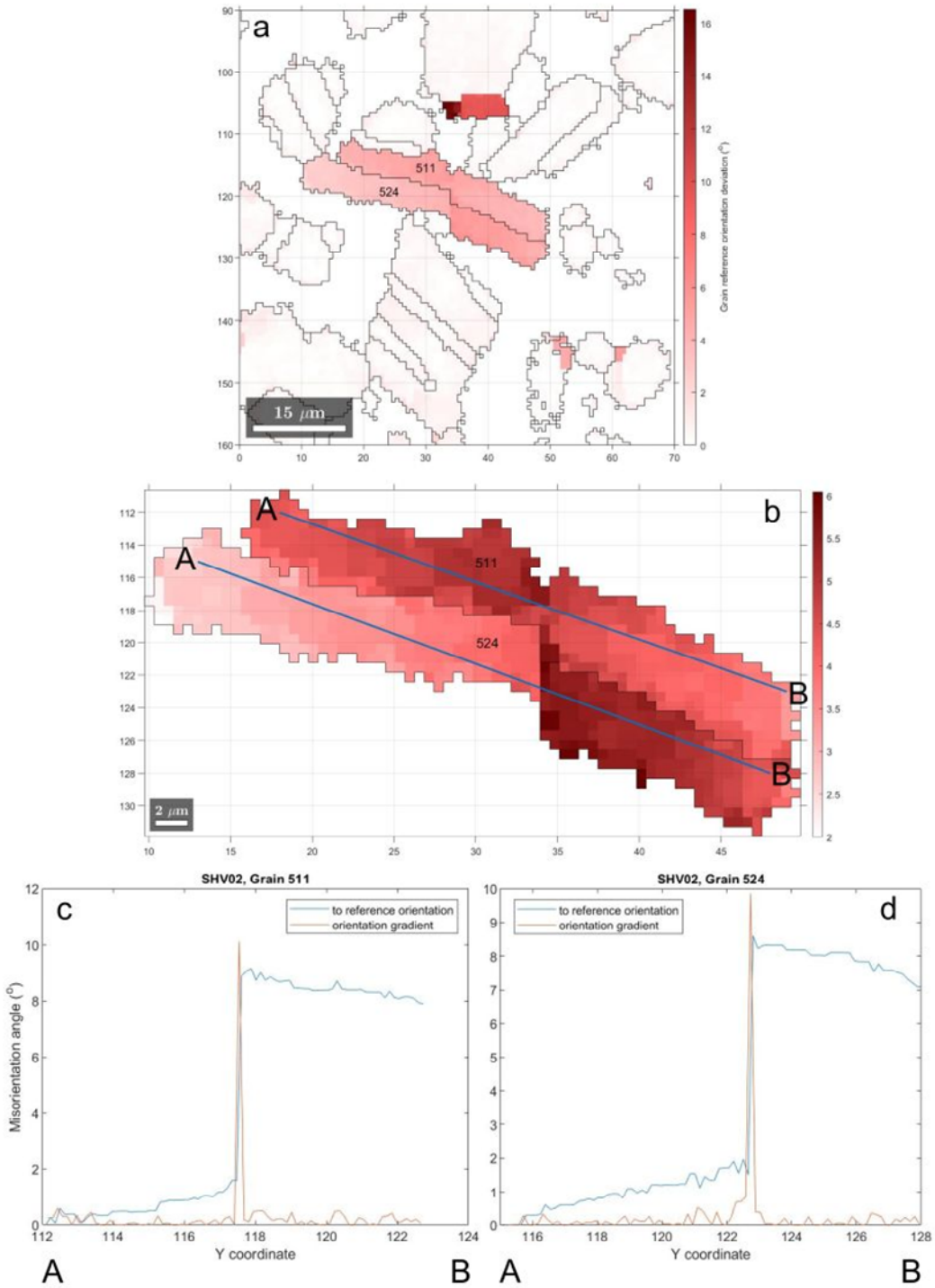


Figure 4.17. a) Grain reference orientation deviation (GROD) map showing the location of grains 511 and 524 within sample SHV02. b) Grain reference orientation deviation map of anorthite grains 511 and 524. Blue lines show the location of the profiles in c) and d). c) Misorientation profile across grain 511. d) Misorientation profile across grain 524. For c) and d), the blue line shows misorientation angle relative to point 'A', and the orange line shows misorientation angle relative to the grain orientation gradient.

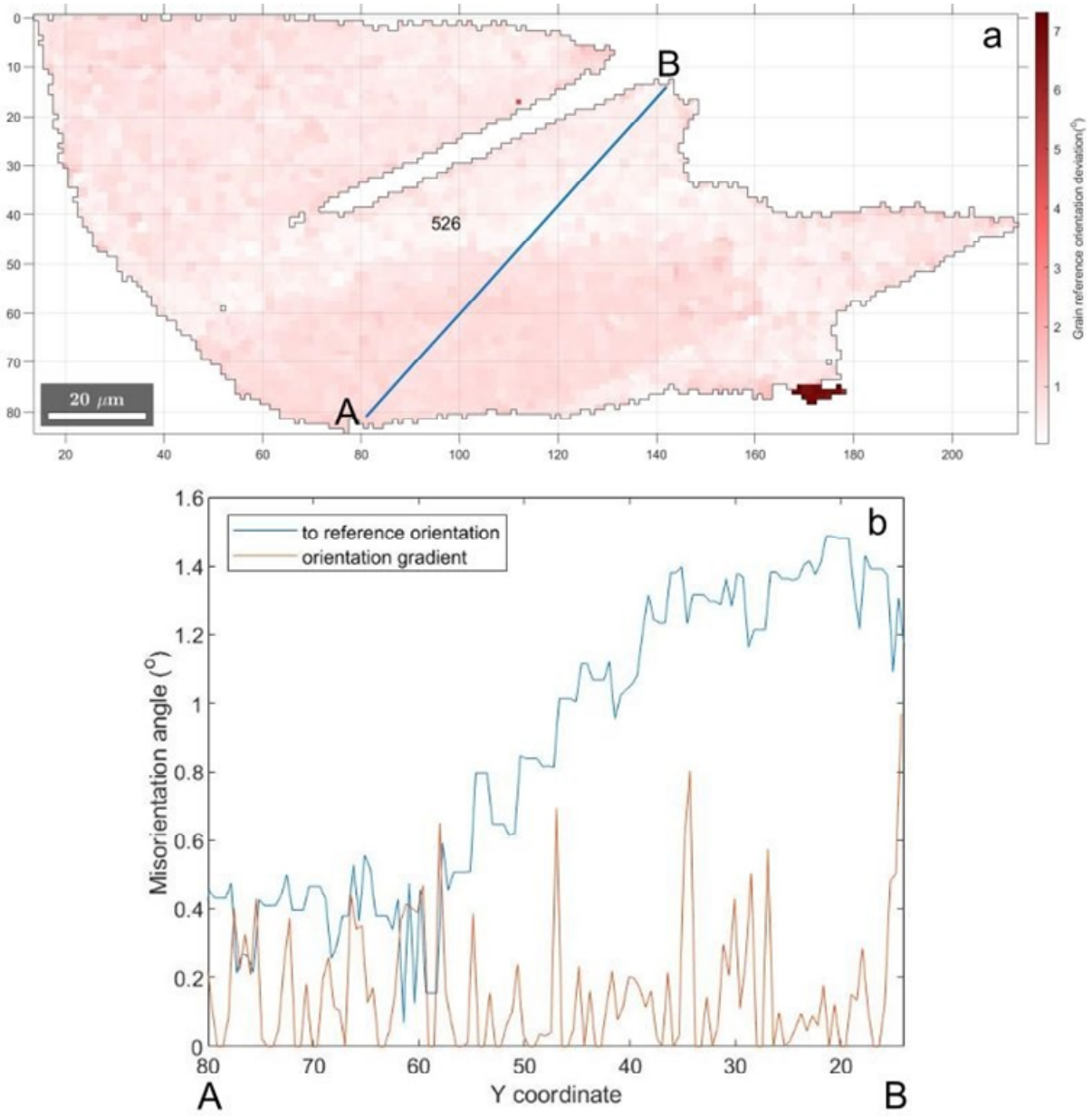


Figure 4.18. a) Grain reference orientation deviation (GROD) map of anorthite grain 526 in sample SHV_04. Blue line shows the location of the profile in b. b) Misorientation profile across grain 526. The blue line shows misorientation angle relative to point 'A'. The orange line shows misorientation angle relative to the grain orientation gradient.

4.4. Discussion

4.4.1 Extent and location of crystal deformation

Our results show that misorientations are concentrated around crystal edges and at curvilinear subgrain boundaries. The misorientations at crystal edges occur across all phases, grain sizes and samples, and occupy a region ~ 0.5-1 μm in width. Although these misorientations are common across all phases, they are not a consistent thickness around all of the grain edges, as shown for example in **figure 4.3c**, where anorthite grains in the natural sample show misorientations along some of their edges but not others. Misorientations associated with subgrain boundaries are also seen across all phases, grain sizes and samples, and have lengths up to 150 μm. The misorientation values associated with subgrain boundaries are generally slightly higher than the values associated with edge misorientations, as illustrated in **figs 4.5 and 4.6**. **Figure 4.5c** highlights subgrain boundaries which have formed within a closely packed area of anorthite, orthopyroxene and magnetite crystals. We hypothesise that areas such as this, with a relatively high number of crystal-crystal contacts, are prime targets to provide information on stress transfer within a crystal-rich magma mush. Crystal-crystal impingement has also potentially generated deformation of the anorthite crystal lattice shown in **figure 4.17**, which shows bending due to opposing forces from the crystals either side of it. Finally, relatively large local misorientations are also associated with crystal inclusions, although these are less abundant in our data set than the edge and subgrain deformation. **Figure 4.4** shows misorientations surrounding a magnetite inclusion within hornblende – the misorientations are highest at the edge of the hornblende in contact with the magnetite. Melt and crystal inclusions might also be a good place to focus on when quantifying deformation in crystal-rich magmas.

4.4.2 Magnitude of crystal deformation

We demonstrate that the misorientations seen in both the natural and experimental samples are relatively low, with all samples showing frequency peaks at misorientation values < 0.5°. Kernel average misorientation values for both magnetite and anorthite show that the

overpressured and low-pressure static samples (SHV01 and SHV02) have normalised frequency peaks at lower values than the natural starting material (**fig 4.8**). One possible reason for this is that experimentally heating these samples has resulted in annealing of dislocations in the crystal lattice, resulting in lower misorientation values than those in the starting material. In contrast, the higher constant experimental pressure (155 MPa) used for the high-pressure static sample (SHV04) may have inhibited annealing. The KAM data do not support our hypothesis that experimental overpressurisation (SHV01) will generate more crystal-plastic deformation than the other experimental samples. In fact, the natural sample and the high-pressure static sample have a higher frequency of pixels with higher misorientations across the 1-4° range for both anorthite and magnetite (**fig 4.8**). This may be because the experimental set-up is only recording the effect of maximum pressure, rather than the intended effect of overpressurisation. Alternatively, the natural and high-pressure static profiles may be similar because 155 MPa is a good match for the pressure conditions which the natural sample experienced prior to eruption. If this is the case, then EBSD analysis of deformation in volcanic rocks has the potential to become another tool used to determine pre-eruptive storage conditions.

For the 0-1° GROD histogram envelopes (**fig 4.14**), the profiles are similar to those shown in the KAM plots. Specifically, the natural and high-pressure static samples have similar misorientation profiles, both of which have frequency peaks at higher values than the overpressured and low-pressure static samples. However, the overpressured and low-pressure static samples have a slightly higher frequency than the natural sample across the 1.5-4° range (**fig 4.14b**), which is not seen in the KAM histograms. One possible reason for this difference is that the KAM and GROD measurements are sensitive to different types of deformation. KAM is good at detecting localised grain misorientations, and so it may be more sensitive to the misorientations concentrated along grain edges. However, GROD is better at detecting broader scale orientation changes across a whole grain, and so is likely to be more sensitive to the misorientations associated with subgrain boundaries and bending. The KAM

and GROD histogram envelopes all show that frequency peaks occur at values < 0.5°, which is below the resolution of the EBSD technique. High-angular resolution EBSD could be used to improve the resolution of these measurements, and allow for a more robust and meaningful comparison of deformation across the samples.

4.4.3 Duration of experimental overpressurisation

We increased the pressure of our overpressured experiment (SHV01) from 120 MPa to 155 MPa on the final day, to match that of the high-pressure static sample. Despite these equal final pressures, we do not see a match in the misorientation profiles between these two experiments (SHV01 and SHV04). In fact, the overpressured sample displays misorientation profiles which are more similar to those seen in the low-pressure static experiment (SHV02), both of which were stored either wholly or partially at 120 MPa. From these results we can speculate that the timescale for our experimental set-up to impart crystal-plastic deformation must take longer than one day, otherwise we would expect to see a match between the profiles in the overpressured and high-pressure static samples. We investigate this further by calculating strain rates in plagioclase for a temperature of 840°C and a pressure of 155 MPa, which matches our experimental conditions for the final stages of the overpressured sample. We use equation 2 of Rybacki and Dresen (2000).

$$\dot{\varepsilon} = A\,\sigma^{n}\,d^{-m}\exp(-Q/RT) \qquad \text{(eq. 4.1)}$$

Where $\dot{\varepsilon}$ is strain rate (s^{-1}), A is a preexponential constant, σ is stress (MPa), n is the stress exponent, d is grain size (μm), m is the grain size exponent, Q is activation energy (kJ mol-1), R is the gas constant and T is temperature (K). For A, n, d, m and Q, we use values for dislocation creep of wet anorthite given in Table 2 of Rybacki and Dresen (2000). We use a stress of 155 MPa and a temperature range of 1073 -1173 K (800-900°C). The results of our calculations (**fig 4.19**) show that at 840°C and 155 MPa, the strain rate for plagioclase is 2.7 x 10^{-8} s^{-1}. Assuming a strain threshold of at least 0.01 in order to generate substructures (dislocations) would require an applied stress duration of 366,300 seconds, or 102 hours. We

therefore conclude that the duration of the pressure increase for the overpressured sample (SHV01) was likely not long enough to record deformation from this experimental process.

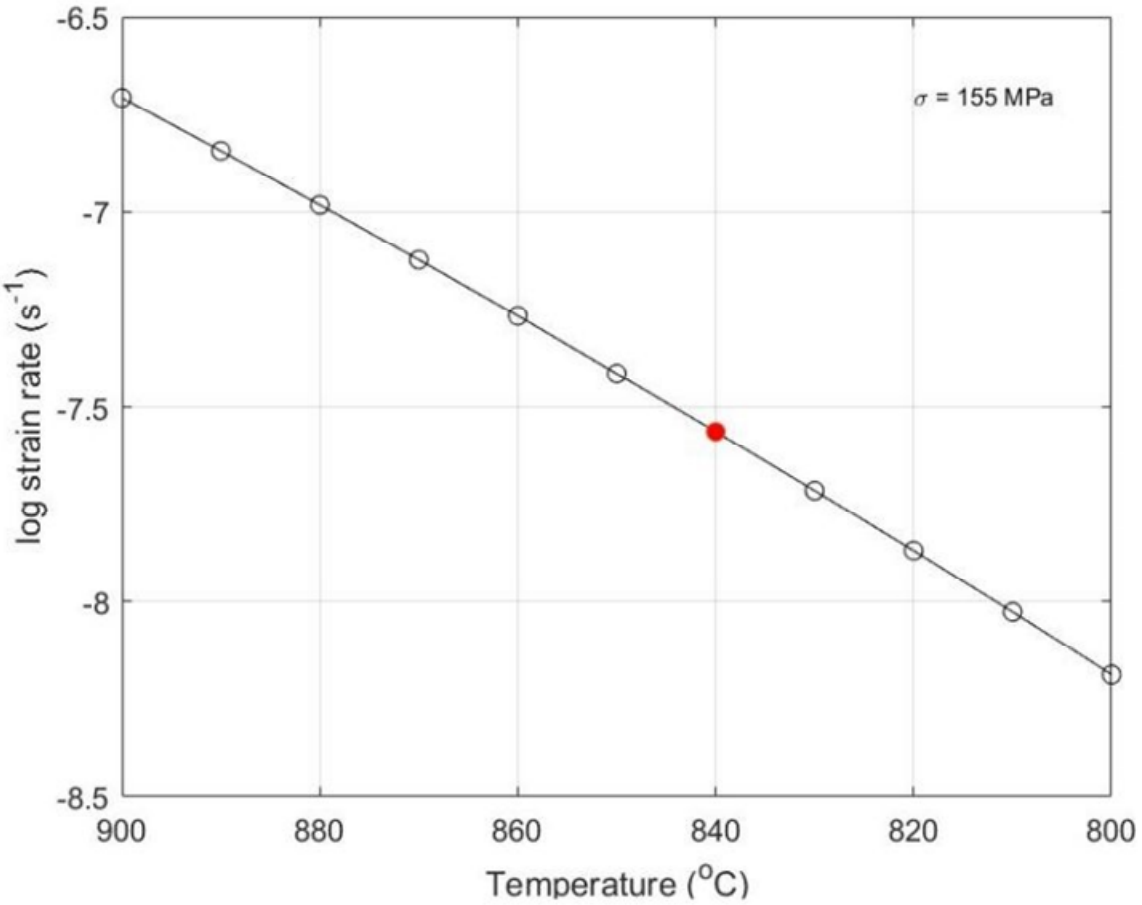


Figure 4.19. Strain rate generated by dislocation creep in wet plagioclase for varying temperatures, calculated from equation 2 of Rybacki and Dresen (2000). We use a preexponential constant (A) of 398.1, a stress exponent (n) of 3, a grain size (d) of 5, and a grain size exponent (m) of 0, all taken from Table 2 of Rybacki and Dresen (2000). We use a stress of 155 MPa, and a temperature range of 800 - 900°C (1073 - 1173 K). The red dot highlights that, at a pressure of 155 MPa and a temperature of 840°C, the strain rate is 2.7 x 10-8 s-1.

4.4.4 Effect of experimental quenching

The experimental quenching process could impart strain within the crystal lattice due to solidification upon cooling. Solidification of the melt and crystals upon quenching may result in varying rates of thermal contraction, which could result in the build-up of stresses, leading to localised crystal-plastic deformation. This deformation would then be recorded in our

measurements as excess misorientations across all of the experimental samples. We do not see excess misorientations in our experimental results, and so do not find any evidence that quenching process is contributing to deformation. Deformation is concentrated around crystal edges and at subgrain boundaries in the natural sample, as well as the experimental ones, so it is unlikely to be an effect of experimental quenching.

4.4.5 Effect of sample preparation

In addition to the methods already used here, band contrast can also be used to determine strain within a sample. Band contrast is a measure of the intensity of the Kikuchi bands which form the electron backscatter patterns - it does not directly measure misorientations with the crystal lattice, but instead evaluates the quality of the image. Higher band contrast values reflect higher intensity patterns, whilst low band contrast values indicate lower quality patterns. Low band contrast values may be due to strain within the crystal lattice, or to sample surface effects such as topography or polishing. **Figure 4.20** shows low band contrast values several pixels wide along the edges of grains in the natural and overpressured samples. This same effect is seen across all of the four samples, across grains of various scales and shapes. Whilst poorly prepared samples or topographic effects can result in low band contrast values, these factors are unlikely to impart deformation in the samples. When viewed in conjunction with the elevated KAM values at the grain edges, it is likely that the high band contrast values are an effect of real crystal distortion, rather than sample topography or polishing.

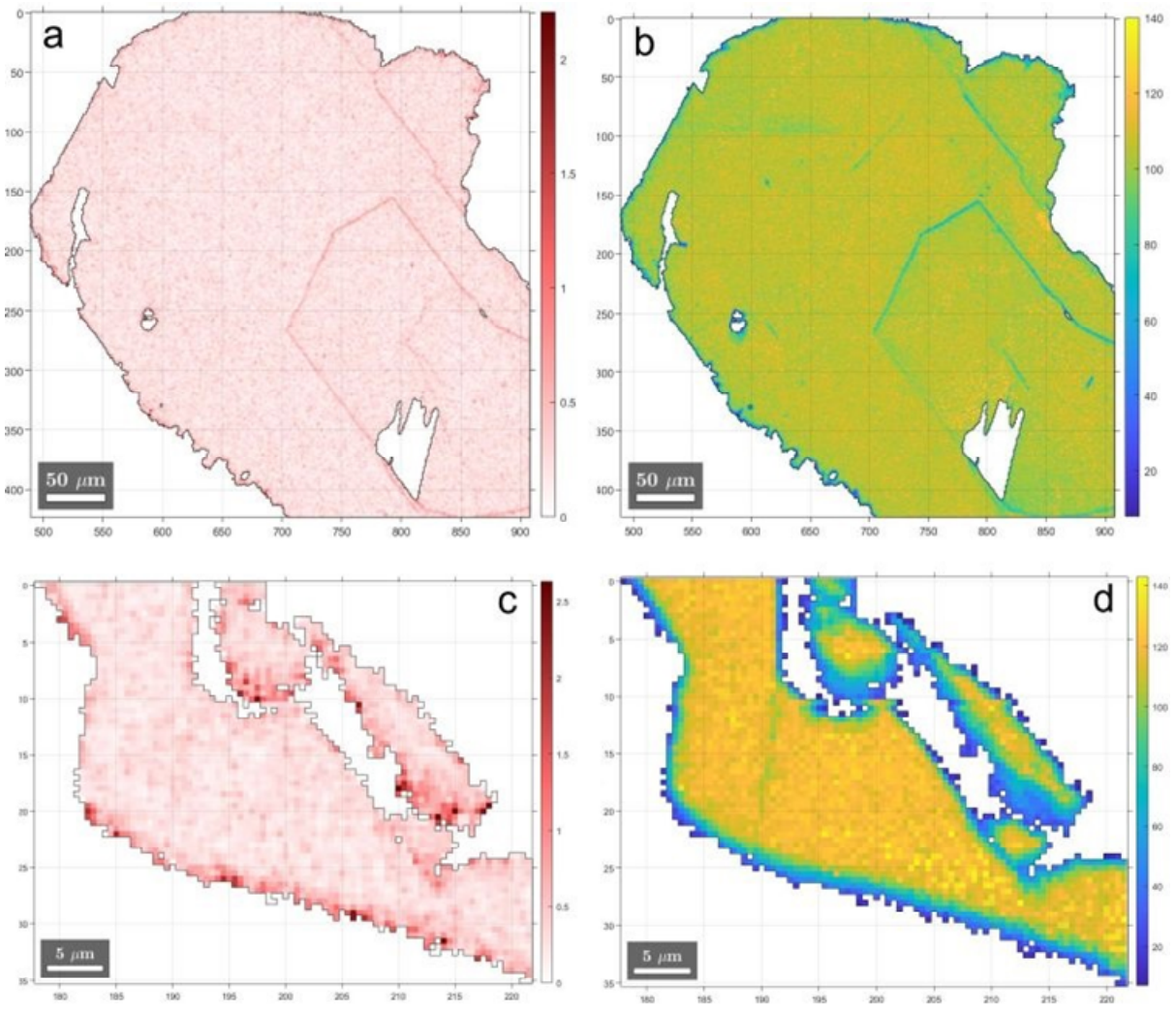


Figure 4.20. a) Kernel average misorientation map (°) for one anorthite grain within sample SHV_00. b) Band contrast map of the same grain shown in a). c) Kernel average misorientation map (°) for one anorthite grain within sample SHV_01. d) Band contrast map of the same grain shown in c). A threshold value of 3° was used to extract KAM.

4.4.6 Assigning deformation to magmatic processes

As noted in Befus *et al.* (2019), there are many mechanisms that can impart deformation within volcanic samples. These include stress redistribution from crystal-crystal contacts in the reservoir, magma fragmentation, and post eruption processes such as lava transport. Befus *et al.* (2019) measure elevated residual stresses in quartz crystals from a variety of eruptions and conclude that they reflect the brittle fragmentation threshold of magma during ascent, rather than deformation in the magma reservoir. Interestingly, some of these elevated stresses

are concentrated along the edges of quartz crystals (see Befus *et al.* (2019) supplementary material fig S9). However, the presence of stresses that are unrelated to crystal contacts, and those which occur away from the grain edges, leads the authors to conclude that the stresses were probably generated due to fragmentation, rather than deformation in a crystal-rich mush. At present we cannot rule out the possibility that the deformation in the natural sample could be due to brittle fragmentation during eruption, which the experimental samples then inherit from the starting material.

If crystal-plastic deformation does occur due to crystal-crystal interactions during magma storage, then we would potentially see higher misorientation values in areas of higher crystallinity, or where crystals are more densely-packed. We compare the number of neighbouring grains (**fig 4.21a**) with the subgrain boundary density per grain (**fig 4.21b**) for the experimentally overpressured sample. The number of neighbouring grains is calculated using the grain shape feature in Channel5 software. The subgrain boundary density is calculated in MTEX by dividing the total subgrain boundary length in each grain by the grain area. This analysis shows that the closely packed areas in SHV01 do have relatively high subgrain boundary densities. However, there are also some areas where the number of neighbouring grains is high, but subgrain boundary density is low. This may reflect the presence of 'spectator' grains within force chains, as identified by Bergantz *et al.* (2017). As magma crystallises, the number of crystal-crystal contacts is likely to increase, potentially leading to more deformation via crystal-crystal impingement. However, the increase in the number of crystal contacts will eventually result in a more even stress distribution, effectively lowering the stress at any given contact. Further analyses of deformation and crystal proximity in other volcanic samples would help to determine the role of crystal-crystal interaction in accommodating and recording stress within magmatic systems. We note that the misorientations measured in our samples may come from different mechanisms. The widespread 'edge' misorientations may be generated by magma fragmentation processes which occur during magma ascent. In contrast, the subgrain boundary misorientations may be

due to crystal-crystal interactions which result in local shear stresses within the mush during magma storage.

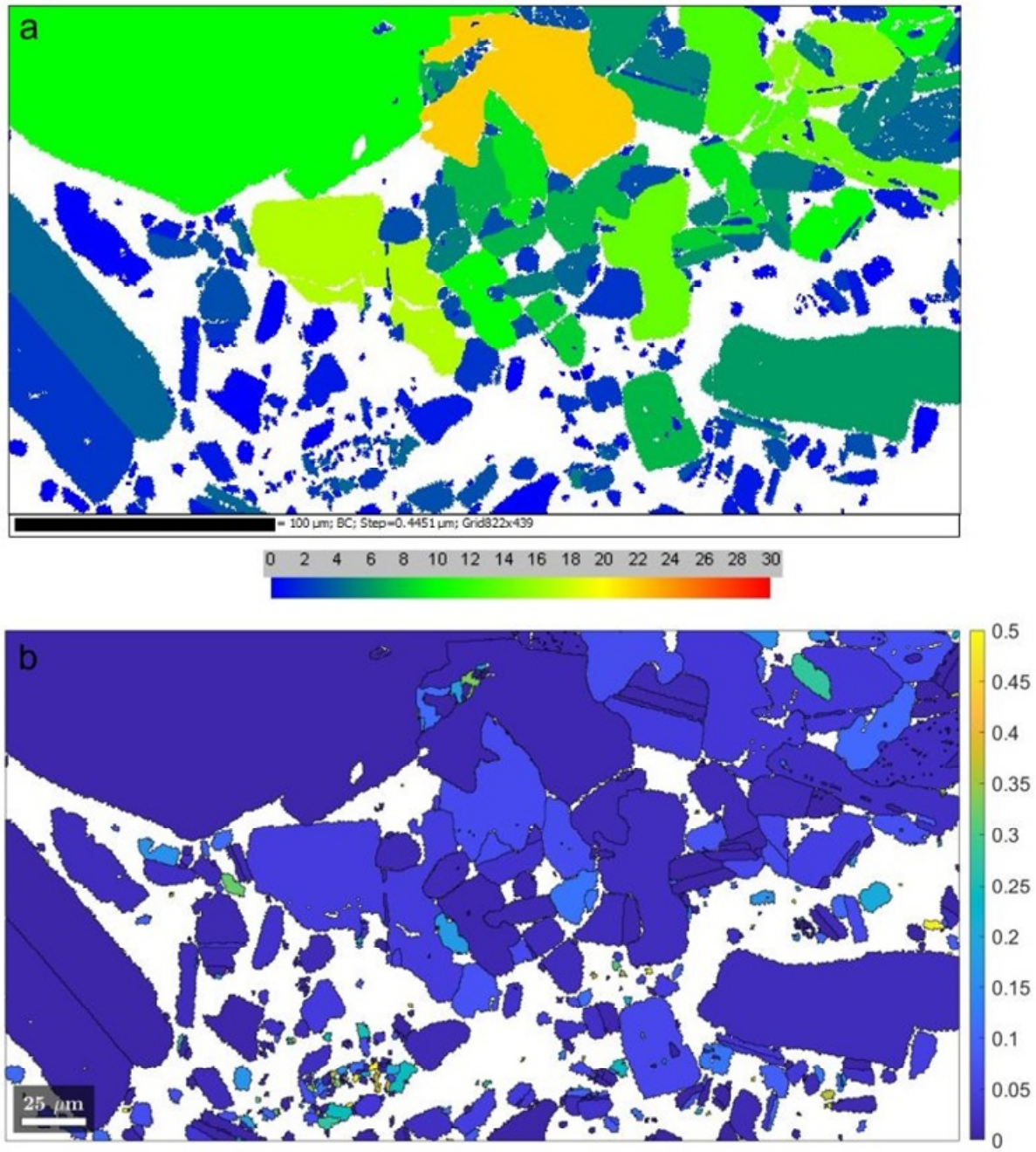


Figure 4.21. Comparison of crystal proximity and crystal deformation in sample SHV01. a) number of neighbouring grains per grain, b) subgrain boundary density per grain.

4.5. Future work

Although we do not find any significant variation in crystal deformation in our overpressured sample, this methodology could be applied to rocks from different volcanic systems, which have been stored at different conditions. Determining the extent to which crystal-plastic deformation occurs within the mush, and under what conditions, would enable us to move forwards with using EBSD to fingerprint the effects of magma overpressurisation during storage. Targeting high-crystallinity material from explosive volcanic eruptions would give us an understanding of the range of deformation that is possible, either due to stress transfer via the mush, crystal-crystal interactions, or both. We highlight the following research topics which would help to establish EBSD as an additional technique for determining pre-eruptive magma storage conditions.

4.5.1 Work on natural volcanic samples

- Map out crystal-plastic deformation within a variety of natural volcanic samples from different systems, focusing on the magnitude, extent and location of deformation. Determine whether misorientations are concentrated at crystal edges and subgrain boundaries in other volcanic systems, and determine whether misorientation angles are significantly different to the ones measured here. We chose samples from Soufrière Hills because of its well-constrained storage conditions and the fact that some overpressure estimates had already been made (see section 4.1) – all of which could inform the experimental set-up. However, our samples may have spent time residing in the conduit system prior to eruption, which could modify deformation signals from within the reservoir. Ideal samples to target next are those from explosive eruptions with rapid ascent rates, for example Izu-Oshima, Japan, and Taupo, New Zealand (see fig 5 of Cassidy *et al.* (2018) and associated references). Biotite crystals from the Youngest Toba Tuff deposits show kinked textures (Bunga Naen *et al.*, 2020) and these would also be good candidates for EBSD analysis.

- In conjunction with the point above, map out crystal-plastic deformation within exposed magmatic plutons and intrusions, for example the Mount Stuart batholith, USA, and the Torres del Paine intrusive complex, Chile. This would provide valuable information on the characteristics of crystal-plastic deformation within the reservoir, prior to any potential modification by magma ascent and eruption processes. There may be some relaxation of stress over the long time periods in which these intrusions solidify, so it would be interesting to focus on a range of intrusions of different sizes

- Further to these two points, it will be important to determine the degree to which strain imparted in the magma reservoir is modified by ascent and eruption. There are many mechanisms which can impart strain in volcanic rocks, making it difficult to categorically attribute deformation to pre-eruptive processes. These questions have been addressed by Befus *et al.* (2019), who use X-ray microdiffraction to show that preserved stresses in quartz crystals occur within pyroclastic fall, flow, and lava deposits, and so cannot be attributed to post-eruption processes. They propose a fragmentation origin for these stresses – but note that a magma reservoir origin is also possible.

- Geochemical mapping should also be incorporated into these analyses, so we can determine the extent to which compositional differences affect crystal-plastic deformation.

4.5.2 Work on experimentally deformed/ synthetic samples

- Quantify crystal-plastic deformation across samples of varying crystallinity, to test the hypothesis that crystal-crystal interactions within the magma generate deformation. A good starting point for this would be to use synthetic mush samples of varying crystallinity, such as those generated by Ryan *et al.* (2022). Although these quartz-based samples are not compositionally representative of most magma mush systems, they allow us to isolate

the effect of crystallinity on crystal deformation, and potentially to calibrate natural samples to certain crystallinity/ stress conditions.

- Use uniaxial deformation apparatus to systematically strain natural samples, and compare the microstructures from these samples to those deformed in hydrostatic apparatus. Pressurization within a magma reservoir can occur due to magma injection, thermal expansion, volatile exsolution or other mechanisms, and the way that this pressure is transferred through reservoirs of varying size, crystallinity and temperature is not well-understood.

- Determine the extent to which deformation is inherited from the natural starting material by performing experiments which heat the material above the liquidus and then cool it.

- Vary experimental temperature and pressure further to map out the conditions under which we expect to see crystal-plastic deformation in natural systems. This would help to determine the limits of the applicability of this technique as a strain marker for explosive volcanic products.

- If it is possible to experimentally replicate the microstructures seen in natural, deformed samples, then there is potential for EBSD to be used as a tool to estimate magma storage conditions from natural samples.

- For both natural and experimentally deformed samples, high-resolution EBSD (HR-EBSD) could be used to obtain greater precision in misorientation measurements. This would be particularly helpful in cases where misorientations are low (<1°), as the angular resolution of HR-EBSD is ~ 0.006°, around two orders of magnitude higher than conventional EBSD (Britton and Hickey, 2018).

Acknowledgements

We would like to thank Dr. Phani Karamched from the Materials Science Department at the University of Oxford for his assistance and expertise in using the SEM facility there. Thanks also to Dr Richard Walshaw from the University of Leeds, for collecting some of the EBSD data used in this project during the Covid lockdown.

Chapter 5 - Conclusions and future work

5.1 Conclusions

A summary of the key findings from each of the research chapters is summarised below.

Chapter 2: Magmatic volatile content and the overpressure 'sweet spot': implications for volcanic eruption triggering and style

- The capacity of magma to generate overpressure via second boiling is conditioned by its initial volatile content.
    - The highest overpressure is generated when magmatic water content is at the H_2O solubility limit. The additional or removal of H_2O results in a decrease in overpressure.
    - The overpressure generated by second boiling decreases as initial X_{H2O} decreases.
- Thermal modelling demonstrates that timescales of overpressurisation to critical levels (20 MPa) are shorter than those of crustal relaxation. This demonstrates the viability of second boiling as an eruption trigger, for the small, shallow reservoir considered here.
- The trend in overpressurisation with varying H_2O content broadly coincides with the trend in eruption style with varying H_2O content. We propose that these increased magmatic overpressures may contribute to faster ascent rates and more explosive eruptions.

Chapter 3: Constraining the magnitude and rate of internal magmatic overpressure build-up with varying magmatic parameters

- Thermal modelling demonstrates that variations in magmatic and crustal properties affect the time taken for average reservoir overpressure to reach critical levels.

    - Smaller, flatter reservoirs consistently pressurize to critical levels more rapidly than their larger, blocky counterparts.
    - Increasing magmatic X_{H2O} increases the rate of overpressurisation.
    - Increasing the thermal conductivity of the crust results in an increased rate of overpressurisation.
- Magmas which are initially H_2O undersaturated consistently take longer to reach critical overpressure levels than their counterparts with higher initial H_2O contents, because they undergo a period of average reservoir underpressurisation. However, these magmas also display the greatest rates of overpressurisation.
- This methodology can be extended to extract average reservoir values for other properties, such as crystallinity or viscosity, providing a snapshot of pre-eruptive magma dynamics which could be used as inputs to magma ascent models.

Chapter 4: Exploring crystal-plastic deformation in natural and experimentally-overpressurised magmas

- Novel analysis of explosive eruption products using electron backscatter diffraction reveals that crystal-plastic deformation is concentrated along crystal edges and at subgrain boundaries.
- The misorientation profile of our experimentally overpressured sample does not show a greater amount of deformation than the low-pressure static sample.
- However there is a good match between misorientation profiles in the natural and high-pressure static samples, suggesting that this method may be able to detect long-term storage conditions.

5.2 Future work

In chapters 2 and 3 we discuss the assumptions and limitations associated with linking two different models to characterise reservoir overpressurisation. In chapter 4 we suggest further analyses which naturally stem from our exploratory EBSD study. The section below summarises future avenues of research, and how they could advance our understanding of overpressurisation.

5.2.1 Coupling magma thermodynamics and crustal thermomechanics

A key limitation of our method for determining overpressurisation rate is that the Rhyolite-MELTS calculations assume a rigid surrounding crust, so do not account for the effect of a viscous crustal response on reservoir volume and overpressure. We consider the effect of a non-rigid crust by comparing timescales of overpressurisation to those of crustal relaxation. However, in reality the crust will relax incrementally, and this effect is not incorporated into our modelling. Thermomechanical models of reservoir pressurisation (for example Gregg *et al.* (2013)) have greatly enhanced our understanding of the effect of crustal viscosity on overpressure. However, a key limitation of these models is that they do not consider how deformation of the crust will affect the thermodynamics of the pressurising magma source. In particular, the effect of an expanding reservoir on total pressure and volatile solubility is not accounted for. Research which fully links the thermodynamic evolution of magma with the mechanics of crustal relaxation would be extremely helpful in improving our assessment of overpressure build-up. Such models could be developed using software such as COMSOL Multiphysics, or the newly released MagamFOAM (Brogi *et al.*, 2022), and would require collaboration between researchers focusing on thermodynamic properties of magma and those focusing on the mechanical properties of the crust.

5.2.2 Linking reservoir and conduit models

This study focuses on the properties of magma in storage, and how these affect overpressure and potentially eruption style. However, processes operating in the volcanic conduit – such as buoyancy, bubble coalescence, permeability development and crystallisation – are equally

important for determining eruption style. Pre-eruptive magma properties are essential inputs into ascent rate and conduit dynamics models. For example, Thomas and Neuberg (2014) model magma ascent in the conduit and determine that chamber overpressure and magmatic H_2O content have a strong, positive influence on ascent rate. Magma ascent models treat these variables as independent from one another, but our research shows that they are dependent – when considering second boiling as a trigger mechanism - as both the rate and magnitude of overpressurisation are conditioned by volatile content. Our method of extracting bulk magma properties at critical points in the evolution of the magmatic system could provide a linked set of magma properties which could be used as an input for conduit models. This would allow for a more accurate characterisation of ascent rate, which is an important part of eruption forecasting and determining eruption style.

5.2.3 Investigating magma storage with EBSD

Our exploratory study of crystal deformation can be seen as springboard for future work to assess EBSD as a tool for probing magma storage conditions. The most useful next step is to analyse natural samples from a range of explosive eruptions, to further characterise the extent and magnitude of crystal deformation. In tandem with this, analysis of deformation within magmatic intrusions would potentially help to isolate the effect of deformation imparted in the reservoir from that generated during magma ascent. Quantifying variations in crystal deformation with varying crystallinity would help assess the hypothesis that crystal-crystal impingement in mushy magma generates deformation, and that this may be linked to pressure conditions. This could use synthetic, experimental samples which span a range of pressure-temperature conditions, such as those of Ryan *et al.* (2022). Our results indicate that EBSD may be useful for recording reservoir pressure conditions, but it is unclear whether our hydrostatic experimental pressurisation set up can replicate overpressurisation. Measuring crystal deformation in experiments performed with uniaxial deformation apparatus is another obvious step, and may provide a more accurate representation of natural overpressurisation.

References

Albino, F., Amelung, F. and Gregg, P. (2018) 'The Role of Pore Fluid Pressure on the Failure of Magma Reservoirs: Insights From Indonesian and Aleutian Arc Volcanoes', *Journal of Geophysical Research: Solid Earth*, 123(2). doi: 10.1002/2017JB014523.

Albino, F., Biggs, J. and Syahbana, D. K. (2019) 'Dyke intrusion between neighbouring arc volcanoes responsible for 2017 pre-eruptive seismic swarm at Agung', *Nature Communications*, 10(1). doi: 10.1038/s41467-019-08564-9.

Albright, J. A. *et al.* (2019) 'Hindcasting Magma Reservoir Stability Preceding the 2008 Eruption of Okmok, Alaska', *Geophysical Research Letters*, 46(15). doi: 10.1029/2019GL083395.

Annen, C. *et al.* (2015) 'Construction and evolution of igneous bodies: Towards an integrated perspective of crustal magmatism', *Lithos*. doi: 10.1016/j.lithos.2015.05.008.

Annen, C. and Burgisser, A. (2021) 'Modeling water exsolution from a growing and solidifying felsic magma body', *Lithos*, 402–403. doi: 10.1016/j.lithos.2020.105799.

Annen, C., Pinel, V. and Burgisser, A. (2023) 'Re-evaluation of the role of volatiles in the rupture of magma chambers and the triggering of crystal-rich eruptions', *Journal of Volcanology and Geothermal Research*, 435. doi: 10.1016/j.jvolgeores.2023.107755.

Arzilli, F. *et al.* (2019) 'The unexpected explosive sub-Plinian eruption of Calbuco volcano (22–23 April 2015; southern Chile): Triggering mechanism implications', *Journal of Volcanology and Geothermal Research*, 378. doi: 10.1016/j.jvolgeores.2019.04.006.

Bachmann, F., Hielscher, R. and Schaeben, H. (2011) 'Grain detection from 2d and 3d EBSD data-Specification of the MTEX algorithm', *Ultramicroscopy*, 111(12). doi: 10.1016/j.ultramic.2011.08.002.

Barclay, J. *et al.* (1998) 'Experimental phase equilibria constraints on pre-eruptive storage conditions of the Soufriere Hills magma', *Geophysical Research Letters*. doi: 10.1029/98GL00856.

Barclay, J. *et al.* (2010) 'Caught in the act: Implications for the increasing abundance of mafic enclaves during the recent eruptive episodes of the Soufrière Hills Volcano, Montserrat', *Geophysical Research Letters*, 37(19). doi: 10.1029/2010gl042509.

Bato, M. G., Pinel, V. and Yan, Y. (2017) 'Assimilation of Deformation Data for Eruption Forecasting: Potentiality Assessment Based on Synthetic Cases', *Frontiers in Earth Science*, 5. doi: 10.3389/feart.2017.00048.

Befus, K. S. *et al.* (2019) 'Supervolcanoes erupt stressed quartz crystals', *Geophysical Research Letters*. doi: 10.1029/2019GL083619.

Bergantz, G. W., Schleicher, J. M. and Burgisser, A. (2017) 'On the kinematics and dynamics of crystal-rich systems', *Journal of Geophysical Research: Solid Earth*. doi: 10.1002/2017JB014218.

Bertolett, E. M. *et al.* (2019) 'Compacted cumulates revealed by electron backscatter diffraction analysis of plutonic lithics', *Geology*. doi: 10.1130/G45616.1.

Blake, S. (1984) 'Volatile oversaturation during the evolution of silicic magma chambers as an eruption trigger.', *Journal of Geophysical Research*, 89(B10). doi: 10.1029/JB089iB10p08237.

Boulanger, M. *et al.* (2021) 'Magma-Mush Interactions in the Lower Oceanic Crust: Insights From Atlantis Bank Layered Series (Southwest Indian Ridge)', *Journal of Geophysical Research: Solid Earth*, 126(9). doi: 10.1029/2021JB022331.

Britton, T. B. and Hickey, J. L. R. (2018) 'Understanding deformation with high angular resolution electron backscatter diffraction (HR-EBSD)', *IOP Conference Series: Materials Science and Engineering*, 304(1). doi: 10.1088/1757-899X/304/1/012003.

Brogi, F. *et al.* (2022) 'MagmaFOAM-1.0: A modular framework for the simulation of magmatic systems', *Geoscientific Model Development*, 15(9). doi: 10.5194/gmd-15-3773-2022.

Bunga Naen, G. N. R. *et al.* (2020) 'The Youngest Toba Tuff Crystals Characterization', in *European Geoscience Union*, p. 21. Available at: https://presentations.copernicus.org/EGU2020/EGU2020-6694_presentation.pdf.

Burgisser, A. *et al.* (2019) 'Conduit processes during the February 11, 2010 Vulcanian eruption of Soufrière Hills, Montserrat', *Journal of Volcanology and Geothermal Research*. Elsevier B.V., 373, pp. 23–35. doi: 10.1016/j.jvolgeores.2019.01.020.

Cabaniss, H. E. *et al.* (2020) 'Triggering of eruptions at Axial Seamount, Juan de Fuca Ridge', *Scientific Reports*, 10(1). doi: 10.1038/s41598-020-67043-0.

Cañón-Tapia, E. (2014) ‘Volcanic eruption triggers: A hierarchical classification’, *Earth-Science Reviews*, 129, pp. 100–119. doi: 10.1016/j.earscirev.2013.11.011.

Caricchi, L. *et al.* (2014) ‘Frequency and magnitude of volcanic eruptions controlled by magma injection and buoyancy’, *Nature Geoscience*, 7(2), pp. 126–130. doi: 10.1038/ngeo2041.

Caricchi, L. *et al.* (2021) ‘The build-up and triggers of volcanic eruptions’, *Nature Reviews Earth and Environment*. doi: 10.1038/s43017-021-00174-8.

Caricchi, L., Sheldrake, T. E. and Blundy, J. (2018) ‘Modulation of magmatic processes by CO2 flushing’, *Earth and Planetary Science Letters*, 491. doi: 10.1016/j.epsl.2018.03.042.

Cashman, K. V. (2004) ‘Volatile controls on magma ascent and eruption’, in *The State of the Planet: Frontiers and Challenges in Geophysics. Geophysical Monograph Series*. International Union of Geodesy and Geophysics and the American Geophysical Union. doi: 10.1029/150GM10.

Cassidy, M. *et al.* (2016) ‘Volatile dilution during magma injections and implications for volcano explosivity’, *Geology*, 44(12). doi: 10.1130/G38411.1.

Cassidy, M. *et al.* (2018) ‘Controls on explosive-effusive volcanic eruption styles’, *Nat. Commun.*, 9(1). doi: 10.1038/s41467-018-05293-3.

Cassidy, M. *et al.* (2019) ‘Explosive Eruptions With Little Warning: Experimental Petrology and Volcano Monitoring Observations From the 2014 Eruption of Kelud, Indonesia’, *Geochemistry, Geophysics, Geosystems*. doi: 10.1029/2018gc008161.

Cooper, K. M. and Kent, A. J. R. (2014) ‘Rapid remobilization of magmatic crystals kept in cold storage’, *Nature*, 506(7489), pp. 480–483. doi: 10.1038/nature12991.

Degruyter, W. *et al.* (2016) ‘Magma reservoir response to transient recharge events: The case of Santorini volcano (Greece)’, *Geology*. GeoScienceWorld, 44(1), pp. 23–26. doi: 10.1130/G37333.1.

Degruyter, W. *et al.* (2017) ‘Influence of Exsolved Volatiles on Reheating Silicic Magmas by Recharge and Consequences for Eruptive Style at Volcán Quizapu (Chile)’, *Geochemistry, Geophysics, Geosystems*, 18(11). doi: 10.1002/2017GC007219.

Degruyter, W. and Huber, C. (2014) ‘A model for eruption frequency of upper crustal silicic magma chambers’, *Earth and Planetary Science Letters*, 403. doi: 10.1016/j.epsl.2014.06.047.

Folch, A. and Martí, J. (1998) ‘The generation of overpressure in felsic magma chambers by replenishment’, *Earth and Planetary Science Letters*, 163(1–4). doi: 10.1016/S0012-821X(98)00196-4.

Geshi, N., Browning, J. and Kusumoto, S. (2020) ‘Magmatic overpressures, volatile exsolution and potential explosivity of fissure eruptions inferred via dike aspect ratios’, *Scientific Reports*, 10(1). doi: 10.1038/s41598-020-66226-z.

Ghiorso, M. S. and Gualda, G. A. R. (2015) ‘An H2O–CO2 mixed fluid saturation model compatible with rhyolite-MELTS’, *Contributions to Mineralogy and Petrology*, 169(6). doi: 10.1007/s00410-015-1141-8.

Girona, T., Costa, F. and Schubert, G. (2015) ‘Degassing during quiescence as a trigger of magma ascent and volcanic eruptions’, *Scientific Reports*, 5. doi: 10.1038/srep18212.

Gleeson, M. L. M. *et al.* (2017) ‘Constraining magma storage conditions at a restless volcano in the Main Ethiopian Rift using phase equilibria models’, *Journal of Volcanology and Geothermal Research*, 337. doi: 10.1016/j.jvolgeores.2017.02.026.

Gonnermann, H. M. and Manga, M. (2012) ‘Dynamics of magma ascent in the volcanic conduit’, in Fagents, S. A., Gregg, T. K. P., and Lopes, R. M. C. (eds) *Modeling Volcanic Processes: The Physics and Mathematics of Volcanism*. Cambridge University Press. doi: 10.1017/CBO9781139021562.004.

Gottsmann, J. and Odbert, H. (2014) ‘The effects of thermomechanical heterogeneities in island arc crust on time-dependent preeruptive stresses and the failure of an andesitic reservoir’, *Journal of Geophysical Research: Solid Earth*, 119(6), pp. 4626–4639. doi: 10.1002/2014JB011079.

Gregg, P. M. *et al.* (2012) ‘Catastrophic caldera-forming eruptions: Thermomechanics and implications for eruption triggering and maximum caldera dimensions on Earth’, *Journal of Volcanology and Geothermal Research*, 241–242. doi: 10.1016/j.jvolgeores.2012.06.009.

Gregg, P. M., Grosfils, E. B. and de Silva, S. L. (2015) ‘Catastrophic caldera-forming eruptions II: The subordinate role of magma buoyancy as an eruption trigger’, *Journal of Volcanology and Geothermal Research*, 305. doi: 10.1016/j.jvolgeores.2015.09.022.

Gregg, P. M., de Silva, S. L. and Grosfils, E. B. (2013) ‘Thermomechanics of shallow magma chamber

pressurization: Implications for the assessment of ground deformation data at active volcanoes', *Earth and Planetary Science Letters*. doi: 10.1016/j.epsl.2013.09.040.

Grosfils, E. B. (2007) 'Magma reservoir failure on the terrestrial planets: Assessing the importance of gravitational loading in simple elastic models', *Journal of Volcanology and Geothermal Research*. doi: 10.1016/j.jvolgeores.2007.06.007.

Grosfils, E. B. *et al.* (2015) 'Elastic models of magma reservoir mechanics: A key tool for investigating planetary volcanism', *Geological Society Special Publication*, 401. doi: 10.1144/SP401.2.

Gualda, G. A. R. *et al.* (2012) 'Rhyolite-MELTS: A modified calibration of MELTS optimized for silica-rich, fluid-bearing magmatic systems', *Journal of Petrology*, 53(5). doi: 10.1093/petrology/egr080.

Gualda, G. A. R. and Ghiorso, M. S. (2015) 'MELTS_Excel: A Microsoft Excel-based MELTS interface for research and teaching of magma properties and evolution', pp. 315–324. doi: 10.1002/2014GC005545.Received.

Gudmundsson, A. (1983) 'Form and dimensions of dykes in eastern Iceland', *Tectonophysics*, 95, pp. 295–307.

Gudmundsson, A. (2011) *Rock Fractures in Geological Processes*, *Rock Fractures in Geological Processes*. doi: 10.1017/cbo9780511975684.

Gudmundsson, A. (2012) 'Magma chambers: Formation, local stresses, excess pressures, and compartments', *Journal of Volcanology and Geothermal Research*. Elsevier B.V., 237–238, pp. 19–41. doi: 10.1016/j.jvolgeores.2012.05.015.

Hall, R. (2002) 'SE Asian Heatflow: call for new data', *IPA newsletter*. Available at: http://searg.rhul.ac.uk/searg_uploads/2015/01/hf.pdf.

Hautmann, S. *et al.* (2009) 'Modelling ground deformation caused by oscillating overpressure in a dyke conduit at Soufrière Hills Volcano, Montserrat', *Tectonophysics*, 471(1–2). doi: 10.1016/j.tecto.2008.10.021.

Hautmann, S. *et al.* (2010) 'Effect of mechanical heterogeneity in arc crust on volcano deformation with application to Soufrière Hills Volcano, Montserrat, West Indies', *Journal of Geophysical Research: Solid Earth*, 115(9). doi: 10.1029/2009JB006909.

Hautmann, S. *et al.* (2014) ‘Strain field analysis on Montserrat (W.I.) as tool for assessing permeable flow paths in the magmatic system of Soufrière Hills Volcano’, *Geochemistry, Geophysics, Geosystems*. John Wiley & Sons, Ltd, 15(3), pp. 676–690. doi: 10.1002/2013GC005087.

Head, M. *et al.* (2019) ‘The Influence of Viscoelastic Crustal Rheologies on Volcanic Ground Deformation: Insights From Models of Pressure and Volume Change’, *Journal of Geophysical Research: Solid Earth*, 124(8). doi: 10.1029/2019JB017832.

Head, M. *et al.* (2022) ‘Rheological Controls on Magma Reservoir Failure in a Thermo-Viscoelastic Crust’, *Journal of Geophysical Research: Solid Earth*, 127(7). doi: 10.1029/2021JB023439.

Heap, M. J. *et al.* (2020) ‘Towards more realistic values of elastic moduli for volcano modelling’, *Journal of Volcanology and Geothermal Research*, 390(xxxx), pp. 1–32. doi: 10.1016/j.jvolgeores.2019.106684.

Heap, M. J. *et al.* (2022) ‘The tensile strength of hydrothermally altered volcanic rocks’, *Journal of Volcanology and Geothermal Research*. Elsevier B.V., 428(January), p. 107576. doi: 10.1016/j.jvolgeores.2022.107576.

Huppert, H. E. and Woods, A. W. (2002) ‘The role of volatiles in magma chamber dynamics’, *Nature*. Nature Publishing Group, 420(6915), pp. 493–495. doi: 10.1038/nature01211.

Jaupart, C. and Allègre, C. J. (1991) ‘Gas content, eruption rate and instabilities of eruption regime in silicic volcanoes’, *Earth and Planetary Science Letters*, 102(3–4). doi: 10.1016/0012-821X(91)90032-D.

Jeffery, A. J. *et al.* (2013) ‘The pre-eruptive magma plumbing system of the 2007-2008 dome-forming eruption of Kelut volcano, East Java, Indonesia’, *Contributions to Mineralogy and Petrology*, 166(1). doi: 10.1007/s00410-013-0875-4.

Jellinek, A. M. and DePaolo, D. J. (2003) ‘A model for the origin of large silicic magma chambers: Precursors of caldera-forming eruptions’, *Bulletin of Volcanology*. doi: 10.1007/s00445-003-0277-y.

Kelly, L. J. *et al.* (2021) ‘Hydrothermal Cooling as a Requirement for Short Storage of Silicic Magmas’, *Geochemistry, Geophysics, Geosystems*, 22(9). doi: 10.1029/2021GC009794.

Kendrick, J. E. *et al.* (2017) ‘Crystal plasticity as an indicator of the viscous-brittle transition in

magmas', *Nature Communications*. Springer US, 8(1), pp. 1–12. doi: 10.1038/s41467-017-01931-4.

Kent, A. J. R. *et al.* (2007) 'Vapor transfer prior to the October 2004 eruption of Mount St. Helens, Washington', *Geology*, 35(3). doi: 10.1130/G22809A.1.

Kent, A. J., Till, C. B. and Cooper, K. M. (2021) 'Studying the initiation of volcanic eruptions: Time for a petrologic perspective', *Nature geoscience (in review)*.

Kilbride, B. M. C., Edmonds, M. and Biggs, J. (2016) 'Observing eruptions of gas-rich compressible magmas from space', *Nature Communications*. Nature Publishing Group, 7, pp. 1–8. doi: 10.1038/ncomms13744.

Klein, J., Mueller, S. P. and Castro, J. M. (2017) 'The Influence of Crystal Size Distributions on the Rheology of Magmas: New Insights From Analog Experiments', *Geochemistry, Geophysics, Geosystems*, 18(11). doi: 10.1002/2017GC007114.

Lisowski, M. (2007) 'Analytical volcano deformation source models', in *Volcano Deformation*. Springer Praxis Books., pp. 279–304.

Maeno, F. *et al.* (2019) 'A sequence of a plinian eruption preceded by dome destruction at Kelud volcano, Indonesia, on February 13, 2014, revealed from tephra fallout and pyroclastic density current deposits', *Journal of Volcanology and Geothermal Research*, 382. doi: 10.1016/j.jvolgeores.2017.03.002.

Masterlark, T. *et al.* (2010) 'Rheologic and structural controls on the deformation of Okmok volcano, Alaska: FEMs, InSAR, and ambient noise tomography', *Journal of Geophysical Research: Solid Earth*, 115, pp. 1–22. doi: 10.1029/2009JB006324.

McNamara, D. D., Lister, A. and Prior, D. J. (2016) 'Calcite sealing in a fractured geothermal reservoir: Insights from combined EBSD and chemistry mapping', *Journal of Volcanology and Geothermal Research*, 323. doi: 10.1016/j.jvolgeores.2016.04.042.

McTigue, D. F. (1987) 'Elastic stress and deformation near a finite spherical magma body: Resolution of the point source paradox', *Journal of Geophysical Research*, 92(B12), p. 12931. doi: 10.1029/jb092ib12p12931.

Melnik, O. and Sparks, R. S. J. (1999) 'Nonlinear dynamics of lava dome extrusion', *Nature*,

402(6757), pp. 37–41. doi: 10.1038/46950.

Melnik, O. and Sparks, R. S. J. (2002) ‘Dynamics of magma ascent and lava extrusion at Soufrière Hills Volcano, Montserrat’, *Geological Society Memoir*. doi: 10.1144/GSL.MEM.2002.021.01.07.

Mittal, T. and Richards, M. A. (2019) ‘Volatile Degassing From Magma Chambers as a Control on Volcanic Eruptions’, *Journal of Geophysical Research: Solid Earth*, 124(8). doi: 10.1029/2018JB016983.

Mittal, T. and Richards, M. A. (2021) ‘The Magmatic Architecture of Continental Flood Basalts: 2. A New Conceptual Model’, *Journal of Geophysical Research: Solid Earth*, 126(12). doi: 10.1029/2021JB021807.

Mogi, K. (1958) ‘Relations between the eruptions of various volcanoes and the deformations of the ground surfaces around them’, *Bulletin of the Earthquake Research Institute*. doi: 10.1016/j.epsl.2004.04.016.

Morales Rivera, A. M. *et al.* (2019) ‘Impact of Crustal Rheology on Temperature-Dependent Viscoelastic Models of Volcano Deformation: Application to Taal Volcano, Philippines’, *Journal of Geophysical Research: Solid Earth*. doi: 10.1029/2018JB016054.

Morgavi, D. *et al.* (2019) ‘Magma Mixing: History and Dynamics of an Eruption Trigger’, in *Advances in Volcanology*. doi: 10.1007/11157_2017_30.

Mullet, B. and Segall, P. (2022) ‘The Surface Deformation Signature of a Transcrustal, Crystal Mush-Dominant Magma System’, *Journal of Geophysical Research: Solid Earth*, 127(5). doi: 10.1029/2022JB024178.

Murphy, M. *et al.* (2000) ‘Remobilization of Andesite Magma by Intrusion of Mafic Magma at the Soufriere Hills Volcano, Montserrat, West Indies’, *Journal of Petrology*, 41(41), pp. 21–42.

Del Negro, C., Currenti, G. and Scandura, D. (2009) ‘Temperature-dependent viscoelastic modeling of ground deformation: Application to Etna volcano during the 1993-1997 inflation period’, *Physics of the Earth and Planetary Interiors*, 172(3–4). doi: 10.1016/j.pepi.2008.10.019.

Odbert, H. M., Ryan, G. A., *et al.* (2014) ‘Chapter 11 Volcano geodesy at the Soufrière Hills Volcano, Montserrat: a review’, *Geological Society, London, Memoirs*, 39(1), pp. 195–217. doi:

10.1144/m39.11.

Odbert, H. M., Stewart, R. C. and Wadge, G. (2014) ‘Chapter 2 Cyclic phenomena at the Soufrière Hills Volcano, Montserrat’, in *Geological Society Memoir*, pp. 41–60. doi: 10.1144/M39.2.

Okumura, S. *et al.* (2019) ‘Caldera-forming eruptions of mushy magma modulated by feedbacks between ascent rate, gas retention/loss and bubble/crystal framework interaction’, *Scientific Reports*. Nature Publishing Group, 9(1). doi: 10.1038/S41598-019-52272-9.

Papale, P., Neri, A. and MacEdonio, G. (1998) ‘The role of magma composition and water content in explosive eruptions. 1. Conduit ascent dynamics’, *Journal of Volcanology and Geothermal Research*, 87(1–4). doi: 10.1016/S0377-0273(98)00101-2.

Parfitt, E. A., Wilson, L. and Head, J. W. (1993) ‘Basaltic magma reservoirs: factors controlling their rupture characteristics and evolution’, *Journal of Volcanology and Geothermal Research*, 55(1–2). doi: 10.1016/0377-0273(93)90086-7.

Parmigiani, A. *et al.* (2016) ‘Bubble accumulation and its role in the evolution of magma reservoirs in the upper crust’, *Nature*, 532(7600). doi: 10.1038/nature17401.

Parmigiani, A. *et al.* (2017) ‘The mechanics of shallow magma reservoir outgassing’, *Geochemistry, Geophysics, Geosystems*, 18(8). doi: 10.1002/2017GC006912.

Paulatto, M. *et al.* (2022) ‘Advances in seismic imaging of magma and crystal mush’, *Frontiers in Earth Science*, 10(October), pp. 1–31. doi: 10.3389/feart.2022.970131.

Peacock, D. C. P. *et al.* (2017) ‘The interdisciplinary use of “overpressure”’, *Journal of Volcanology and Geothermal Research*, 341, pp. 1–5. doi: 10.1016/j.jvolgeores.2017.05.005.

Petrelli, M. *et al.* (2023) ‘Pre-eruptive dynamics at the Campi Flegrei Caldera: from Evidence of Magma Mixing to timescales estimates’, *Earth, Planets and Space*. Springer Berlin Heidelberg. doi: 10.1186/s40623-023-01765-z.

Pollard, D. D. (1987) ‘Elementary fracture mechanics applied to the structural interpretation of dykes’, in Halls, H. . . and Fahrig, W. . (eds) *Mafic dyke swarms*. 34th edn. Geological Association of Canada, pp. 5–24.

Popa, R. G. *et al.* (2019) ‘A connection between magma chamber processes and eruptive styles

revealed at Nisyros-Yali volcano (Greece)', *Journal of Volcanology and Geothermal Research*, 387. doi: 10.1016/j.jvolgeores.2019.106666.

Popa, R. G., Tollan, P., *et al.* (2021) 'Water exsolution in the magma chamber favors effusive eruptions: Application of Cl-F partitioning behavior at the Nisyros-Yali volcanic area', *Chemical Geology*, 570. doi: 10.1016/j.chemgeo.2021.120170.

Popa, R. G., Bachmann, O. and Huber, C. (2021) 'Explosive or effusive style of volcanic eruption determined by magma storage conditions', *Nature Geoscience*. Springer US, 14(10), pp. 781–786. doi: 10.1038/s41561-021-00827-9.

Pyle, D. M. and Pyle, D. L. (1995) 'Bubble migration and the initiation of volcanic eruptions', *Journal of Volcanology and Geothermal Research*, 67(4). doi: 10.1016/0377-0273(94)00111-S.

Rasmussen, D. J. *et al.* (2022) 'Magmatic water content controls the pre-eruptive depth of arc magmas', *Science*, 375(6585). doi: 10.1126/science.abm5174.

Rivalta, E. and Segall, P. (2008) 'Magma compressibility and the missing source for some dike intrusions', *Geophysical Research Letters*, 35(4). doi: 10.1029/2007GL032521.

Rubin, A. M. (1995a) 'Getting granite dikes out of the source region', *Journal of Geophysical Research*. doi: 10.1029/94JB02942.

Rubin, A. M. (1995b) 'Propagation of magma-filled cracks', *Annual Review of Earth & Planetary Sciences*, 23. doi: 10.1146/annurev.ea.23.050195.001443.

Ruprecht, P. and Bachmann, O. (2010) 'Pre-eruptive reheating during magma mixing at Quizapu volcano and the implications for the explosiveness of silicic arc volcanoes', *Geology*, 38(10). doi: 10.1130/G31110.1.

Rutherford, M. J. and Devine, J. D. (2003) 'Magmatic Conditions and Magma Ascent as Indicated by Hornblende Phase Equilibria and Reactions in the 1995-2002 Soufriere Hills Magma', *Journal of Petrology*. doi: 10.1093/petrology/44.8.1433.

Ryan, A. G. *et al.* (2022) 'Melt Migration in Crystal Mushes by Viscous Fingering: Insights From High-Temperature, High-Pressure Experiments', *Journal of Geophysical Research: Solid Earth*, 127(8), pp. 1–22. doi: 10.1029/2022JB024447.

Rybacki, E. and Dresen, G. (2000) ‘Dislocation and diffusion creep of synthetic anorthite aggregates’, *Journal of Geophysical Research: Solid Earth*, 105(B11). doi: 10.1029/2000jb900223.

Salzer, J. T. *et al.* (2014) ‘Satellite radar data reveal short-term pre-explosive displacements and a complex conduit system at Volcán de Colima, Mexico’, *Frontiers in Earth Science*. Frontiers Research Foundation, 2(Jun). doi: 10.3389/feart.2014.00012.

Segall, P. (2019) ‘Magma chambers: What we can, and cannot, learn from volcano geodesy’, *Philosophical Transactions of the Royal Society A: Mathematical, Physical and Engineering Sciences*. doi: 10.1098/rsta.2018.0158.

Seropian, G. *et al.* (2021) ‘A review framework of how earthquakes trigger volcanic eruptions’, *Nature Communications*. doi: 10.1038/s41467-021-21166-8.

Sigmundsson, F. *et al.* (2020) ‘Unexpected large eruptions from buoyant magma bodies within viscoelastic crust’, *Nature Communications*. Springer US, 11(1), pp. 1–11. doi: 10.1038/s41467-020-16054-6.

Smith, R., Sammonds, P. R. and Kilburn, C. R. J. (2009) ‘Fracturing of volcanic systems: Experimental insights into pre-eruptive conditions’, *Earth and Planetary Science Letters*, 280(1–4). doi: 10.1016/j.epsl.2009.01.032.

La Spina, G. *et al.* (2022) ‘Role of volatiles in highly explosive basaltic eruptions’, *Nature Communications: earth and environment*. Springer US, 3(156). doi: 10.1038/s43247-022-00479-6.

Stock, M. J. *et al.* (2016) ‘Late-stage volatile saturation as a potential trigger for explosive volcanic eruptions’, *Nature Geoscience*, 9(3). doi: 10.1038/ngeo2639.

Tait, S., Jaupart, C. and Vergniolle, S. (1989) ‘Pressure, gas content and eruption periodicity of a shallow, crystallising magma chamber’, *Earth and Planetary Science Letters*. doi: 10.1016/0012-821X(89)90025-3.

Thomas, M. E. and Neuberg, J. W. (2014) ‘Understanding which parameters control shallow ascent of silicic effusive magma’, *Geochemistry, Geophysics, Geosystems*, 15(11). doi: 10.1002/2014GC005529.

Townsend, M. *et al.* (2019) ‘Magma Chamber Growth During Intercaldera Periods: Insights From

Thermo-Mechanical Modeling With Applications to Laguna del Maule, Campi Flegrei, Santorini, and Aso', *Geochemistry, Geophysics, Geosystems*, 20(3). doi: 10.1029/2018GC008103.

Tramontano, S., Gualda, G. A. R. and Ghiorso, M. S. (2017) 'Internal triggering of volcanic eruptions: tracking overpressure regimes for giant magma bodies', *Earth and Planetary Science Letters*. Elsevier B.V., 472, pp. 142–151. doi: 10.1016/j.epsl.2017.05.014.

Trasatti, E. *et al.* (2019) 'Magma Degassing as a Source of Long-Term Seismicity at Volcanoes: The Ischia Island (Italy) Case', *Geophysical Research Letters*, 46(24). doi: 10.1029/2019GL085371.

Trasatti, E., Giunchi, C. and Bonafede, M. (2005) 'Structural and rheological constraints on source depth and overpressure estimates at the Campi Flegrei caldera, Italy', *Journal of Volcanology and Geothermal Research*. doi: 10.1016/j.jvolgeores.2004.11.019.

Troise, C. *et al.* (2019) 'The Campi Flegrei caldera unrest: Discriminating magma intrusions from hydrothermal effects and implications for possible evolution', *Earth-Science Reviews*. doi: 10.1016/j.earscirev.2018.11.007.

Wadge, G., Mattioli, G. S. and Herd, R. A. (2006) 'Ground deformation at Soufrière Hills Volcano, Montserrat during 1998-2000 measured by radar interferometry and GPS', *Journal of Volcanology and Geothermal Research*, 152(1–2). doi: 10.1016/j.jvolgeores.2005.11.007.

Wallace, P. A. *et al.* (2019) 'Petrological Architecture of a Magmatic Shear Zone: A Multidisciplinary Investigation of Strain Localisation During Magma Ascent at Unzen Volcano, Japan', *Journal of Petrology*. Oxford University Press (OUP), 60(4), pp. 791–826. doi: 10.1093/petrology/egz016.

Wallis, D. *et al.* (2019) 'High-Angular Resolution Electron Backscatter Diffraction as a New Tool for Mapping Lattice Distortion in Geological Minerals', *Journal of Geophysical Research: Solid Earth*, 124(7), pp. 6337–6358. doi: 10.1029/2019JB017867.

Wasser, V. K. *et al.* (2021) 'Multidisciplinary Constraints on Magma Compressibility, the Pre-Eruptive Exsolved Volatile Fraction, and the H2O/CO2 Molar Ratio for the 2006 Augustine Eruption, Alaska', *Geochemistry, Geophysics, Geosystems*, 22(9). doi: 10.1029/2021GC009911.

Weber, G., Simpson, G. and Caricchi, L. (2020) 'Magma diversity reflects recharge regime and thermal structure of the crust', *Scientific Reports*, 10(1). doi: 10.1038/s41598-020-68610-1.

White, S. M., Crisp, J. A. and Spera, F. J. (2006) ‘Long-term volumetric eruption rates and magma budgets’, *Geochemistry, Geophysics, Geosystems*, 7(3). doi: 10.1029/2005GC001002.

Whittington, A. G., Hofmeister, A. M. and Nabelek, P. I. (2009) ‘Temperature-dependent thermal diffusivity of the Earth’s crust and implications for magmatism’, *Nature*, 458(7236). doi: 10.1038/nature07818.

Wieser, P. E. *et al.* (2020) ‘Microstructural constraints on magmatic mushes under Kīlauea Volcano, Hawai‘i’, *Nature Communications*. doi: 10.1038/s41467-019-13635-y.

Wilkinson, A. J. (1996) ‘Measurement of elastic strains and small lattice rotations using electron back scatter diffraction’, *Ultramicroscopy*, 62(4). doi: 10.1016/0304-3991(95)00152-2.

Wilkinson, A. J. and Britton, T. Ben (2012) ‘Strains, planes, and EBSD in materials science’, *Materials Today*. doi: 10.1016/S1369-7021(12)70163-3.

Wilkinson, A. J., Meaden, G. and Dingley, D. J. (2006) ‘High-resolution elastic strain measurement from electron backscatter diffraction patterns: New levels of sensitivity’, *Ultramicroscopy*, 106(4–5). doi: 10.1016/j.ultramic.2005.10.001.

Woods, A. W. and Koyaguchi, T. (1994) ‘Transitions between explosive and effusive eruptions of silicic magmas’, *Nature*, 370(6491). doi: 10.1038/370641a0.

Woods, A. W. and Pyle, D. M. (1997) ‘The control of chamber geometry on triggering volcanic eruptions’, *Earth and Planetary Science Letters*, 151(3–4). doi: 10.1016/s0012-821x(97)81845-6.

Wright, S. I., Nowell, M. M. and Field, D. P. (2011) ‘A review of strain analysis using electron backscatter diffraction’, *Microscopy and Microanalysis*. doi: 10.1017/S1431927611000055.

Žák, J., Verner, K. and Týcová, P. (2008) ‘Grain-scale processes in actively deforming magma mushes: New insights from electron backscatter diffraction (EBSD) analysis of biotite schlieren in the Jizera granite, Bohemian Massif’, *Lithos*, 106(3–4). doi: 10.1016/j.lithos.2008.08.006.

Zhan, Y. and Gregg, P. M. (2019) ‘How Accurately Can We Model Magma Reservoir Failure With Uncertainties in Host Rock Rheology?’, *Journal of Geophysical Research: Solid Earth*, 124(8). doi: 10.1029/2019JB018178.

Appendices

Appendix 1: Rhyolite-MELTS P-T-composition table

Input parameters	Volcanic system			
	Nisyros-Yali	**Kelud**	**Mount St. Helens**	**Calbuco**
Starting composition type	Bulk rock pumice	Pumice	Bulk rock lava dome sample	Bulk rock scoria sample
Starting composition sample #	SL30	KLT-901	/	DF2A_ves
Starting composition reference	Popa *et al*. (2019)	Jeffery *et al*. (2013)	Pallister *et al.* (2008)	Arzilli *et al.* (2019)
Reservoir pressure (MPa)	160	100	130	230
Reservoir pressure reference	Popa *et al.* (2019)	Cassidy *et al.* (2019)	Rutherford and Devine (2008)	Arzilli *et al.* (2019)
~ Reservoir depth (km)	6 - 8	4	4 - 5	8
Temperature range (°C)	1300 - 700	1200 - 700	1200 - 700	1160 - 920
Temperature range reference	Popa *et al*. (2019)	Cassidy *et al*. (2019)	Rutherford and Devine (2008)	Namur *et al*. (2020)
Liquidus temp (°C) (for simulation at H_2O solubility)	892	1078	982	1052
H_2O solubility (at above temperature) (wt%)	5.4	3.4	4.5	5.9
Oxygen fugacity	NNO	NNO	NNO	NNO

Appendix 2: Rhyolite-MELTS composition plots

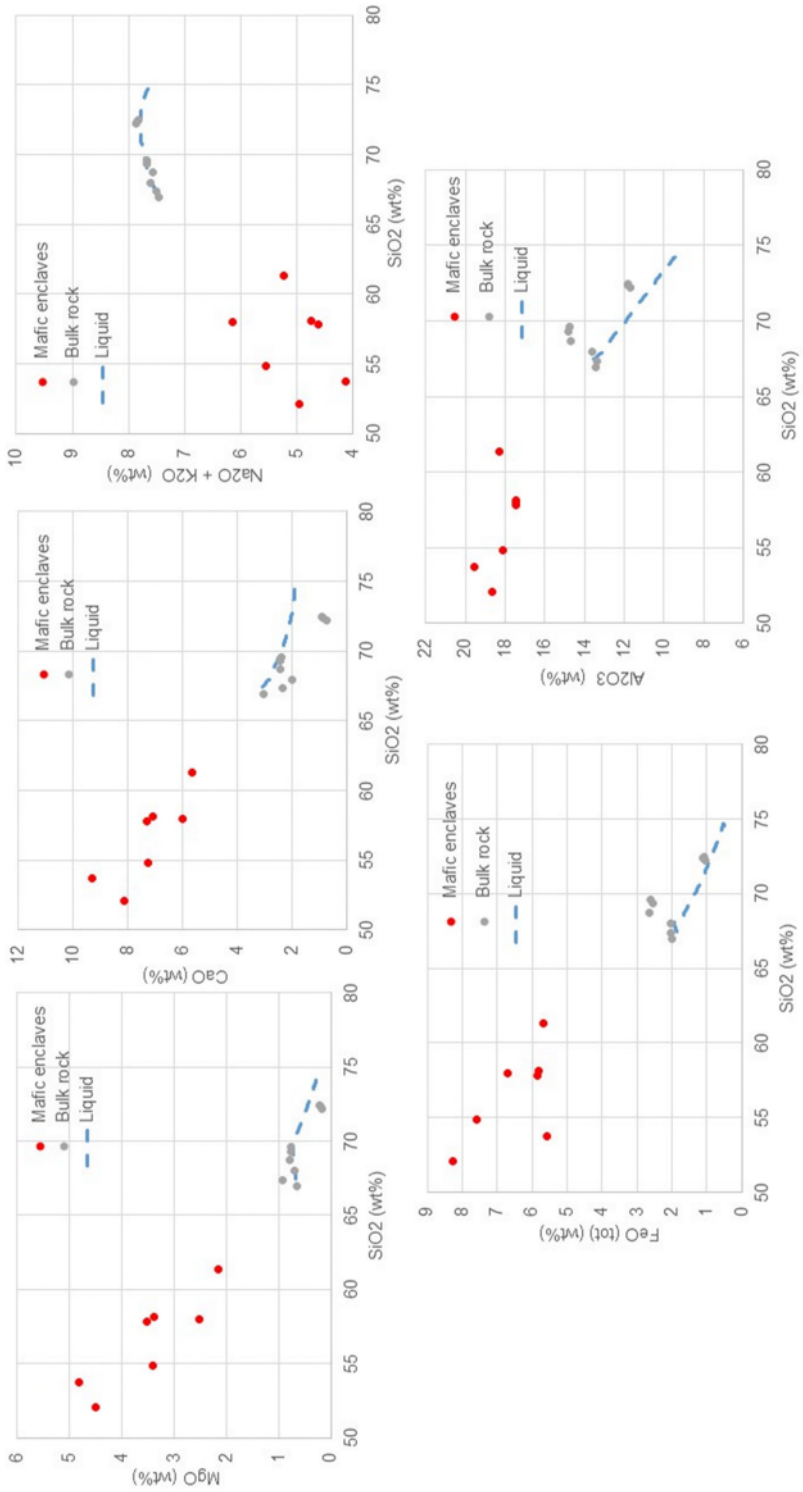


Figure A2a. Rhyolite-MELTS liquid composition plots (blue dashed line) for Nisyros-Yali, 5.4 wt% H_2O simulation, 160 MPa, shown in Figure 2.1a. Bulk rock data from Popa *et al*. (2019). Mafic enclave data from Klaver *et al*. (2017) and Popa *et al*. (2019).

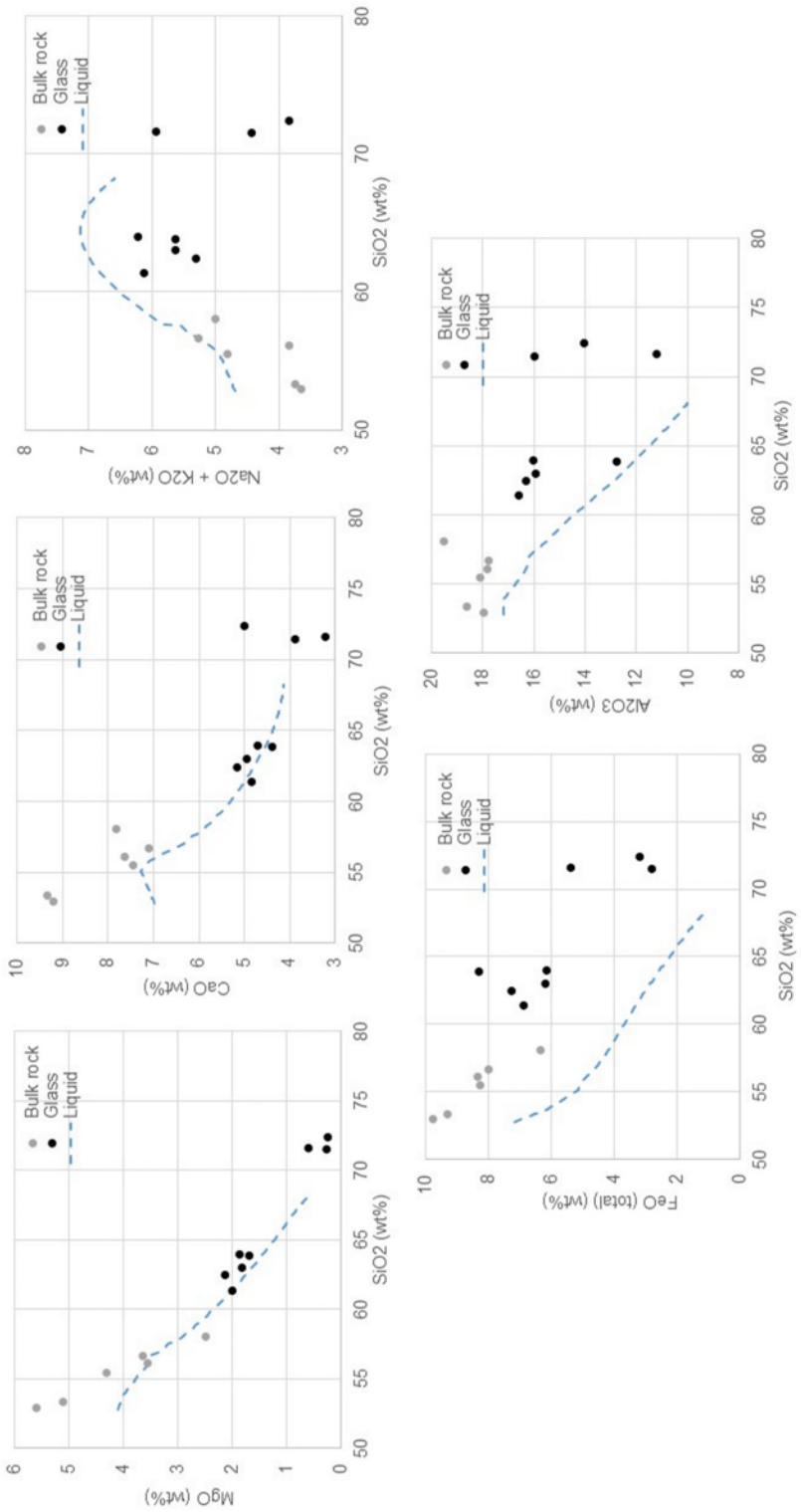


Figure A2b. Rhyolite-MELTS liquid composition plots (blue dashed line) for Calbuco, 5.9 wt% H_2O simulation, 230 MPa, shown in Figure 2.1b. Bulk rock data from Arzilli *et al* (2019) and Namur *et al* (2020). Glass composition from Namur *et al* (2020).

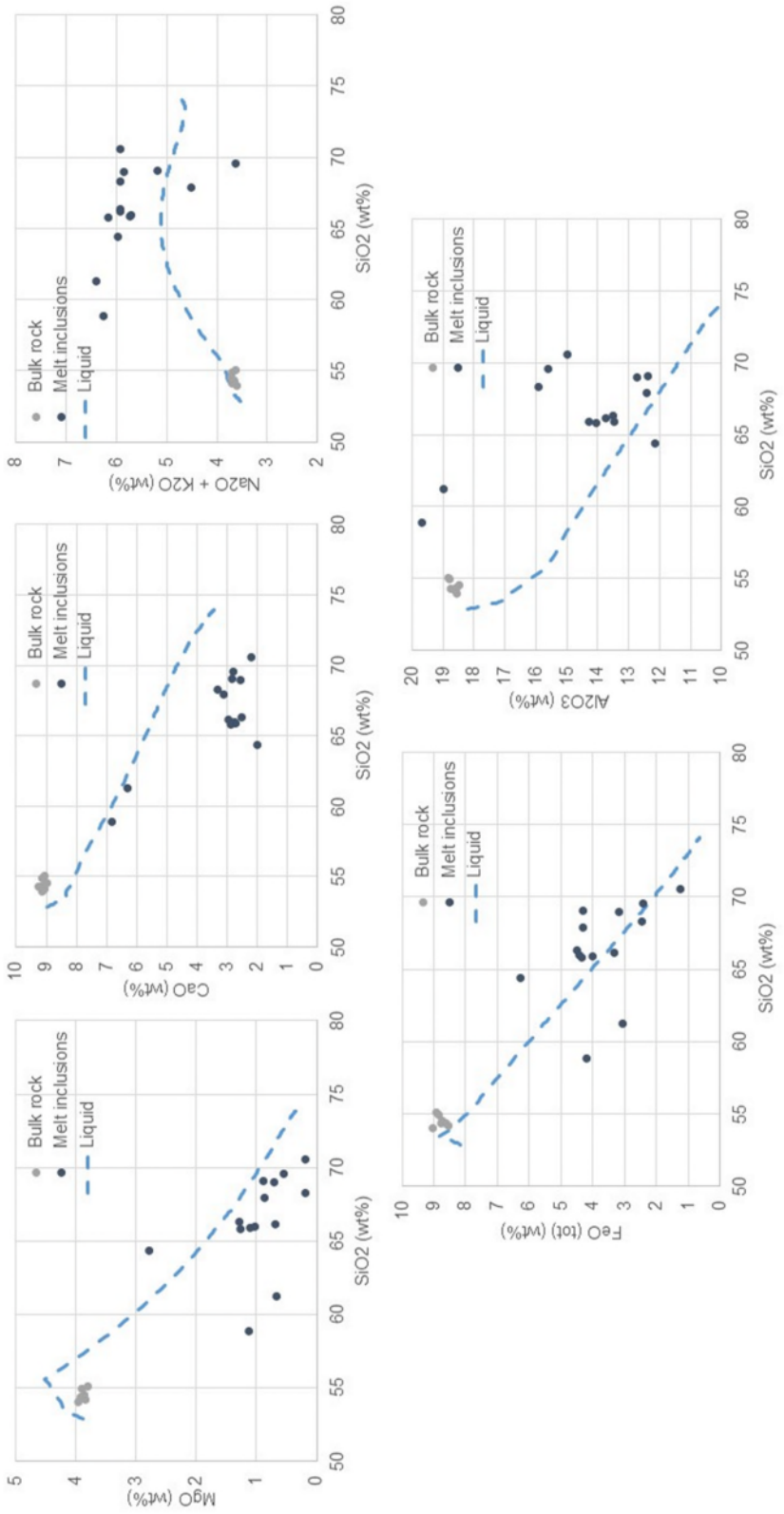


Figure A2c. Rhyolite-MELTS liquid composition plots (blue dashed line) for Kelud, 3.4 wt% H_2O simulation, 100 MPa, shown in Figure 2.1c. Bulk rock data from Jeffery *et al*. (2013). Melt inclusion data from Cassidy *et al*. (2016).

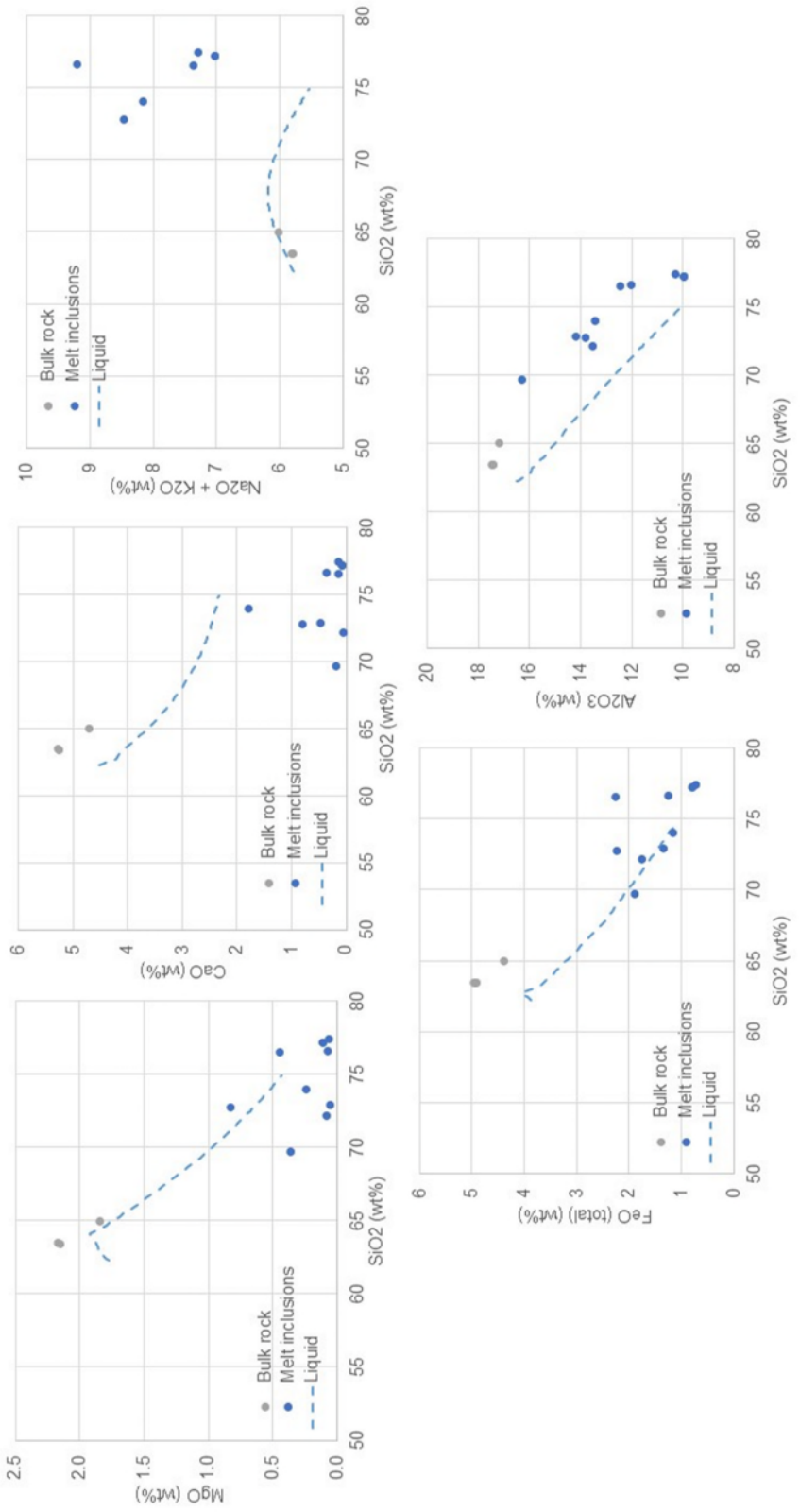


Figure A2d. Rhyolite-MELTS liquid composition plots for Mount St Helens, 4.5 wt% H_2O simulation, 130 MPa shown in Figure 2.1d. Bulk rock data from Pallister *et al*. (2008). Melt inclusion data from Blundy *et al*. (2008).

Appendix 3: Melt fraction- temperature curves

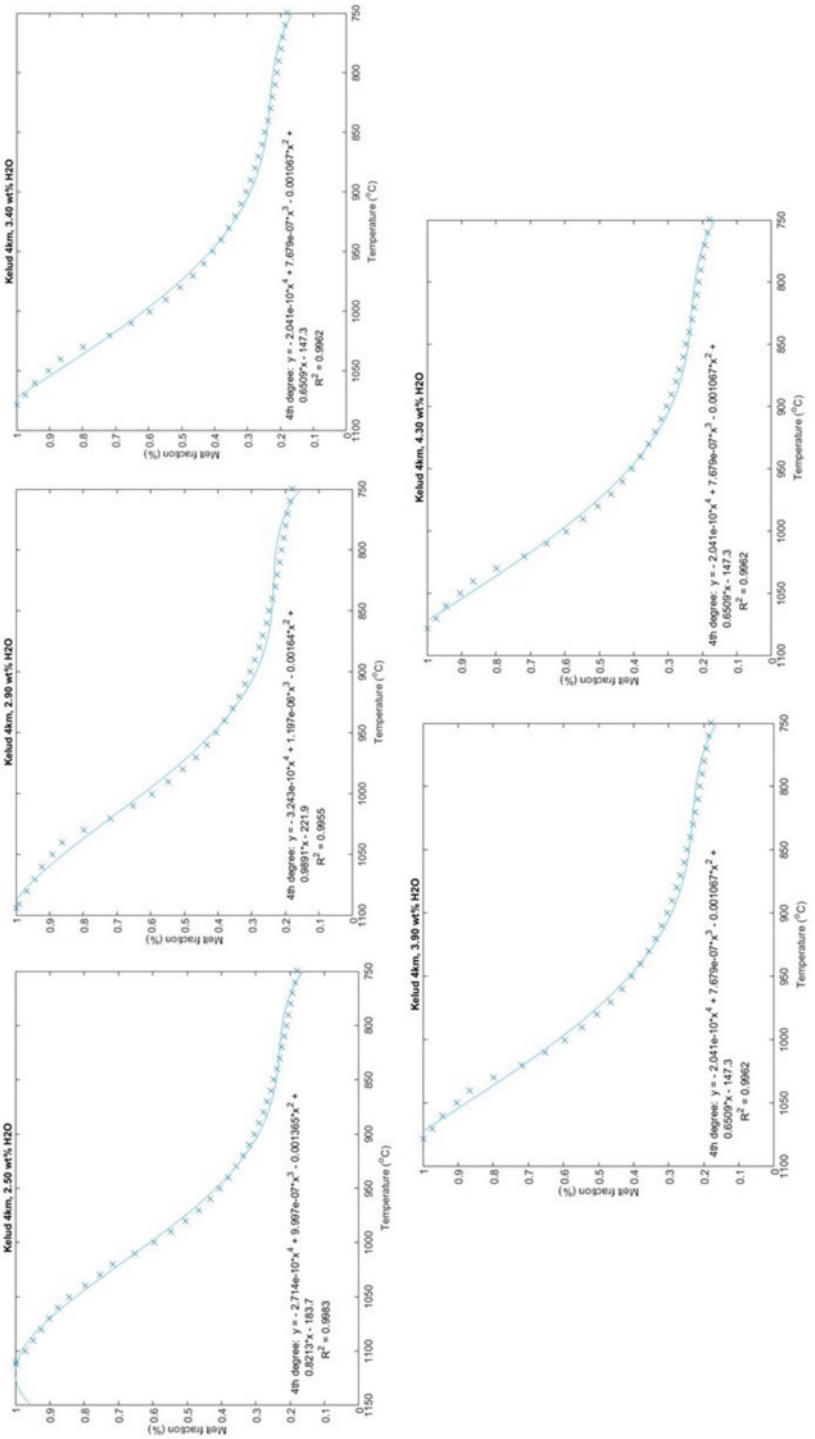


Figure A3. Fourth order polynomial curve fit to melt-fraction – temperature data from Rhyolite-MELTS. Blue crosses indicate data from MELTS. This relationship is used to implement latent heat of crystallisation in each thermal modelling scenario.

Appendix 4: Overpressure evolution at 0.05 wt% H_2O increments

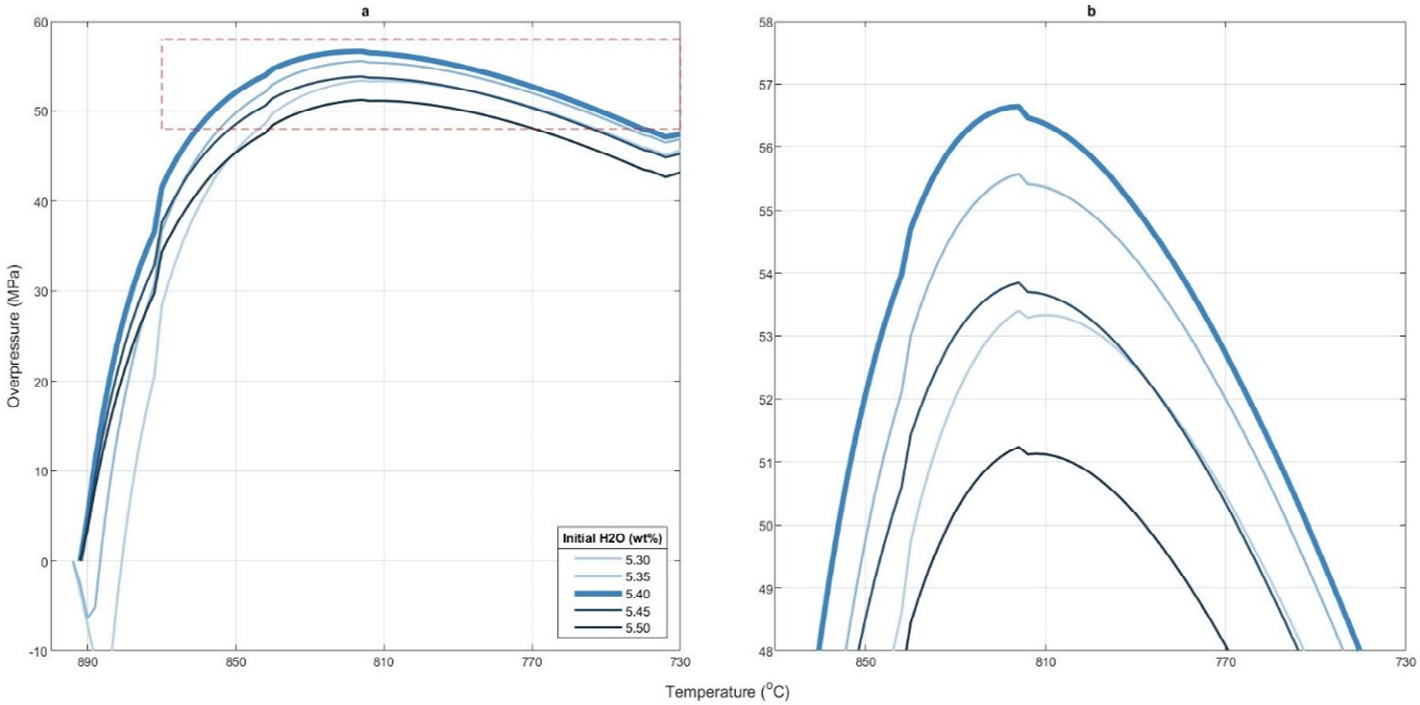


Figure A4. Overpressure evolution for Nisyros-Yali calculated from Rhyolite-MELTS. Varying initial H_2O content, run in increments of 0.05 wt% H_2O. No CO_2. Dashed red box in a) denotes overpressure-temperature space shown in b). Thicker lines indicate simulations with H_2O contents which are initially at the H_2O solubility limit.

Appendix 5: Overpressure evolution for basalt and rhyolite end-members

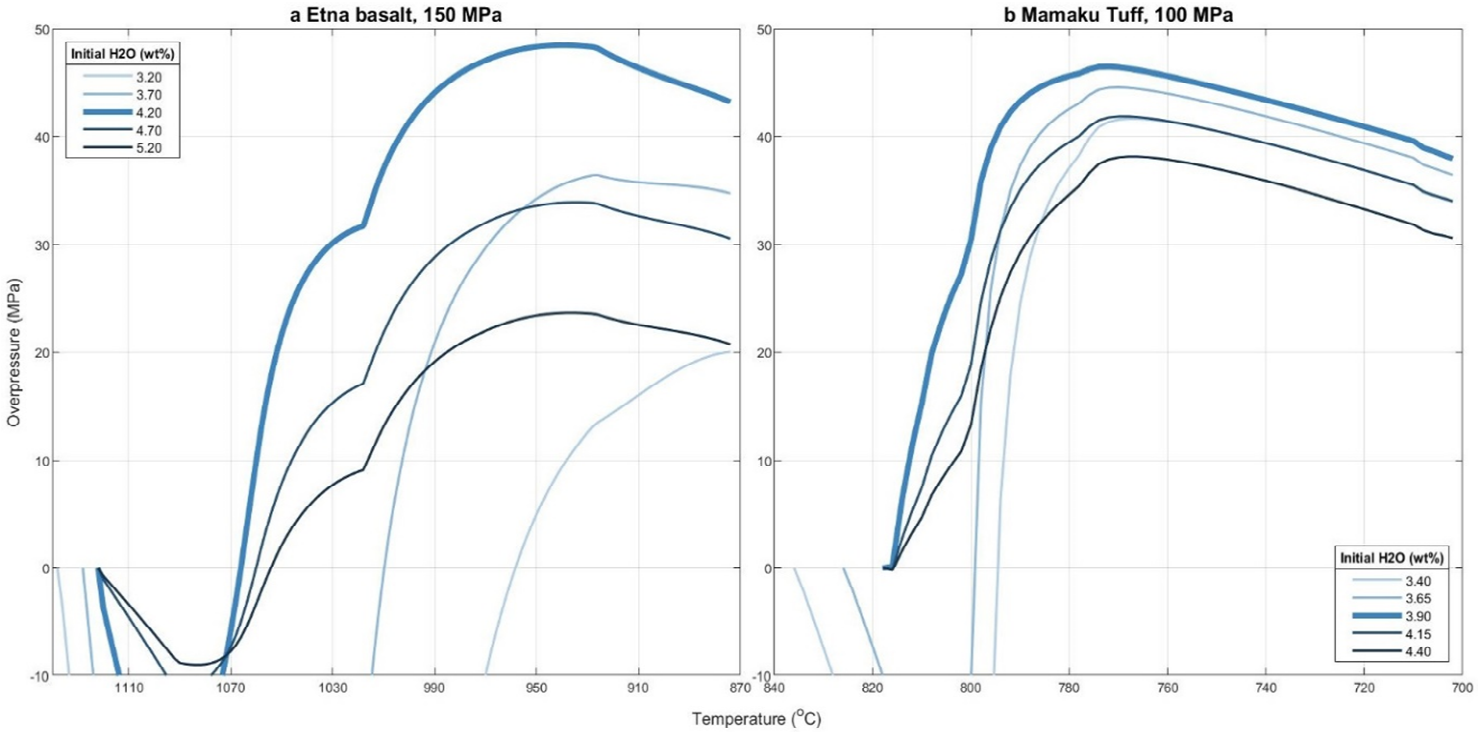


Figure A5. Overpressure evolution for a) Etna basalt bulk rock composition (46% SiO2), from Kahl *et al*. (2015). b) Mamaku tuff rhyolite bulk composition (76% SiO2), from Tramontano *et al*. (2017). Thicker lines indicate simulations with initial H2O contents at the solubility limit.

Appendix 6: Overpressure with reservoir compressibility term

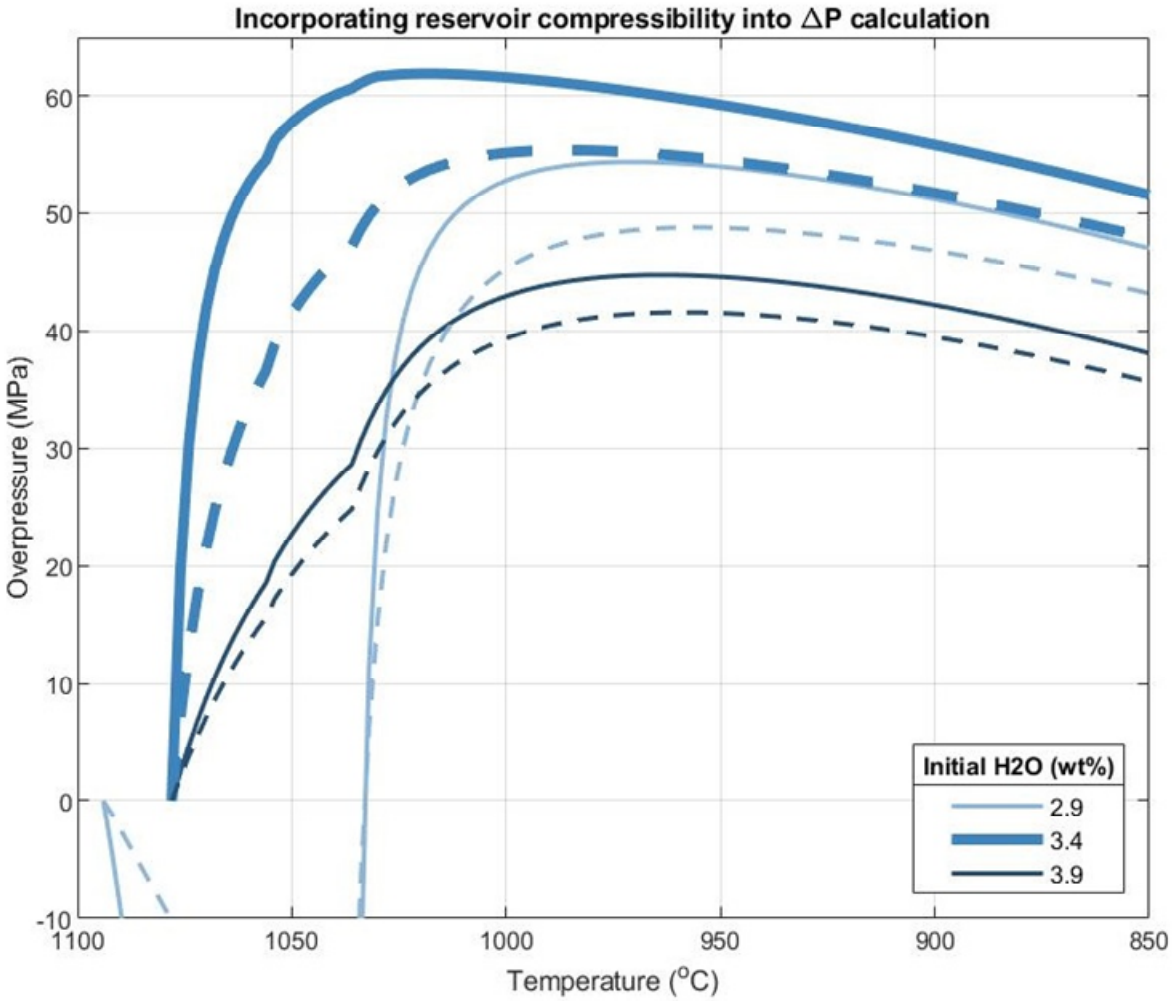


Figure A6. Shows the effect of incorporating a reservoir compressibility term into the overpressure calculations for Kelud (100 MPa). We use a reservoir compressibility value of 2 x 10^{-10} Pa^{-1}, based on Wasser *et al*. (2021). Solid lines show overpressure evolution without reservoir compressibility, dashed lines show overpressure with reservoir compressibility accounted for.

Appendix 7: Overpressure evolution for varying reservoir size

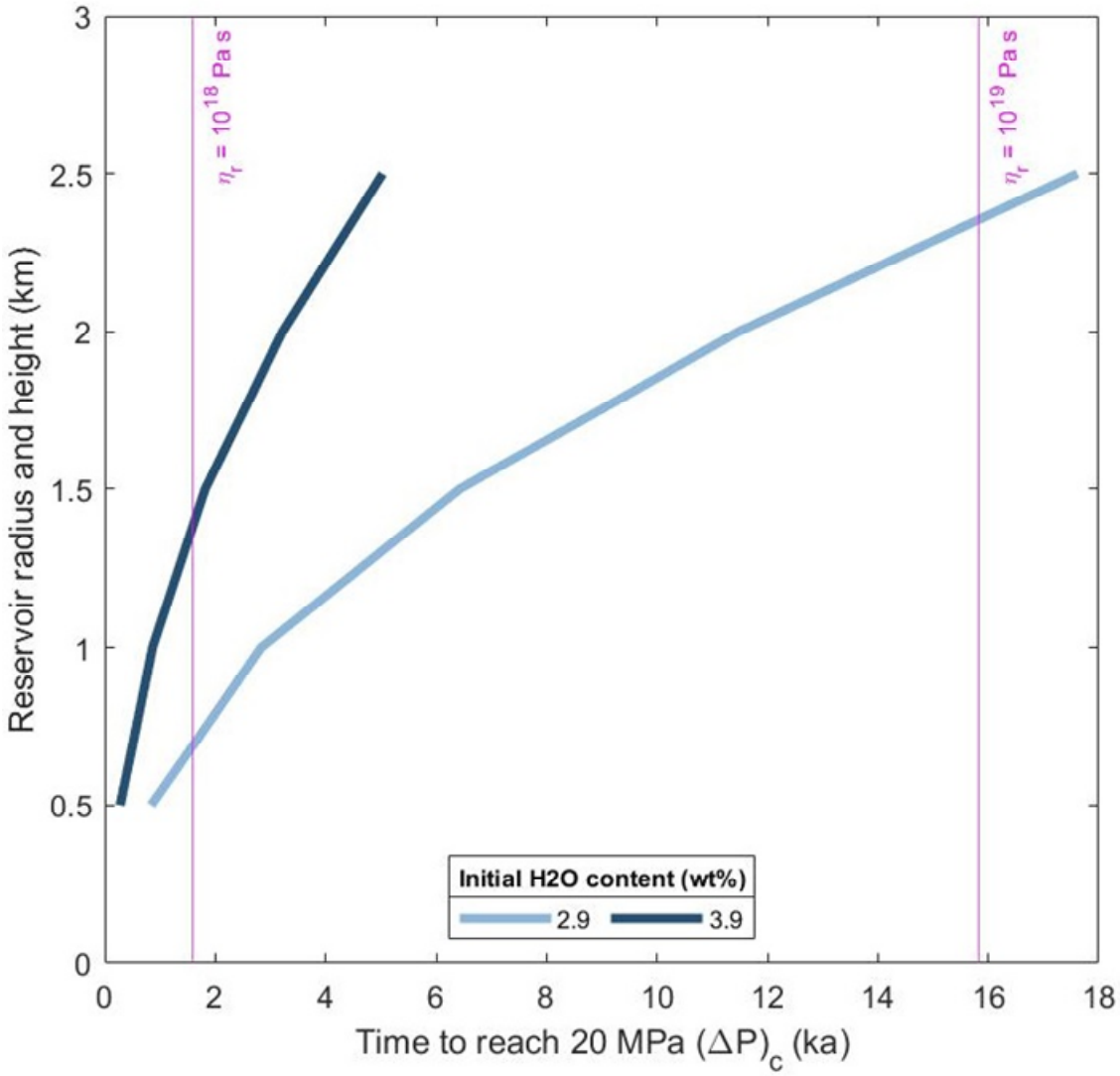


Figure A7. Time taken to reach 20 MPa overpressure with reservoirs of varying size, for the 2.9 wt% H_2O (initially fluid undersaturated) and 3.9 wt% H_2O (initially fluid-oversaturated) scenarios shown in figure 2.3. Relaxation timescales relevant for different crustal viscosities are shown by pink lines. Both reservoir radius and height are increased by 0.5 km increments in the thermal model, from 0.5 km to 2.5 km. This results in reservoir volumes of 0.4, 3.1, 10.6, 25.0 and 49.0 km3 respectively.

Appendix 8: Volume change and compressibility evolution

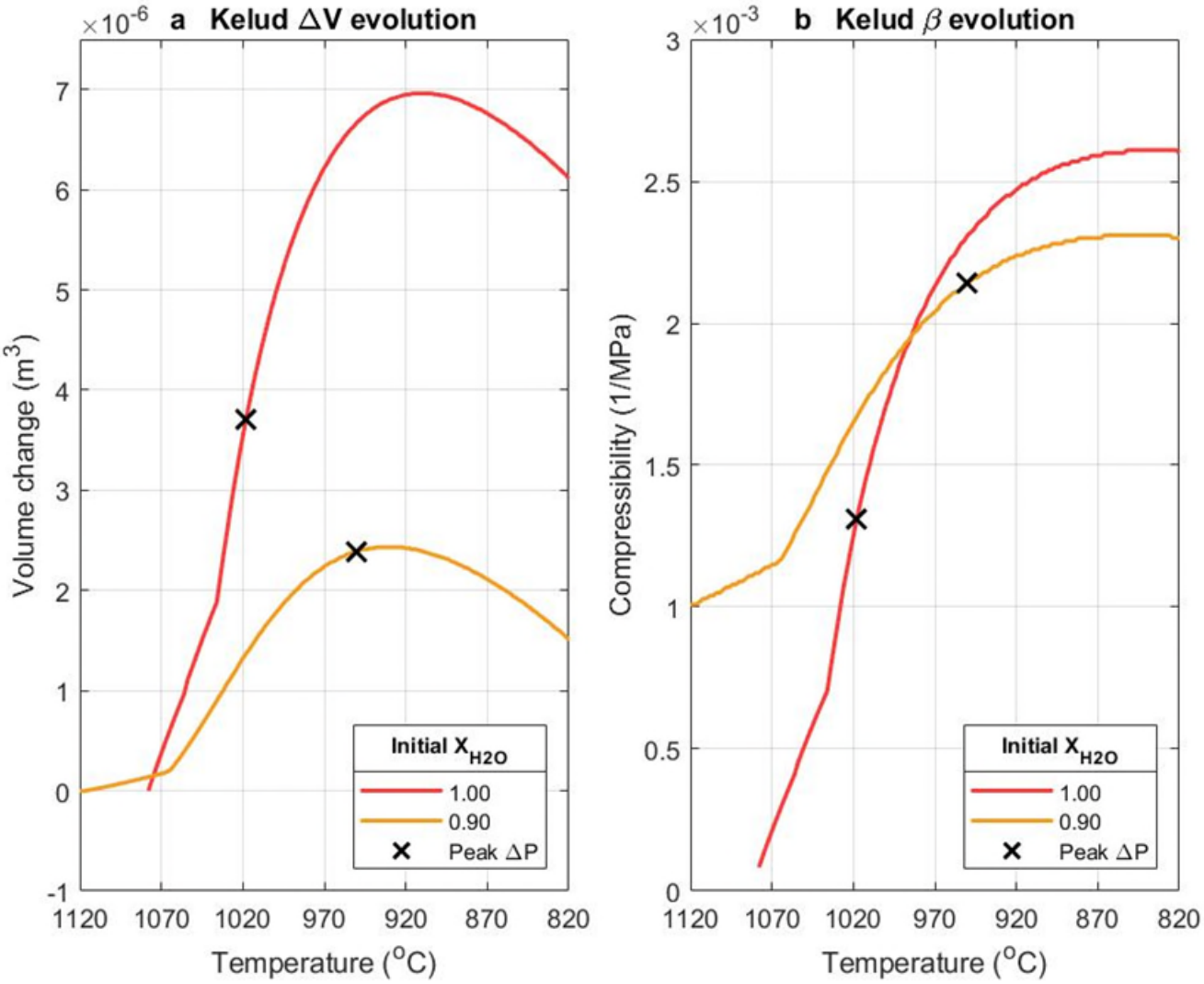


Figure A8. Evolution of a) potential volume change and b) system compressibility, for the X_{H2O} = 1 and X_{H2O} = 0.9 cases shown in figure 2.2c (Kelud, 100 MPa). Crosses indicate values at peak overpressure.

Appendix 9: EBSD map step sizes

Sample	Map name	Map width (μm)	Map height (μm)	Map area ($μm^2$)	Indexed pixels	Step size (μm)
SHV_00	2019_SHV00_finegrained	908	424	384798	126495	1.2
SHV_00	2019_SHV00_hbrim	690	420	289800	24959	3
SHV_01	2019_SHV01	222	152	33744	80833	0.5
SHV_01	Leeds_SHV01_map1	401	263	105625	328651	0.51
SHV_01	Leeds_SHV01_map2	366	195	71459	256019	0.445
SHV_02	Leeds_SHV02_map1	158	641	100936	169367	0.59
SHV_02	Leeds_SHV02_map2	139	609	84780	144704	0.59
SHV_01	Materials_SHV01_map1	629	471	295844	59723	0.9993
SHV_01	Materials_SHV01_map2	441	331	146234	65898	1.0009
SHV_02	Materials_SHV02_map1	330	248	81791	49298	0.9997
SHV_02	Materials_SHV02_map2	467	250	116680	42068	0.9994
SHV_02	Materials_SHV02_map3_upper	497	190	94430	31463	0.9991
SHV_02	Materials_SHV02_map3_lower	497	137	68089	22876	0.9991
SHV_04	Materials_SHV04_map1	518	389	201381	58202	0.9997
SHV_04	Materials_SHV04_map2	539	336	181104	48821	1.0396

Appendix 10: Phase maps

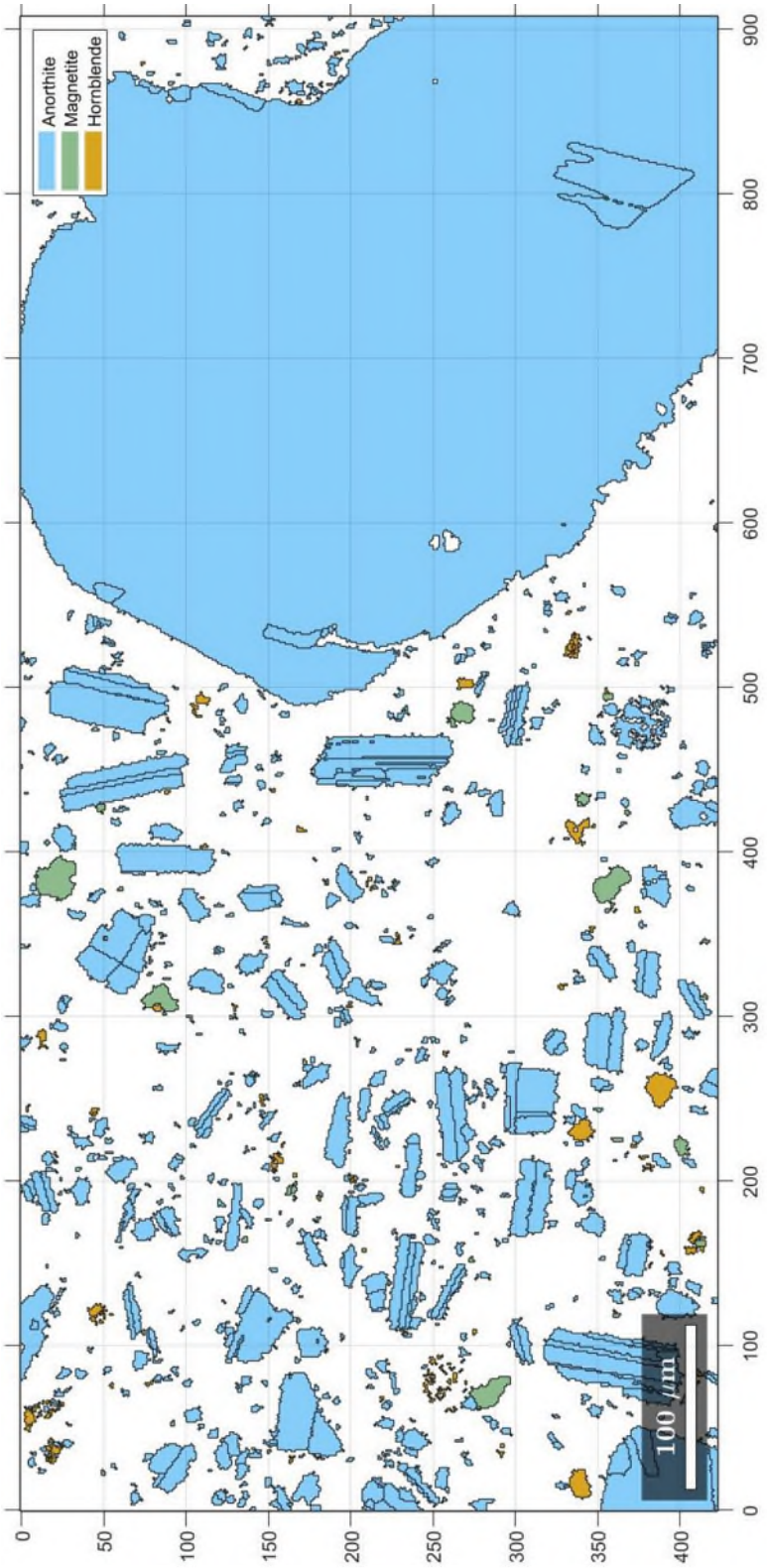


Figure A10a. Map showing the phases present in sample 2019_SHV00_finegrained, determined by EBSD analysis.

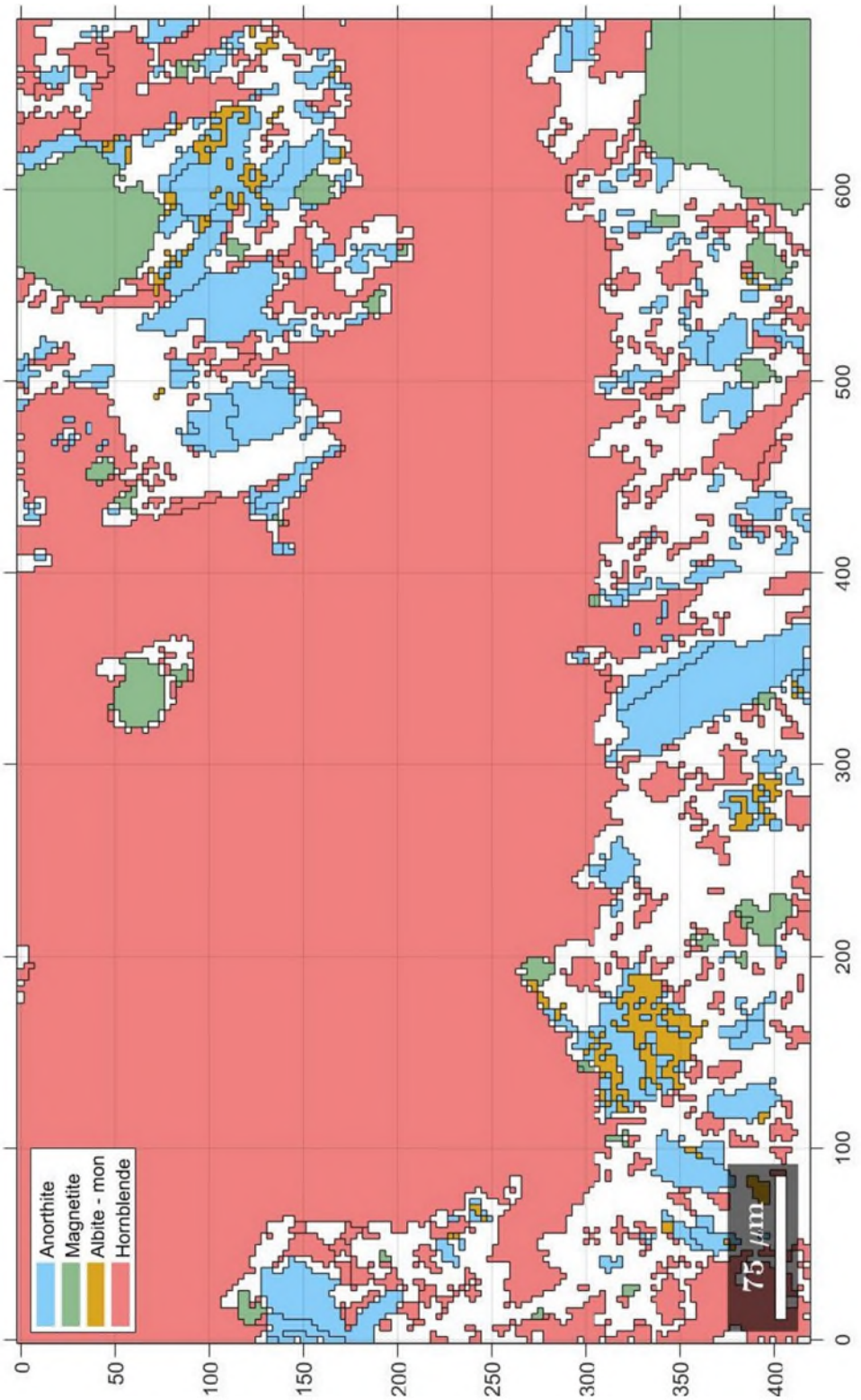


Figure A10b. Map showing the phases present in sample 2019_SHV00_hbrim, determined by EBSD analysis.

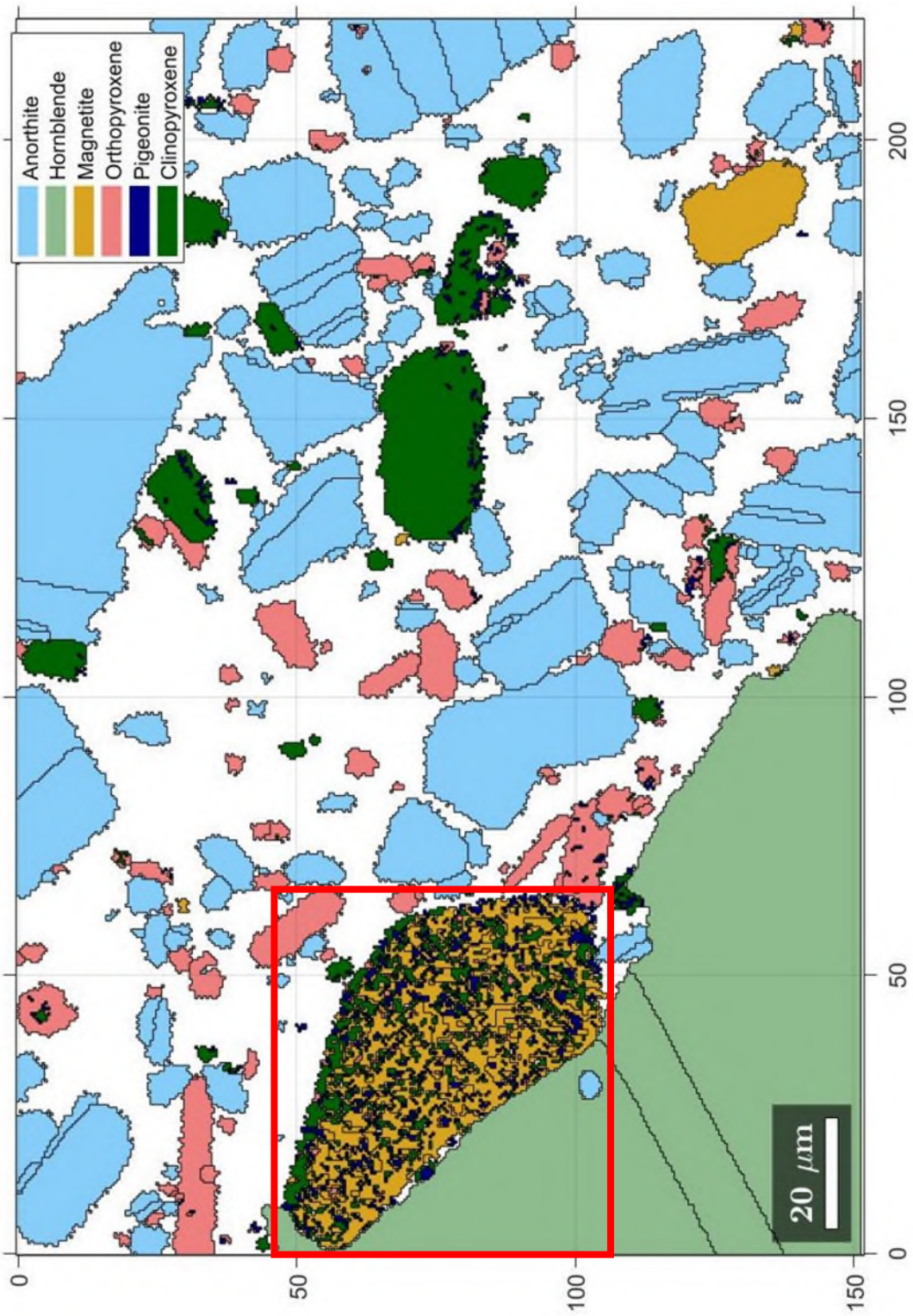


Figure A10c. Map showing the phases present in sample 2019_SHV01, determined by EBSD analysis. The data points shown within the red rectangle have not been included in the magnetite KAM histograms

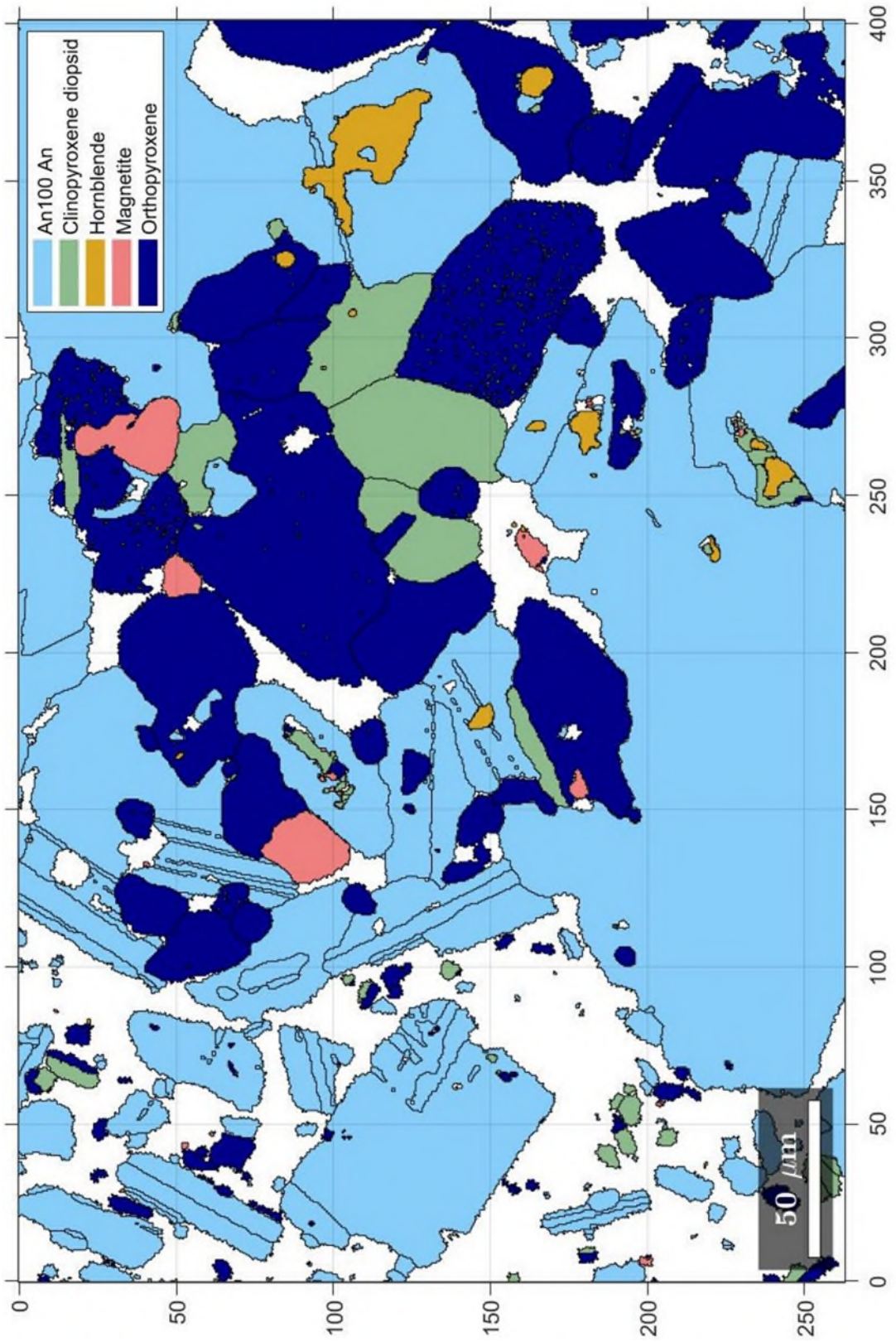


Figure A10d. Map showing the phases present in sample Leeds_SHV01_map1, determined by EBSD analysis.

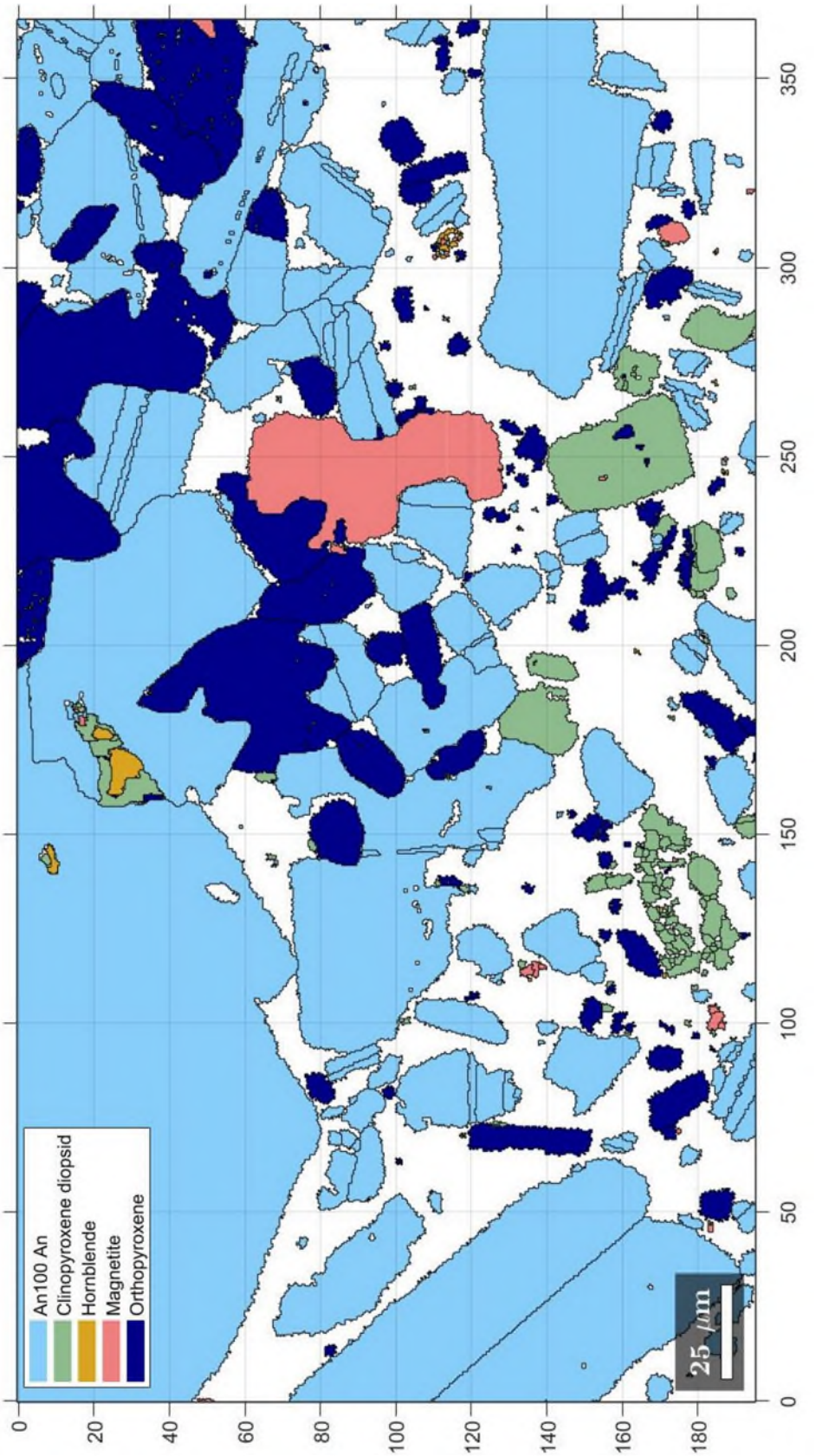


Figure A10e. Map showing the phases present in sample Leeds_SHV01_map2, determined by EBSD analysis.

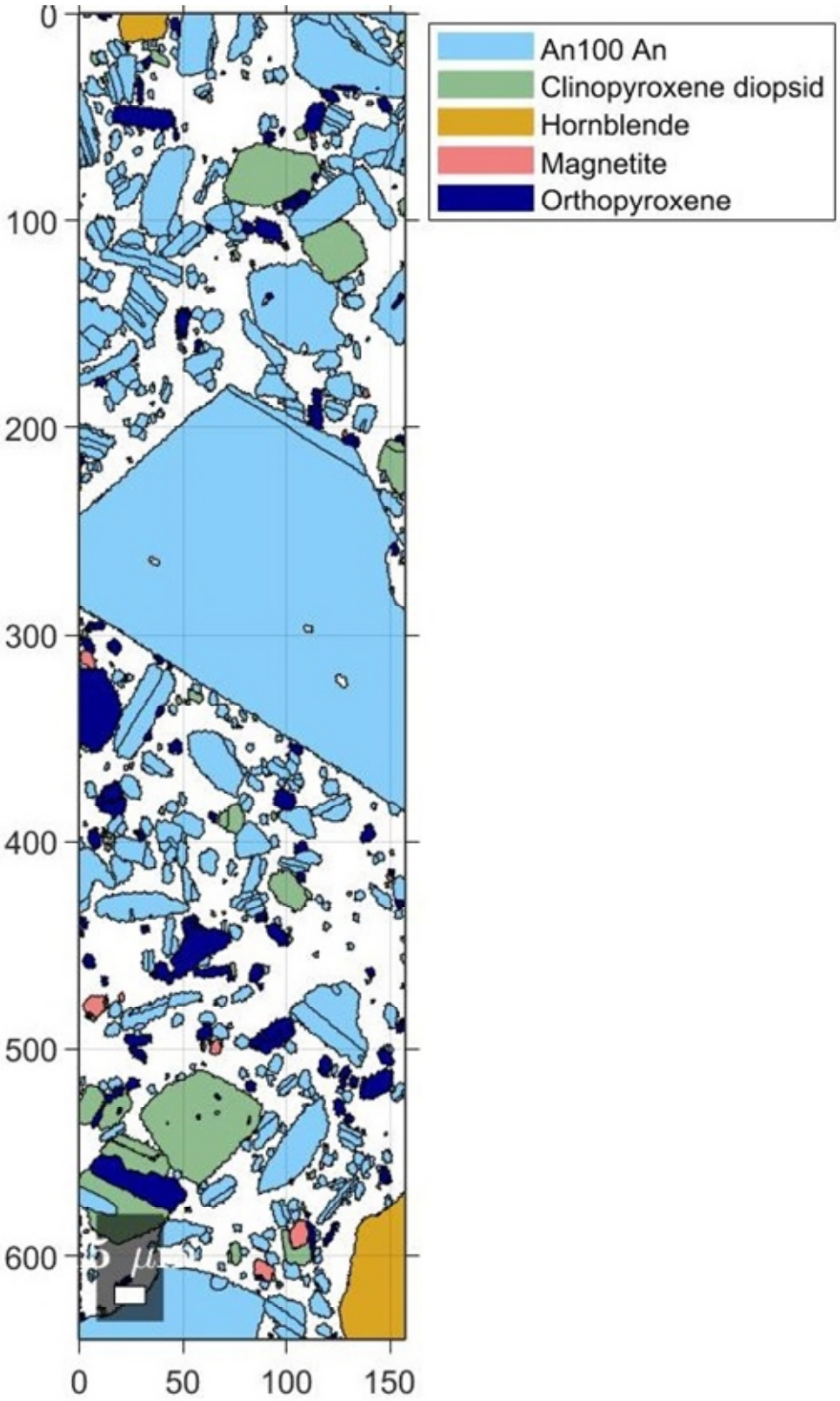


Figure A10f. Map showing the phases present in sample Leeds_SHV02_map1, determined by EBSD analysis.

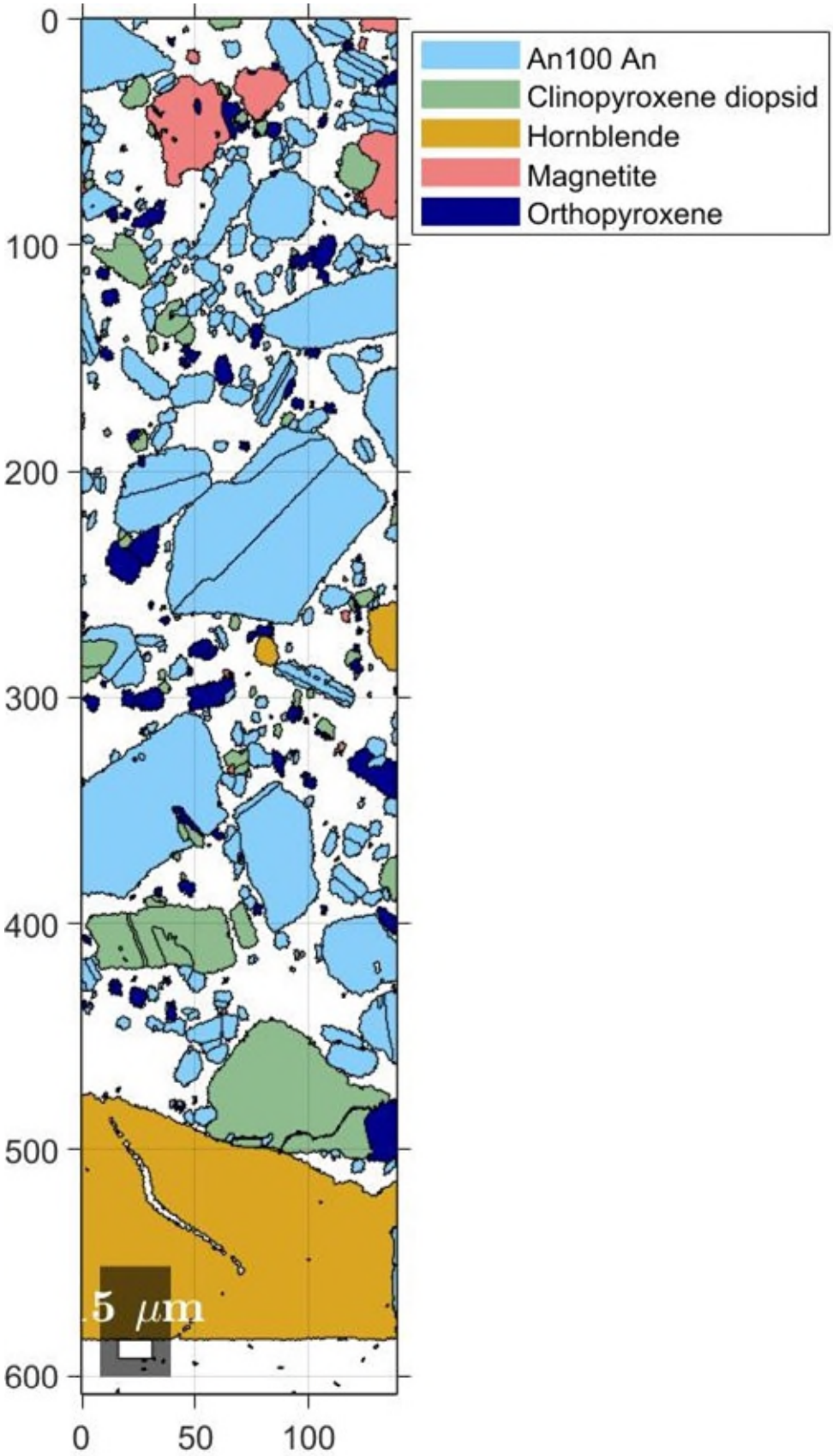


Figure A10g. Map showing the phases present in sample Leeds_SHV02_map2, determined by EBSD analysis.

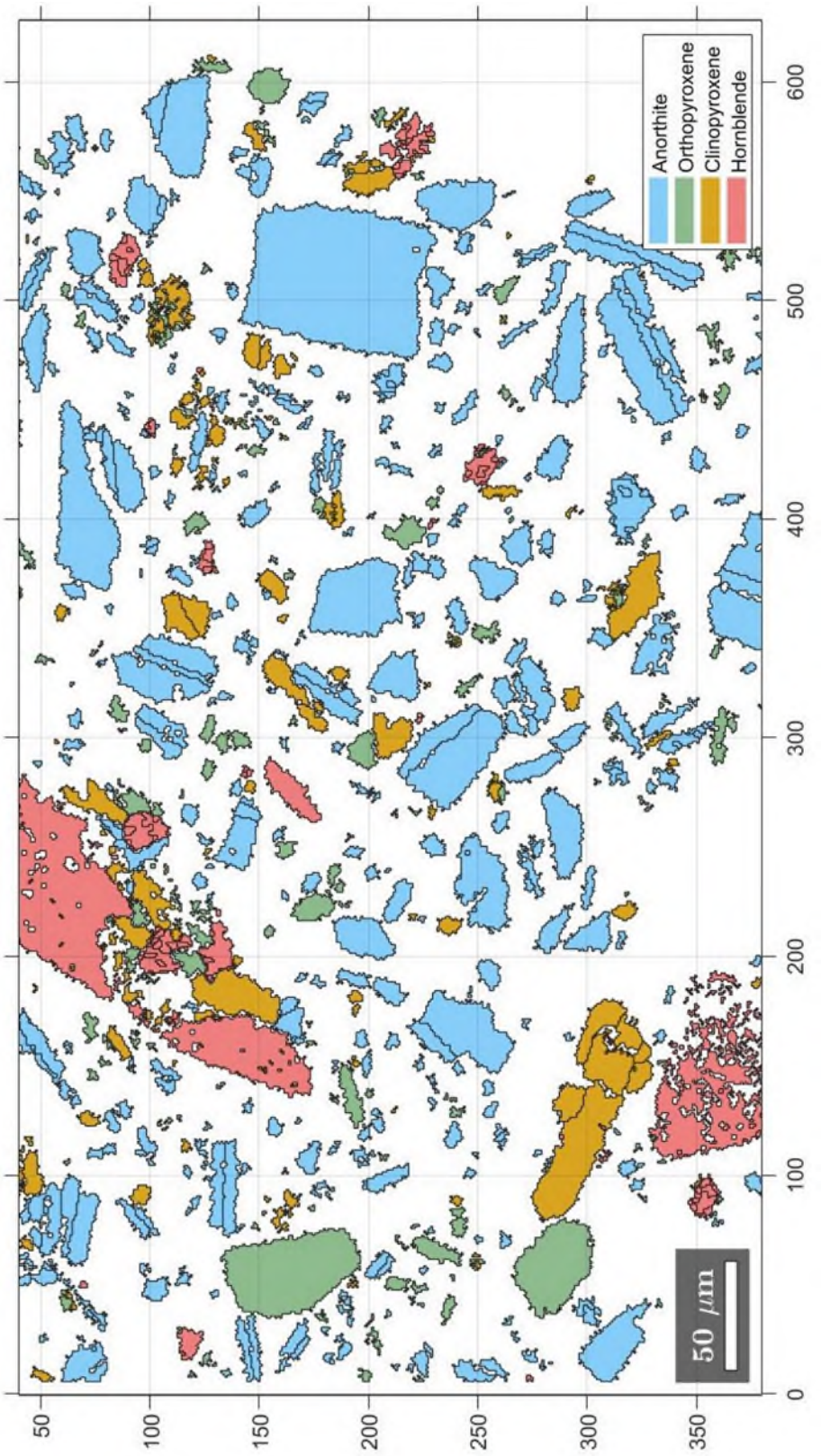


Figure A10h. Map showing the phases present in sample Materials_SHV01_map1, determined by EBSD analysis.

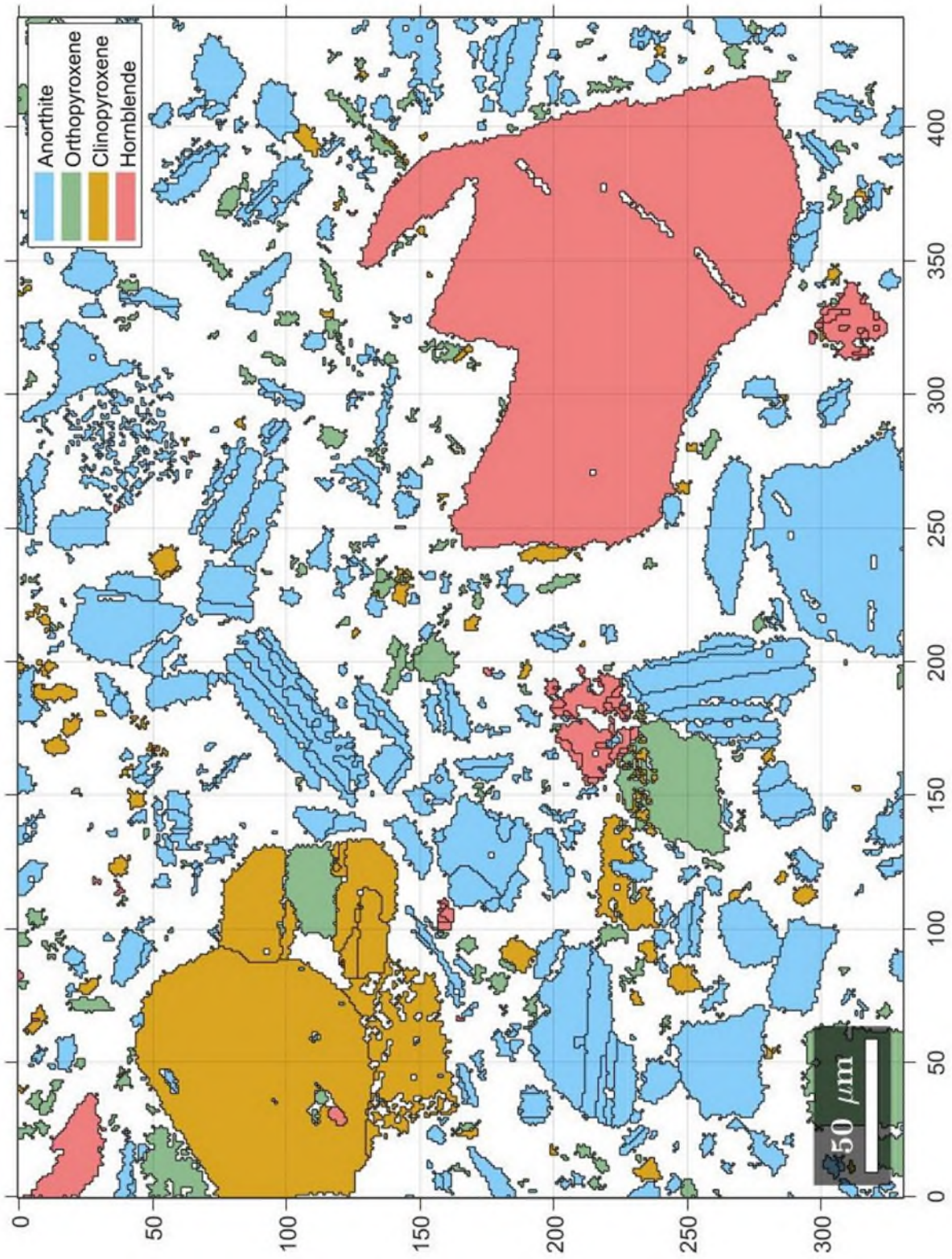


Figure A10i. Map showing the phases present in sample Materials_SHV01_map2, determined by EBSD analysis.

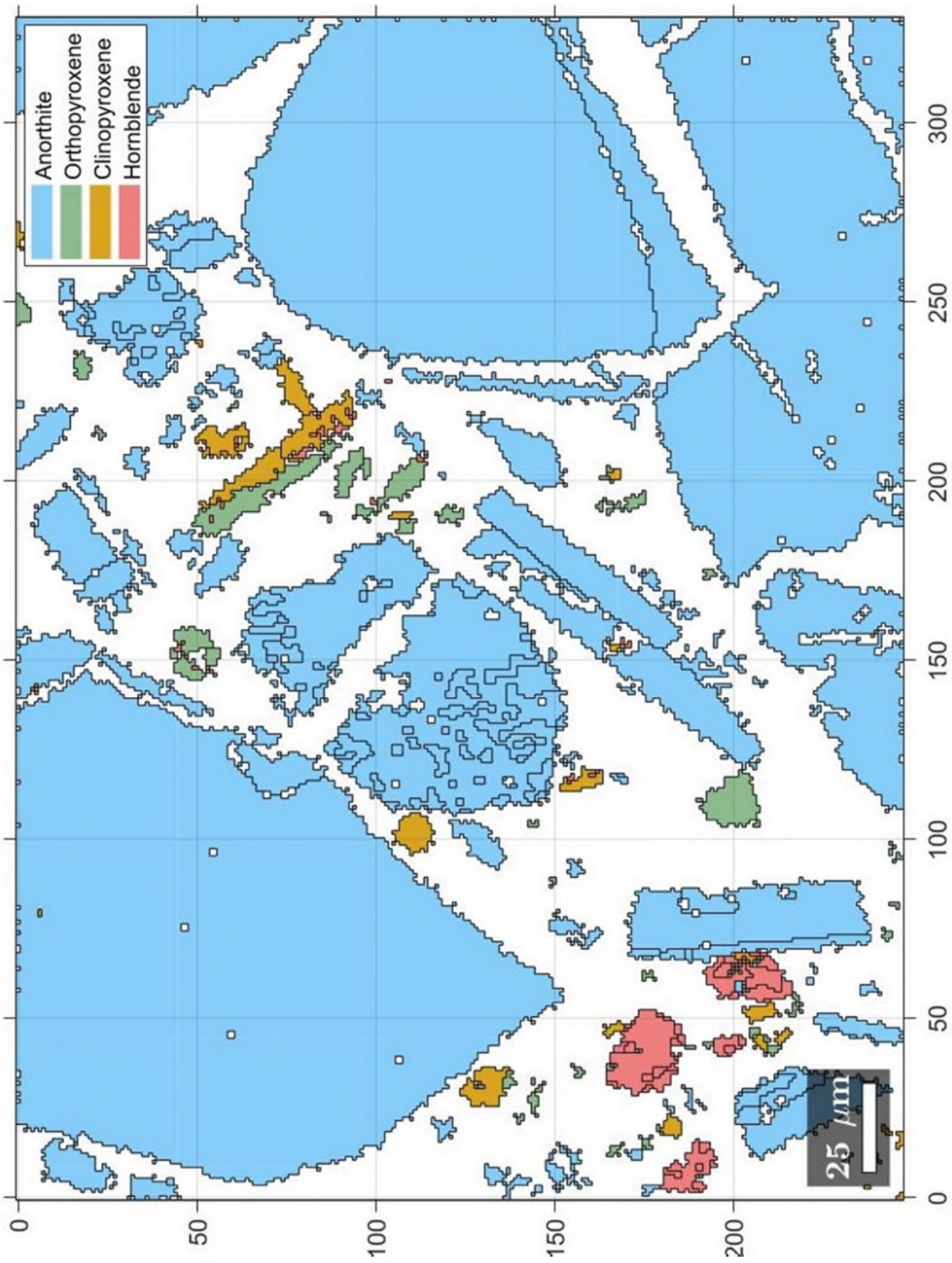


Figure A10j. Map showing the phases present in sample Materials_SHV02_map1, determined by EBSD analysis.

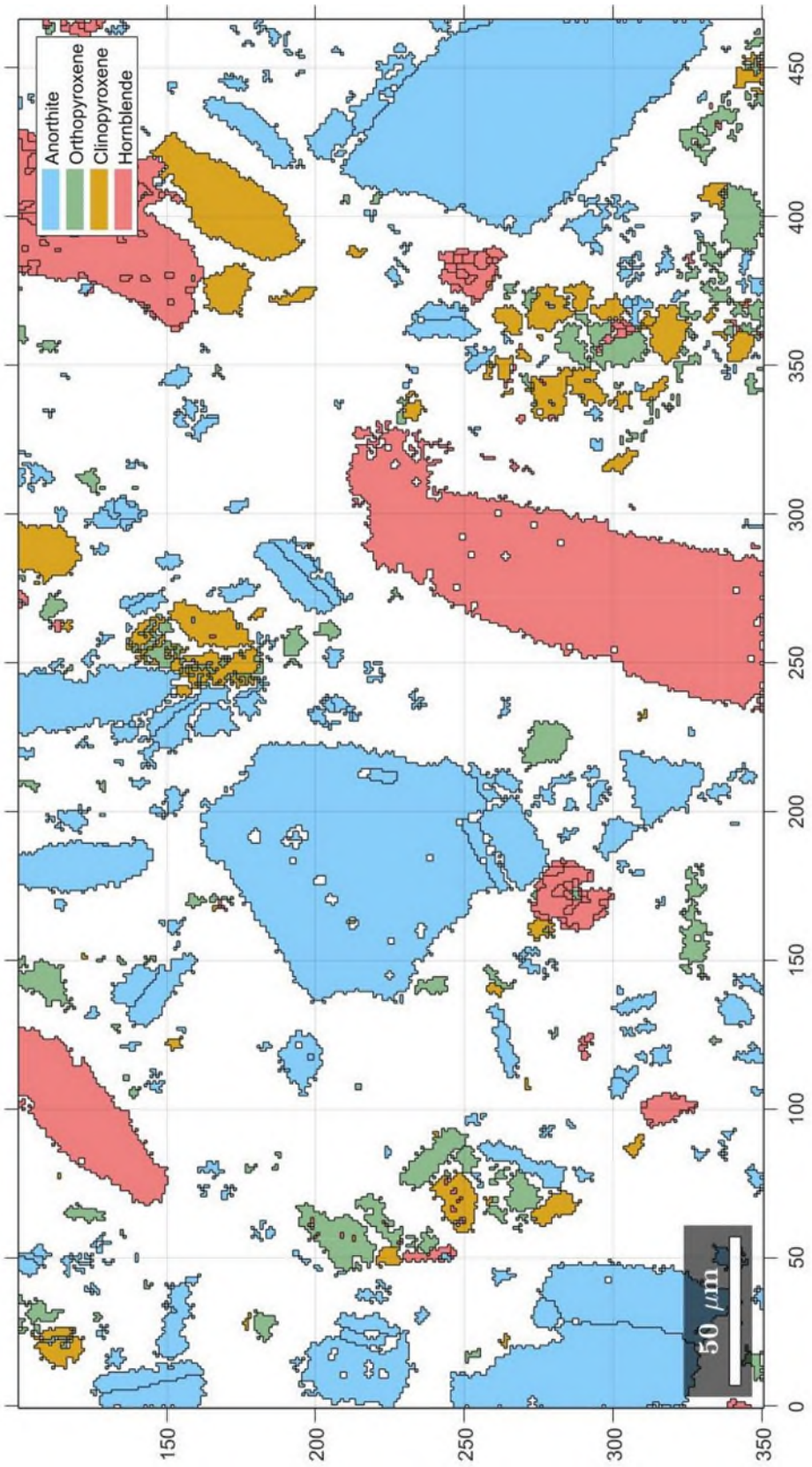


Figure A10k. Map showing the phases present in sample Materials_SHV02_map2, determined by EBSD analysis.

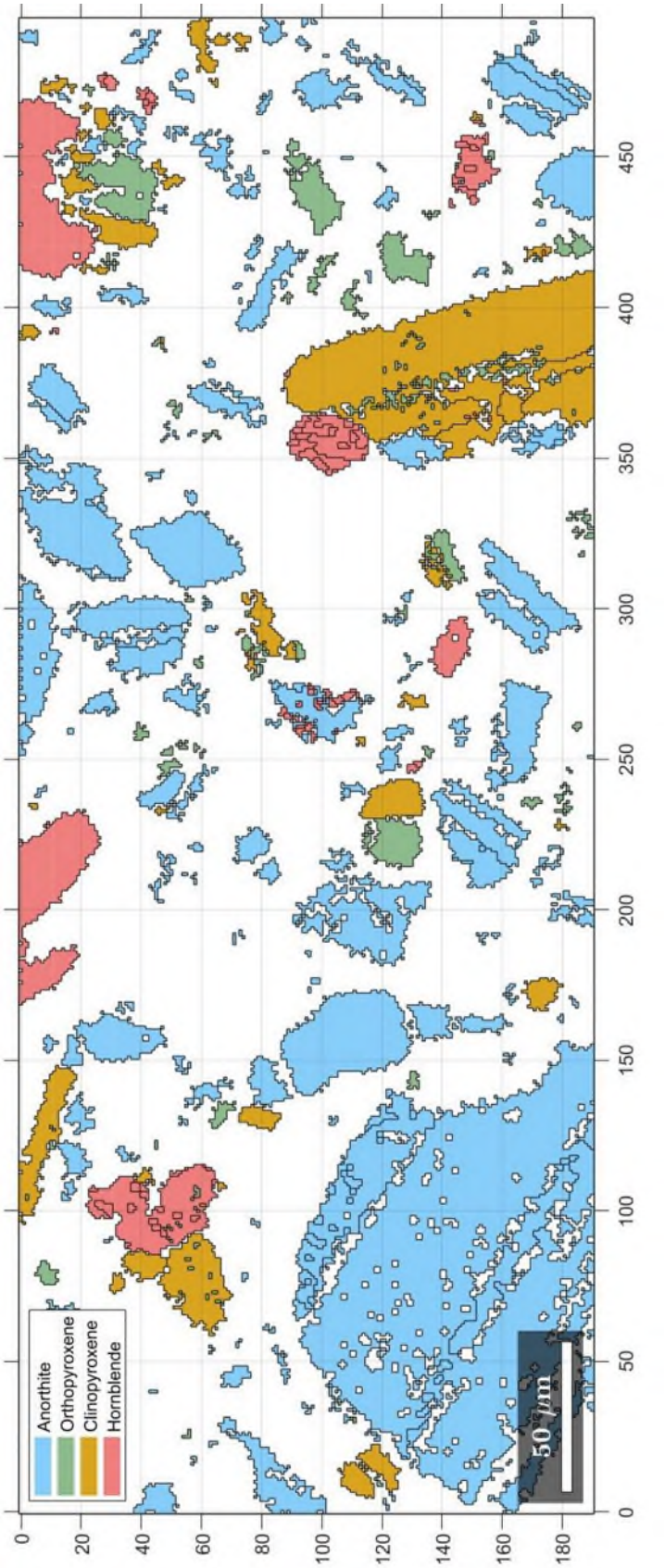


Figure A10l. Map showing the phases present in sample Materials_SHV02_map3_upper, determined by EBSD analysis.

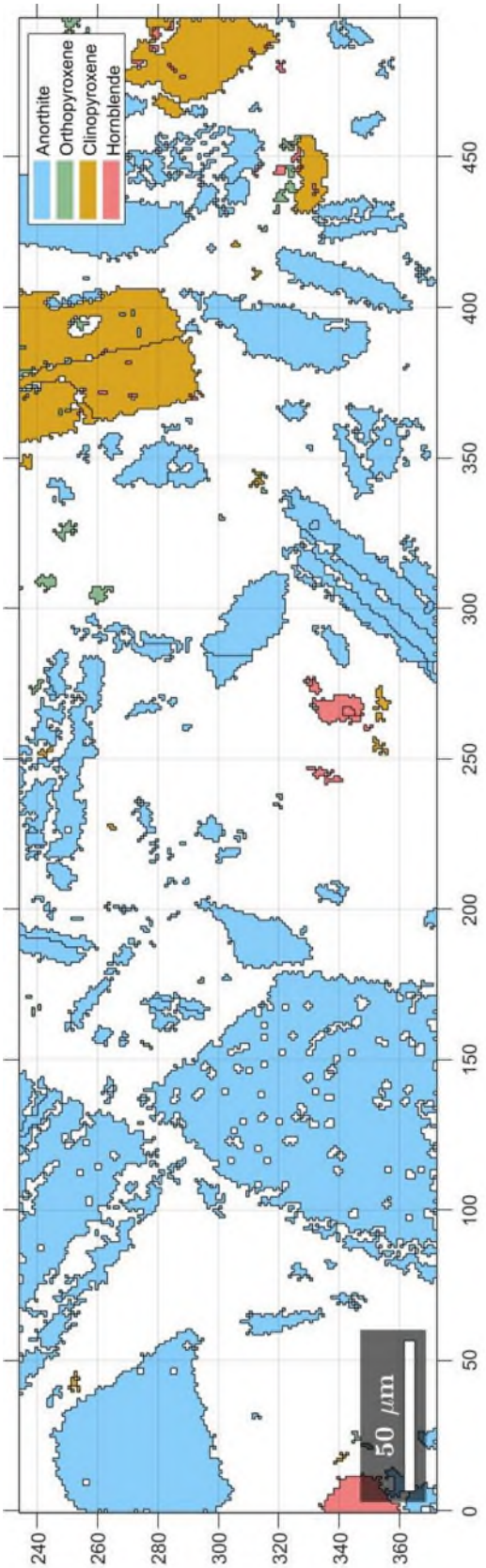


Figure A10m. Map showing the phases present in sample Materials_SHV02_map3_lower, determined by EBSD analysis.

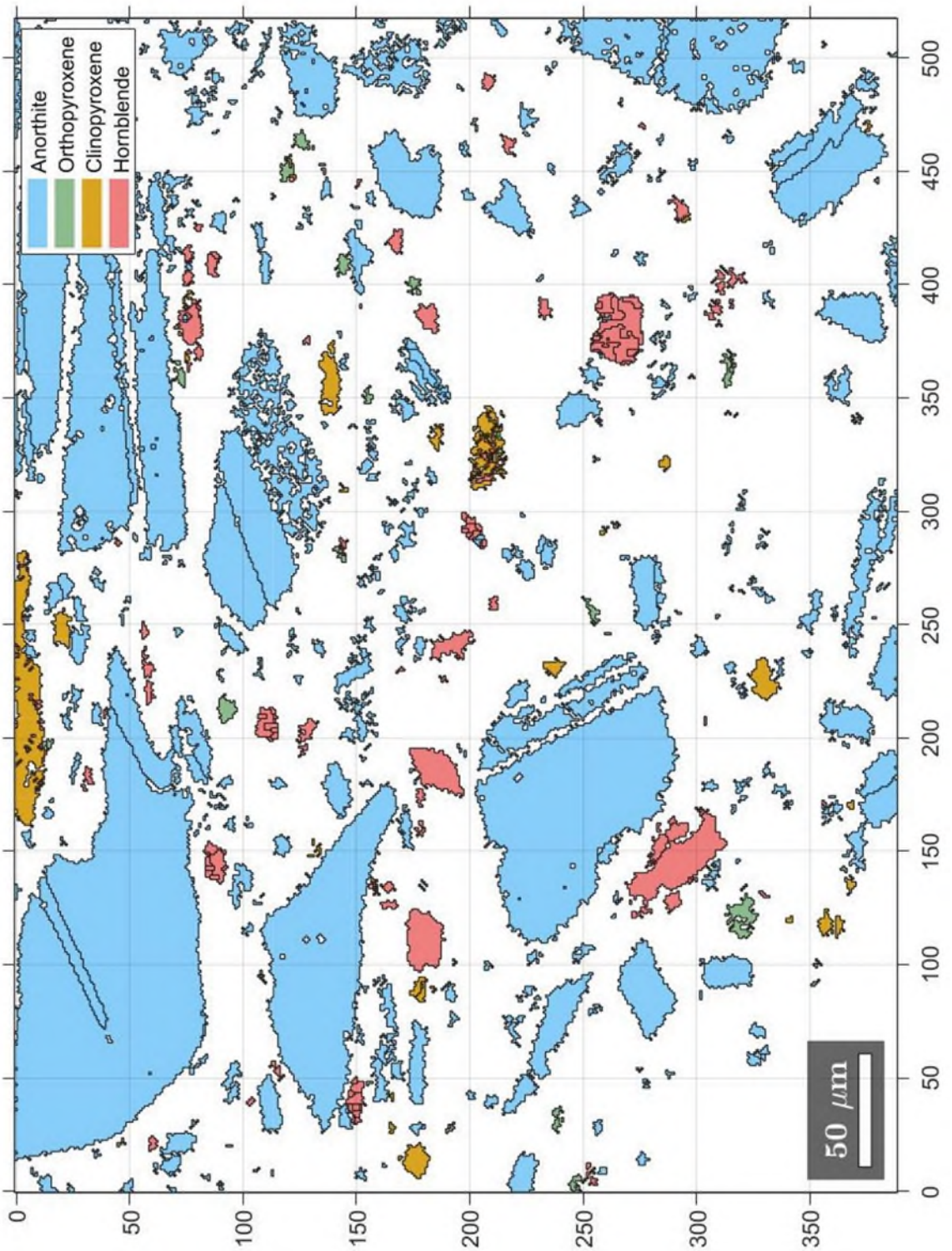


Figure A10n. Map showing the phases present in sample Materials_SHV04_map1, determined by EBSD analysis.

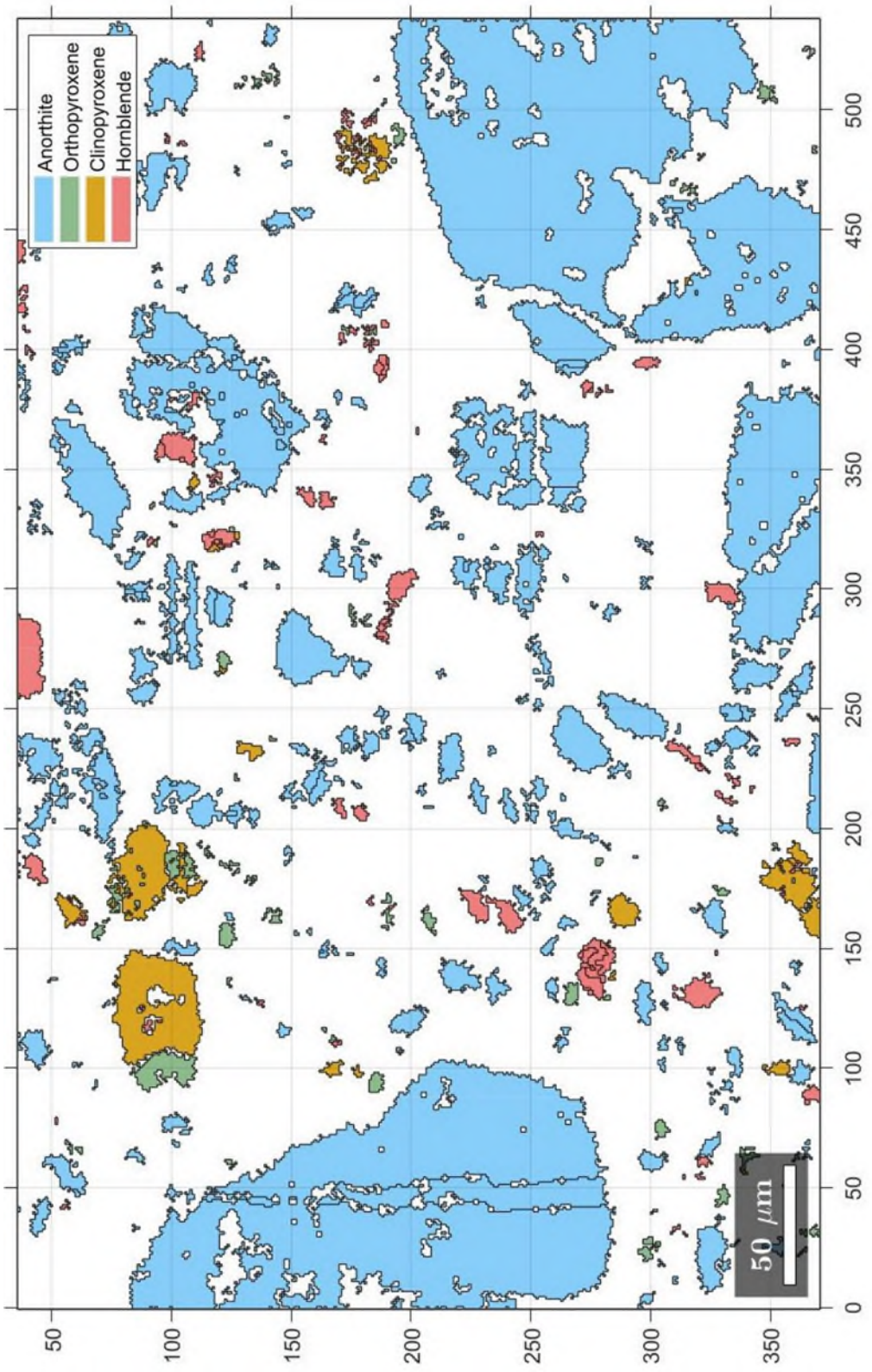


Figure A10o. Map showing the phases present in sample Materials_SHV04_map2, determined by EBSD analysis.

Appendix 11: KAM maps with no threshold

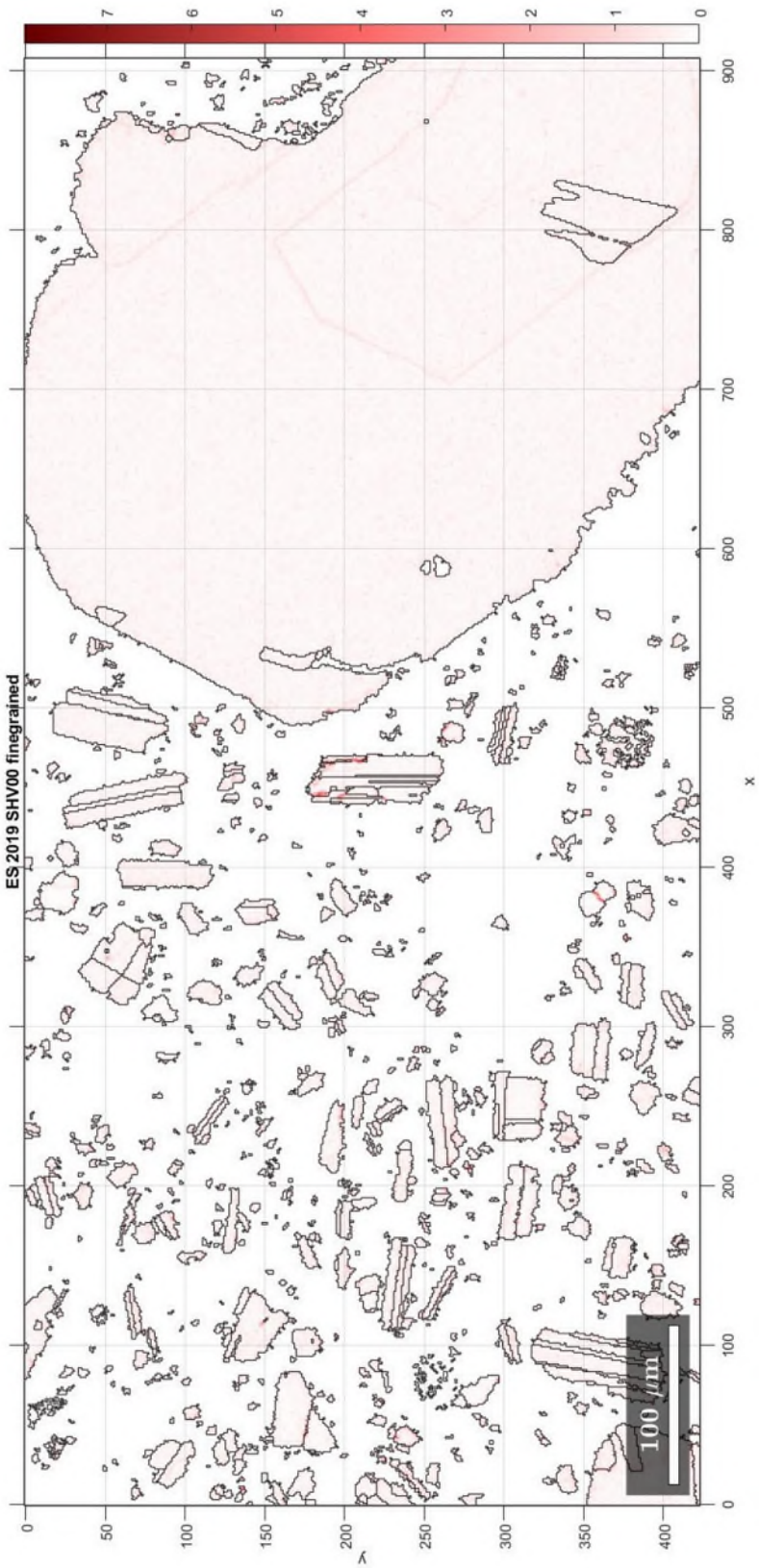


Figure A11a. Kernel average misorientation map for sample 2019_SHV00_finegrained. 'Unbounded' map, produced without a threshold angle for the KAM data extraction.

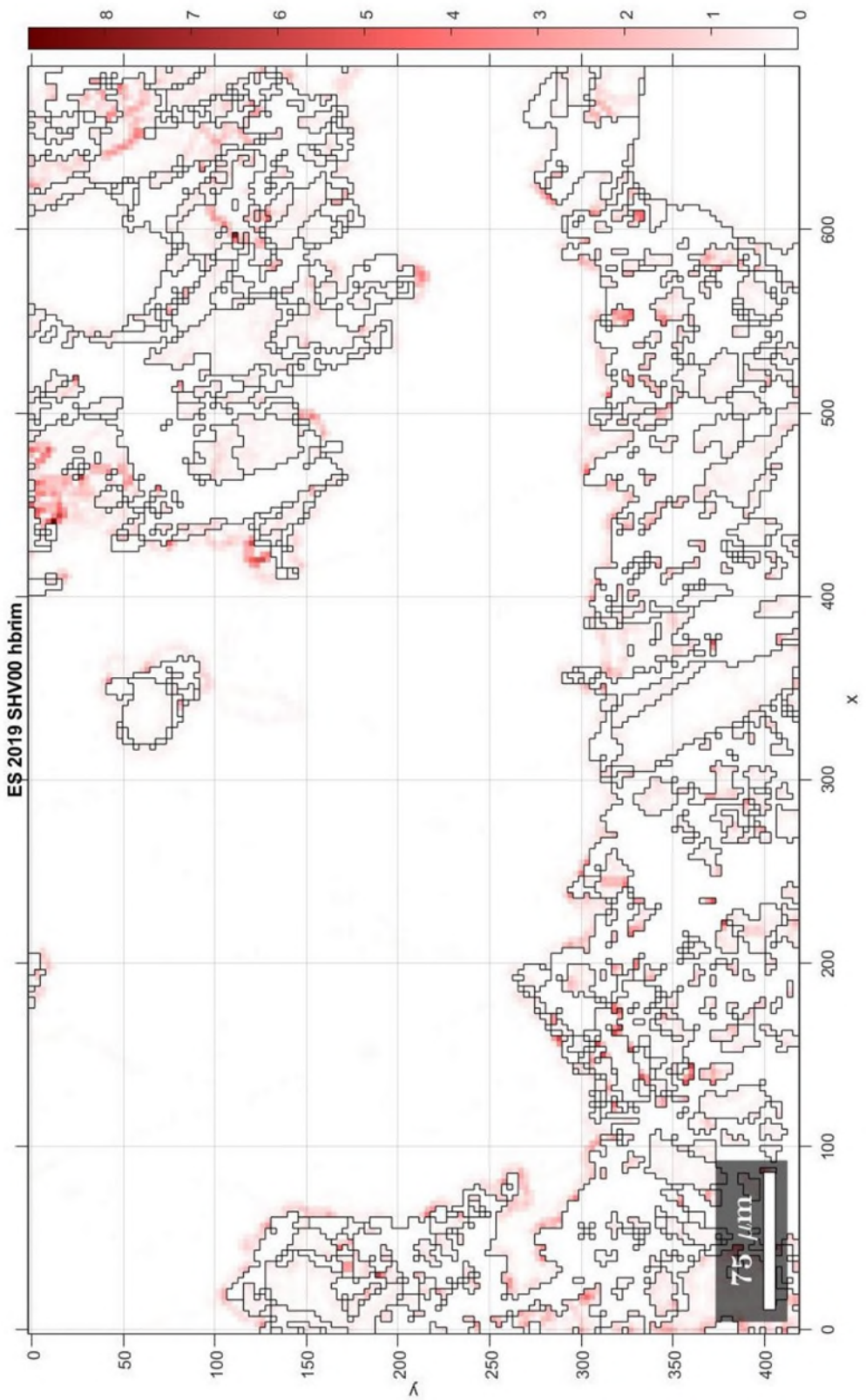


Figure A11b. Kernel average misorientation map for sample 2019_SHV00_hbrim. 'Unbounded' map, produced without a threshold angle for the KAM data extraction.

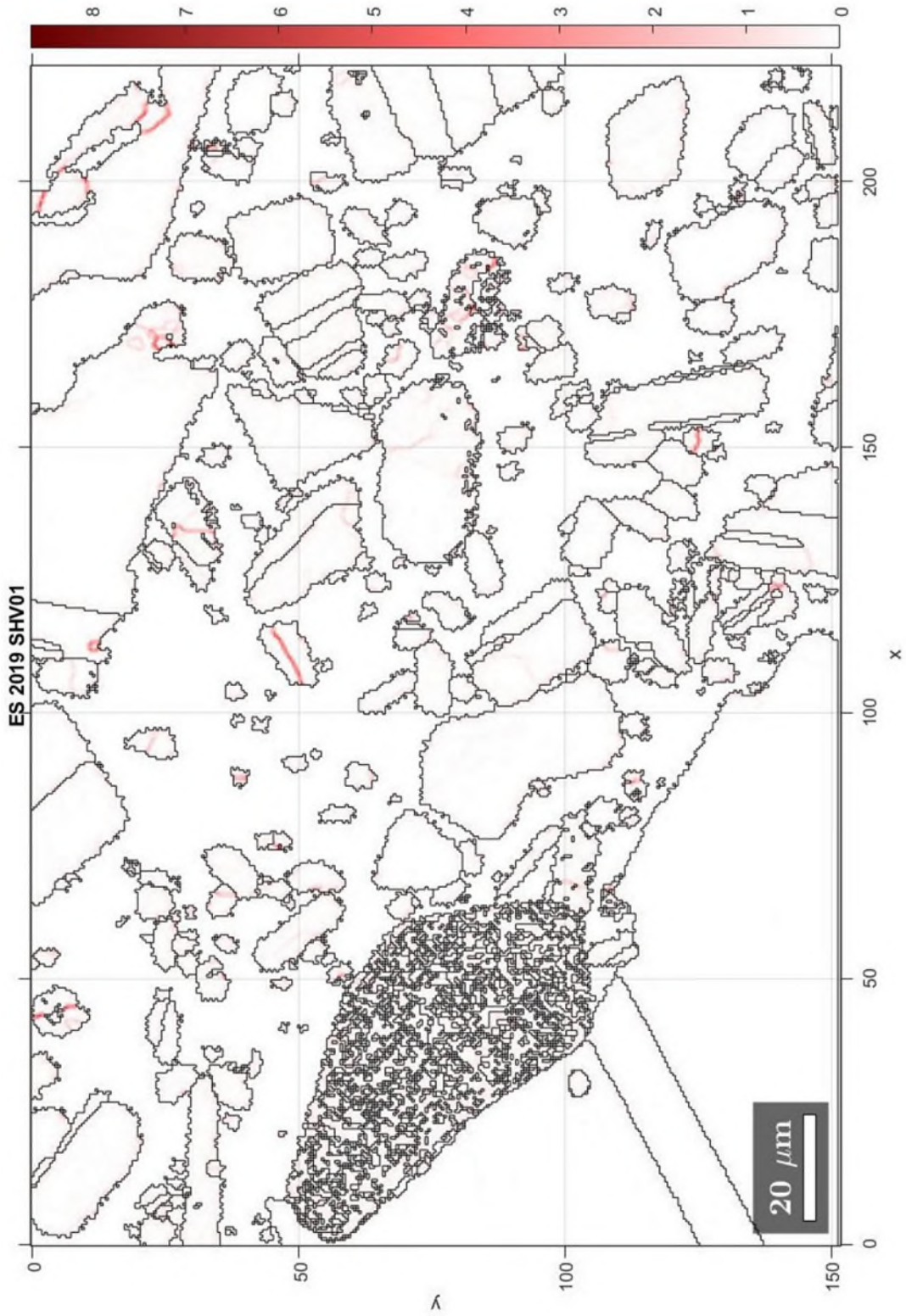


Figure A11c. Kernel average misorientation map for sample 2019_SHV01. 'Unbounded' map, produced without a threshold angle for the KAM data extraction.

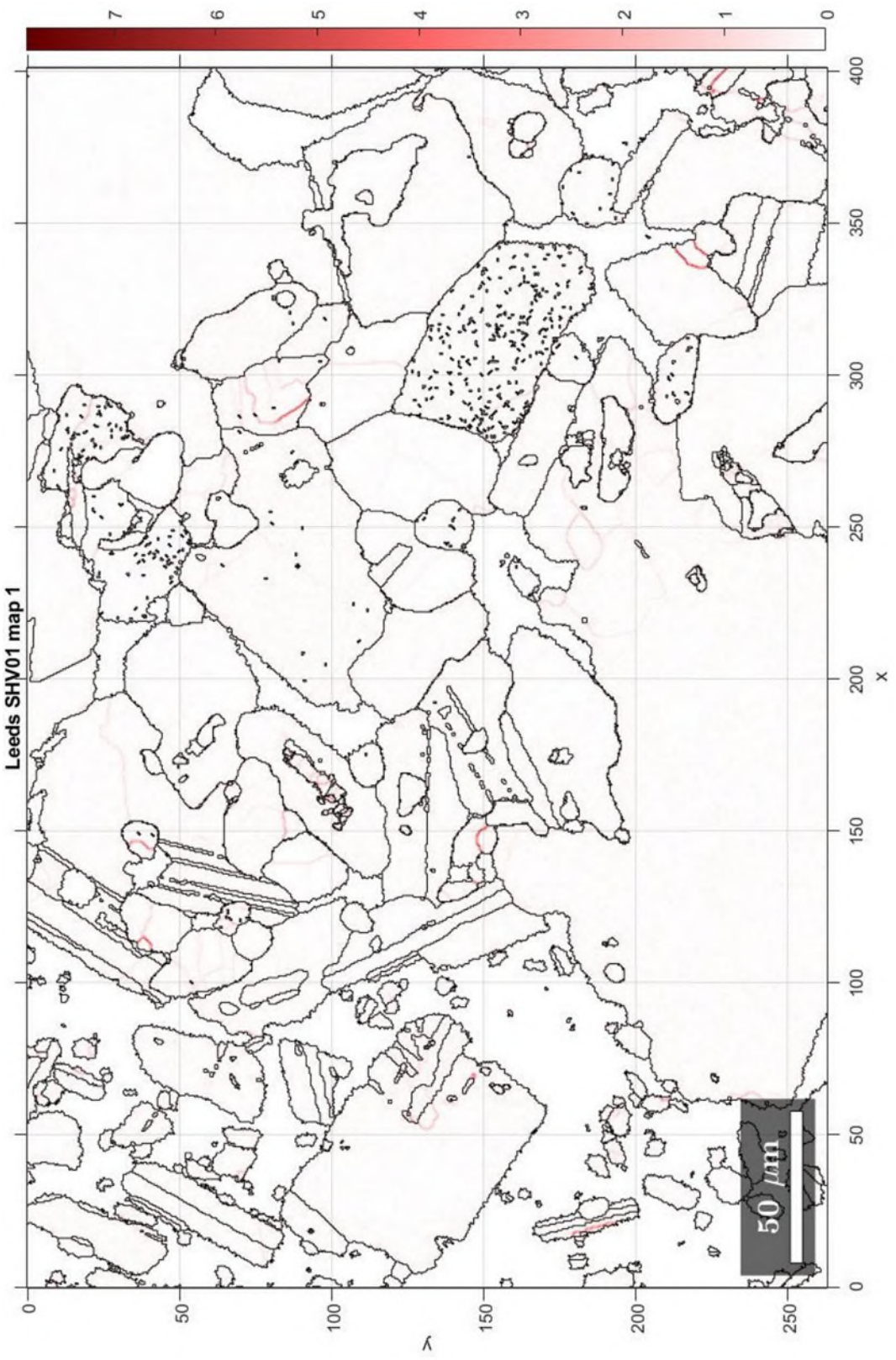


Figure A11d. Kernel average misorientation map for sample Leeds_SHV01_map1. 'Unbounded' map, produced without a threshold angle for the KAM data extraction.

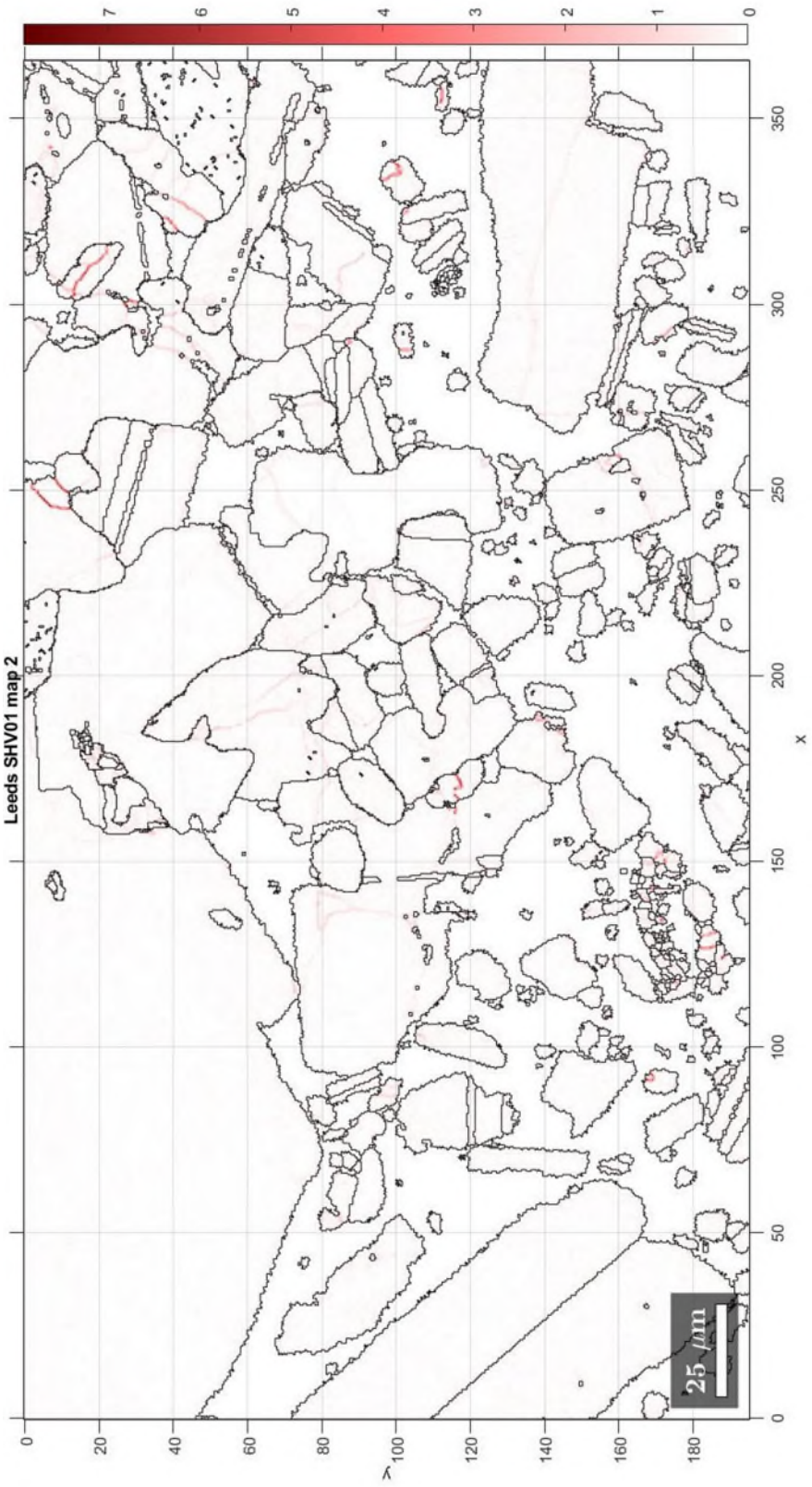


Figure A11e. Kernel average misorientation map for sample Leeds_SHV01_map2. 'Unbounded' map, produced without a threshold angle for the KAM data extraction.

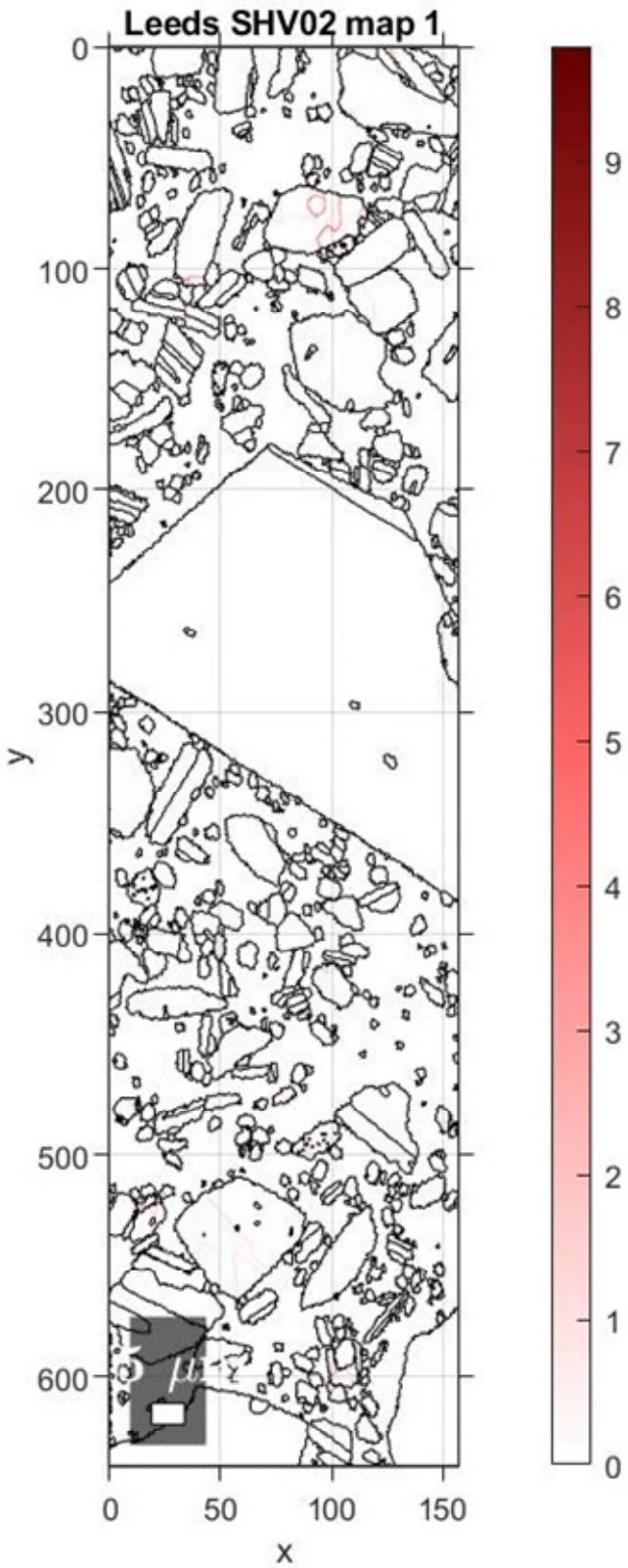


Figure A11f. Kernel average misorientation map for sample Leeds_SHV02_map1. 'Unbounded' map, produced without a threshold angle for the KAM data extraction.

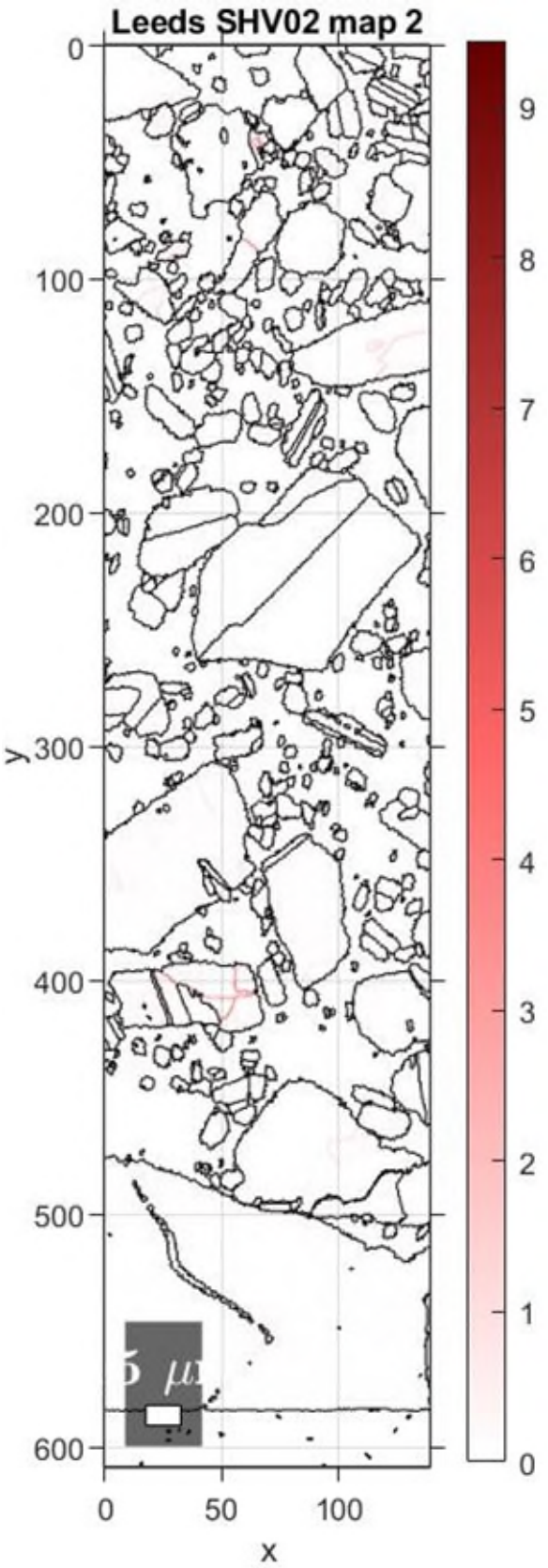


Figure A11g. Kernel average misorientation map for sample Leeds_SHV02_map2. 'Unbounded' map, produced without a threshold angle for the KAM data extraction.

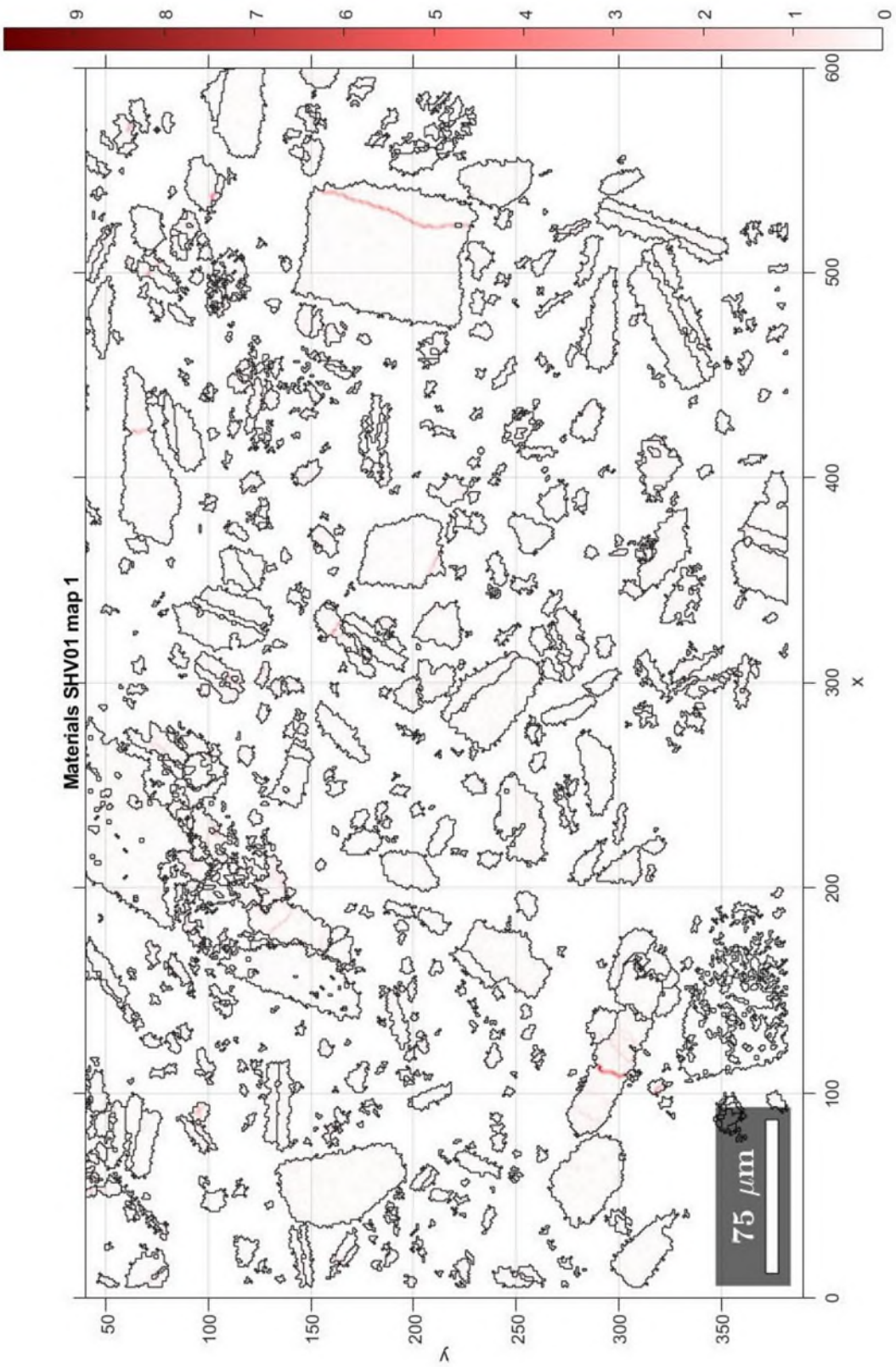


Figure A11h. Kernel average misorientation map for sample Materials_SHV01_map1. 'Unbounded' map, produced without a threshold angle for the KAM data extraction.

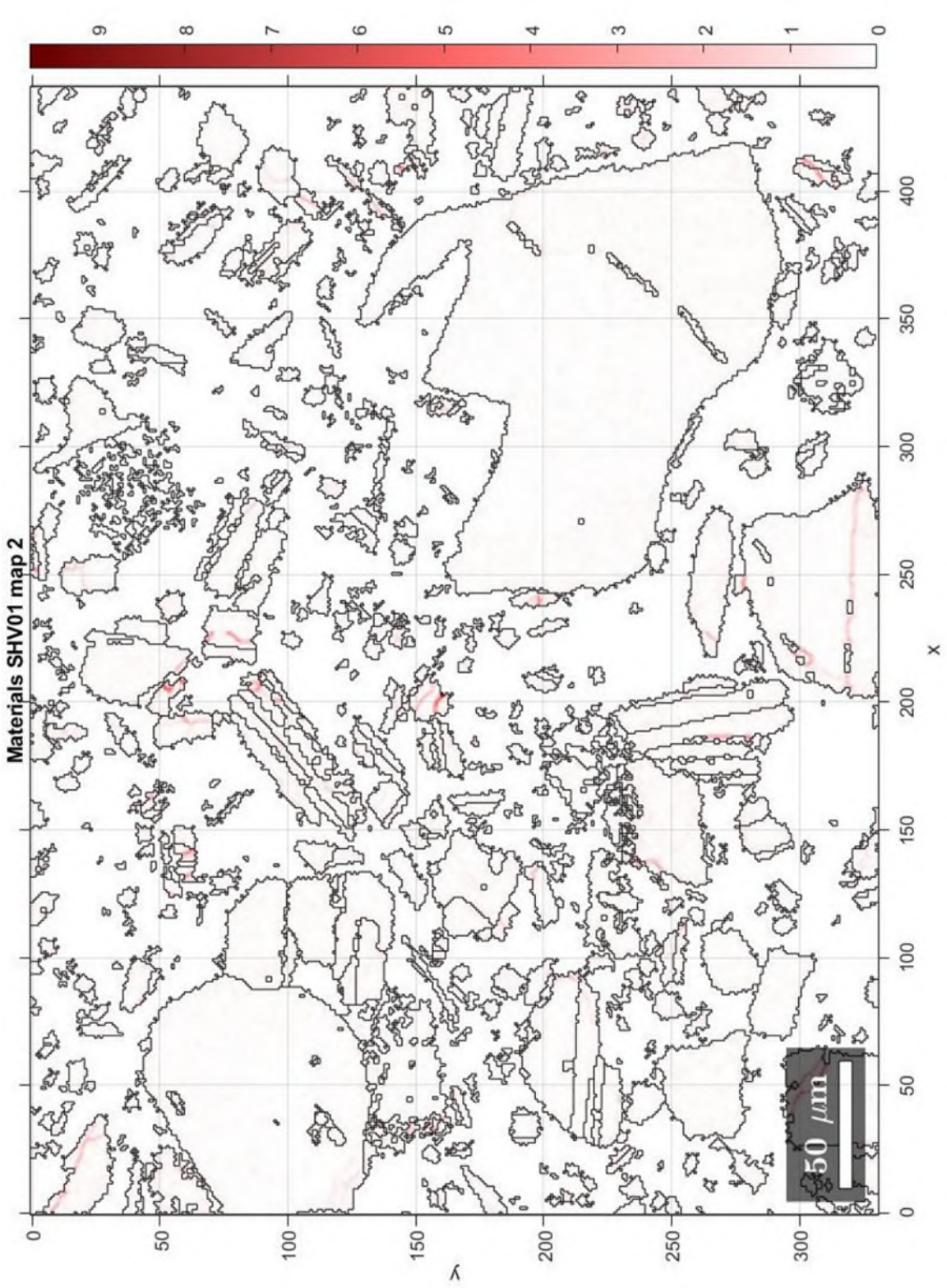


Figure A11i. Kernel average misorientation map for sample Materials_SHV01_map2. 'Unbounded' map, produced without a threshold angle for the KAM data extraction.

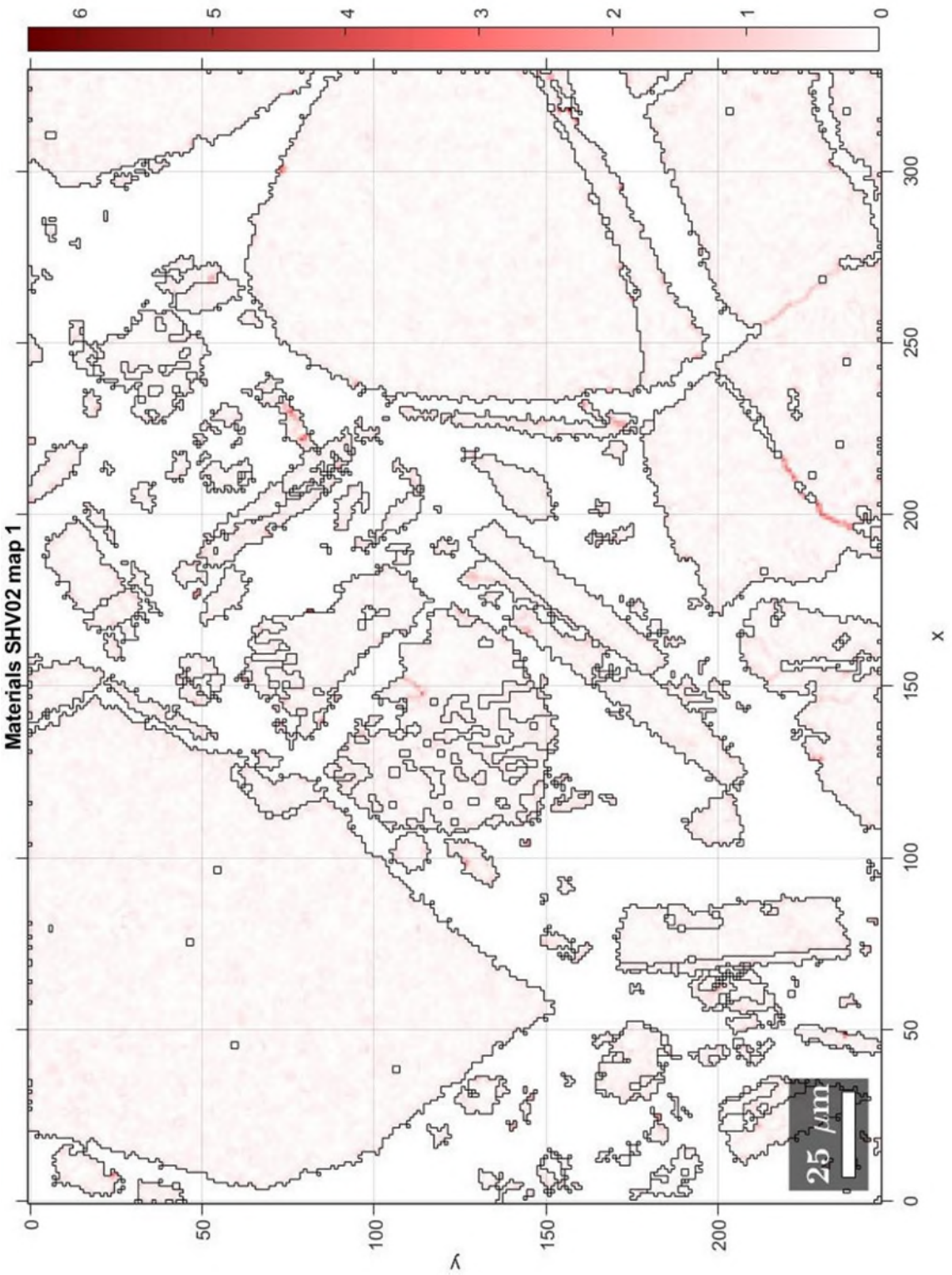


Figure A11j. Kernel average misorientation map for sample Materials_SHV02_map1. 'Unbounded' map, produced without a threshold angle for the KAM data extraction.

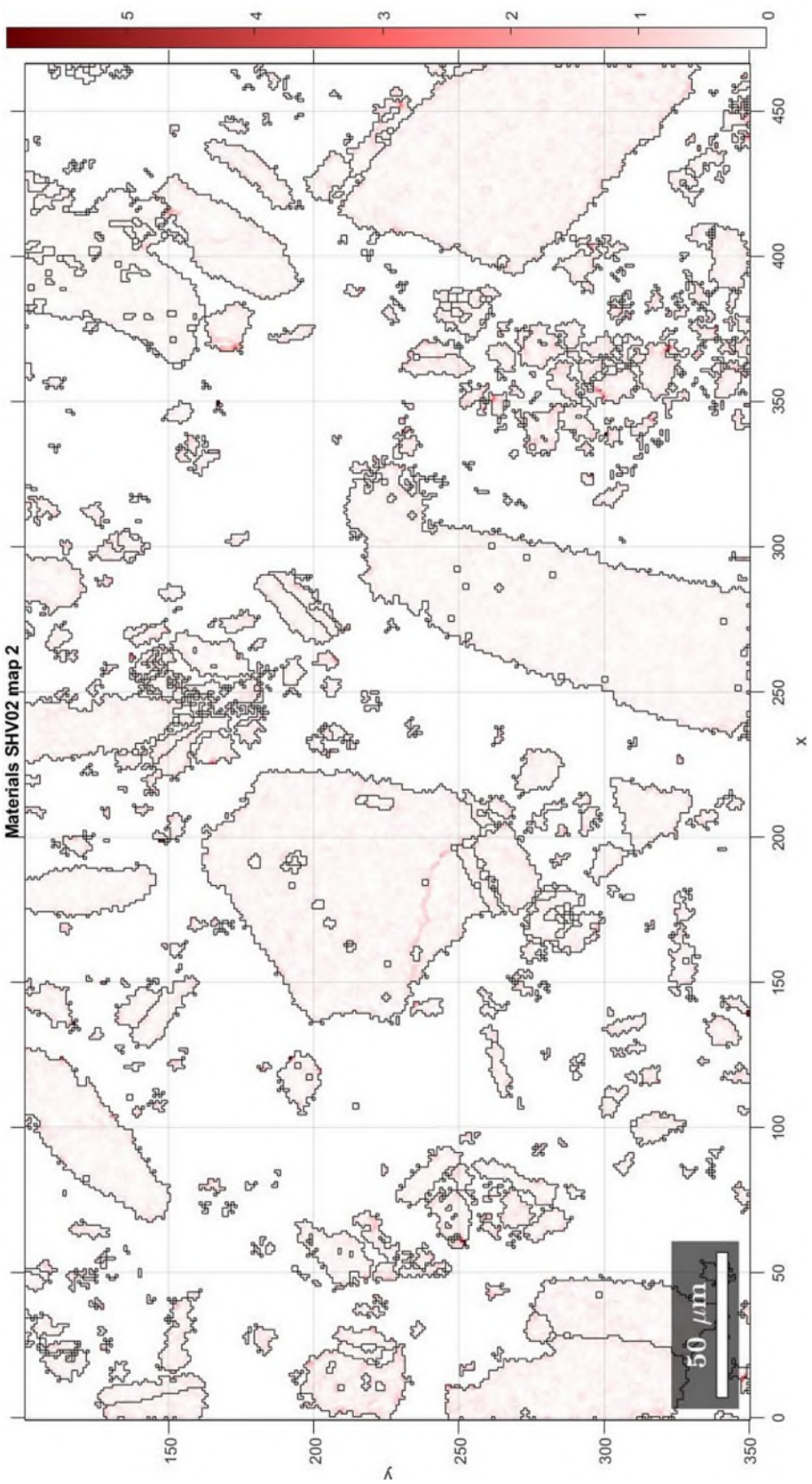


Figure A11k. Kernel average misorientation map for sample Materials_SHV02_map2. 'Unbounded' map, produced without a threshold angle for the KAM data extraction.

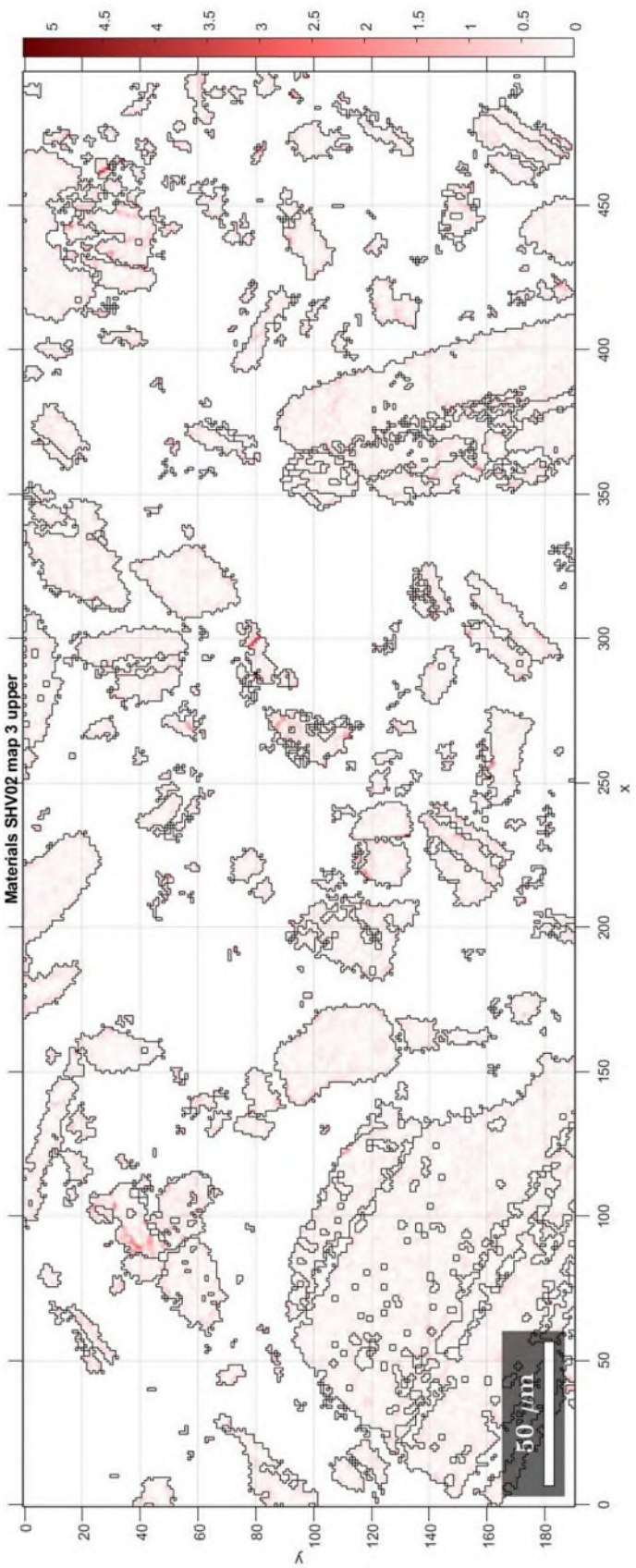


Figure A11l. Kernel average misorientation map for sample Materials_SHV02_map3_upper. 'Unbounded' map, produced without a threshold angle for the KAM data extraction.

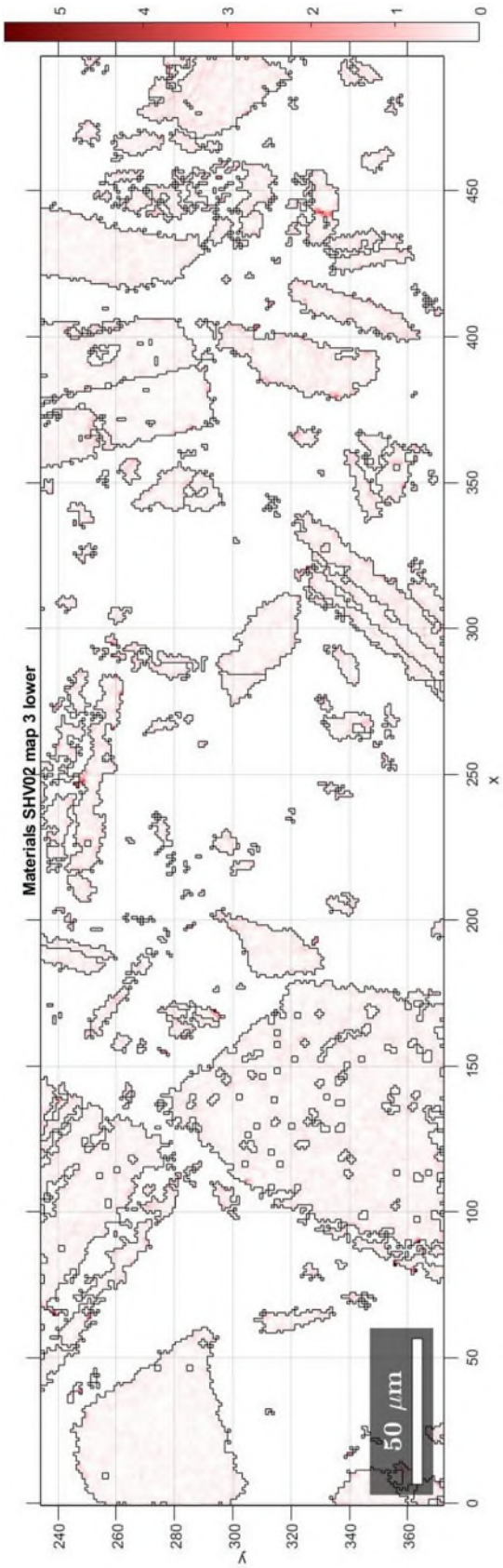


Figure A11m. Kernel average misorientation map for sample Materials_SHV02_map3_lower. 'Unbounded' map, produced without a threshold angle for the KAM data extraction.

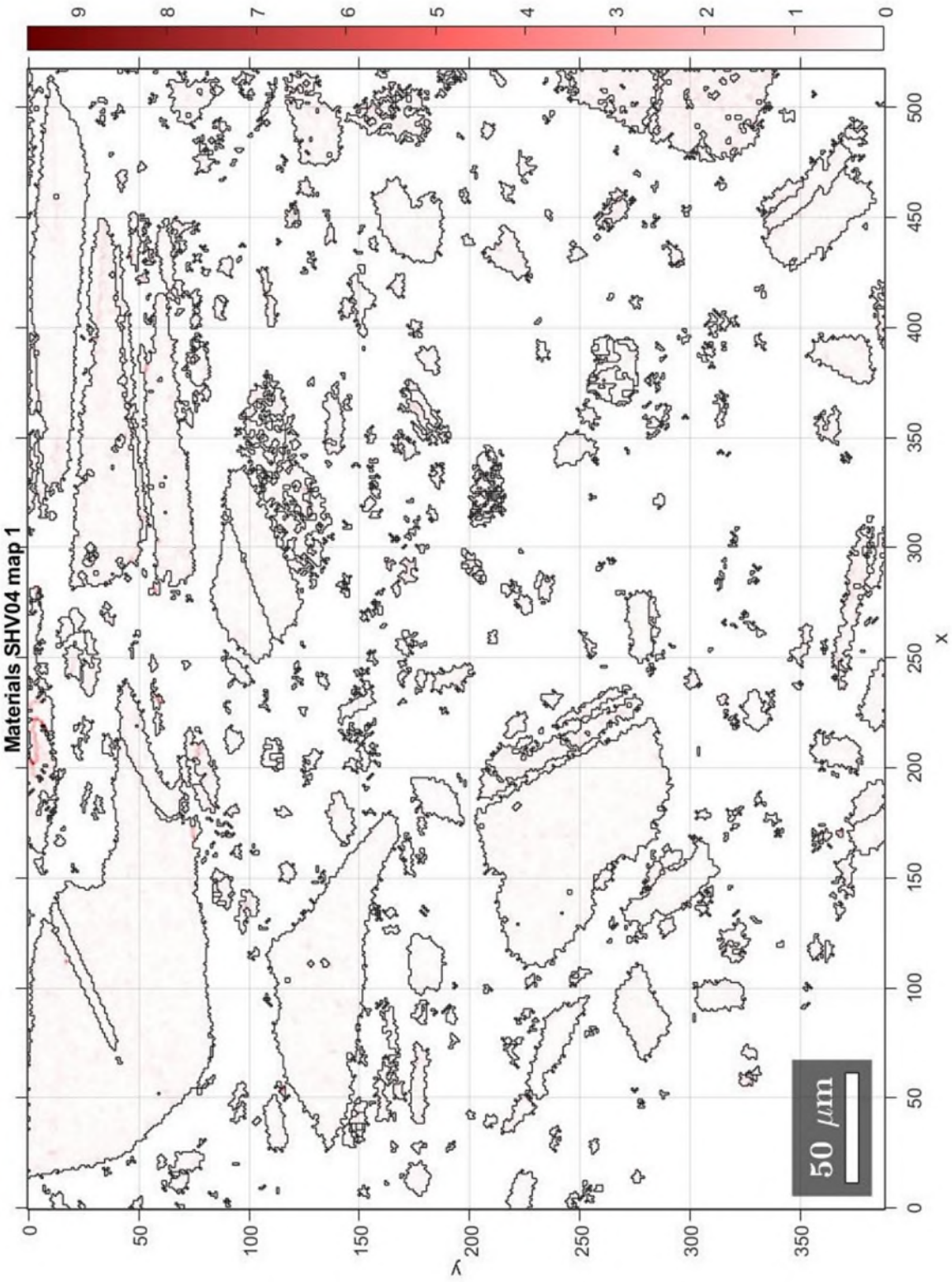


Figure A11n. Kernel average misorientation map for sample Materials_SHV04_map1. 'Unbounded' map, produced without a threshold angle for the KAM data extraction.

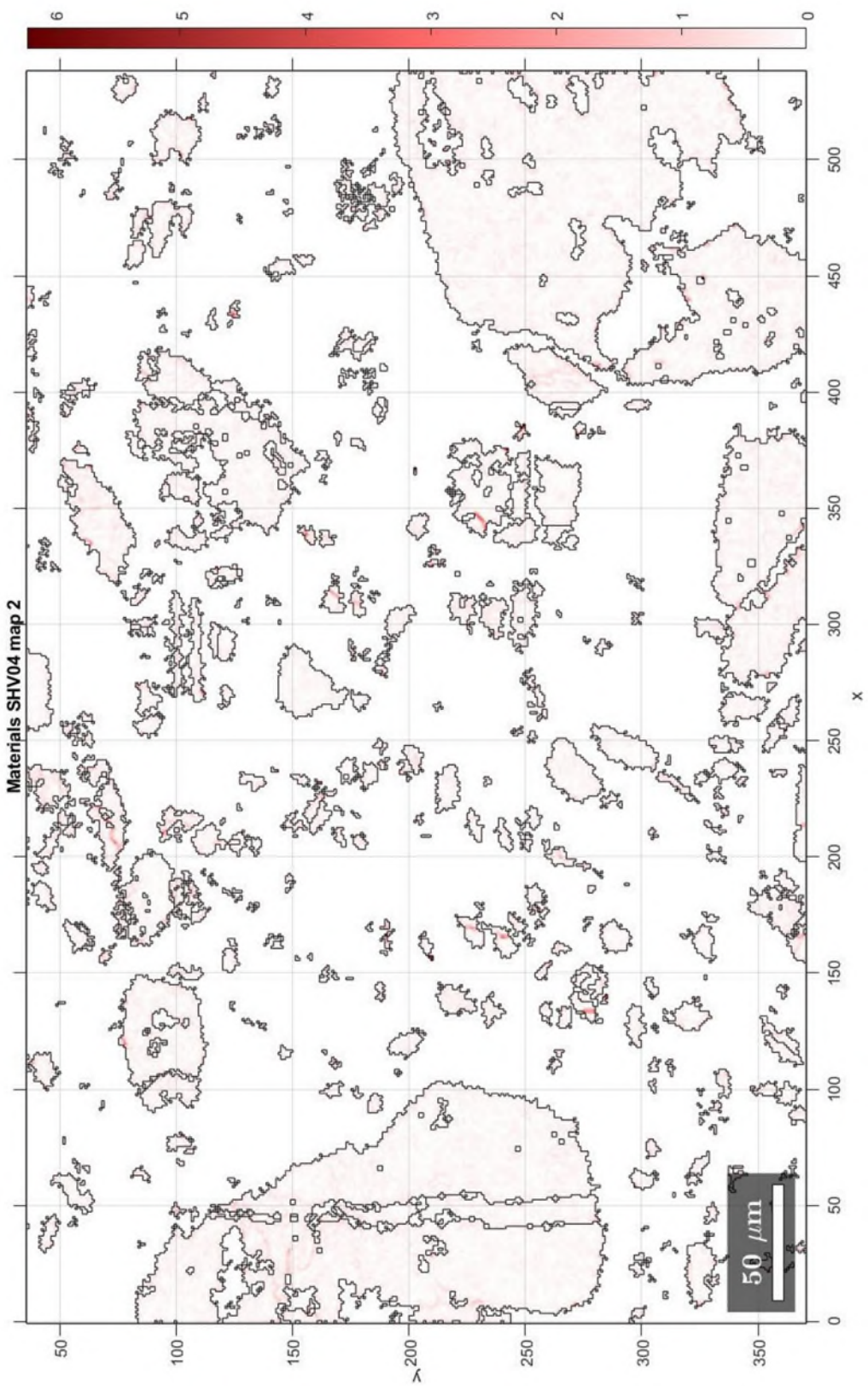


Figure A11o. Kernel average misorientation map for sample Materials_SHV04_map2. 'Unbounded' map, produced without a threshold angle for the KAM data extraction.

Appendix 12: KAM histograms raw data.

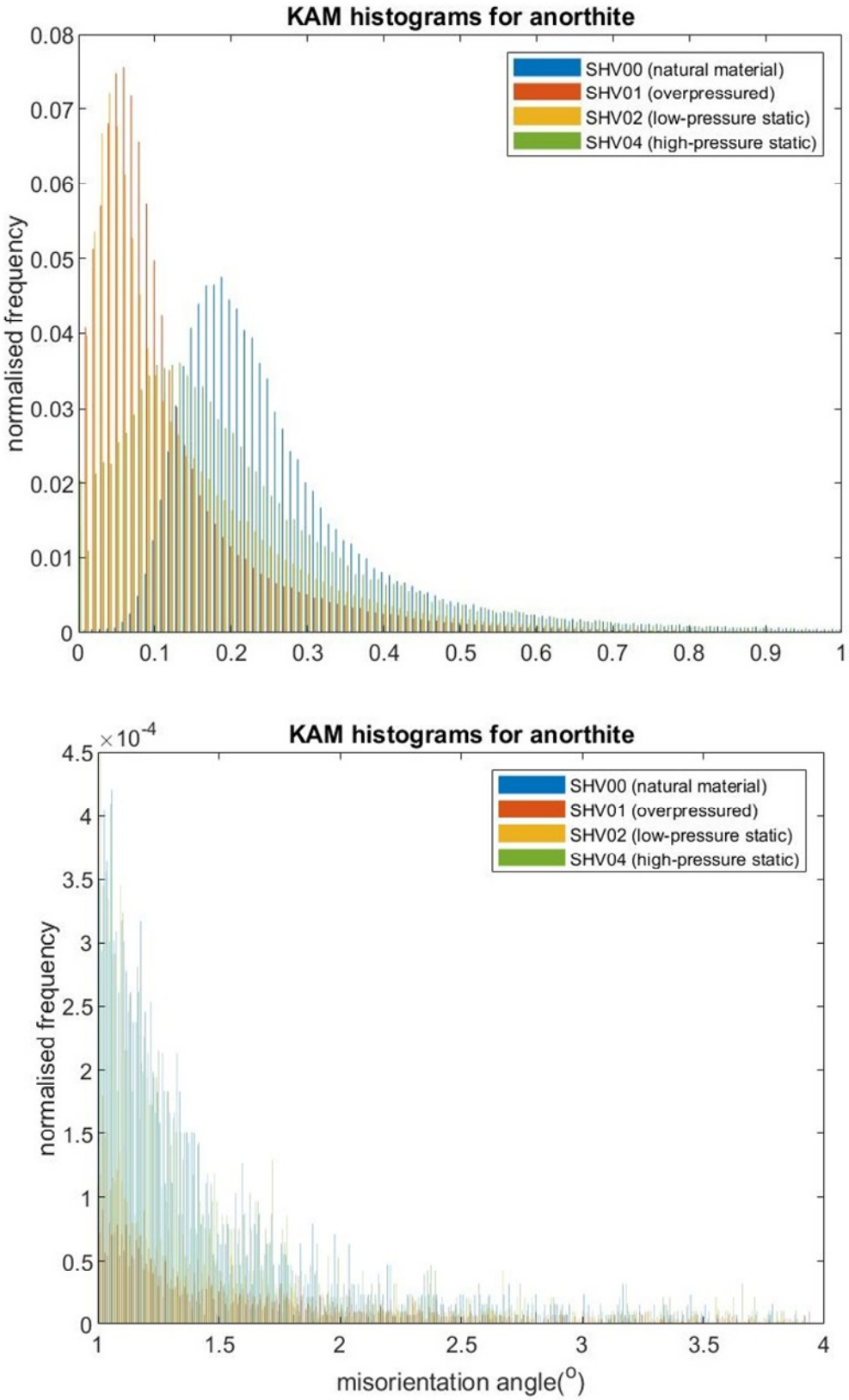


Figure A12a. Kernel average misorientation histograms for the anorthite phase only, for misorientation ranges of 0-1° (upper) and 1-4° (lower).

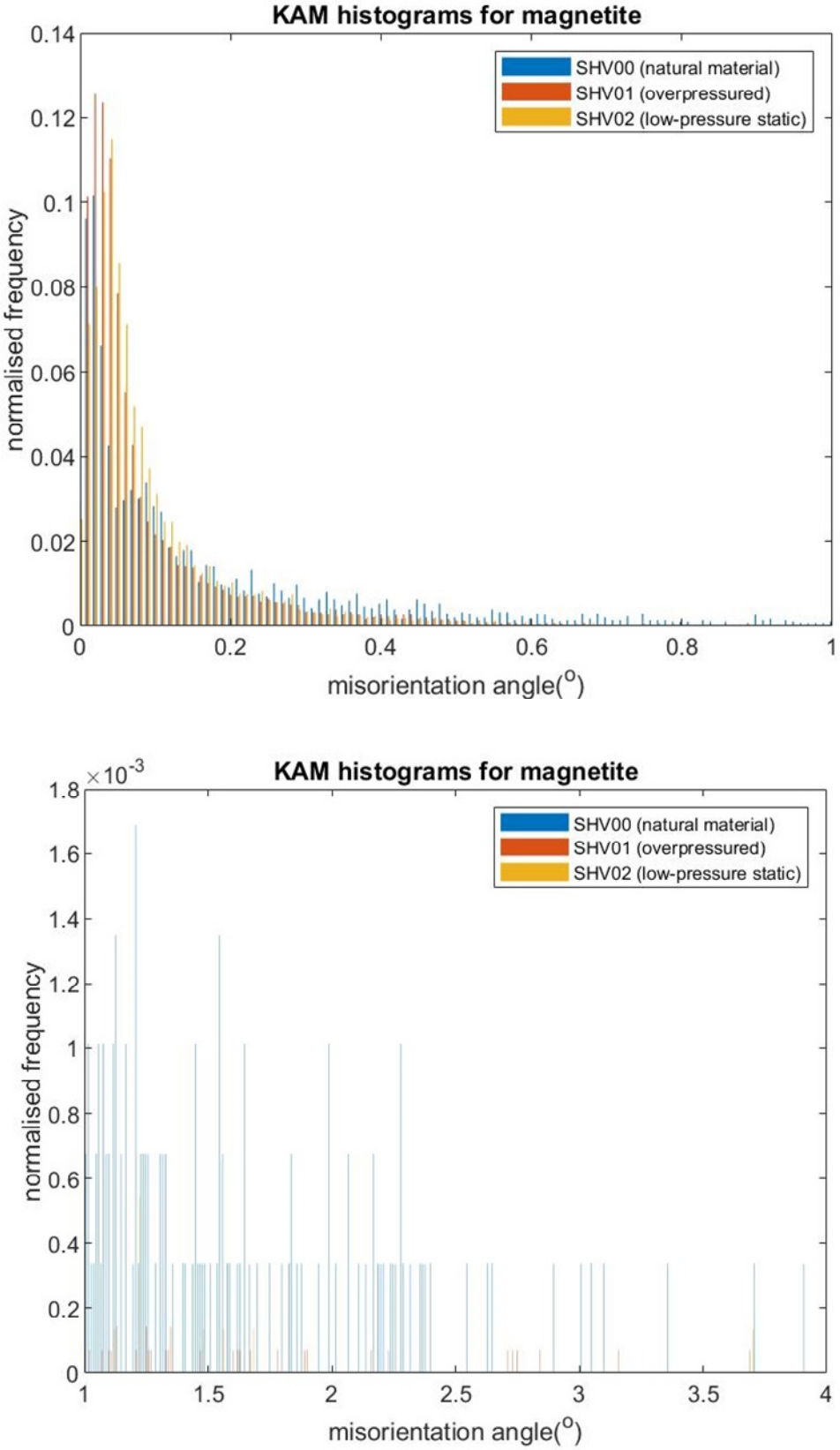


Figure A12b. Kernel average misorientation histograms for the magnetite phase only, for misorientation ranges of 0-1° (upper) and 1-4° (lower).

Data appendices

Data appendix 1

Rhyolite-MELTS outputs used to calculate the overpressure plots shown in figure 2.1 can be found at the following location

http://dx.doi.org/10.5287/ora-g7jvkvpxz

Rhyolite-MELTS outputs used to calculate the overpressure plots shown in figure 2.2 can be found at the following location

http://dx.doi.org/10.5287/ora-j5bjxv6b1

These excel files show changes in system volume, compressibility, volume change and overpressure during cooling for simulations with varying volatile contents.

Data appendix 2

A sample of the Matlab code developed by Weber *et al*. (2020) and modified for use in this thesis can be found at the following location

http://dx.doi.org/10.5287/ora-7jknvngrg

This code will generate the overpressure evolution for a reservoir embedded at 4 km depth, with a radius and height of 1 km. This example uses MELTS outputs for Kelud, for the 3.4 wt% H_2O (no CO_2) simulation, shown by the thicker line in figure 2.3a. Temporal evolution of overpressure is contained in the 'Op_vector' variable. It can be modified for other systems by changing the 'data' (temperature-melt fraction) and 'Op_data' (temperature-overpressure) inputs.

Data appendix 3

The raw data used for the EBSD analysis in chapter 3 can be found at the following locations.

http://dx.doi.org/10.5287/ora-7qawwqkqa

http://dx.doi.org/10.5287/ora-vjxran7bx

http://dx.doi.org/10.5287/ora-8j7qve9n9

http://dx.doi.org/10.5287/ora-nzxnperb4

http://dx.doi.org/10.5287/ora-6qyobdrvd

http://dx.doi.org/10.5287/ora-pvadm5me0

http://dx.doi.org/10.5287/ora-8r5gngbn9

http://dx.doi.org/10.5287/ora-2anmaaj2e

http://dx.doi.org/10.5287/ora-b7bzqkvgo

http://dx.doi.org/10.5287/ora-r5kpeo084

http://dx.doi.org/10.5287/ora-go4zeypko

http://dx.doi.org/10.5287/ora-qzpvxagnz

http://dx.doi.org/10.5287/ora-b7mpvo2mb

http://dx.doi.org/10.5287/ora-9o8bwznvv

These files can be imported into MTEX to generate the maps presented in this thesis. The name of the files indicates where the data was collected. Data labelled '_Oxford_ES' was collected in the Earth Sciences department at the University of Oxford, '_Leeds' was collected by Dr Richard Walshaw in the School of Earth and Environment at the University of Leeds, and '_Oxford_Mat' refers to data collected in the Materials Department at the University of Oxford.